Transmission-Line Modelling of Microstrip Antennas and Their Application in Fixed-Frequency Beam Steering

By

Budhaditya Majumdar

A thesis submitted to Macquarie University

for the degree of

Doctor of Philosophy

Department of Engineering

January 2017

MACQUARIE
University
SYDNEY·AUSTRALIA
FACULTY OF SCIENCE AND ENGINEERING

Typeset in LaTeX 2_ε.

Except where acknowledged in the customary manner, the material presented in this thesis is, to the best of my knowledge, original and has not been submitted in whole or part for a degree in any university.

Budhaditya Majumdar

To my parents

Acknowledgements

After a long and hard three years, the time has come to write the last part of my thesis and acknowledge those who have helped me to get to this point. Writing this last bit feels like moving back in a time machine, where everything started from scratch. A lot of people have supported me during the tenure of Ph.D. fellowship both inside and outside of the University. I thank all of them and mention a few here.

First of all, I would like to thank my supervisor, Professor Karu Esselle, for giving me the opportunity and guiding me as I have delved deeply and thoroughly into microwave theory and antennas. Without his support, I would not have gotten to this stage. I would also like to thank my associate supervisor, Professor Mike Heimlich, for continuous motivation and enlightenment.

I would like to thank Mr. Peter Ronald Moore for motivating me to come to Australia. I would not have known him if I had not read his article, "An Ordinary Bloke," about his late father Mr. Ronald Allen Moore, IPS.

I would like to thank Late Emeritus Professor Subhas Chandra Chakravartty, who acted as a referee for my Ph.D. application but left this world on the week of my enrolment. I only came to know of his passing a year after I had been in Australia wondering continuously why he never replied to my e-mail.

I would like to thank Mr. Varun Bijlani, Managing Partner and General Manager, IBM UK, Mr. Deepak Arora, Delivery Leader, IBM GBS India, and Mr. Pavi Agarwal, Associate Director, Cognizant US for acting as referees from the industry for my Ph.D. application.

I am immensely grateful to my uncle, Dr. Rahul Basu, and my aunt, Mrs. Ritta Martin Basu for their help during my applications. Without them, I could never have written this page in the first place.

I am thankful to the faculty members and my colleagues for helping and guiding me initially and continuously. And I am grateful to my housemates, Dr. Usman Afzal and Dr. Ishan Rastogi for bearing with my tantrums and helping with the house whenever required. Additionally, I thank Usman for helping me with some initial measurements at AusAMF, CSIRO.

I am sincerely grateful to my dear friend, colleague and would be Dr. Sudipta Chakraborty for being with me, supporting me and helping me with free food as well as manufacturing of the prototypes required as a part of my Ph.D.

No amount of acknowledgements will ever be sufficient when it comes to my parents, Mr. Byomkesh Majumdar, WBCS (Retd) and Mrs. Bichitra Majumdar. My parents are the primary reason I became an engineer a decade before I was formally trained as one. They have sacrificed everything to help me grow and succeed, and whenever I failed, they have provided caring support. I dedicate this thesis to them.

Last but not the least, I am thankful to Macquarie University for granting me the iMQRES Scholarship.

List of Publications

Articles

- B. Majumdar and K. P. Esselle *Fixed frequency broadside–endfire beam steerable antennas.*. Electronics Letters **52**, 1282-1284 (2016)

- B. Majumdar and K. P. Esselle *Extended transmission-line modelling of inset-fed reconfigurable rectangular microstrip antennas.* Progress In Electromagnetics Research B **68**, 128-140 (2016)

- B. Majumdar and K. P. Esselle *A dual-mode reconfigurable patch antenna and an extended transmission line model.* Microwave and Optical Technology Letters **58**, 57-61 (2016)

Conferences

- B. Majumdar and K. P. Esselle *Modelling the effect of a thin shorting post in an arbitrary position along the outer radiating edge of a rectangular patch antenna.* (2015 International Symposium on Antennas and Propagation (ISAP), Hobart, Tasmania, Australia)

- B. Majumdar and K. P. Esselle *A Single Band Beam Scanning Active Phased Array.* (2016 International Conference on Electromagnetics in Advanced Applications (ICEAA / IEEE AWPC), Cairns, Queensland, Australia)

- B. Majumdar and K. P. Esselle *A Simple Reconfigurable Patch Antenna for Mobile Applications.* (2015 IEEE International Symposium on Antennas and Propagation & USNC/URSI National Radio Science Meeting, Vancouver, British Columbia, Canada)

Others

- S. Chakraborty, B. Majumdar, M. Heimlich and K. P. Esselle *A Simple Reconfigurable BiCMOS Active Inductor and Its Implementation in A Phase-Shifter Unit Cell.* (2015 International Symposium on Antennas and Propagation (ISAP), Hobart, Tasmania, Australia)

- S. Chakraborty, B. Majumdar, M. Heimlich and K. P. Esselle *SiGe HBT Based Impedance Switch for On-Chip Antenna Reconfigurability.* (2015 Australian Symposium on Antennas, Sydney, New South Wales, Australia)

- B. Majumdar, D. Baer, S. Chakraborty, K. P. Esselle and M. Heimlich *A 3D Printed Dual-Ridged Horn Antenna.* (2016 International Conference on Electromagnetics in Advanced Applications (ICEAA / IEEE AWPC), Cairns, Queensland, Australia)

- B. Majumdar, D. Baer, S. Chakraborty, K. P. Esselle and M. Heimlich *Additive Manufacturing of a Dual-Ridged Horn Antenna.* Progress in Electromagnetics Research Letters **59**, 109-114 (2016)

- B. Majumdar, D. Baer, S. Chakraborty, K. P. Esselle and M. Heimlich *Advantages and limitations of 3D printing a dual-ridged horn antenna.* Microwave and Optical Technology Letters **58**, 2110-2117 (2016)

Abstract

Planar antennas are paramount in today's world because they can be embedded easily into portable devices such as laptops, mobile phones, etc. *Beam* or the radiation with directivity is important because it gives a suitable range advantage than omnidirectionally radiating antennas with the same power. *Steerability* can provide the flexibility of the omnidirectional antenna and the benefit of a directional antenna; provided that multiplexing is possible. Reconfigurable antennas that can radiate multiple patterns at a single frequency or a single spectrum are necessary for modern telecommunication systems. The requirements for increased functionalities like direction finding, beam steering, radar, control, and command, within a confined volume place a greater burden on today's transmitting and receiving systems. Reconfigurable antennas offer an exceptional solution to this complex engineering problem.

This thesis contains the design of two particular fixed frequency beam-steerable antennas. The antennas are cost effective from the industrial perspective, and reliable for long term maintenance free use. The first one is a fixed frequency active phased array antenna. The relevant chapter showcases the layouts and results for two 1×2 variants and one 2×2 variant. Initial development of accurate transmission-line models gave the insight of developing a fixed frequency active phased array antenna. Initial chapters outline the transmission-line modelling of single tunable and reconfigurable rectangular microstrip antenna elements. Analytically obtained values reasonably agree with the results achieved from measurements and simulations, for numerous designs based on multiple substrates. The active phased array antenna can steer its beam up

to 25°.

The limitations of the phased array antennas led to the design of the second fixed frequency beam-steerable antenna. The second beam-steerable relies on a switchable ground plane that can reflect or transmit electromagnetic waves. The second antenna has a steerable beam that radiates either in the broadside or the endfire region. The antenna can cover up to 133° in the H-plane. Later chapters in this thesis discuss the transmission-line modelling of the reconfigurable surface with numerous examples, and its operation as a surface waveguide. The examples for the transmission-line model demonstrate reasonable agreement with simulation results for different substrate thickness and with or without a dielectric cover.

The thesis presents a comprehensive overview of simulation and measurement results for multiple antenna designs backed by a reliable transmission-line model insight. Substantial area coverage is possible with the proposed antennas. Behavioural modelling software can benefit from the models discussed to create quick design solutions without wasting time for full-wave numerical calculations.

Contents

List of Figures

List of Tables

"The true laboratory is the mind, where behind illusions we uncover the laws of truth."

Acharya Sir Jagadish Chandra Bose

1

Introduction

Antenna, as we know it today is much more than a translation of 'pole' from Italian, since its first use by Guglielmo Marconi in 1895. It is a word that made the world smaller, the universe closer and the beyond visible. Technically it is a device that helps in the translation of electrical signals into electromagnetic waves that spread out into space and vice-versa. Most common forms of this device spread out this form of energy equally in all directions and are known as *Omnidirectional Antennas*. Some of the specially designed antennas are made to radiate the waves in a fixed direction of space and are known as *Directional Antennas*. Any particular antenna that has the capability of selecting one of many courses in a defined time of space is called a *Beam Steerable Antenna*, where the obvious point is the shape of the radiation pattern, termed as the *Beam*.

RADAR, the acronym for **RA**dio **D**etection **A**nd **R**anging, was possibly the first

FIGURE 1.1: Lee Davenport (left) leaning against his invention, an SCR-584, in 1942, with Ivan Getting and Lt. Col. Arthur H. Warner. *(Image courtesy of MIT Radiation Laboratory)*

Beam Steerable Antenna designed in and around the Second World War. Electro-mechanical systems supported the movement of the Beam. Figure 1.1 shows a RADAR from the World War II era. During the same period, another RADAR design was demonstrated by Nobel Laureate Luis Alvarez using *Phased Arrays*. A Phased Array system has multiple antenna components, each of which radiates with a phase difference that either is constructive or destructive with others. This phenomenon helps the overall Beam to be directive in nature.

Phased array antennas are still the dominant *Beamforming* antenna, but a lot of research is going on in the areas of Beam Steering with other kinds of structures such as *Lens*, *Metamaterials* and *MEMS*. Some of the recent work has been covered in the Literature Survey.

A revolutionary antenna came into existence in the 1970s that changed the antenna designers' viewpoint and went on to become the most successful antenna regarding

production and use. The *Microstrip Antenna* is a low-profile, planar, lightweight and easy to manufacture antenna that can also be integrated with semiconductor devices. As of 2010, 82 out of 528 papers published in *IEEE Transactions on Antennas and Propagation* address microstrip antennas [1].

1.1 Motivation

Beam steerable antennas, if they are made low-profile and cheap, have a lot of commercial interests. One of the most appealing prospects for this technology would be wireless connectivity with external drives and devices, or better Wi-Fi connectivity at lower power consumption. Steering of the radiation using an antenna which can scan at a fixed frequency is an attractive solution. An added advantage would be the possibility of multiplexing between two devices or two simultaneous connections over the same frequency.

The choice of planar antennas seems obvious, as the status of microstrip antennas suits the very necessity of the commercial interests. The low-profile, low-power planar antenna would be easy to integrate into laptops, external drives, mobile phones, etc. So much is the benefit that it can also be printed on paper and used inside gaunt devices.

The planar antennas are also equally important for satellite and space communications, where, it is preferred to have a planar surface than to have an antenna with protruding structures.

1.2 Reconfigurable Antennas

As technology progresses, the demand for small devices has increased. However, mechanical tuning consumes a lot of space. For smaller devices, electronic reconfiguration is always advantageous. Reconfiguration is possible for the resonance frequency of the antenna, the direction of radiation or its polarization. Traditionally reconfiguration is done with the help of PIN diodes or varactor diodes. In recent times, MEMS

switches have gained popularity. Modern PIN diodes and varactor diodes have minuscule foot-stamps and easily integrates within miniature antennas. In this thesis, frequency reconfigurable and pattern reconfigurable antennas are discussed.

1.3 Transmission-Line Modelling

Analytical models provide better insights into an antenna. Cavity models and transmission-line models are the most common form of analysis of microstrip antennas. Among these two, transmission-line models are easily understood and visualised. The insights obtained from an antenna model can be used to re-create prototypes in another band or with any other dielectric substrate with ease. Such models may be used to create software programs to generate physical dimensions from input specifications. In this thesis, some transmission-line models are analysed and discussed.

1.4 Objectives

The objectives of this thesis are:

(i) Accurate modelling of the inset-feed of a rectangular microstrip antenna.

(ii) Modelling of a rectangular microstrip antenna with a thin shorting post arbitrarily placed at any position of the outer radiating edge.

(iii) Modelling of frequency reconfigurable antennas and testing the accuracy with multiple test cases.

(iv) Designing an array of the reconfigurable rectangular microstrip antenna previously analysed to achieve voltage controlled beam steering.

(v) Creating a reconfigurable meta-surface to stop or allow electromagnetic waves incident on it.

(vi) Creating a surface waveguide using the reconfigurable meta-surface.

(vii) Creating a different beam steerable antenna to achieve broad-side end-fire pattern reconfiguration using the reconfigurable meta-surface.

1.5 Thesis Overview

This thesis documents two entirely different beam steerable antennas and relevant transmission-transmission line models. Chapter 3 to Chapter 6 develops the transmission-line model of tunable rectangular microstrip antennas and their application to fixed frequency voltage controlled beam steering. Chapter 7 to Chapter 9 documents a reconfigurable meta-surface and its use in a surface waveguide and a broadside-endfire beam steering. The following paragraphs provide a brief summary of the thesis chapters.

Short literature reviews in Chapter 2 covers all the work done in this thesis. Each chapter from Chapter 3 onwards also contains explicit background information. Chapter 2 mostly gives an idea about the existing models and antennas already available.

Measured complex reflection coefficients are in good agreement with the empirical transmission-line model for inset-feed rectangular microstrip antenna documented in Chapter 3. Two different rectangular microstrip antennas were used to verify the accuracy of the inset-feed transmission-line model.

Tuning a rectangular microstrip antenna with one thin shorting post placed at any arbitrary position of the outer radiating edge is documented in Chapter 4. Measurements are in alignment with transmission-line model results derived in this part.

Extensions of the previously derived model to include lumped models of PIN diodes and varactor diodes are available in Chapter 5. Comparison of forty-two test cases over five different rectangular microstrip antennas with varactor diodes concluded the limitations of the model. This part also contains a brief discussion of the transmission-line model extension with PIN diodes.

Designs of fixed frequency beam-steerable antennas with two and four active rectangular microstrip elements are conducted and documented in Chapter 6. The antennas use voltage controlled beam-steering.

Chapter 7 contains the transmission-line analysis of a reconfigurable meta-surface. The surface either reflects or allows the incident wave to pass through it depending on the status of different PIN diodes.

Chapter 8 used the unit-cell described in Chapter 7 to demonstrate a periodically

loaded surface waveguide.

Chapter 9 finally documents a novel broadside-endfire beam-steerable antenna. The single element antenna radiates towards broadside or endfire direction depending on the PIN diodes. This antenna uses the reconfigurable surface introduced in Chapter 7.

Finally, Chapter 10 concludes the thesis with the most likely future extensions of the work and its industrial applications.

"In Science, it is when we take some interest in the great discoverers and their lives that it becomes endurable, and only when we begin to trace the development of ideas that it becomes fascinating."

James Clerk Maxwell

2

Reconfigurable Antennas: Background

Resonance frequency, bandwidth, polarisation or radiation characteristics specify any form of antenna systems and variation of those parameters produce reconfigurability. Modern wireless and satellite communications systems heavily depend on reconfigurable antennas and the industry is moving towards a smart, software-defined and cognitive, radio-frequency and microwave systems. Reconfigurability helps to cope with extendable and reconfigurable multiservice, multistandard, and multiband operations, as well as with efficient spectrum and power utilisation.

Four domains primarily dominate the reconfigurable antenna design and manufacturing. The most primitive among these is the frequency-reconfigurable antenna. A tuning procedure changes the resonance frequency of the radiating structure. Polarisation reconfigurability was the next improvement. Dual polarisation and cross

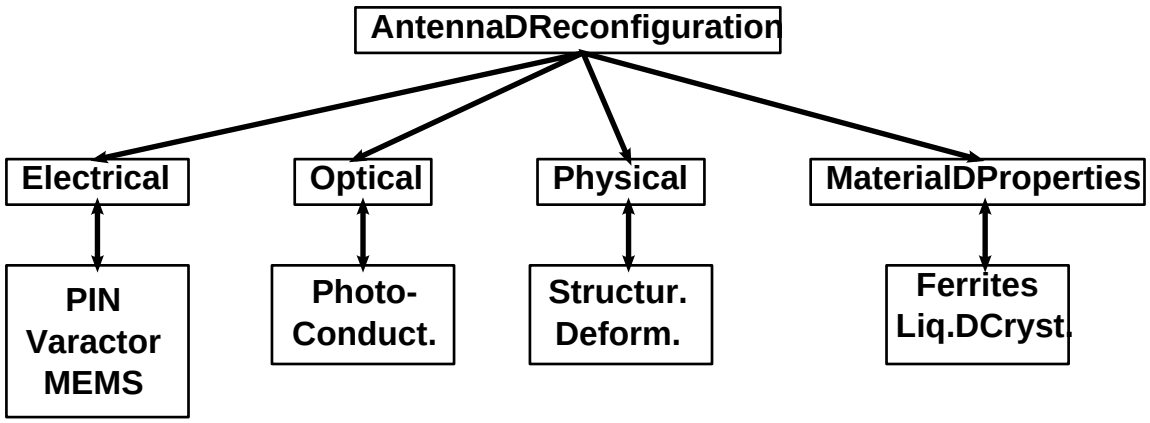

FIGURE 2.1: Common reconfiguration processes for antennas.

polarisation reconfigurable antennas became very popular. Radiation pattern reconfigurable antennas or beam steering antennas are in focus over the last two decades, and many different topologies are dominating the scientific community over the past ten years. The industries are trying to achieve all of these properties together in their new designs.

Many parameters of the antenna design are responsible for different kinds of reconfigurability. The physical structure, feeding network, surface current distribution, or modification in the radiating edges. Any change in any one of these can bring out a parasitic change among one or all the other parameters. It is a challenge for the antenna designers to meet the specifications after neutralising all the parasitic changes.

Few primary methods of reconfiguration include electrical, optical, structural and material properties. Fig. 2.1 shows the different categories used to implement a reconfigurable antenna. Electrical tuning using varactor diodes [2–7] and PIN diodes [8–19] are the most common with microelectromechanical switches (MEMS) [20–25] becoming a real choice for microwave and millimeter wave reconfigurable antennas. Optical switching of photoconductive element is also possible by illumination [26–30]. The movement of electrons from the valence band to the conduction band switches ON when there is an illumination. If there is no illumination, then the switch is turned OFF. Structural deformation also affects the antenna parameters [31–34]. Ferrites and

liquid crystals are examples of materials whose properties are variable. These kinds of materials are used to implement reconfigurable antennas [35–38].

The advantages of reconfigurable antennas are multifold [39–41]. Reconfigurable antennas are the ideal choice for software-defined radios. Low manufacturing costs and area requirements make them friendly towards handheld and low power consumer electronic products. Electronic control makes it easier to align with microcontrollers or other programmable devices. The design overhead naturally includes the bias networks for switching or tuning the active elements. Harmonics and intermodulation products are also a side effect of the active elements which have to be kept in mind.

2.1 Electrical Reconfiguration

Electrical reconfiguration is possible with RF field-effect transistors, RF bipolar junction transistors, PIN diodes, varactor diodes and MEMS. Out of these options, PIN diodes, varactors and MEMS are very commonly found in the existing literature. Easy integration is a tremendous advantage of using these devices. The effects of nonlinearity, losses, biasing, harmonics and interference would have to be kept in mind.

2.2 Optical Reconfiguration

A beam of light incident on silicon or gallium arsenide excites electrons, and they jump from the valence band to the conduction band. This phenomenon helps to create an optical switch [42]. Optical switches are usually linear, and they do not need biaslines. The most important aspect to keep in mind is the focus of light. Optical sources typically include laser diodes [27, 29].

2.3 Physical Reconfiguration

Modification of parts of the antenna or physical deformation can also change the antenna parameters. This reconfiguration method does not depend on any form of switching or biasing or illumination. Performance and reconfigurability, on the other hand, is depended on the physical modification or deformation limitations. For example, a moveable parasitic plate over a patch antenna can affect the radiation pattern [32]. With the availability of many flexible substrates, physical deformation of antennas are possible now. Effects of physical strain show up for resonance frequency, impedance bandwidth as well as gain [43].

2.4 Material Properties Reconfiguration

Electric permittivity or magnetic permeability are the properties of a substrate that are of importance to antenna designers. An external electric or magnetic field can change the permeability of a ferrite. Different voltages can align the liquid crystals in many ways, thus changing the effective dielectric constant of the structure. Reflectarray antennas using liquid crystals over a ground place can generate a reconfigurable sum or difference radiation pattern [36]. Similarly, the resonance frequency can be changed by using a liquid crystal based substrate for a patch antenna [37] where the applied voltage changes the dielectric constant. A microstrip antenna can be reconfigured using a ferrite substrate by modifying its permeability [38].

2.5 Frequency Reconfigurable Antennas

Active elements can change the effective electrical length of an antenna. The operating frequency depends on the electrical length of an antenna and will shift based on the reconfiguration. Addition and alteration of coupled radiating structures are possible with all forms of switches discussed previously.

Varactor-loaded antennas can bring a shift of the resonance frequency depending on its intrinsic capacitance. The inherent capacitance of a varactor diode depends on

the reverse-bias voltage across its terminals. With the change of the reverse-bias, a smooth shift of the operating frequency is possible.

2.6 Polarization Reconfigurable Antennas

The surface current of an antenna is responsible for the polarisation characteristics of the radiation in the far-field. Polarisation reconfiguration would be possible if a combination of changes in the antenna structure, material properties, and feed mechanism can alter the direction of the surface current. Different types of polarisation reconfigurations are possible. It can be between two kinds of linear polarisation, between right and left-handed circular polarisations, or between linear and circular polarisations. The tools used can be the same as described in Fig. 2.1, but the design and implementation may be different than that are used to create frequency reconfigurations. The design challenges are to keep the resonance frequency and impedance bandwidth or the gain bandwidth intact for all possibilities of reconfiguration.

2.7 Radiation Reconfigurable Antennas

The radiation pattern of an antenna is related to the arrangement of currents and the relevant field distributions. The impedance of an antenna linked to this currents and field distributions make it difficult to design a beam-steerable antenna at a fixed resonant frequency. A designer would have to keep in mind the current and field distributions including the magnitude and phase for all reconfigurations. Mapping the currents and field distributions for the fundamental design is the primary task. Array type synthesis can follow to obtain secondary designs to cater to all possible reconfiguration specifications. If impedance mismatch remains, tunable matching circuits can be used for compensation.

Changing the reflection properties of reflector antennas can modify the radiation pattern at far-field [44]. A phase gradient across the reflector surface can also help to achieve radiation reconfiguration. The varying capacitance between resonant elements

of the reflector can create a reconfigurable phase gradient [45] for beam-steering. In a similar fashion, reconfigurable leaky-wave antennas can be designed. An energy source can induce leaky transverse electric waves on a reconfigurable surface to steer the radiation pattern [46].

2.8 Applications

The primary uses of reconfigurable antennas for cognitive radios, multiple-input-multiple-output (MIMO) channels, and satellite communication [47]. A cognitive radio system communicates across a channel by altering the operating frequency. The decision to change the operating frequency depends on the channel spectrum congestion and gaps. Once it finds a space, it changes the operating frequency and starts communication in that frequency.

A MIMO system adjusts the modulation level, coding rate, and transmission signalling schemes depending on varying channel conditions. The system usually employs multiple antennas to communicate various information simultaneously. Reconfigurable antennas can help MIMO systems to maintain good communication links.

Diverse space applications with limited space and weight constraints made reconfigurable antennas a fundamental choice. It is important to reconfigure the antenna to tackle new coverage areas, keep up communication links in harsh weather and maintain high data rate to transmit pictures and other data. Deployable antennas made quite an impact for space applications. Deployable antennas are usually for high gain and highly directive communications which depend on the antenna aperture. The launch vehicles often hold the antenna in a folded form and takes it final shape when deployed.

"It doesn't matter how beautiful your theory is, it doesn't matter how smart you are. If it doesn't agree with experiment, it's wrong."

Richard P. Feynman

3

Rectangular Microstrip Antennas: A Transmission-Line Approach

3.1 Introduction

Rectangular microstrip antennas have been around for over half a century and numerous experimental, and theoretical studies revealed the different properties of the antenna. The transmission-line model of the rectangular microstrip patch antenna [40, 48–51], detailed on many occasions, showcase the variation of input impedance with the location of the feed probe [40, 50, 51]. Analysis of the inset-feed is not very proclaimed in the literature. Some of the empirical works done in the recent past are focused on the cos^4 reduction of input impedance [52, 53] instead of the traditional cos^2 reduction mentioned in the early literature [40, 50, 51]. Another formulation for

designs with the inset very close to the centre is based on the shifted cos^2 was recently presented [52, 54]. This chapter focusses on the accuracy of inset-feed transmission-line modelling of the rectangular microstrip antenna by implementing the cos^4 reduction formula with a new corrective inset-feed length extension. The transmission-line model, discussed in Section 3, agrees to the cos^4 impedance variation for inset-fed microstrip antennas with an addition of a corrective extended feed length to the inner radiating edge. The corrective inset feed length is equal to the inset length of the antenna multiplied by 1.25. Verification of the model's complex reflection coefficient was concluded with good agreements with the measured results.

3.2 Antenna Configurations

Two different microstrip antennas were designed and manufactured to verify the empirical model (discussed in Section 3.3). The two types are termed as 'Base Antenna' designs, as these designs would also be used in later chapters. Both antennas use different substrates and resonate at different frequencies.

3.2.1 Base Antenna Designs

A low-permittivity substrate, Rogers 5880 ($\epsilon_r = 2.2$, $tan\,\delta = 0.0009$) with a thickness of 0.787mm was used to design and manufacture the first fundamental microstrip patch antenna. This design will be known as 'Base Design I' for the rest of the thesis. The length and width of the substrate are $L_{S1} = 120$ and $W_{S1} = 100$mm, respectively. The length and width of the patch are $L_{P1} = 58$mm and $W_{P1} = 70$mm, respectively. Matching has been achieved with a quarter wave transformer, which is directly connected to the 50Ω feed-line. The length and width of the transformer are $L_{T1} = 31$mm and $W_{T1} = 1.1$mm, respectively. The length and width of the feed-line are $L_{50\Omega 1} = 17.5$mm and $W_{50\Omega 1} = 2.25$mm, respectively. The cut-out of the inset has the dimensions are $L_{In1} = 10$mm and $W_{In1} = 4.1$mm, respectively. The aspect ratio of the patch (W_{P1}/L_{P1}) is 1.21 and the inset-feed width ratio (W_{in1}/W_{T1}) is 3.73.

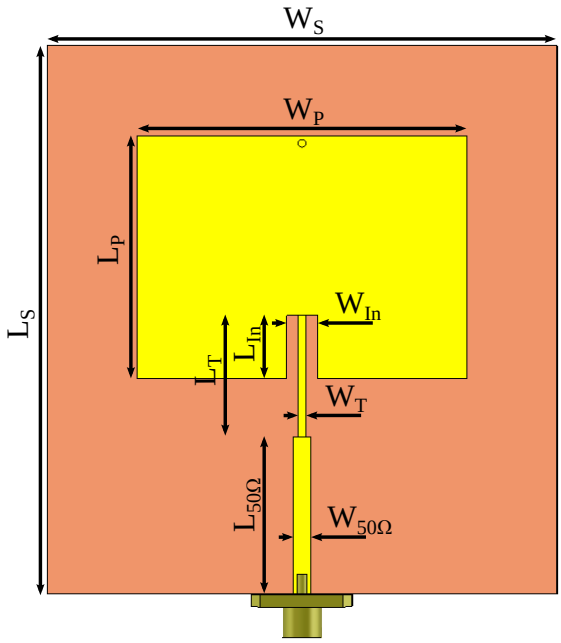

Figure 3.1: Layout of base antennas. Respective dimensions are provided in Section 3.2

A Taconic TRF-43 substrate ($\epsilon_r = 4.3$, $tan\,\delta = 0.0035$), having a thickness of 1.2mm was used for the second fundamental microstrip patch antenna, 'Base Design II'. Similar to 'Base Design I', the design is shown in Fig. 3.1 but with different values. The length and width of the substrate are $L_{S2} = 70$mm and $W_{S2} = 65$mm, respectively. The length and width of the patch are $L_{P2} = 31$mm and $W_{P2} = 42$mm, respectively. The length and width of the transformer are $L_{T2} = 15.5$mm and $W_{T2} = 1$mm. The length and width of the feed-line are $L_{50\Omega 2} = 20$mm and $W_{50\Omega 2} = 2.2$mm, respectively. The cut-out of the inset has the dimensions $L_{In2} = 8$mm and $W_{In2} = 4$mm, respectively. The aspect ratio of the patch (W_{P2}/L_{P2}) is 1.36 and the inset-feed width ratio (W_{in2}/W_{T2}) is 4.

3.3 Corrected Inset-Feed Transmission-Line Model

The transmission-line model for a rectangular microstrip antenna has been extensively discussed in the literature [40, 51]. Two slots, each having a complex admittance, are placed at a distance of about $\lambda_{eff}/2$ (Fig. 3.2) [40]. For a standard rectangular patch

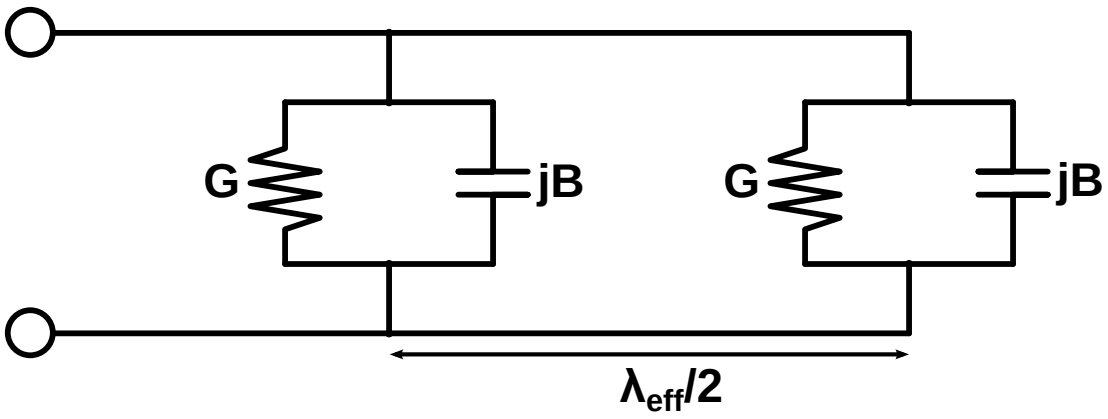

FIGURE 3.2: Transmission-line model of a rectangular microstrip antenna.

antenna, each of the complex slot admittance is denoted by $G + jB$ where G is the slot conductance, and B is the slot susceptance, respectively. The formulas for the slot conductance and susceptance are given in [40]. For a desired width w of the patch antenna and a thickness h of the substrate, the respective values are given by:

$$G = -2 + cos\, k_0 w + k_0 w Si\, k_0 w + sinc\, k_0 w \tag{3.1a}$$

$$B = \frac{w}{120\lambda_0}\left[1 - 0.636 log_e\, k_0 h\right] \tag{3.1b}$$

where G and B are the slot conductance and susceptance, respectively, k_0 is the free space wave number, and $Si\, X$ and $sinc\, X$ are the sine integral function and the cardinal sine function, respectively. For transmission line calculations the effective width of the patch is $w = W_P\sqrt{\epsilon_{eff}}$. The effective dielectric constant ϵ_{eff} can be given as [40]:

$$\epsilon_{eff} = \frac{\epsilon_r + 1}{2} + \frac{\epsilon_r - 1}{2}\left[1 + 12\frac{h}{W_P}\right]^{-1/2} \tag{3.2}$$

where ϵ_r is the relative permittivity of the substrate. It has to be kept in mind during the analytical calculation that the width of the patch and the width of the feed lines including the quarter wave transformer are different and should result in different values of ϵ_{eff} from Eq. (3.2). For a given effective free space length of the patch, the input admittance of the conventional rectangular microstrip patch antenna can be

given expressed as [49]:

$$Y_{inp}^{0} = G + jB + Y_p \frac{G + j\left(B + Y_p tan\, kL_P\right)}{Y_p - B tan\, kL_P + jG tan\, kL_P} \tag{3.3}$$

where k is the effective wave number. L_P is the length of the patch and Y_p is its respective characteristic impedance.

3.3.1 Inset Feed

Conventionally, the inset probe feed is modelled with an admittance incremental factor of $sec^2\left(\frac{\pi}{L_P} L_{in}\right)$ [40, 50, 51] and some literature do mention the same for microstrip line inset feeds as well. This theory has been contradicted in the recent past [52–54] and a new admittance factor of $sec^4\left(\frac{\pi}{L_P} L_{in}\right)$ has been proven to be more valid for microstrip line inset feeds where the feed end is closer to the inner edge of the microstrip patch. In the empirical models published lately [52–54], the aspect ratio of the patch (W_P/L_P) was considered to be 1.5 and inset gap to inset feed width ratio (W_{in}/W_T) was 3. In the design mentioned in this chapter, the aspect ratio is 1.36, and the inset gap to inset feed width ratio is 4. The overall antenna impedance is derived in the next subsection.

3.3.2 Antenna Admittance

A generic rectangular microstrip antenna with a microstrip edge feed would not require the implementation of the inset feed model. The prototype antenna described in this chapter is particularly designed with an inset feed to showcase the below empirical model.

Inset Feed Admittance

The overall antenna admittance depends on the length of the inset, quarter wave transformer and the 50Ω feed-line, respectively. Admittance for an inset-fed patch is given

by [52, 53]:

$$Y_{inp'} = Y_{inp}^{0} sec^{4}\left(\frac{\pi}{L_P} L_{In}\right) \tag{3.4}$$

where L_{in} is the inset feed length and Y_{inp}^{0} is the edge impedance of the patch as given in Eq. (3.3). Another admittance transformation takes place with the quarter-wave transformer and the admittance of the patch at the input of the quarter-wave transformer is given by:

$$Y_{inp''} = Y_T \frac{Y_{inp'} + jY_T tan\, k\,(L_T + 1.25L_{In})}{Y_T + jY_{inp'} tan\, k\,(L_T + 1.25L_{In})} \tag{3.5}$$

where L_T is the length of the quarter-wave transformer and Y_T is the characteristic admittance of the transformer.

In the process of this research, it was empirically found out after comparison with measurement results that the complex impedance obtained from the extended transmission-line model match up with the measurements and simulations when a corrective feed length to the inner radiating edge is considered. The corrective feed length from the feed point to the inner radiating edge is equal to the length of the inset (L_{In}) with a linear coefficient of 1.25, thus making the total feed length equal to the length of the quarter wave transformer (L_T) added to the inset length ($1.25L_{In}$).

Edge Feed Admittance

For an edge fed microstrip antenna, the empirical modelling described in the aforesaid section will be no longer required and the admittance of the patch at the input of the quarter-wave transformer is given by:

$$Y_{inp''} = Y_T \frac{Y_{inp'} + jY_T tan\, kL_T}{Y_T + jY_{inp'} tan\, kL_T} \tag{3.6}$$

where L_T is the length of the quarter-wave transformer, and Y_T is the characteristic admittance of the transformer.

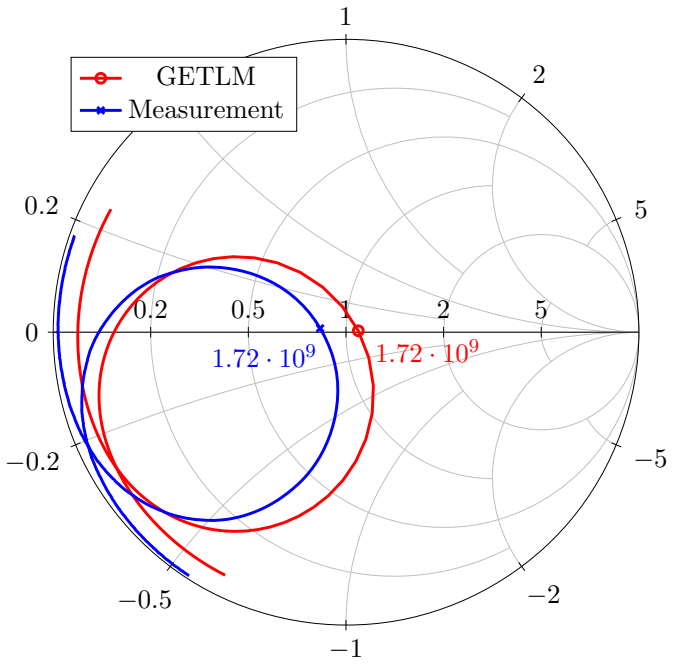

(a) Base Antenna I

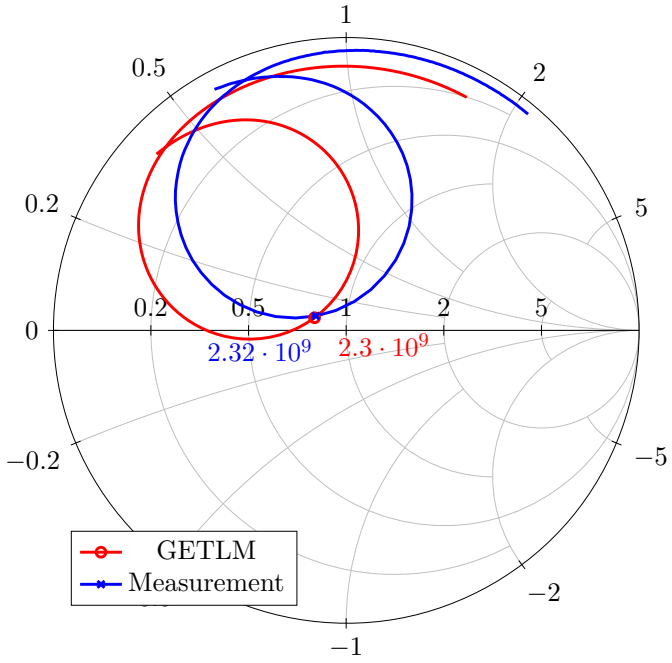

(b) Base Antenna II

Figure 3.3: The complex impedance of Base Design I and II obtained using the empirical inset-fed transmission-line model and measurements. The Smith Chart is normalised to 50Ω and shows the complex impedance between 1500 MHz and 2000 MHz for Base Design I, and between 2200 MHz and 2700 MHz for Base Design II, respectively.

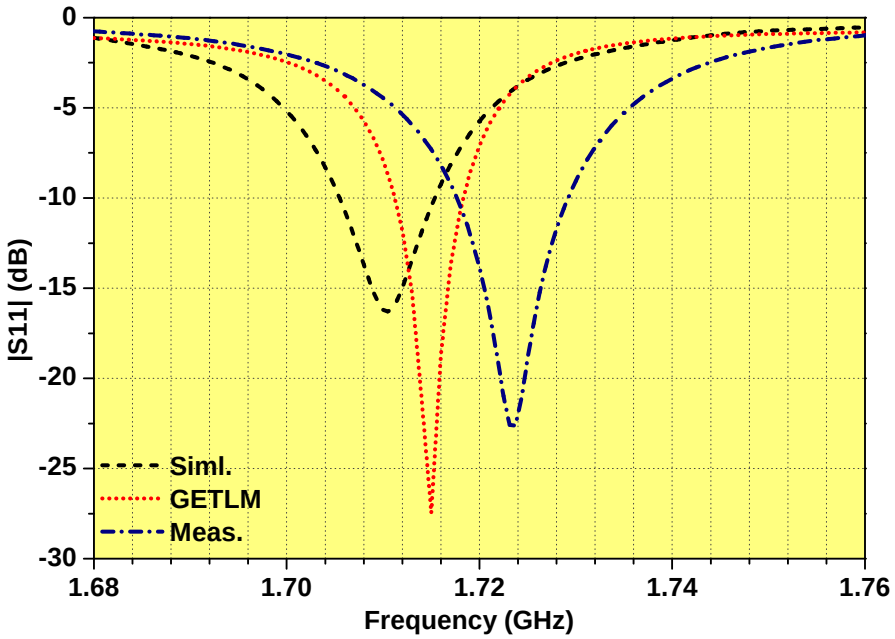

(a) Base Antenna I

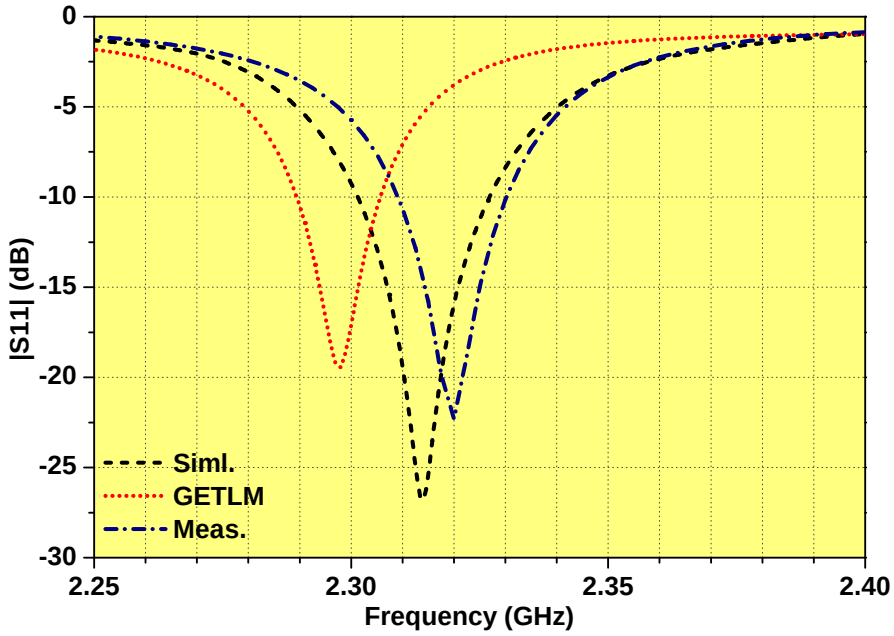

(b) Base Antenna II

FIGURE 3.4: Complex reflection coefficient magnitude of Base Design I and II obtained from simulations, the empirical inset-fed transmission-line model, and measurements.

Overall Admittance

The overall admittance at the SMA port is given by:

$$Y_{inp50\Omega} = Y_{50\Omega}\frac{Y_{inp''} + jY_{50\Omega}tan\, kL_{50\Omega}}{Y_{50\Omega} + jY_{inp''}tan\, kL_{50\Omega}} \tag{3.7}$$

where $Y_{50\Omega}$ is approximately $0.02S$, and $L_{50\Omega}$ is the length of the feed-line as shown in Fig. 3.1.

3.4 Implementation and Results

Implementation of the general inset-fed transmission-line model (GETLM) was done in Matlab using Eq. (3.3) - Eq. (3.7). Empirical extension of the inset feed was considered during the implementation. For accuracy of results, the respective effective relative permittivity was calculated for every different width (of the patch, transformer, and the feed-line), and used to obtain their equivalent free-space values. 'Base Design I' and 'Base Design II' were manufactured in-house using CNC router isolation milling and chemical etching and the return loss characteristics were measured. Full-wave simulations were conducted using CST Microwave Studio 2015 to compare results obtained with the general inset-fed transmission-line model (GETLM).

3.4.1 Base Antenna Designs

The analytically obtained complex impedance (normalised to 50Ω) for 'Base Design I', achieved through the general inset-fed transmission-line model (GETLM) is compared to the measured impedance (using an Agilent PNA-X vector network analyser) in Fig. 3.3(a). Complex impedance normalised to 50Ω, for 'Base Design II', obtained through the model along with its measured counterpart is shown in Fig. 3.3(b). Both the results are in good agreement with each other.

The measured resonance frequency of the 'Base Design I' is 1723 MHz and the resonance frequency of the 'Base Design II' is 2320 MHz. The return loss comparisons are

Table 3.1: Comparison of predicted resonant frequencies for 'Antenna I' along with those obtained from measurements, under different bias conditions. Percentage deviation of predicted value is relative to simulation and measurement results, respectively.

Antenna	GETLM	CST	% Devn.	Measured	% Devn.
Base Design I	1715	1711	0.23	1723	0.46
Base Design II	2298	2314	0.69	2320	0.95

shown in Fig. 3.4 for both the antennas. The results obtained from CST, GETLM and measurements are in good agreement with each other. The deviation is less than one percent for both antennas, without considering the manufacturing tolerances. Table 3.1 displays the exact resonance frequencies obtained with simulations, GETLM and measurements and the respective deviations.

3.5 Conclusion

These two results verified the accuracy of the inset-feed transmission line model described in Sec. 3.3, and it can be extensively used for the reconfigurable antennas. The GETLM is successful for different rectangular microstrip antennas with multiple substrates and resonance frequencies. This transmission-line model will be used as a fundamental framework for the next few chapters.

"There is synthesis when, in combining therein judgments that are made known to us from simpler relations, one deduces judgments from them relative to more complicated relations. There is analysis when from a complicated truth one deduces more simple truths."

Andre-Marie Ampere

4

Arbitrary Position of a Shorting Post: Modelling and Effects

4.1 Introduction

Shorted microstrip patch antennas have been analysed in various forms. The earliest form of patch reduction was done by shorting the microstrip patch antenna size along the H-plane [55]. Further improvements in size reduction were achieved with the help of multiple shorting posts instead of using one long and continuous metal strip across the H-plane [56–58]. Transmission-line modelling of rectangular microstrip patch antenna with shorting posts along the line of magnetic symmetry to demonstrate the change of antenna resonance frequency was also discussed [59, 60]. The model mentioned above only considered posts placed in the centre of the width of the patch but at

any position along the length (E-plane). Similar tuning with circular patch antennas is also possible [61, 62]. Accurate results can also be obtained for shorted microstrip antennas using cavity model and this was presented for circular patch antennas [63, 64]. Rectangular microstrip antennas can be designed to have their non-radiating edges shorted to ground to reduce cross polarised radiation significantly and was recently analysed using the cavity model [65]. Compact designs and larger impedance can also be achieved using a secondary coupled patch with shorting posts implemented in both the primary and secondary patches [66]. Models of rectangular microstrip antennas with shorting posts placed at various positions of the outer radiating edge to tune the antenna was recently communicated [67, 68]. A design with shorted circular patch over a ring resonator for multiband operations was also recently expressed [69]. Transmission line modelling for rectangular patch antenna with superstrates are also possible and was recently communicated [70].

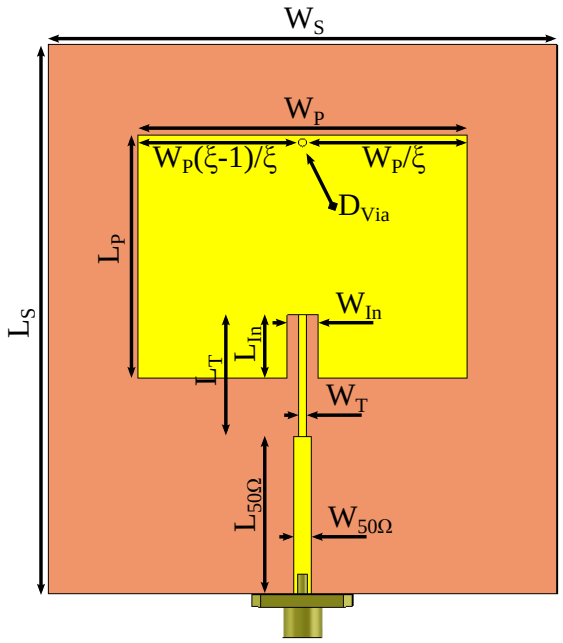

FIGURE 4.1: Layout of the rectangular microstrip patch antenna.

This chapter focusses on the accuracy of inset-feed transmission-line modelling of the rectangular microstrip antenna discussed in Chapter 3, and its extension due to a relatively thin shorting post. Comparative study of the change of resonant frequency

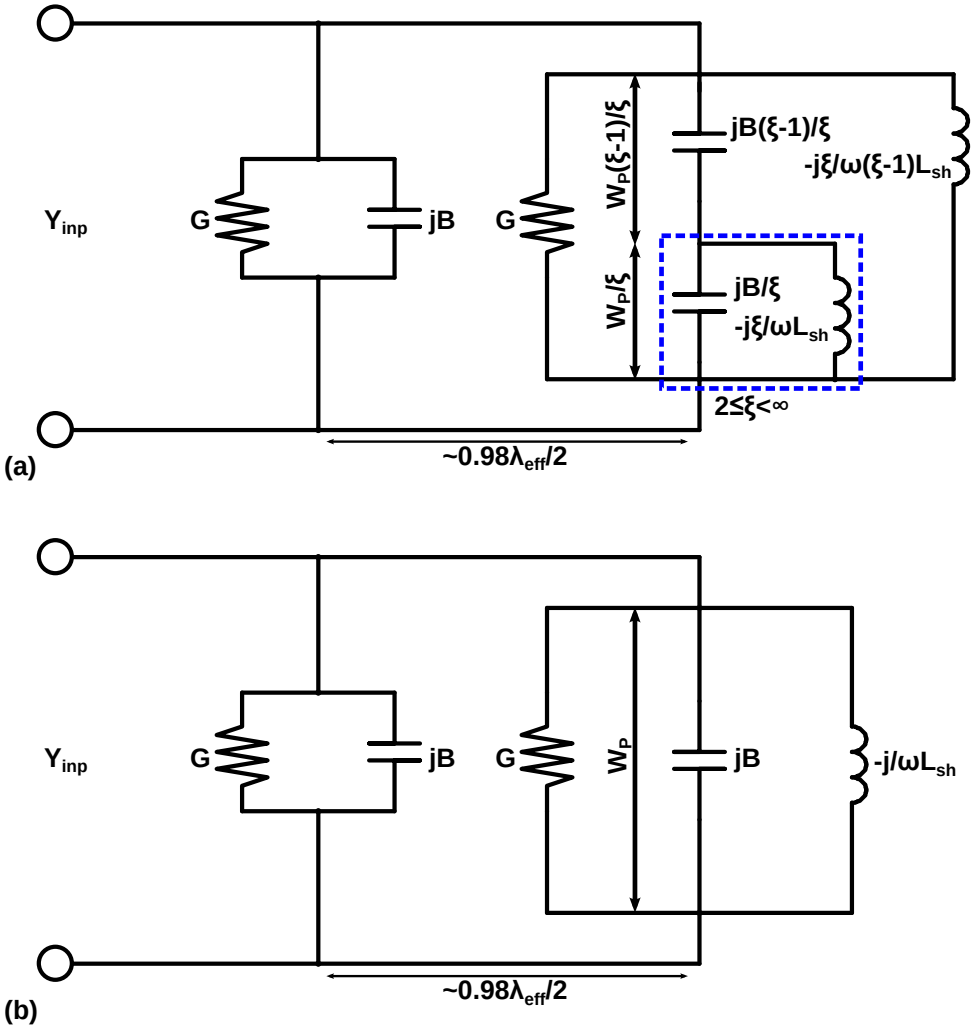

Figure 4.2: Transmission-line model of a microstrip patch antenna with a thin shorting post placed (a) in an arbitrary position of the outer radiating slot of the patch, and (b) placed at one of the two outer vertices of the patch.

of the antenna, when the thin shorting post is placed in an arbitrary position along the outer radiating edge of the patch, is conducted in this Chapter. The post electrically shorts the outer edge of the patch to the ground plane of the antenna. The effect of the load is not similar to a full edge short of a quarter wave patch and is different to a quarter wave patch. The transmission-line model of a rectangular microstrip patch antenna [40, 48–51] is modified to archetype the effect of the relative position of the shorting post and analytically obtained results are compared with results from a 3D full-wave solver and measurements.

4.2 Antenna Configuration

Validation of the general extended transmission-line model (GETLM) is done with three manufactured conventional rectangular microstrip patch antennas with dimensions same as 'Base Design II'. Further one single manufactured prototype of 'Base Design I' was used to verify the special extended transmission-line (SETLM) discussed later. The manufactured 'Base Design II' antennas are shorted in different positions with a thin shorting post. A 20AWG wire forms the 'via' with a diameter (D_{Via}) of 0.8mm. The manufactured 'Base Design I' was verified with the 'via' shorted only at one of the outer vertex as per the conditions of SETLM.

It can be noted from Fig. 4.1 that the relative position of the thin shorting post is denoted by a factor $\{1/\xi\}$ from one end. The relative position of the shorting post then has a different factor $\{(\xi - 1)/\xi\}$ from the other end. The summation of both factors is always 1.

The design was chosen to have the tunable resonance frequencies around the 3G, LTE and WiFi bands for any further practical applications.

4.3 Arbitrary Short Model

An outer vertex for a rectangular microstrip is any one end of the outer edge of the radiating slot. When a thin 'via' ($D_{Via} \ll W_P$) is shorted at the outer vertex of the rectangular patch, it can be approximated that the susceptance of the 'via', $-j\omega L_{sh}$, added in parallel to the complex admittance of the outer slot. The admittances of both the slots remain unchanged. The extended transmission-line model for this special case (SETLM) is illustrated in Fig. 4.2(b).

When the thin 'via' is placed in an arbitrary position along the radiating slot of the antenna the slot susceptance and the susceptance of the 'via' are proportionally divided. The position of the shorting post can be measured by a factor of $1/\xi$ from one end and $(\xi - 1)/\xi$ from the other. The slot susceptance jB is divided into jB/ξ and $jB(\xi - 1)/\xi$, respectively. The shorting post susceptance $-j/\omega L_{sh}$ is divided

into $-j\xi/\omega L_{sh}$ and $-j\xi/(\omega(\xi-1)L_{sh}$, respectively. Due to the negligible diameter of the shorting post, the conductance of the outer slot remains unaffected. The general extended transmission-line model (GETLM) for this case is illustrated in Fig. 4.2(a).

Due to the asymmetric nature of the transmission-line model a limiting condition of $2 \leq \xi < \infty$ is implemented. That means the lower LC resonator (marked with a blue boundary in Fig. 4.2(a) can have a slot capacitance to a maximum of half of the original value B from a minimum of 0. Similarly, the shunt inductance can have a maximum of half of the original value of the L_{sh} from a minimum of 0. When $\xi = 2$ the value of B and L_{sh} is equally divided into two half and denotes the fact that the shorting post is at the centre of the outer edge of the radiating slot of the patch antenna. With $\xi \to \infty$ both the values becomes negligible, and the GETLM transforms itself into the SETLM shown in Fig. 4.2(b). The actual patch antenna has a magnetic symmetry across the centre of the radiating slot. The shorting position on either side of the magnetic symmetry can be implemented in the GETLM by interchanging the factors mentioned before in this section.

4.3.1 Patch Admittance - GETLM

The input impedance of the patch model, shown in Fig. 4.2(a) can be expressed as:

$$Y_{inp} = G + jB + Y_p \frac{G + j\left(\Psi + Y_p tan\, kL_P\right)}{Y_p - \Psi tan\, kL_P + jG tan\, kL_P} \tag{4.1a}$$

where

$$\Psi = \frac{B\left(1-\frac{1}{\xi}\right)^2\left(\frac{\omega BL_{sh}}{\xi^2}-1\right) - \frac{B}{\xi} + \frac{1}{\omega L_{sh}}}{\left(1-\frac{1}{\xi}\right)\left(\frac{\omega BL_{sh}}{\xi}-1\right)} \tag{4.1b}$$

and k is the effective wave number. L_P is the length of the patch and Y_p is its respective characteristic impedance.

4.3.2 Patch Admittance - SETLM

As the factor $\xi \to \infty$, it is understood that the shorting post is moved extremely towards one of the outer vertices. The effective value of the slot susceptance changes to:

$$\Psi_{\xi\to\infty} = B - \frac{1}{\omega L_{sh}} \tag{4.2}$$

resulting in special patch admittance of:

$$\begin{aligned} Y_{inp} &= G + jB + \\ & Y_p \frac{G + j\left(B - 1/\omega L_{sh} + Y_p tan\, kL_P\right)}{Y_p - \left(B - 1/\omega L_{sh}\right) tan\, kL_P + jG tan\, kL_P} \end{aligned} \tag{4.3}$$

4.4 Implementation and Results

Implementation of the GETLM and SETLM was done in Matlab using Eq. (3.3) - Eq. (3.7) from the previous chapter and Eq. (4.1) - Eq. (4.3). The full-wave numerical simulation was done using CST Microwave Studio 2015 and the results obtained were used to validate the results predicted by the GETLM and SETLM. One prototype of 'Base Design I' was prototyped to verify SETLM and three prototypes of 'Base Design II' were also fabricated and measured for three different positions of the shorting post, and to verify GETLM.

The shorting post for the base antenna I was placed at one of the outer vertexes of the antenna. Before the shorting posts were soldered in the 'Base Design II' based antennas, each of the three manufactured conventional rectangular microstrip antennas was measured. Fig. 4.3(a) shows the prototypes before the shorting posts were soldered. They are marked 'A', 'B' and 'C' for ease of reference. The prototype picture of the 'Base Design I' has not been shown separately.

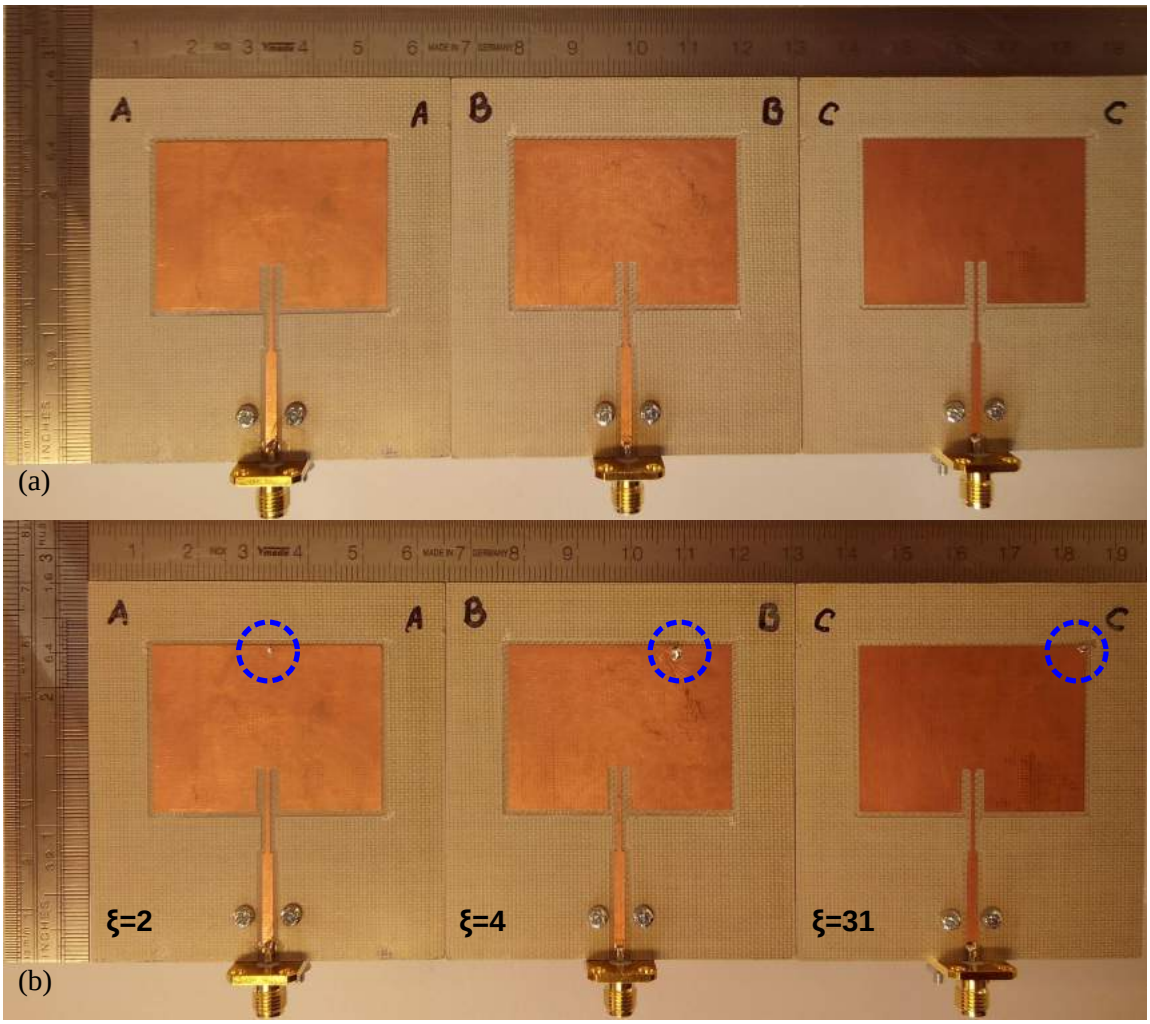

Figure 4.3: Manufactured prototypes 'A', 'B' & 'C', (a) before soldering shorting posts, and (b) after soldering shorting posts at $\xi = 2, 4, 31$, respectively.

The accuracy of the SETLM is verified with a Smith chart of the complex impedances of the 'Base Design I' as obtained through measurements and the transmission-line model is shown in Fig. 4.4(a). Fig. 4.4(b), Fig. 4.5(a) and Fig. 4.5(b) shows the normalized complex impedance of antenna ('Base Design II') obtained through GETLM and measurements for various shorting positions ($\xi = 2, 4, 31$). The results are in good agreement with respect to the value of Γ at the resonance frequency.

Fig. 4.6(a) shows the predicted return loss obtained with GETLM for different values of ξ and with SETLM for the 'Base Design II' antennas. It also shows the base resonance frequency of the patch without a shorting post. Fig. 4.6(b) shows

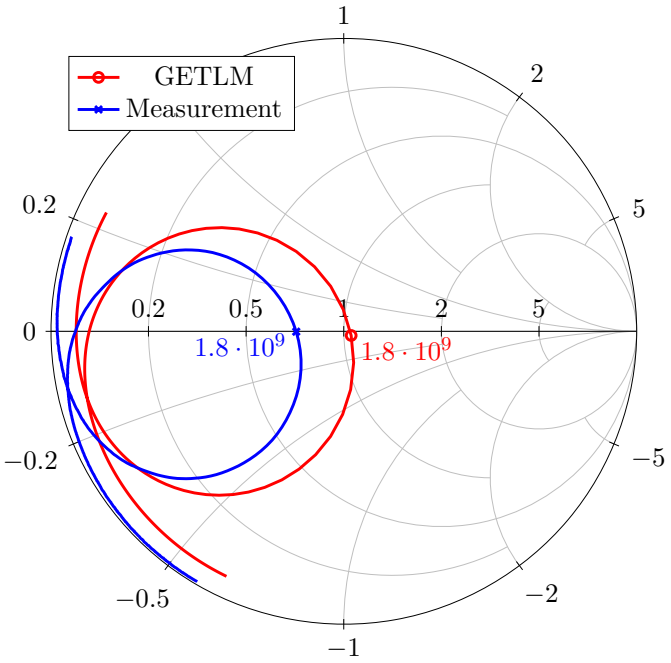

(a)

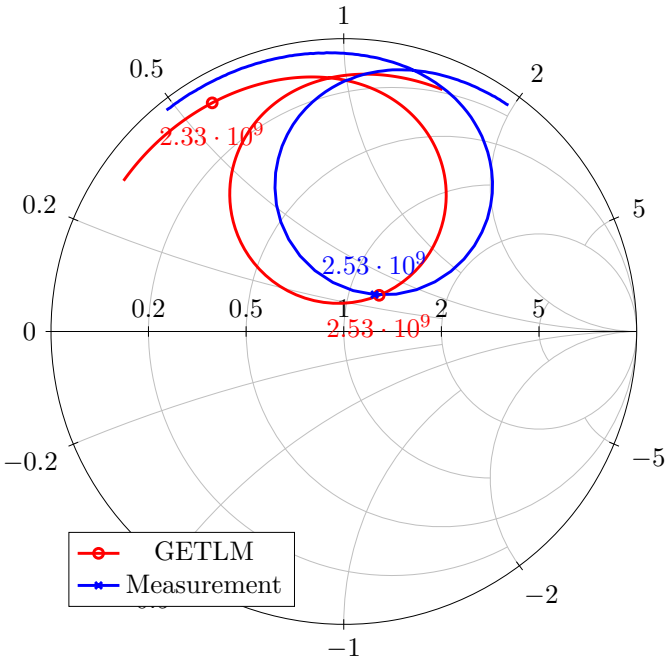

(b)

FIGURE 4.4: Complex impedances of (a) 'Base Design I' with with a shorting post at $\xi = \infty$, (b) 'Base Design II' with a shorting post at $\xi = 2$, obtained using the empirical inset fed transmission-line model and measurements. The Smith Charts are normalized to 50Ω and shows the complex impedance between 1500 MHz and 2000 MHz for Base Design I, and between 2200 MHz and 2700 MHz for Base Design II, respectively.

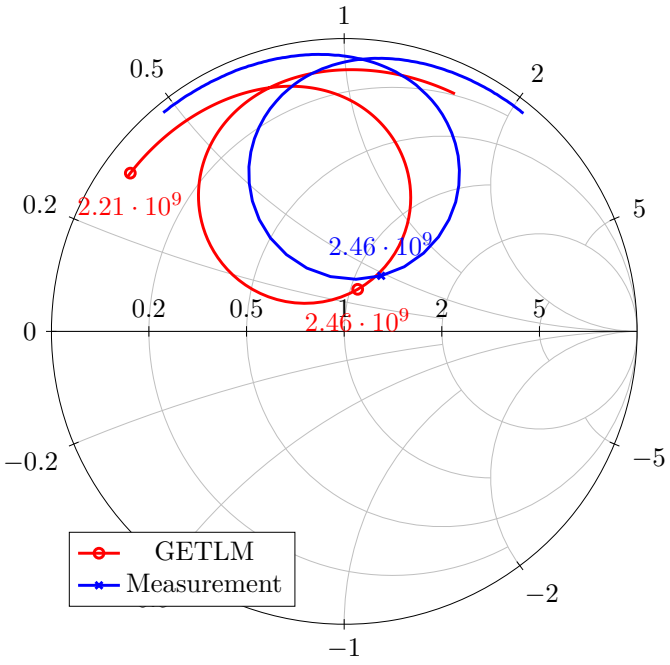

(a)

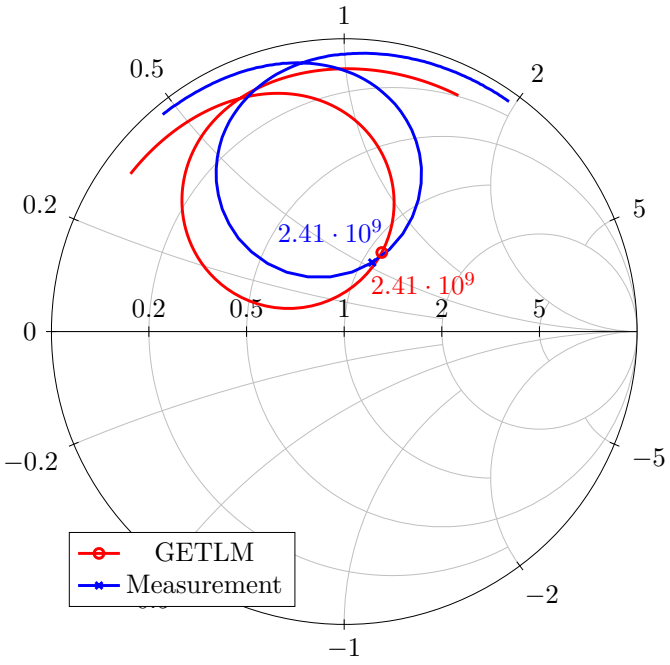

(b)

Figure 4.5: Complex impedances of (a) 'Base Design II' with a shorting post at $\xi = 4$, and (b) 'Base Design II' with a shorting post at $\xi = 31$, obtained using the empirical inset fed transmission-line model and measurements. The Smith Charts are normalized to 50Ω and shows the complex impedance between 2200 MHz and 2700 MHz.

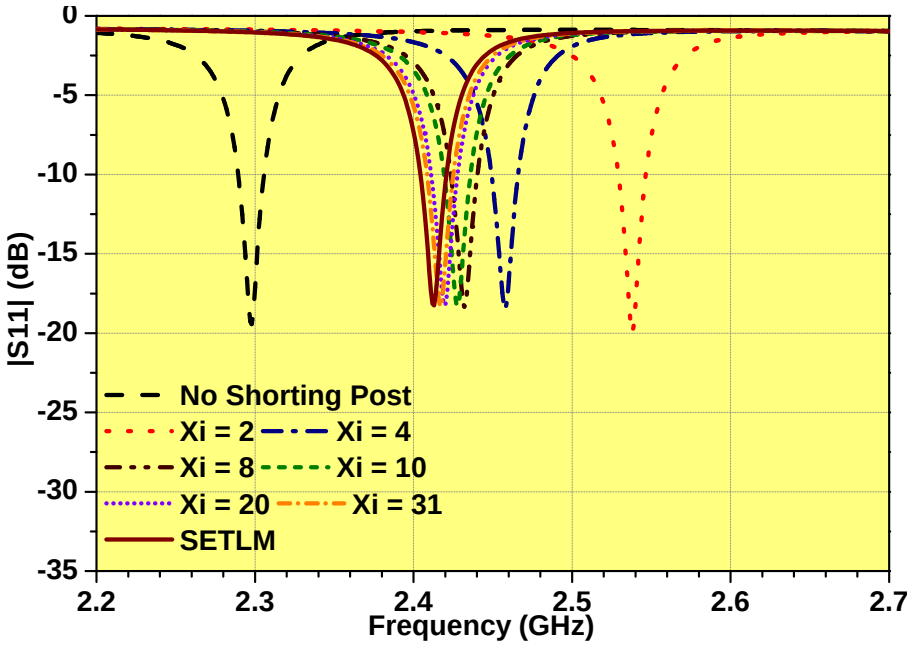

(a)

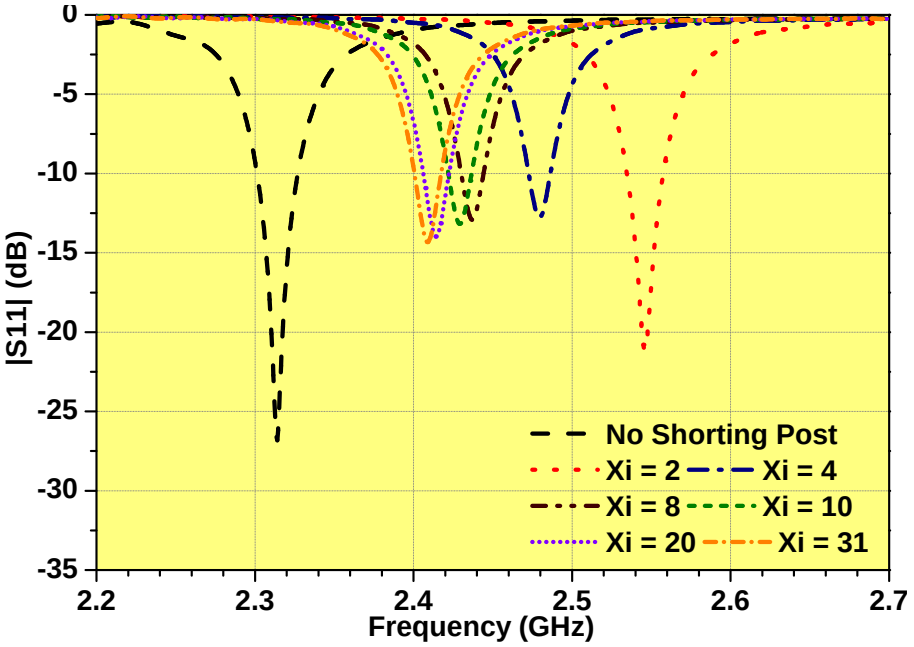

(b)

FIGURE 4.6: (a) Predicted return loss of the 'Base Design II' obtained using GETLM and SETLM, and (b) Predicted return loss of the 'Base Design II' obtained using CST Microwave Studio 2015.

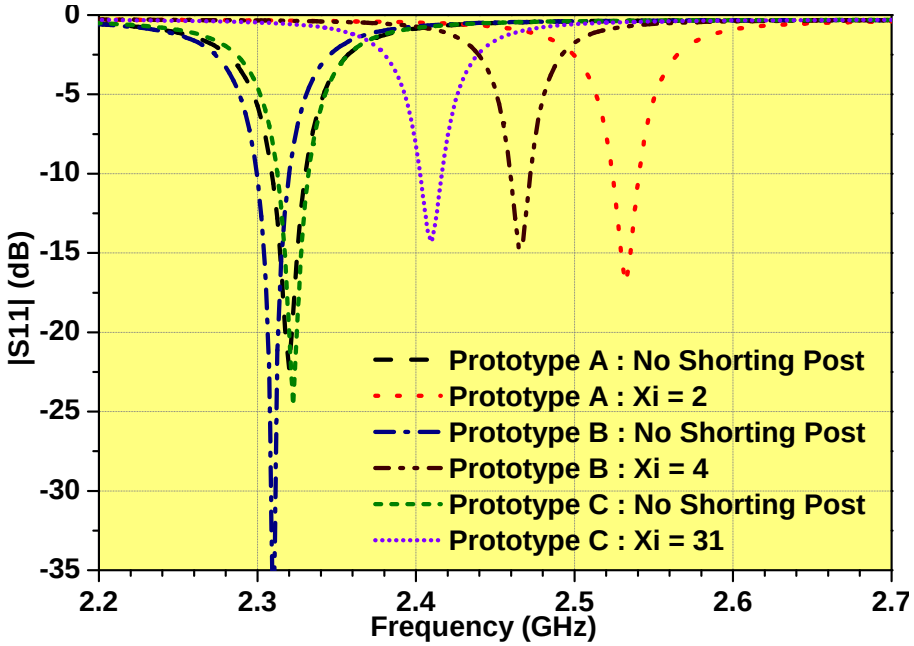

(a)

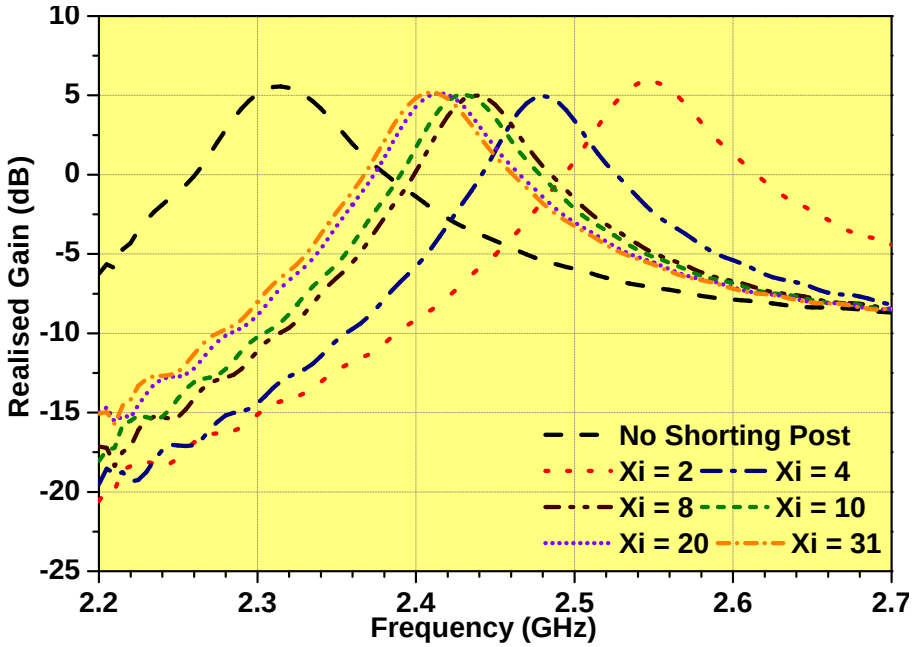

(b)

Figure 4.7: (a) Measured return loss of the 'Base Design II' prototypes before and after soldering the shorting posts, and (b) The realized gain with respect to frequency for the different positions of the shorting post on the outer edge of the 'Base Design II' prototypes.

the predicted return loss obtained using 3D full-wave simulation in CST Microwave Studio. The transmission-line model results are in good agreement with the full-wave simulation results. Fig. 4.3(b) shows the base antenna II prototypes after soldering. The three cases considered for manufacturing are for $\xi = 2, 4, 31$, respectively. Fig. 4.7(a) shows the resonance frequencies for all the three prototypes without any shorting post as well as after shorting posts were soldered at the respective positions mentioned before. The measured base resonance frequencies for prototype 'A', 'B' and 'C' are 2320 MHz, 2310 MHz, and 2323 MHz, respectively. There are some manufacturing tolerances which affected the base resonance frequency even though all the three patch antennas are of same design dimensions. The measured base resonance frequency of the 'Base Design I' prototype is 1723 MHz. Table 4.2 shows a comparison of the resonance frequencies for different values of ξ. (Table 4.1 shows a comparison for 'Base Design I' only with $\xi = \infty$). The maximum deviation relative to the full-wave results occurs at the value of $\xi = 4$ and the value of $\xi = 31$ for 'Base Design II' when measurement results are considered. All the deviation values are less than 1%.

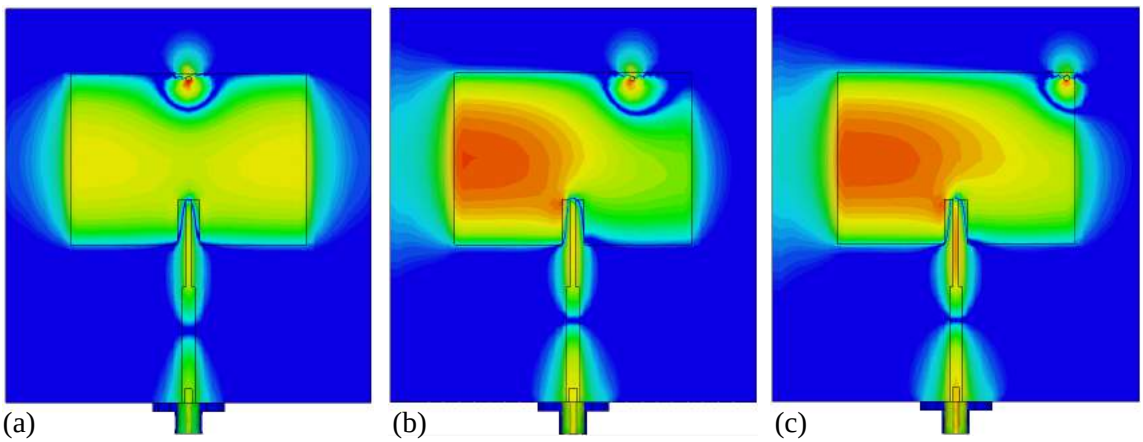

FIGURE 4.8: Surface current distribution of the patch antenna with the shorting post placed at (a) $\xi = 2$, (b) $\xi = 4$, and $\xi = 31$.

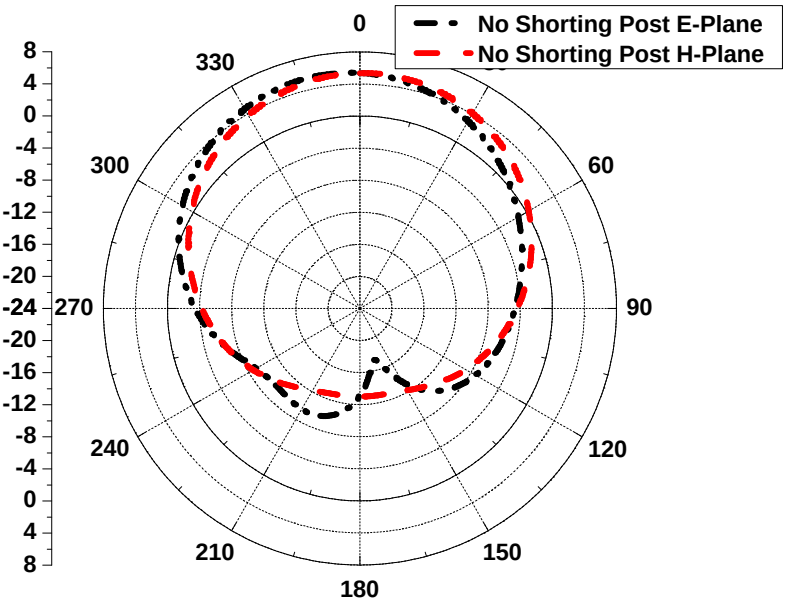

(a)

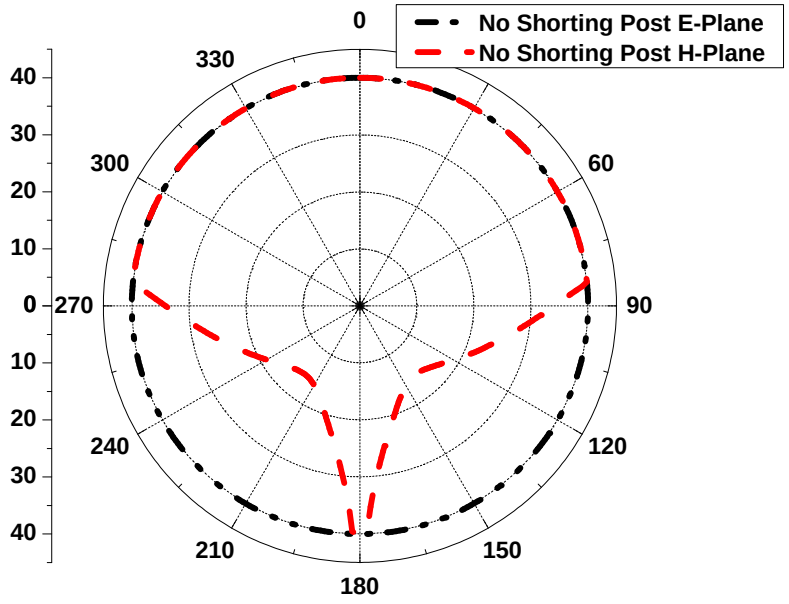

(b)

Figure 4.9: (a) Realised Gain pattern of the 'Base Design II' antenna prototype in the E-Plane and H-Plane, respectively, (b) Axial Ratio of the 'Base Design II' antenna prototype in the E-Plane and H-Plane, respectively.

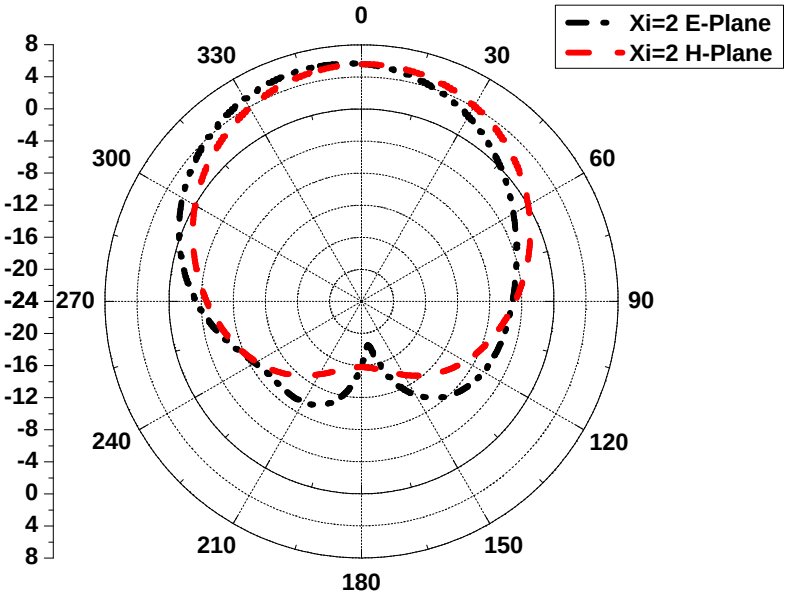

(a)

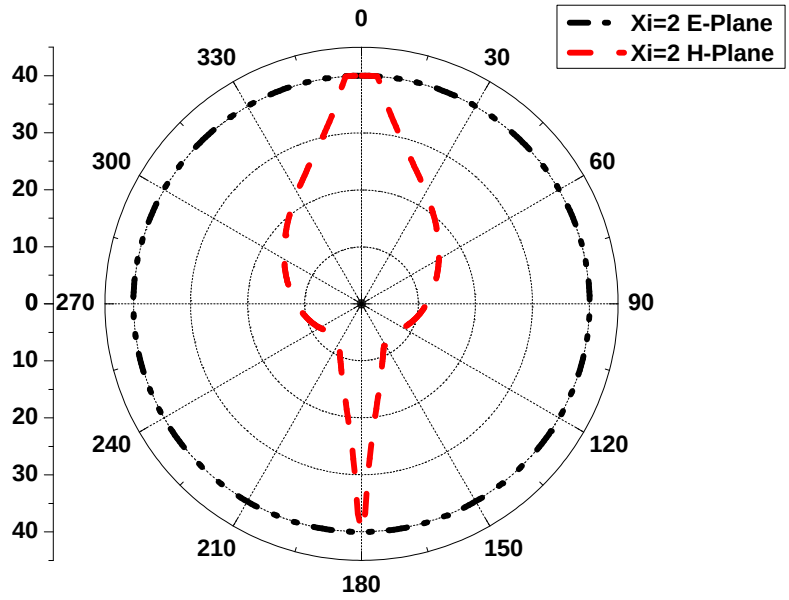

(b)

FIGURE 4.10: (a) Realised Gain pattern of the 'Base Design II' antenna prototype with a shorting post at $\xi = 2$, in the E-Plane and H-Plane, respectively, and (b) Axial Ratio pattern of the 'Base Design II' antenna prototype with a shorting post at $\xi = 2$, in the E-Plane and H-Plane, respectively.

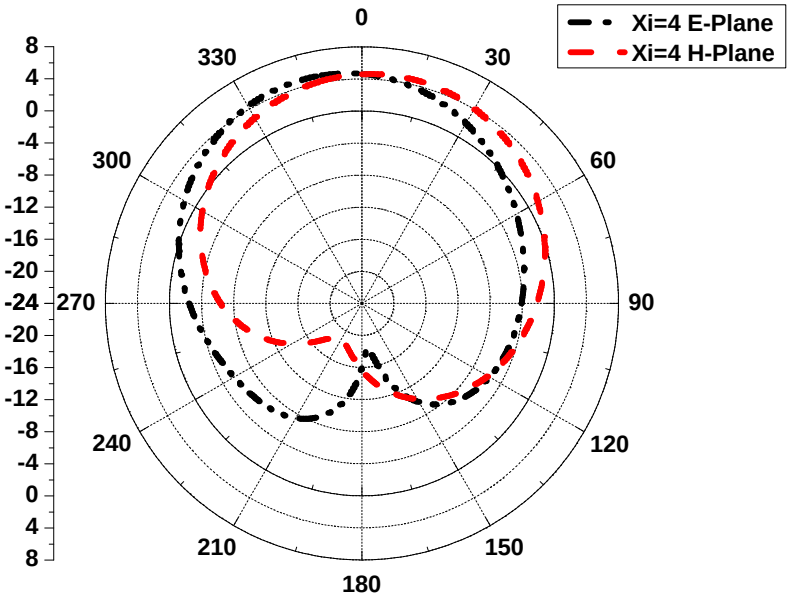

(a)

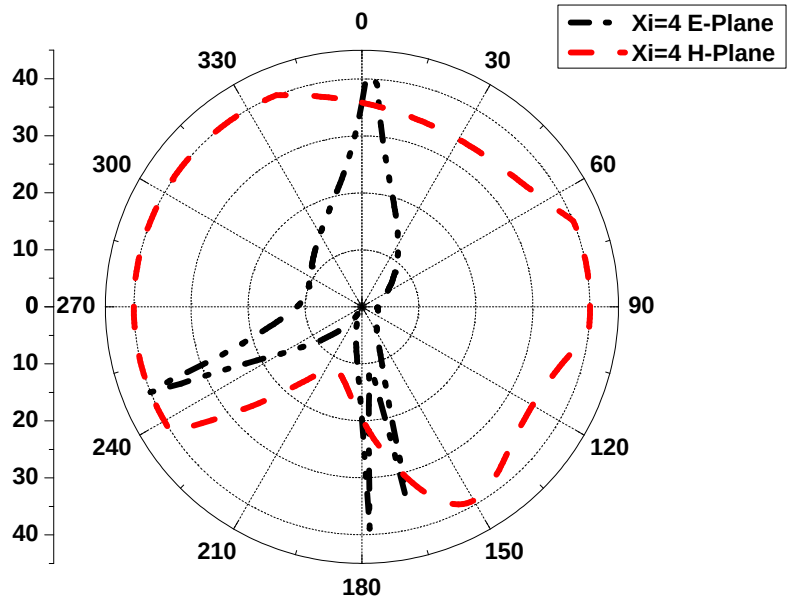

(b)

Figure 4.11: (a) Realised Gain pattern of the 'Base Design II' antenna prototype with a shorting post at $\xi = 4$, in the E-Plane and H-Plane, respectively, (b) Axial Ratio pattern of the 'Base Design II' antenna prototype with a shorting post at $\xi = 4$, in the E-Plane and H-Plane, respectively.

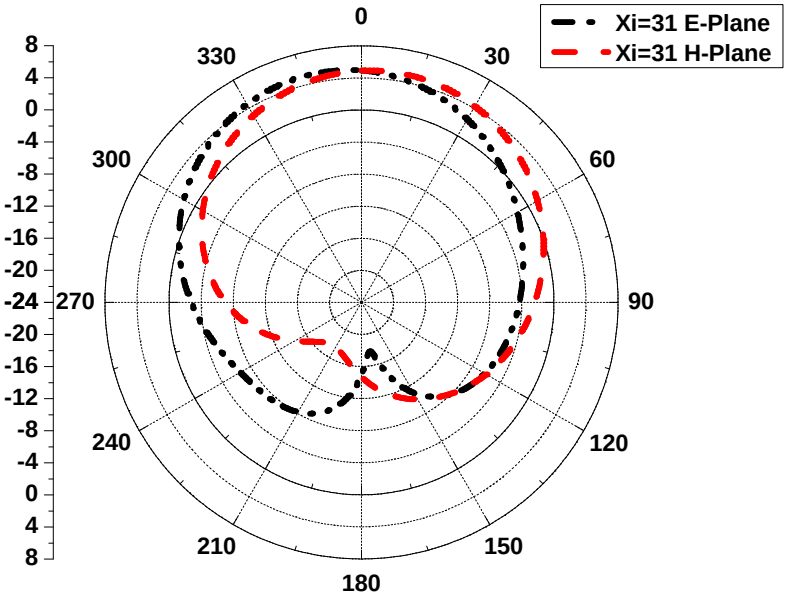

(a)

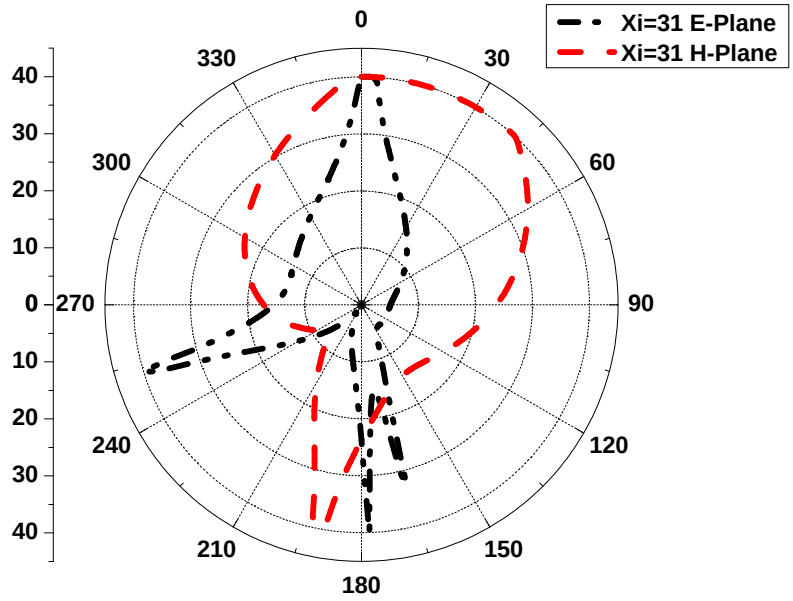

(b)

FIGURE 4.12: (a) Realised Gain pattern of the 'Base Design II' antenna prototype with a shorting post at $\xi = 31$, in the E-Plane and H-Plane, respectively, and (b) Axial Ratio pattern of the 'Base Design II' antenna prototype with a shorting post at $\xi = 31$, in the E-Plane and H-Plane, respectively.

Table 4.1: Comparison of predicted resonant frequencies for the patch antenna (Base Design I), along with those obtained from measurements. Percentage deviation is relative to ETLM results. All frequencies are in MHz.

ξ	ETLM	CST	Devn. (%)	Measured	Devn. (%)
∞	1800	1794	0.33	1797	0.17

Table 4.2: Comparison of predicted resonant frequencies for the patch antenna (Base Design II), along with those obtained from measurements. Percentage deviation is relative to ETLM results. All frequencies are in MHz.

ξ	ETLM	CST	Devn. (%)	Measured	Devn. (%)
2	2537	2546	0.35	2532	0.19
4	2457	2480	0.93	2465	0.32
8	2432	2437	0.21	-	-
10	2428	2429	0.04	-	-
20	2420	2414	0.25	-	-
31	2417	2409	0.33	2410	0.29
∞	2413	-	-	-	-

Maximum shift of resonance frequency due to the shorting post occurs when $\xi = 2$, or in other words when the thin shorting post is placed right in the middle of the outer radiating slot of the patch. For this particular patch antenna, this shift is around 212 MHz from the base resonance frequency of prototype 'A'. The minimum shift occurs when the thin shorting post is placed at one of the extreme ends of the slot (outer vertex) of the patch. For prototype 'C' this shift is 87 MHz. But changing the value of ξ, the resonance frequency can be tuned to about 127 MHz for the particular prototypes shown here.

The surface current density of the patch antenna due to different positions of the shorting post is shown in Fig. 4.8. It can be noted pictorially that the effective size of the patch antenna changes with the change of position of the shorting post and the effect is minimal when the post is placed in one of the outer vertices of the patch antenna.

The gain roll-over about various positions of the shorting post is shown in Fig. 4.7(d). The realised gain is 5.6 dBi without a shorting post and 5.87 dBi with a shorting post placed right in the middle of the outer edge of the patch ($\xi = 2$). For the other positions, the respective gain is about 5 dBi. The far-field pattern and axial

ratio of the conventional microstrip antenna and the three manufactured antennas with shorting posts placed at various positions ($\xi = 2, 4, 31$) are shown in Fig. 4.9, Fig. 4.10, Fig. 4.11 and Fig. 4.12. Fig. 4.9(a) and Fig. 4.9(b) shows the radiation pattern, and axial ratio of the 'Base Design II' antenna prototype without any shorting post. It can be seen from Fig. 4.9(b) that for a conventional microstrip antenna, the polarisation purity is very high all throughout across the E-Plane and over the entire broadside on the H-Plane. Fig. 4.10(a) shows the radiation pattern with the shorting post at the middle of the outer radiating edge ($\xi = 2$). The second best polarisation purity is obtained with the shorting post at the middle of the outer radiating edge ($\xi = 2$), as shown in Fig. 4.10(b). Fig. 4.10(b) shows that the polarisation purity is very high for the E-Plane. In the H-Plane, the polarisation purity is very high in the boresight, but the axial ratio drops significantly at other angles. The overall polarisation purity at $\xi = 4$ and $\xi = 31$ is quite good across the boresight but is distorted slightly at other angles of propagation. The relevant diagrams are shown in Fig. 4.11 and Fig. 4.12 for $\xi = 4$ and $\xi = 31$. In overall, the antenna remains linearly polarised irrespective of the position of the shorting post.

4.5 Conclusion

An extended transmission-line model is presented to model a thin shorting post at the outer radiating slot of a conventional rectangular microstrip patch antenna at any location. Derivations of the input admittance for inset fed and edge fed rectangular microstrip patch antenna is extensively discussed. Quick design solutions can be obtained when the model is implemented in Matlab and can be applied to a wide range of designs. The model provides insight about how a conventional rectangular patch antenna can be re-tuned to few other frequencies by selecting the position of a thin shorting post. Further software development is ongoing for quick design generations from input specifications of rectangular microstrip antennas of commercial interest.

"As an answer to those who are in the habit of saying to every new fact, 'What is its use?' Dr. Franklin says to such, 'What is the use of an infant?' The answer of the experimentalist would be, 'Endeavour to make it useful.' "

Michael Faraday

5

Active Rectangular Microstrip Antenna: Limitations of the Model

5.1 Introduction

Use of variable capacitors or varactor diodes for polarisation agility was mentioned as early as 1981 [59, 71] and was extended for arrays later [72–74]. The next improvement happened with the use of a BAR28 Schottky barrier diode operating in reverse-bias to reconfigure the resonance frequency [75]. Further modelling and investigations were also discussed on probe-fed microstrip patch antennas and arrays loaded with varactor diodes (Schottky barrier diodes) [76–78]. A detailed model and explanation of a varactor-loaded patch antenna can again be found in [79]. A cavity model of varactor loaded circular microstrip antenna can be accessed in [80]. Improvement of scan

performance of microstrip patch array antennas are also possible by using shorting posts and diodes [81] and possibility of using diodes to replace the shorting posts were discussed in the past. Multiple diodes were also mentioned in the past for polarisation agility [73, 74] and also for dual-frequency operations [77]. Modern polarisation agile microstrip antennas use only an SPDT switch with a hybrid coupler to limit design complications, and efficient operation [82]. In most of the previously mentioned papers, the diode is modelled inside a hole similar to a 'via' or shorting post, and may have been difficult to solder. With present day packaging of RF diodes (e.g. SC-79 package), they would be impossible to solder inside a hole to replace a shorting post, as mentioned in the literature. Resistor loading was investigated as a replacement of shorting posts and varactor diodes, and it was found that resistor loading benefits the return-loss bandwidth up to an extent [83, 84].

While most of the publications have focused on the advantages of using a diode for various kinds of reconfigurability, this chapter concentrates on the accuracy of inset-feed transmission-line modelling of the rectangular microstrip antenna and its extension with one or more diodes. Multiple diodes were used to emulate one diode with higher junction capacitance to test the transmission-line model rigorously. Most previous publications (to the best of the authors' knowledge) have discussed the probe fed models only with return-loss diagrams of calculated and measured results [59, 78, 79]. In this chapter, an empirically model of inset-feed was verified, which is rarely discussed, with complex impedance results plotted on a Smith chart. The transmission-line model of a rectangular microstrip patch antenna [40, 48–51] is modified to archetype the effect of the one or more varactor diodes and 'vias'. Forty-two test cases are used to obtain the highly accurate, and less precise results across five different reconfigurable rectangular microstrip antennas.

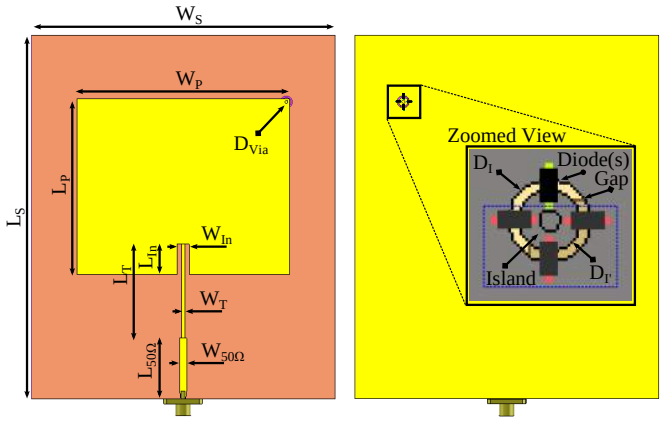

(a) Layout used for Antenna I - IV

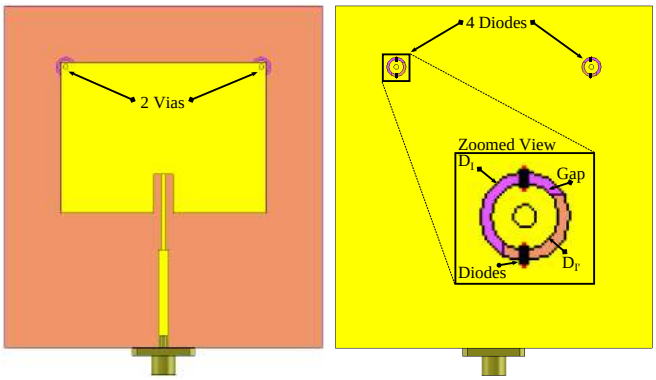

(b) Layout used for Antenna V

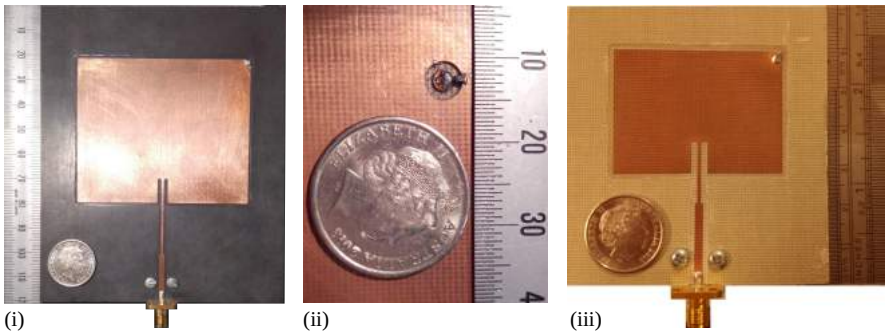

(c)

Figure 5.1: Layout (top and bottom view) of the investigated antennas (a) for Antenna I to IV, and (b) for Antenna V; along with the fabricated patch antennas showing (c)(i) the top view of 'Antenna I' with the short at the upper right vertex, (c)(ii) zoomed in view of a varactor diode soldered to the island in the ground plane, in comparison to an Australian five-cent coin, and (c)(iii) the top view of 'Antenna II' with the short at the upper right vertex of the patch.

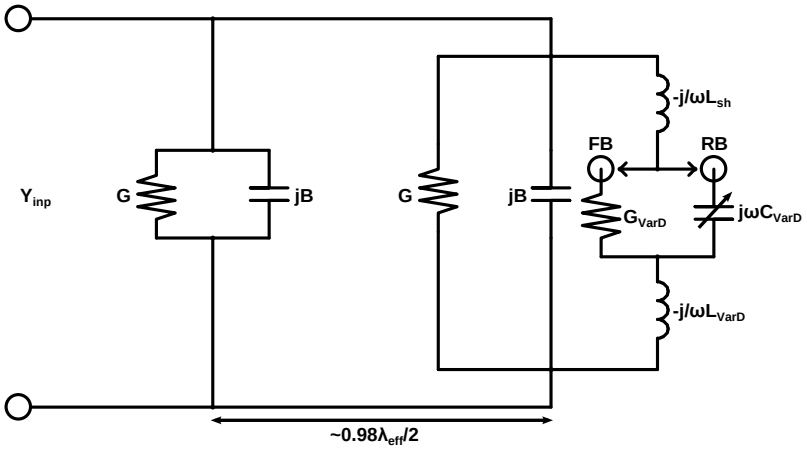

(a) Transmission-line model diagram for Antenna I and II

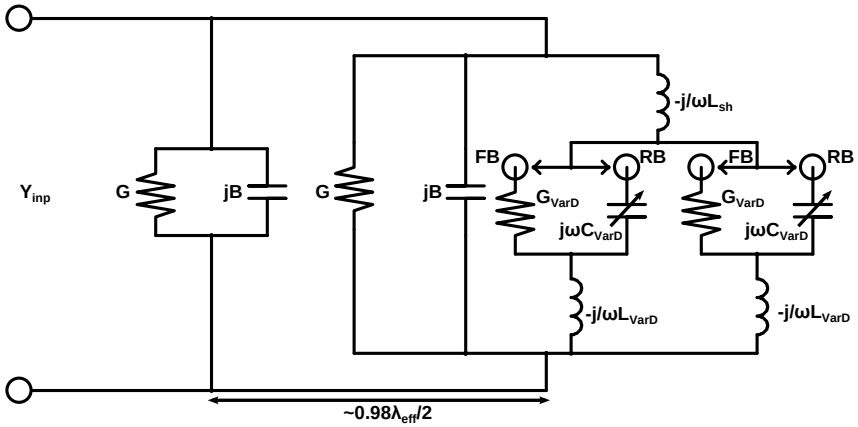

(b) Transmission-line model diagram for Antenna III and IV

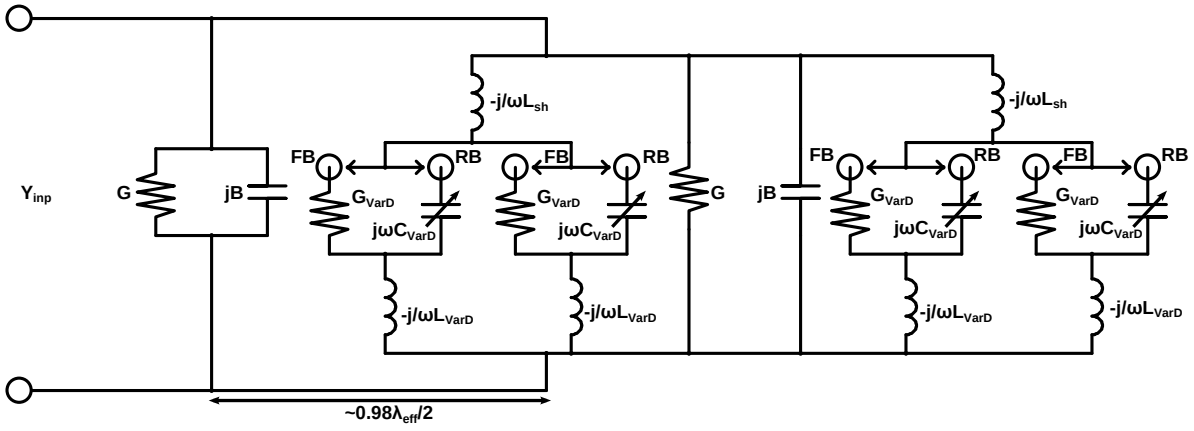

(c) Transmission-line model diagram for Antenna V

Figure 5.2: Extended transmission-line model diagrams of the five antennas investigated in this chapter.

5.2 Varactor Based Antenna Configurations

Five separate antenna designs are discussed below in different subsections. All the five antennas are based on two major base designs discussed in previous chapters. Two different substrates and different resonance frequencies are used for the design of the base antennas. The base antennas are modelled and manufactured first and verified in Chapter 2 and 3. Five extended reconfigurable antennas are then designed and validated with transmission-line results. All of them follow the same design layout shown in Fig. 5.1(a) except last one, which is given in Fig. 5.1(b).

5.2.1 Varactor Loaded Antenna Designs

Reconfigurability is implemented in the 'Base Design I' with the help of an actively operated 'via' located close to one of the outer vertex opposite to the feed in the patch element. Fig. 5.1(c)(i) shows the photograph of 'Antenna I'. The 'via' is connected to the patch and a small island in the ground plane (Fig. 5.1(c)(ii)) . An annular gap separates the island from the greater ground plane. One or few varactor diodes are connected across this gap, and they act as a load on the radiating slot of the patch antenna. In 'Antenna I' only one varactor diode is used. The outer and inner diameter of gap surrounding the island are $D_I = 4$mm and $D_{I'} = 3$mm. The 'via' is formed by an 18AWG wire with a diameter (D_{Via}) of 1mm. The diode(s) make an impedance bridge across the terminals of the SMA port and only a DC offset with a correct polarity is required across the SMA port to control the state of the varactor diode(s), which can be either forward or reverse-biased. This design methodology eliminates the requirement of any printed bias lines or dangling bias wires that can affect the resonance frequency and gain. Instead, only a bias-tee is required for tuning.

5.3 Varactor Extended Transmission-Line Model

When a thin via ($D_{Via} \ll W_P$) is soldered at the outer vertex of the rectangular patch, it can be approximated that the admittances of both the slots have the same

values as before, with the susceptance of the via, $-j/\omega L_{sh}$, added in parallel to the complex admittance of the outer slot [67]. With an island created and a varactor diode soldered to bridge the island and the greater ground plane as shown in Fig. 5.1, the transmission-line model can be extended as shown in Fig. 5.2(a). Depending on diode polarity, the transmission-line model changes to represent the state of the varactor diode. A forward-bias diode conductance G_{VarD} or a reverse-bias junction susceptance ωC_{VarD} along with the package-lead susceptance $-j/\omega L_{VarD}$ is added in series with the via susceptance. Then the patch input admittance for the extended transmission-line model is given by:

$$Y_{inp} = G + jB + Y_p \frac{G + j\left(B - \Psi + Y_p tan\, kL_P\right)}{Y_p - (B - \Psi) tan\, kL_P + jG tan\, kL_P} \tag{5.1a}$$

where

$$\Psi = \frac{G_{VarD}}{\omega G_{VarD}\left(L_{sh} + L_{VarD}\right) - j} \tag{5.1b}$$

in the forward-biased mode, and

$$\Psi = -\frac{\omega C_{VarD}}{1 - \omega^2 C_{VarD}\left(L_{sh} + L_{VarD}\right)} \tag{5.1c}$$

in the reversed-biased mode, k is the effective wave number and Y_p is the characteristic admittance of the patch. Notice that in the forward-biased mode, junction susceptance ωC_{VarD} is ignored. Likewise, diode conductance G_{VarD} is ignored for the reverse-biased mode.

5.3.1 Admittance with Two Diodes

More than one varactor diodes can be connected across the annular gap to connect one via to the ground plane. The extended transmission-line model with two varactor

diodes connected to one via is shown in Fig. 5.2(b). The patch input admittance for the extended transmission-line model given in Eq. (5.1a) remain the same with the value of Ψ, given in Eq. (5.1b) and Eq. (5.1c), modified as:

$$\Psi = \frac{2G_{VarD}}{\omega G_{VarD}\left(2L_{sh} + L_{VarD}\right) - j} \tag{5.2a}$$

in the forward-biased mode, and

$$\Psi = -\frac{2\omega C_{VarD}}{1 - \omega^2 C_{VarD}\left(2L_{sh} + L_{VarD}\right)} \tag{5.2b}$$

in the reverse-biased mode. All other parameters remain the same as mentioned before.

5.3.2 Admittance with Two 'Vias' and Multiple Diodes

The microstrip patch antenna has a magnetic symmetry across the centre of the radiating slots [68] and when two thin 'vias' ($D_{Via} \ll W_P$) are connected near two outer vertices, the extended transmission-line model (considering that two diodes are connected to each 'via') shown in Fig. 5.2(a) and 5.2(b), is further extended and shown in Fig. 5.2(c). The value of Ψ given in Eq. (5.1b) and Eq. (5.1c) can be re-written as:

$$\Psi = \frac{4G_{VarD}}{\omega G_{VarD}\left(2L_{sh} + L_{VarD}\right) - j} \tag{5.3a}$$

in the forward-biased mode, and

$$\Psi = -\frac{4\omega C_{VarD}}{1 - \omega^2 C_{VarD}\left(2L_{sh} + L_{VarD}\right)} \tag{5.3b}$$

in the reverse-biased mode. All other parameters remain the same as stated before.

5.4 Results - Varactor-Loaded Antennas

Primarily, the inset-fed transmission-line model was coded into Matlab using Eq. (3.3), (3.4)-(3.7). The base antenna designs were manufactured, and measurements were compared with the general inset-fed transmission-line model (GETLM) for accuracy. Transmission-line models of the reconfigurable antennas were then further incorporated into Matlab code using Eq. (5.1)-(5.3). Corresponding varactor junction capacitance and forward series resistance values were taken from the Skyworks SMV1232-079LF varactor diode datasheet. 'Base Design I' and 'Base Design II' were manufactured in-house using CNC router isolation milling and chemical etching and the return loss characteristics were measured. Full-wave simulations were conducted using CST Microwave Studio 2015 to compare results obtained with the extended transmission-line model (ETLM). Results obtained for the antennas are discussed in the following subsections. The base resonance frequency (without any modification to the simple patch antenna) for 'Base Design I', 'Antenna I' and 'Antenna III' is 1800 MHz and for 'Base Design II', 'Antenna II', 'Antenna IV' and 'Antenna V' is 2280 MHz. For brevity measured normalised far-field patterns are shown only for 'Antenna I' and the other antennas have similar patterns.

Table 5.1: Comparison of predicted resonant frequencies for 'Antenna I' along with those obtained from measurements, under different bias conditions. Percentage deviation of predicted value is relative to simulation and measurement results, respectively.

Bias (V)	Bias Type	ETLM	CST	% Devn.	Measured	% Devn.
1.0	Forward	1773	1766	0.40	1766	0.40
2.0	Reverse	1653	1651	0.12	1650	0.18
3.0	Reverse	1676	1674	0.12	1676	0.00
4.0	Reverse	1687	1686	0.06	1690	0.18
5.0	Reverse	1692	1691	0.06	1698	0.35
7.0	Reverse	1697	1697	0.00	1705	0.47
9.0	Reverse	1699	1699	0.00	1708	0.53

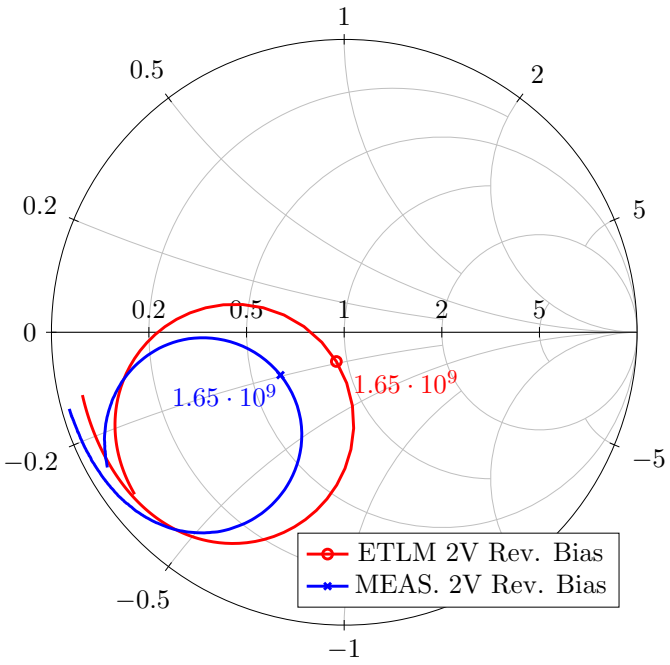

(a) Antenna I with 2V Reverse-Bias

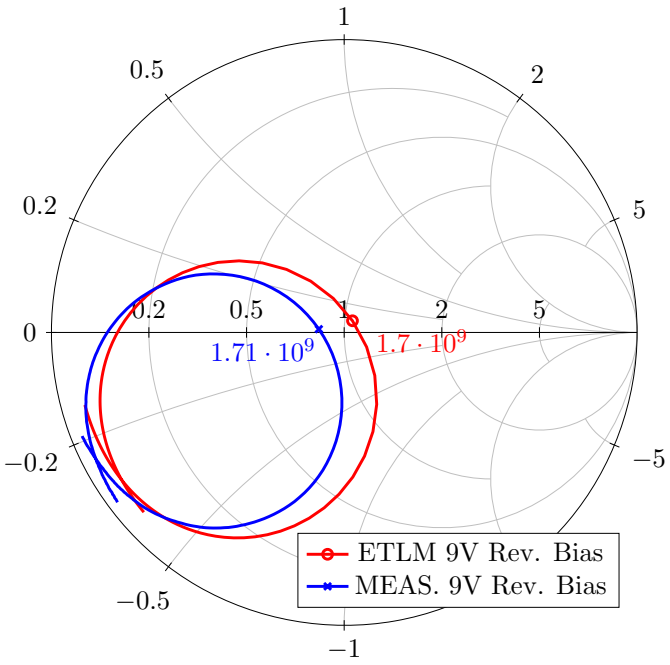

(b) Antenna I with 9V Reverse-Bias

Figure 5.3: Complex impedance of 'Antenna I', under various bias conditions, obtained using ETLM and measurements. The Smith Chart is normalized to 50Ω and shows the complex impedance between 1600 MHz and 1800 MHz.

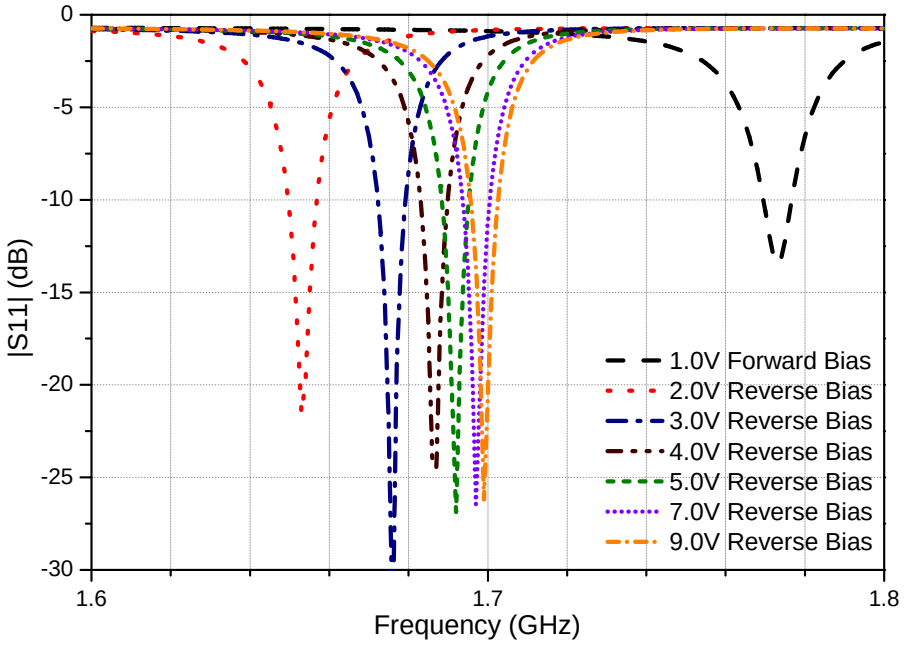

(a) Analytical result obtained using Eq. (3.3) - (3.7) and Eq. (5.1)-(5.3)

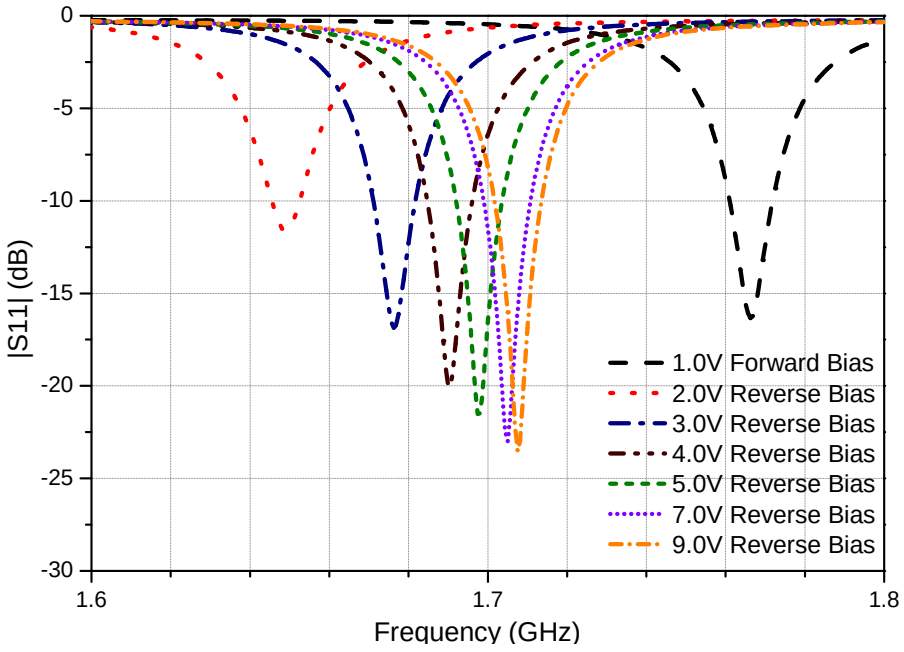

(b) Measured result

Figure 5.4: Predicted and measured return loss of 'Antenna I' with a single varactor diode under different bias conditions.

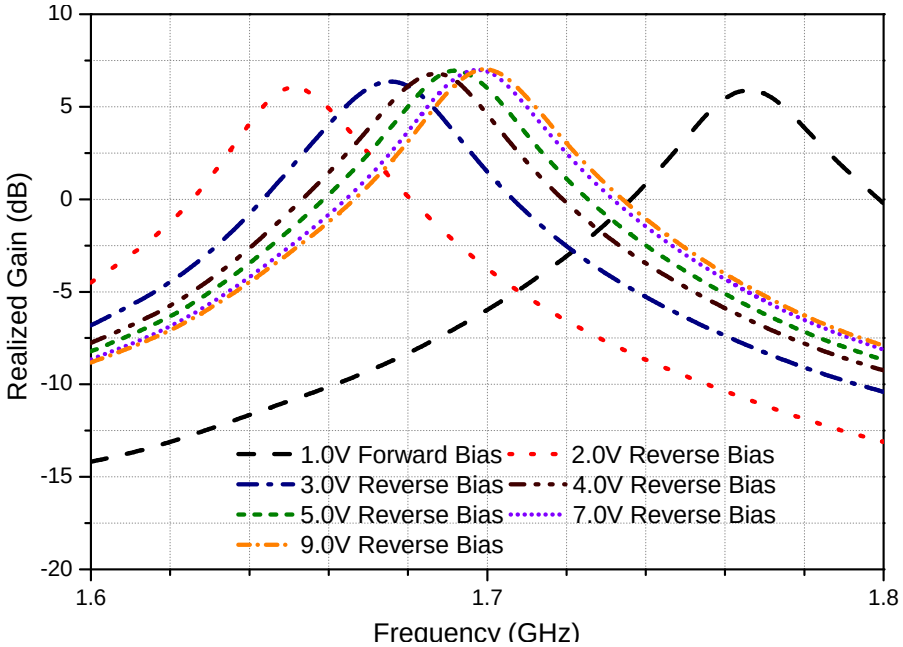

(a) Realized gain over the tunable range obtained using CST MWS 2015

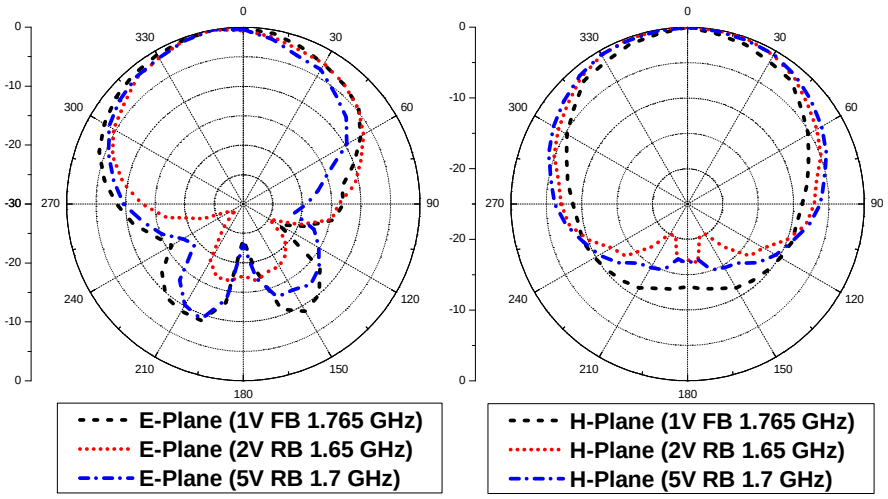

(b) Measured farfield pattern in the E-plane and H-plane

Figure 5.5: Realized gain and farfield pattern of 'Antenna I' with a single varactor diode under different bias conditions.

5.4.1 Antenna I

Complex impedance for 'Antenna I' is shown in Fig. 5.3(a) and Fig. 5.3(b) for the reverse-bias voltages of 2V and 9V, respectively. The analytically obtained input reflection coefficient magnitude $|S_{11}|$ obtained using the ETLM discussed earlier is shown in Fig. 5.4(a). Fig. 5.4(b) shows the measured $|S_{11}|$ obtained from an Agilent PNA-X vector network analyser. The ELTM results are in good agreement with the measured results, and a comparison is tabulated in Table 5.1. Deviations from all the bias conditions is given as a percentage in Table 5.1. The maximum deviation for the ELTM with respect to simulations is 0.40% and is 0.53% when compared to measurements.

Tuning is achieved between 1650 MHz and 1708 MHz with the varactor diode biased into reversed-mode and reverse voltage swept between 2V and 9V. The antenna also resonates at a frequency of 1766 MHz when the varactor diode is forward-biased. Fig. 5.5(b) shows the measured normalised far-field patterns for the reverse-bias voltages of 2V and 5V and a forward-bias voltage of 1V, at the corresponding resonance frequencies of 1650 MHz, 1700 MHz, and 1765 MHz, respectively. Peak realised gain is 5.86 dBi, 6.82 dBi and 5.83 dBi at these frequencies, respectively. The pattern is consistent across the entire tuning range, but the gain varies slightly due to variation in active device losses.

The variation of realised gain is shown in Fig. 5.5(a), under different bias conditions. The efficiency of the antenna is low for low reverse-bias voltages but increases with the increase of the tuning voltage. The reason behind this phenomenon is that the intrinsic capacitance of the varactor diode decreases with increasing voltage resulting a very low susceptance and thus it is less prone to allow lossy currents at a given frequency of operation. Additionally, even though the patch is being tuned to operate at a lower frequency, the length of the patch is not ideal to produce maximum radiation and hence the radiation efficiency starts to deteriorate. In forward-biased operation, the loss is due to the forward-bias diode resistance. In the forward-bias mode, 'Antenna I' has a total efficiency of 63%. In the 9V reverse-bias, the efficiency is 88%, and it is 73%

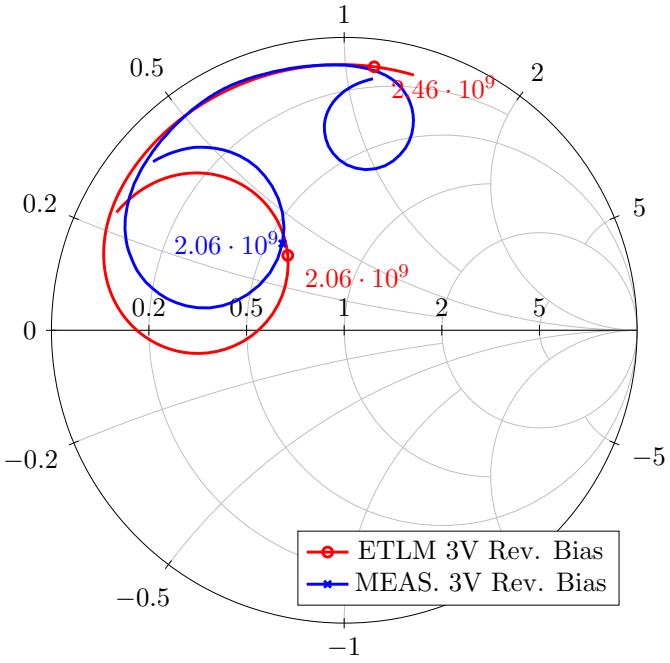

(a) Antenna II with 3V Reverse-Bias

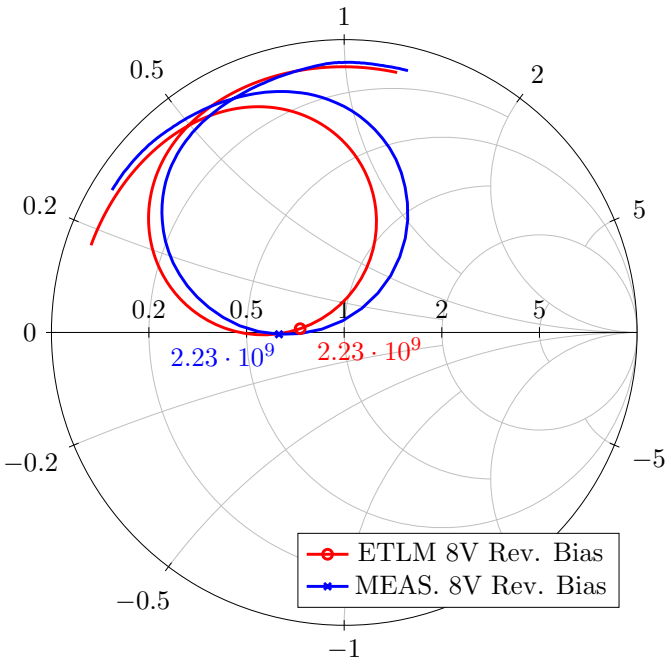

(b) Antenna II with 8V Reverse-Bias

Figure 5.6: Complex impedance of 'Antenna II', under various bias conditions, obtained using ETLM and measurements. The Smith Chart is normalized to 50Ω and shows the complex impedance between 2000 MHz and 2500 MHz.

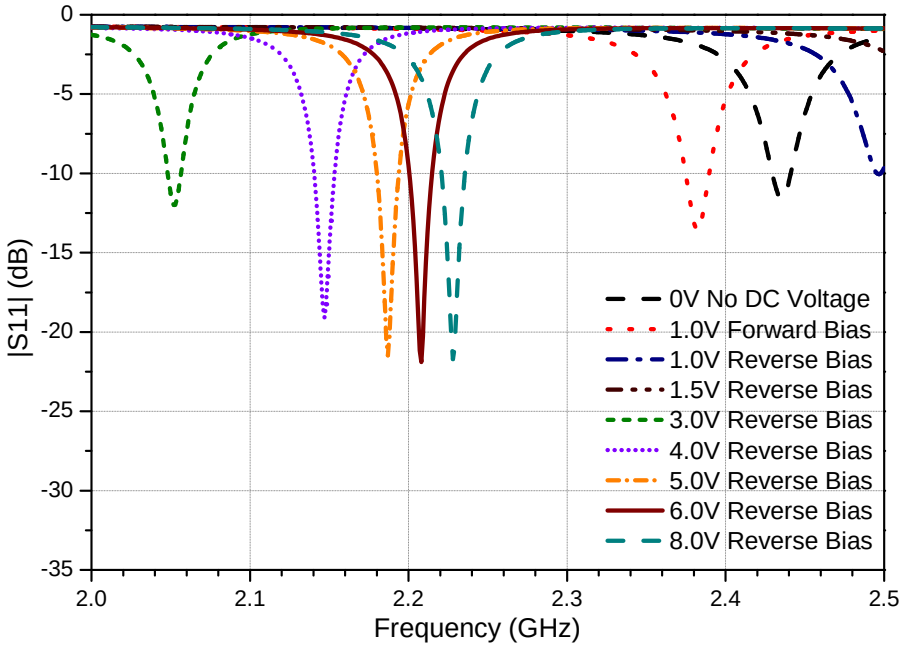

(a) Analytical result obtained using Eq. (3.3) - (3.7) and Eq. (5.1)-(5.3)

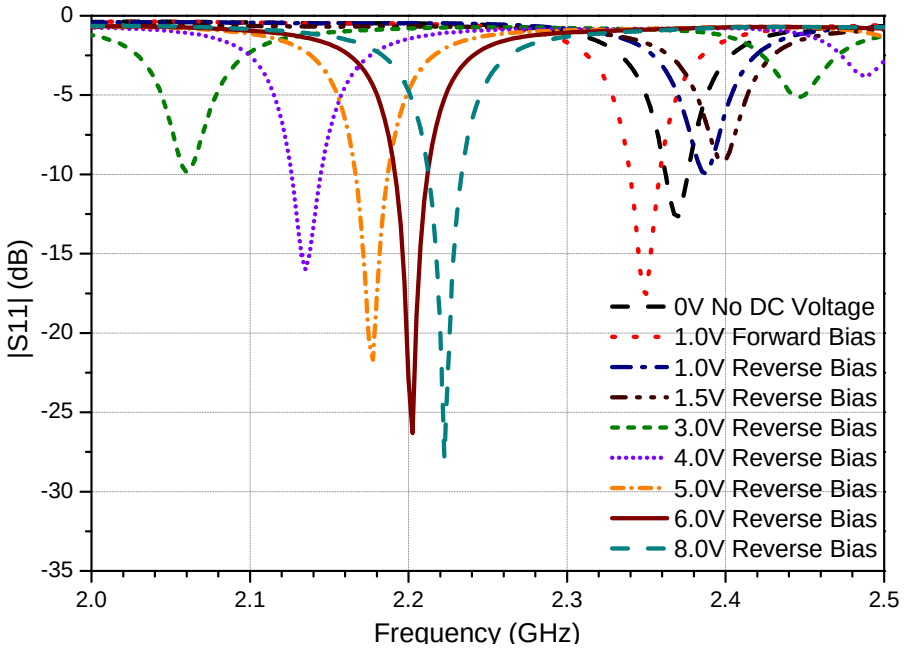

(b) Measured result

Figure 5.7: Predicted and measured return loss of 'Antenna II' with a single varactor diode under different bias conditions.

when the reverse-bias is 2V.

Table 5.2: Comparison of predicted resonant frequencies for 'Antenna II' along with those obtained from measurements, under different bias conditions.

Bias (V)	Bias Type	ETLM	CST	% Devn.	Measured	% Devn.
0.0	Unbiased	2435	2372	2.66	2370	2.74
1.0	Forward	2382	2347	1.49	2350	1.36
1.0	Reverse	2490	2392	4.10	2387	4.32
1.5	Reverse	2531	2403	5.33	2398	5.55
3.0	Reverse	2052	2069	0.82	2060	0.39
4.0	Reverse	2147	2131	0.75	2135	0.56
5.0	Reverse	2187	2164	1.06	2178	0.41
6.0	Reverse	2208	2184	1.10	2203	0.23
8.0	Reverse	2228	2205	1.04	2223	0.22

5.4.2 Antenna II

Complex impedance results in the Smith chart are shown in Fig. 5.6(a) and Fig. 5.6(b) for the reverse-bias voltages of 3V and 8V, respectively. Results obtained through ELTM are in good agreement with the measured results and are shown in Fig. 5.7(a). Fig. 5.7(b) shows the measured results under different bias conditions. It is interesting to note here that the measured results show few more reverse-bias voltage plots that have a resonance frequency higher than the base frequency of the antenna (2280 MHz), similar to the forward-biased case. The upper resonance frequency is the result of the large junction capacitance of the varactor diode, which behaves more like a bypass capacitor creating an AC short. The ELTM does not perform efficiently at this stage, and the deviation is more than 3% in some of the test cases. Table 5.2 compares the ETLM results to simulations and measurements. Two out of nine test cases have a deviation more than 3%.

Fig. 5.8(b) shows the surface current density of the antenna for various configurations. Fig. 5.8(b)(i) shows the surface current of the antenna without any diode bridging the annular gap, even though the 'via' is present. In this case, the 'via' does

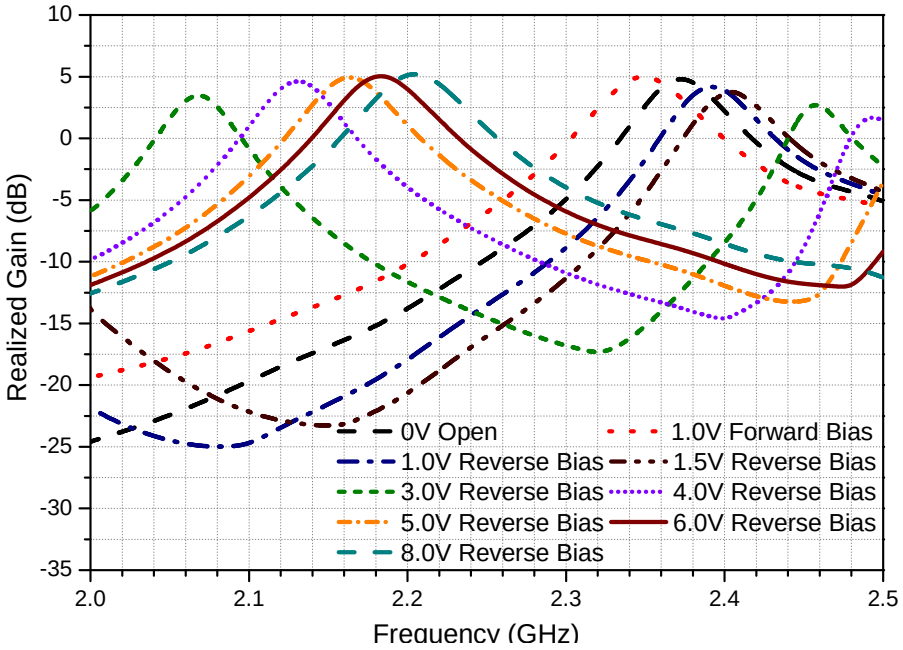

(a) Realized gain over the tunable range obtained using CST MWS 2015

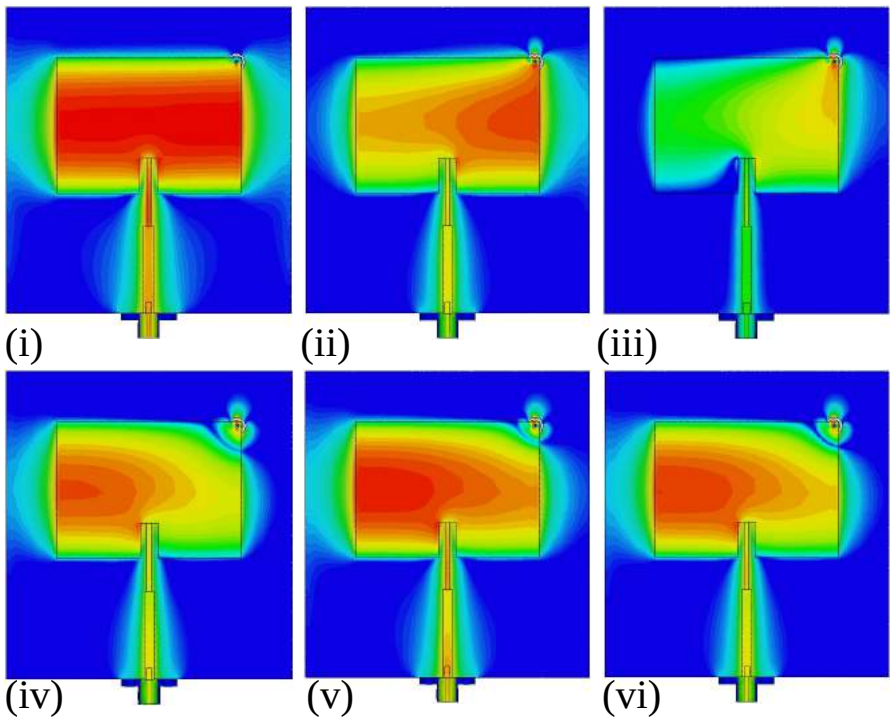

(b) Surface current density with different bias conditions

Figure 5.8: Realized gain of 'Antenna II' with a single varactor diode under different bias conditions along with the surface current density when the (b)(i) patch antenna resonating at 2280 MHz without any diode connected across the annular gap, (b)(ii) patch antenna resonating at 2205 MHz with the diode reverse-biased at 8V, (b)(iii) patch antenna with the diode reverse-biased at 3V, resonating at 2069 MHz, (b)(iv) patch antenna with the diode unbiased (having a large junction capacitance), resonating at 2372 MHz, (b)(v) patch antenna with the diode forward-biased, resonating at 2347 MHz, and (b)(vi) patch antenna with a strip short in place of the diode, resonating at 2345 MHz.

not short to the greater ground plane, and the surface current density is as in a conventional rectangular microstrip patch antenna. The resonance frequency is 2280 MHz. The surface current density with the varactor reverse-biased at 8V is shown in Fig. 5.8(b)(ii). At this voltage, the resonance frequency is 2205 MHz. The loading of the capacitor at one of the vertex disturbed the uniformity of the current density. Fig. 5.8(b)(iii) shows the current density with a reverse-bias of 3V. The 3V reverse-bias is the lowest voltage and the highest value of junction capacitance (1.51pF) which can act as a load for this antenna which resonates at 2069V. Any higher value of the junction capacitance becomes a bypass capacitor. This phenomenon is shown in Fig. 5.8(b)(iv). With an unbiased varactor, the junction capacitance is 4.15pF and acts as a bypass capacitor shorting the vertex of the patch antenna, thus reducing the effective radiating area of the patch. In this case, the resonance frequency is 2372 MHz. When the varactor diode is forward-biased, the surface current distribution is similar to having a bypass capacitor, as shown in Fig. 5.8(b)(v). The resonance frequency with a forward-bias is 2347 MHz. Finally, the surface current density with a strip short (a copper strip soldered in place of the diode as shown in Fig. 5.1(c)) is shown in Fig. 5.8(b)(vi). The resonance frequency with a strip-short is 2345 MHz.

This prototype was mainly chosen to demonstrate the bypass effect of the varactor diode and the disability of the transmission-line model in those test cases. This bypassing effect led to tunable resonance frequencies both above and below the base resonance frequency of the patch antenna (i.e. 2280 MHz). This effect cannot be seen in 'Antenna I' as it operates in a lower frequency range. Frequency reconfigurability is achieved between 2060 MHz and 2223 MHz and again from 2370 MHz and 2398 MHz with the varactor diode biased into reversed-mode and reverse voltage swept between 0V and 8V, for the manufactured prototype. The antenna also resonates at a frequency of 2350 MHz when the varactor diode is forward-biased. The variation of realised gain is shown in Fig. 5.8(a), under different bias conditions. The forward-bias efficiency is 69%, and the reverse-bias efficiencies are 56% and 74% at 3V and 8V, respectively.

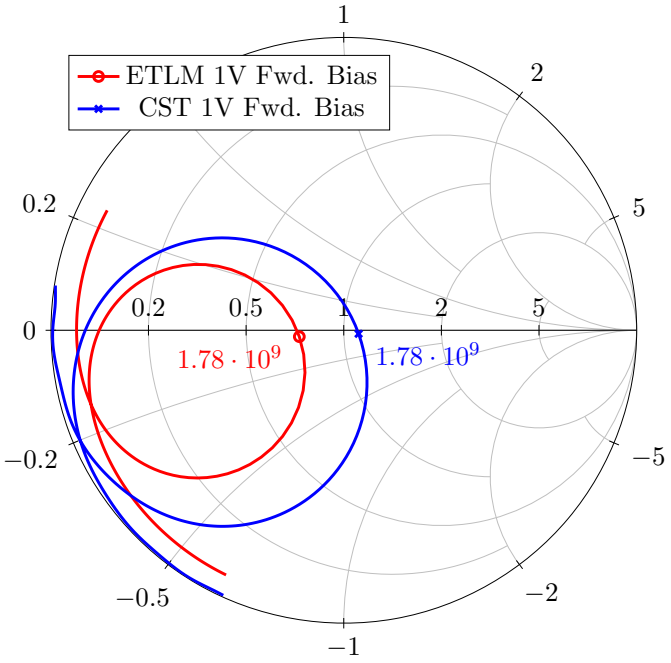

(a) Antenna III with 1V Forward-Bias

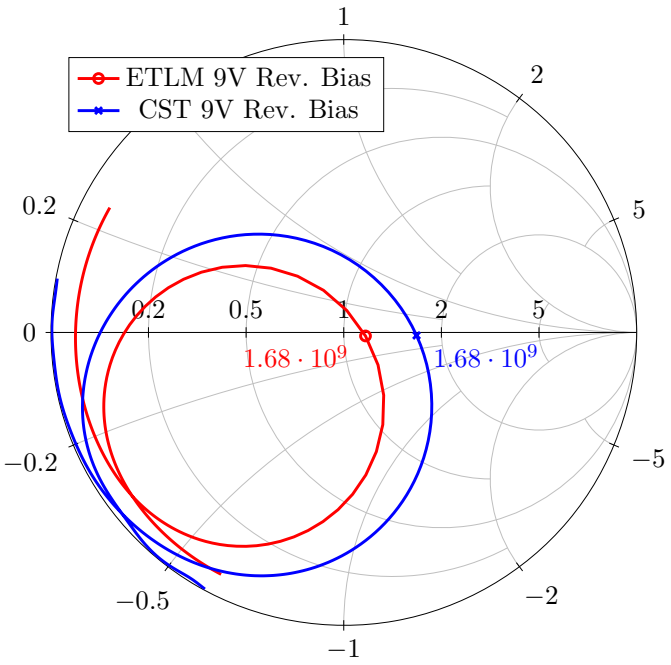

(b) Antenna III with 9V Reverse-Bias

Figure 5.9: Complex impedance of 'Antenna III', under various bias conditions, obtained using ETLM and simulations. The Smith Chart is normalized to 50Ω and shows the complex impedance between 1500 MHz and 2000 MHz.

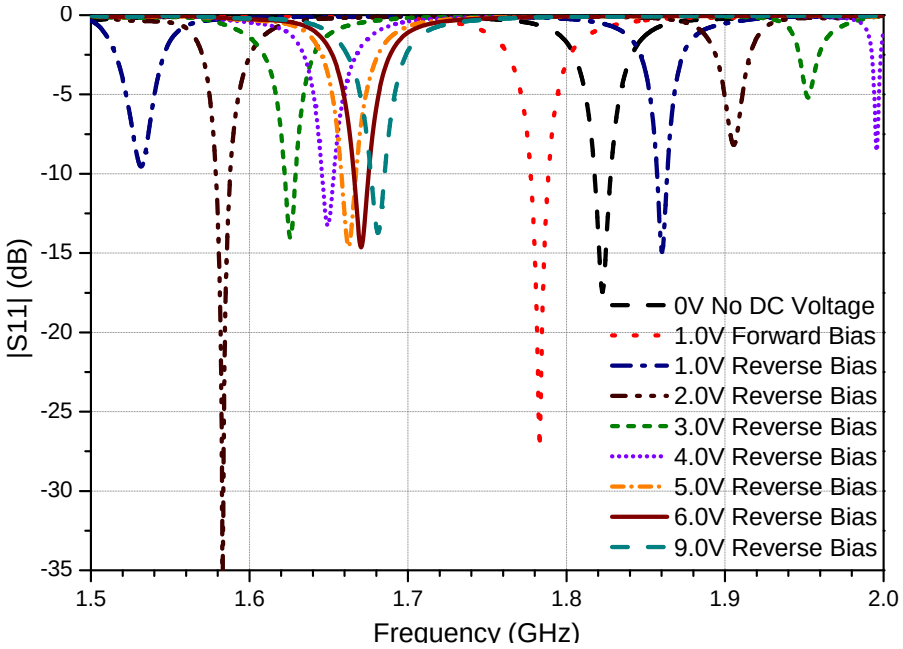

(a) Predicted result for Antenna III using CST MWS & DS 2015

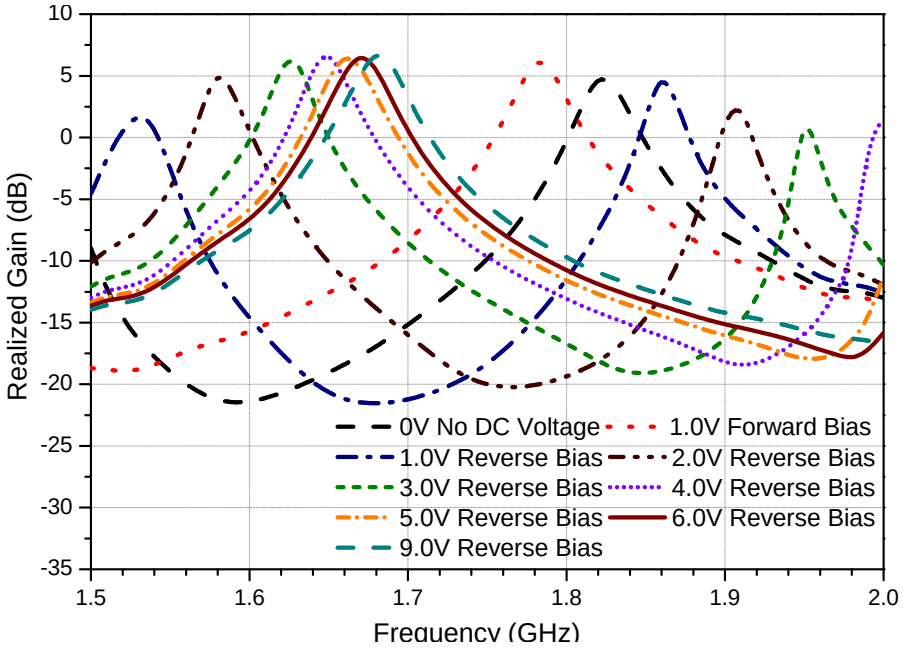

(b) Realized gain for Antenna III over the tunable range obtained using CST MWS 2015

Figure 5.10: Predicted return loss and realized gain of 'Antenna III', under different bias conditions.

Table 5.3: Comparison of predicted resonant frequencies for 'Antenna III' along with those obtained from measurements, under different bias conditions.

Bias (V)	Bias Type	ETLM	CST	% Devn.
0.0	Unbiased	1842	1822	1.10
1.0	Forward	1783	1783	0.00
1.0	Reverse	1905	1861	2.36
2.0	Reverse	1457	1583	7.96
3.0	Reverse	1579	1625	2.83
4.0	Reverse	1630	1649	1.15
5.0	Reverse	1651	1663	0.72
6.0	Reverse	1663	1670	0.42
9.0	Reverse	1677	1681	0.24

5.4.3 Antenna III

Complex impedance results in the Smith chart are shown in Fig. 5.9(a) and Fig. 5.9(b) for the forward-bias at 1V and reverse-bias at 9V, respectively. Table 5.3 compares the resonance frequencies obtained with the ETLM to the simulation results. In eight out of nine test cases, the transmission-line model has an excellent agreement with the simulated complex impedance, with less than 3% deviation with respect to simulations. Four out of nine test cases have less than 1% deviation. Table 5.3 compares the resonance frequencies obtained with the ETLM to the simulation results. Predicted return loss results are presented in Fig. 5.10(a) to provide insight into the tuning range and gain roll-off effects when two varactor diodes are used to connect the via to the greater ground plane. The use of two varactor diodes results in a phenomenon similar to 'Antenna II' where the cumulative capacitance is large enough to create an AC short. The antenna can be tuned between 1530 MHz and 1680 MHz and again from 1823 MHz to 1880 MHz with reverse-bias and to 1780 MHz with forward-bias. The gain roll-off for the antenna across the tuning range is shown in Fig. 5.10(b). The forward-bias efficiency is 67%, and the reverse-bias efficiencies are 58% and 81% at 2V and 9V, respectively.

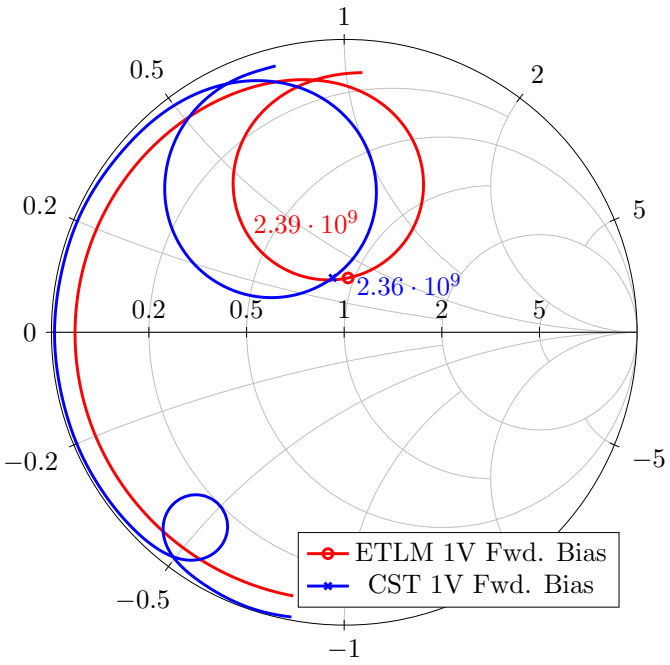

(a) Antenna IV with 1V Forward-Bias

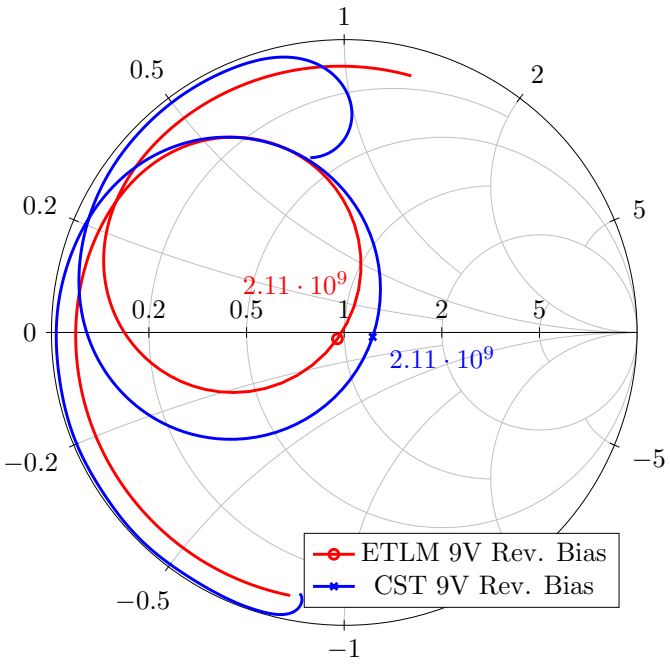

(b) Antenna IV with 9V Reverse-Bias

Figure 5.11: Complex impedance of 'Antenna IV', under various bias conditions, obtained using ETLM and simulations. The Smith Chart is normalized to 50Ω and shows the complex impedance between 1500 MHz and 2500 MHz.

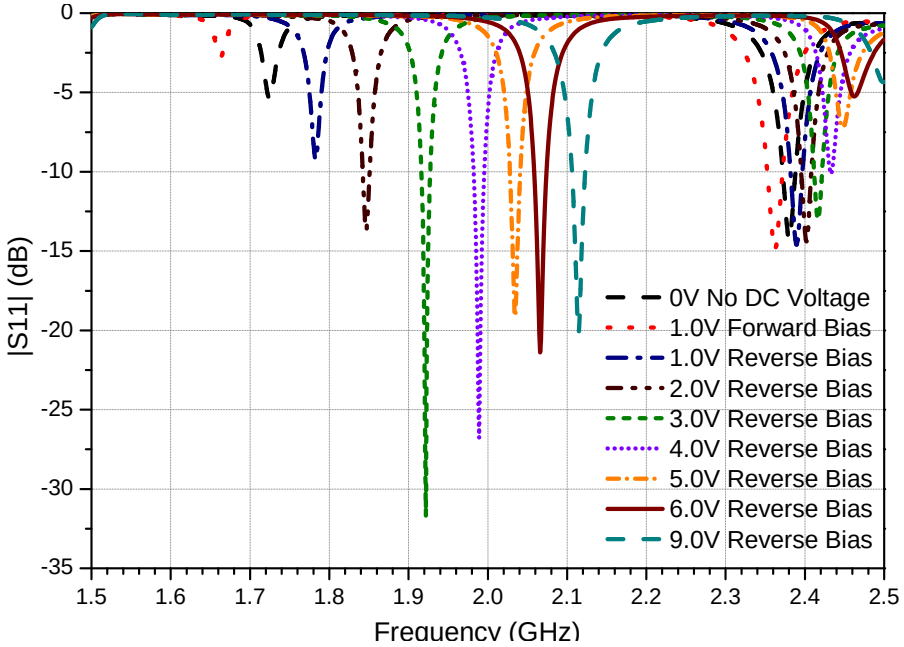

(a) Predicted result for Antenna IV using CST MWS & DS 2015

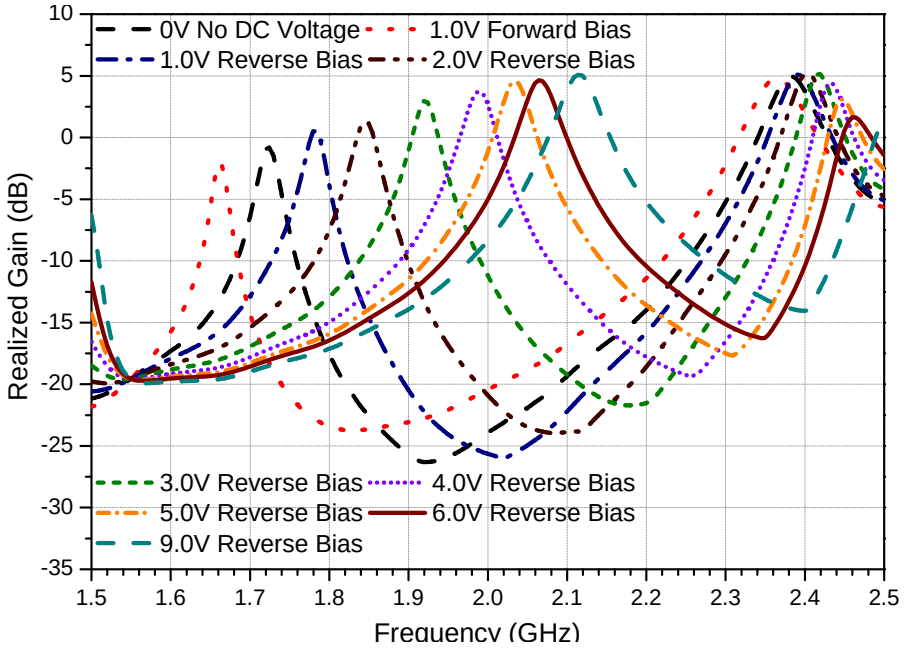

(b) Realized gain for Antenna IV over the tunable range obtained using CST MWS 2015

Figure 5.12: Predicted return loss and realized gain of 'Antenna IV', under different bias conditions.

Table 5.4: Comparison of predicted resonant frequencies for 'Antenna IV' along with those obtained from measurements, under different bias conditions.

Bias (V)	Bias Type	ETLM	CST	% Devn.
0.0	Unbiased	2427	2380	1.97
1.0	Forward	2395	2362	1.40
1.0	Reverse	2452	2390	2.59
2.0	Reverse	1406 & 2485	1847 & 2402	23.88 & 3.46
3.0	Reverse	1598 & 2521	1922 & 2417	16.86 & 4.30
4.0	Reverse	1804 & 2585	1989 & 2433	9.30 & 6.25
5.0	Reverse	1986	2034	2.36
6.0	Reverse	2042	2066	1.16
9.0	Reverse	2111	2114	0.14

5.4.4 Antenna IV

Complex impedance results are shown in Fig. 5.11(a) and Fig. 5.11(b) for 1V forward-bias and 9V reverse-bias, respectively. Table 5.4 shows the comparison between ETLM and simulations for multiple test cases. Only five out of nine test cases have deviations less than 3%. Only one test case has a deviation less than 1%. But the complex impedance for ETLM with less that 3% deviation are in good agreement to simulations, when plotted on a Smith chart. This antenna can be tuned between 1800 MHz and 2115 MHz and again from 2380 MHz to 2418 MHz with reverse-bias and to 2362 MHz with forward-bias. Fig. 5.12(a) shows the return loss predicted by CST Microwave Studio and Design Studio 2015, under different bias conditions. The gain roll-off for the antenna across the tuning range is shown in Fig. 5.12(b). The forward-bias efficiency is 65%, and the reverse-bias efficiencies are 33% and 73% at 2V and 9V, respectively.

5.4.5 Antenna V

Table 5.5 compares the ETLM results with CST simulations. None of the test cases has a deviation less than 1%. Only two of the test cases have deviations less than 3% when compared to simulations, but their complex impedance is in fair agreement with simulations when plotted on a Smith chart. Fig. 5.13(a) and Fig. 5.13(b) shows

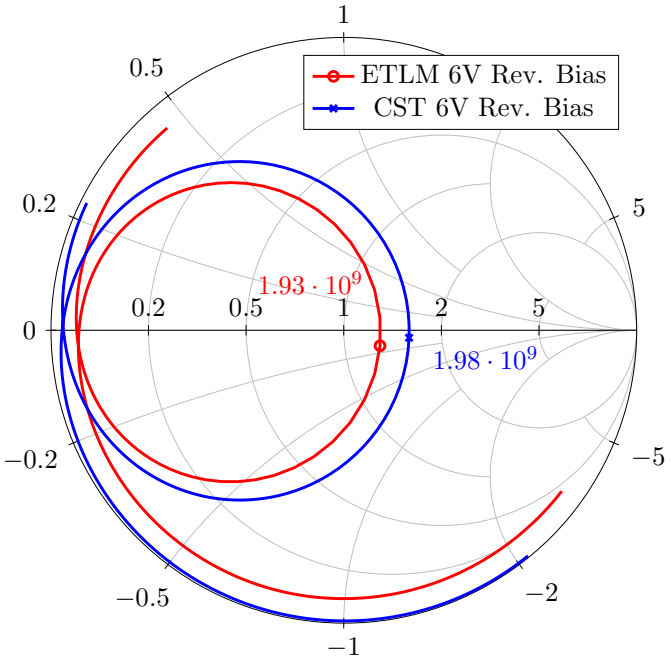

(a) Antenna V with 6V Reverse-Bias

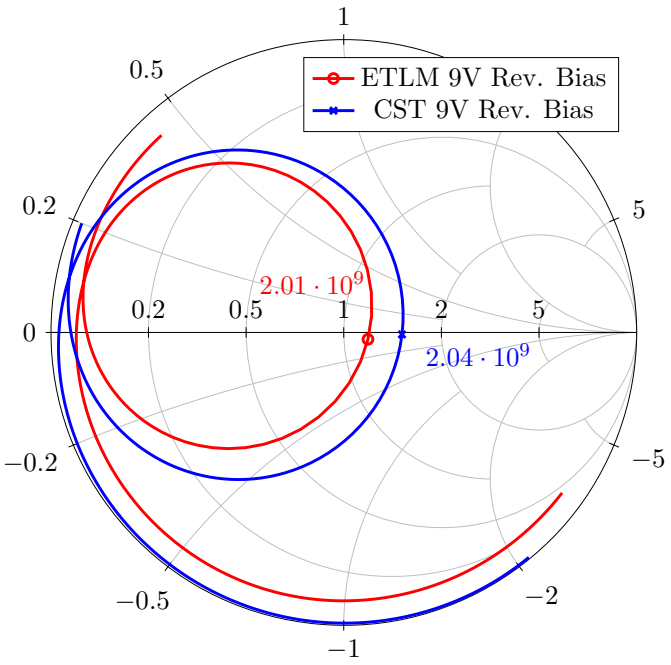

(b) Antenna V with 9V Reverse-Bias

Figure 5.13: Complex impedance of 'Antenna V', under various bias conditions, obtained using ETLM and simulations. The Smith Chart is normalized to 50Ω and shows the complex impedance between 1200 MHz and 2200 MHz.

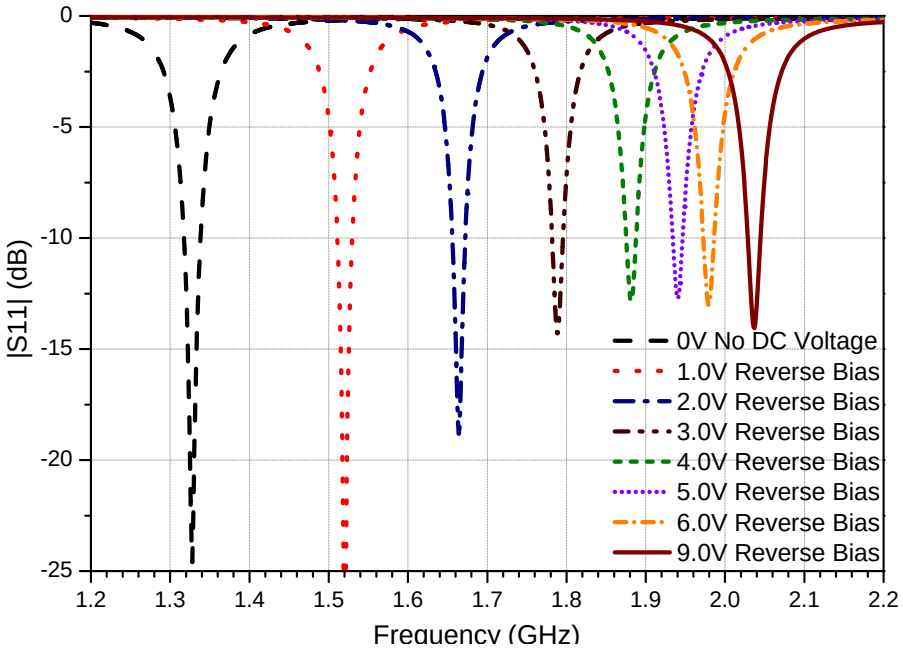

(a) Predicted result using CST MWS & DS 2015

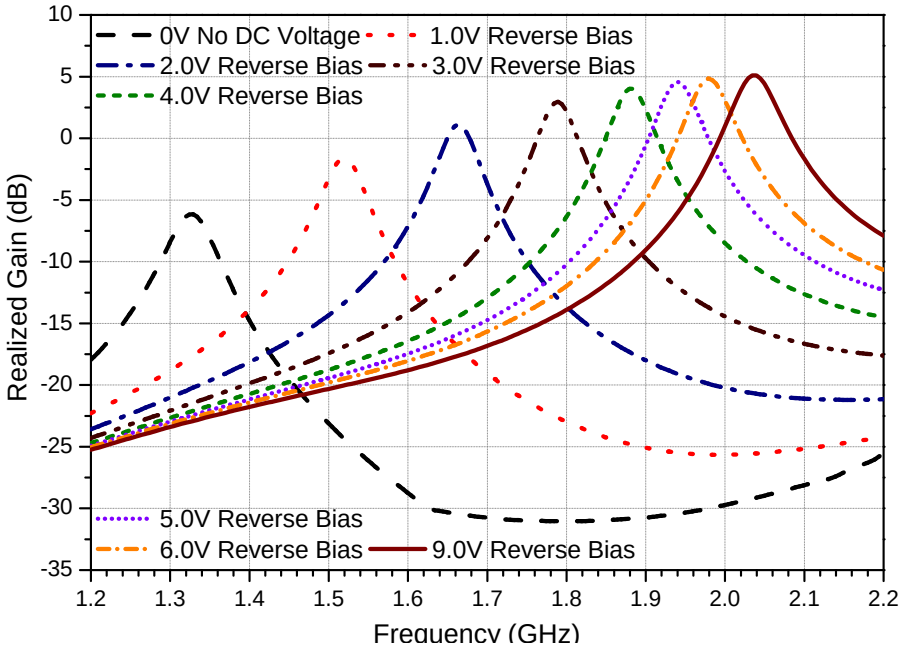

(b) Realized gain over the tunable range obtained using CST MWS 2015

Figure 5.14: Predicted return loss and realized gain of 'Antenna V', under various bias conditions, obtained using ETLM and simulations.

Table 5.5: Comparison of predicted resonant frequencies for 'Antenna IV' along with those obtained from measurements, under different bias conditions.

Bias (V)	Bias Type	ETLM	CST	% Devn.
0.0	Unbiased	927	1328	30.20
1.0	Reverse	1225	1520	19.41
2.0	Reverse	1442	1664	13.34
3.0	Reverse	1640	1789	8.33
4.0	Reverse	1785	1881	5.10
5.0	Reverse	1872	1940	3.51
6.0	Reverse	1928	1979	2.58
9.0	Reverse	2006	2037	1.52

the comparison for reverse-bias at 6V and 9V, respectively. Fig. 5.14(a) shows the tunable range for the antenna under various reverse-bias conditions, as obtained from simulations. The antenna can be tuned between 1328 MHz (with no bias) voltage and 2037 MHz (with 9V reverse-bias). The gain roll-off is shown in Fig. 5.14(b) is quite significant. The realised peak gain varies between -6 dBi at (0V bias) and 5.1 dBi (with 9V reverse-bias), respectively. The reverse-bias efficiencies are 8% and 74% at 0V and 9V, respectively.

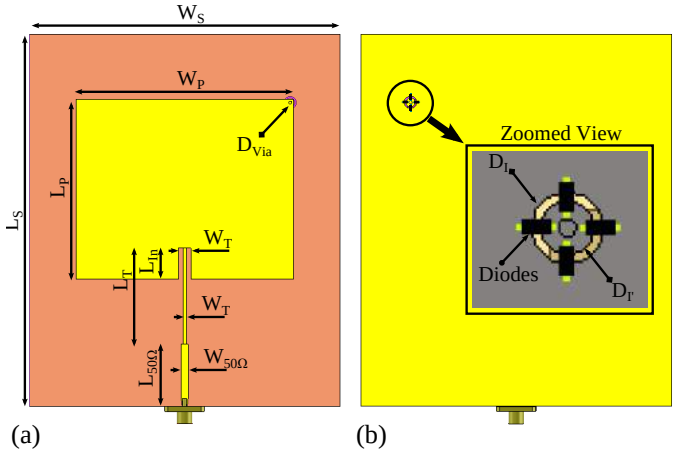

Figure 5.15: Layout of the proposed antenna (a) the top view with the patch and (b) the bottom view with ground plane and PIN diodes zoomed in.

5.5 PIN Based Antenna Configurations

A single antenna design based on a modified Base Antenna I has been used to examine the PIN based extended transmission-line model. Band switching is achieved with the help of a switchable via located close to one of the outer vertex opposite to the feed. The 'via' is connected to the patch and a small island in the ground plane. Four PIN diodes act as switching bridges between the island and the greater ground plane. The outer and inner diameter of the gap surrounding the island are denoted by D_I and $D_{I'}$, respectively. The final dimensions of this gap are D_I = 4mm and $D_{I'}$ = 3mm. An 18AWG wire forms the via with a diameter (D_{Via}) of 1mm. The layout of the PIN diodes is shown in Fig. 5.15(b). The switching diodes make an impedance bridge across the terminals of the SMA port, and only a DC offset is required across the SMA port to control the state of the PIN diode. This design methodology eliminates the requirement of any printed bias lines or dangling bias wires that can affect the resonance frequency and the gain. Instead, only a bias-tee is required for the switching.

A shorted 'via' reduces the effective size of the patch and makes it resonant at a higher frequency than the open-circuit resonance frequency. The overall realised gain and antenna efficiency are slightly affected by the losses incurred by the PIN diode switches. The loss in ON state is reduced with multiple diodes due to the reduction of overall diode impedance. In the OFF state, loss increases with the increase of the number of diodes as the overall parallel impedance acts like a lossy short. Four diodes were selected as a compromise.

5.6 PIN Extended Transmission-Line Model

The proposed design is made reconfigurable with the shorted end soldered to an island in the inner island which itself is connected to the greater ground by four PIN diodes. Each PIN diode can be simply modelled as a resistor parallel to the intrinsic capacitance of the junction where the value of the resistance varies between a high and a low value depending on the bias current applied to it. The transmission line model is shown in

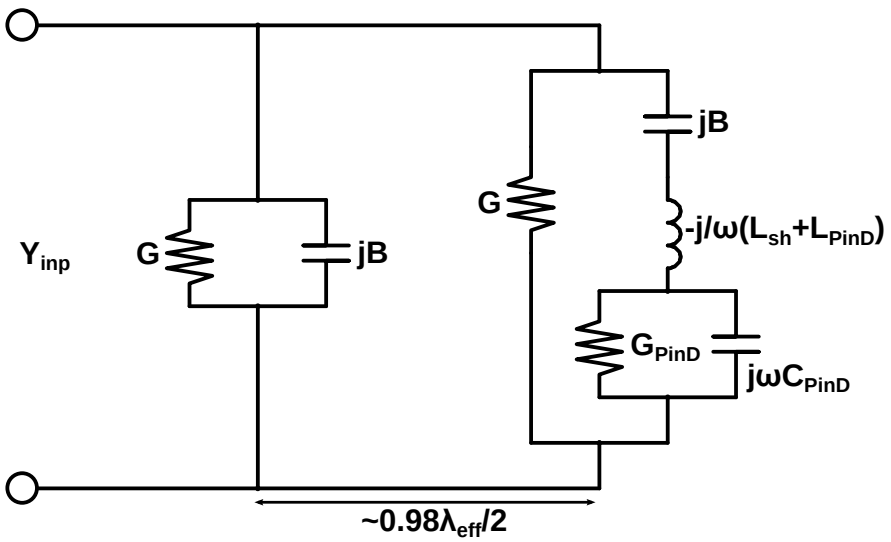

Figure 5.16: Extended transmission-line model for the PIN diode reconfigurable antenna.

Fig. 5.16 to represent this reconfigurable antenna. Its input admittance is given by:

$$Y_{inp} = G + jB + Y_p \frac{G + j\left(B - \Psi + Y_p tan\, kL_P\right)}{Y_p - (B - \Psi) tan\, kL_P + jG tan\, kL_P} \tag{5.4a}$$

$$where\ \Psi = \frac{G_{PinD} + j\omega C_{PinD}}{\omega G_{PinD}(L_{sh} + L_{PinD}) - j\left\{1 - \omega^2 C_{PinD}(L_{sh} + L_{PinD})\right\}} \tag{5.4b}$$

where G_{PinD} is the combined conductance of the PIN diode either in on or off state and C_{PinD} is the combined intrinsic capacitance of the PIN diode junctions. L_{sh} is the 'via' inductance and L_{PinD} is the effective package lead inductance.

Like the previous subsection, it can again be noted here that the resonance frequency varies depending on the value of Ψ, which in turn is dependent on three external values, namely the shorting post inductance, the intrinsic capacitance of the switching diode and the resistance of the diode (depending on either it is turned ON or OFF).

5.7 Results - PIN Loaded Antenna

Return loss has been computed taking into consideration the quarter wave transformer and the 50Ω feed line as shown in Fig. 5.15. Respective characteristic impedance and

effective free space line length have been calculated before the computation of the return loss for accurate results. Effective combined lumped inductance for the shorting pin, the strip island, and the diode terminals has been calculated as $L_{sh}+L_{PinD} = 1.775$nH. Characterizations of Infineon BAR64 PIN diodes have been conducted, and values obtained empirically and from datasheets, for the switch resistance and capacitance for ON and OFF states have been used to simulate the proposed antenna design numerically. For a single BAR64 PIN diode, intrinsic capacitance has been considered as 0.17pF. Four PIN diodes have been used in the design which sums up an effective C_{PinD} of 0.68pF. A single BAR64 PIN diode at around 1.5GHz has an ON conductance of approximately 400mS which makes an effective G_{PinD} of 1.6S in the ON mode. In the OFF mode, a single BAR64 PIN diode has a conductance of 333μS, which makes the effective conductance in OFF mode as G_{PinD} is 1333μS. The practical transformer and feedline impedances have been considered to get accurate solutions using the analytical model.

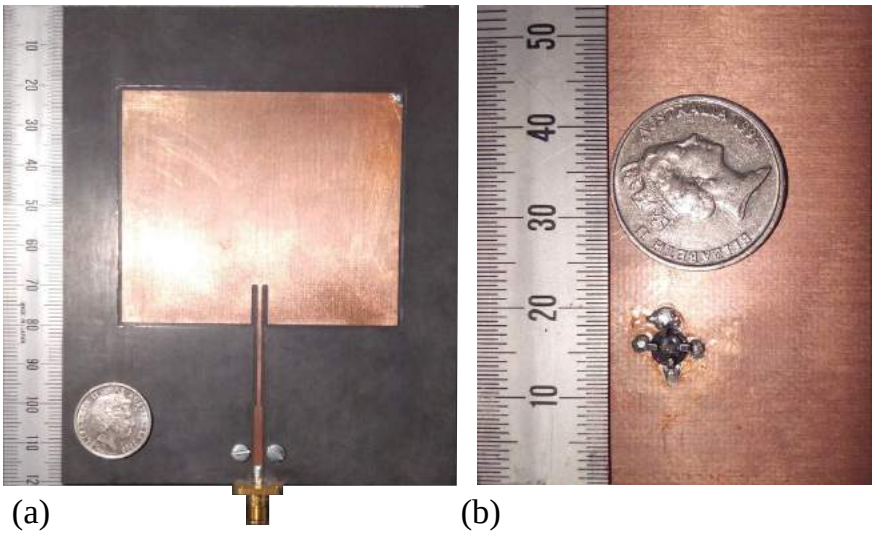

Figure 5.17: Fabricated patch antenna showing (a) the top view with the short at the upper right vertex of the patch, and (b) zoomed in view of the PIN diodes soldered to the island in comparison to an Australian five cent coin.

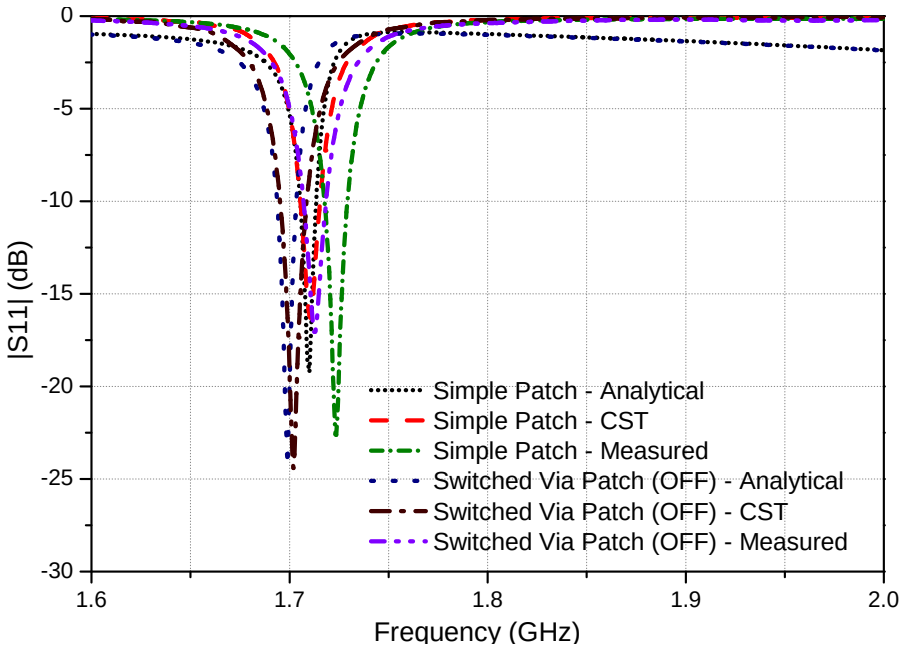

(a)

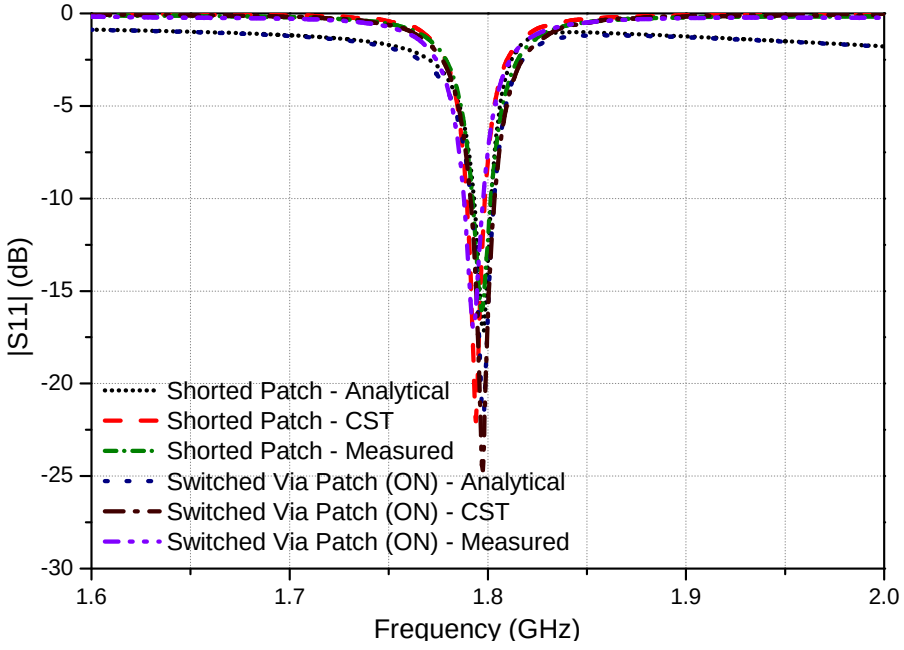

(b)

Figure 5.18: Comparison of measured, analytically computed and numerically predicted return loss of the patch antenna without any short and with a 'via' bridged to the ground plane through switches in the OFF and ON mode, respectively.

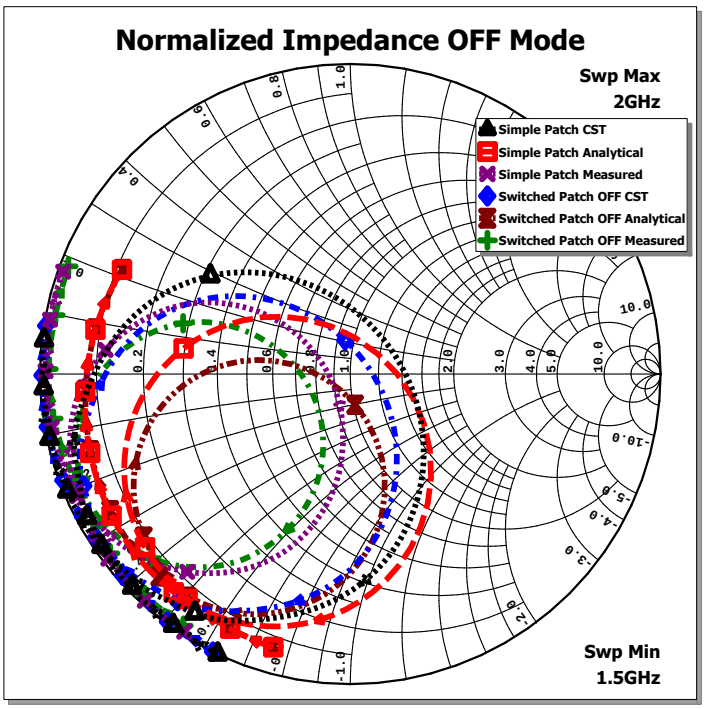

Figure 5.19: Comparison of measured, analytically computed and numerically predicted normalized impedance of the patch antenna without any short and with a 'via' bridged to the ground plane through switches which are in the OFF mode, plotted on a Smith Chart.

Using the given design parameters for a simple patch and a patch antenna with a 'via' bridged to the ground plane through switches which are in the OFF mode, strong resonance is achieved at 1710 MHz and 1699 MHz respectively, with the analytical model. For a patch antenna with a permanently shorted 'via' and a patch antenna with a 'via' bridged to the ground plane through switches which are in the ON mode, strong resonance is achieved at 1798 MHz with the same model.

A prototype was manufactured to compare with the results obtained through the analytical model and the numerically predicted results. A combination of CNC routing and chemical etching was used to fabricate the antenna due to the soft nature of the Rogers 5880 substrate. Isolation routing of the patch was done on a 3040 CNC router with an IsoPro control software using the Gerber files exported from CST Microwave Studio. Rest of the copper was dissolved with hydrochloric acid and hydrogen peroxide solution to get the final product. A subminiature version A connector with tab terminal

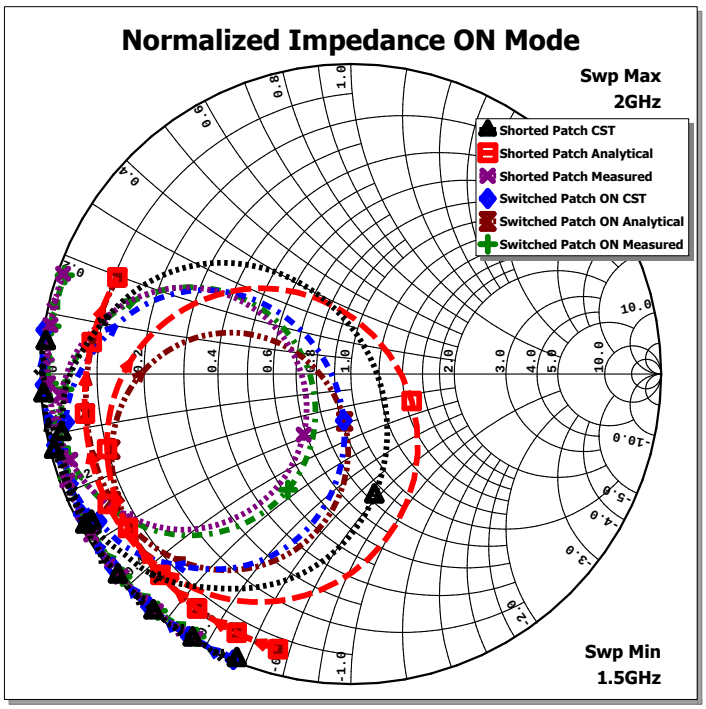

Figure 5.20: Comparison of measured, analytically computed and numerically predicted normalized impedance of the patch antenna with a permanent short and with a 'via' bridged to the ground plane through switches which are in the ON mode, plotted on a Smith Chart.

from Huber & Suhner was soldered to the microstrip feed to measure and obtain the results. Fig. 5.17 shows the picture of the fabricated antenna and the PIN diodes soldered to the island with which the 'via' is connected, along with an Australian five cent coin.

Fig. 5.18(a) compares return loss measured from the fabricated prototype and calculated with the analytical model and numerically predicted with CST Microwave Studio 2013, for a simple patch antenna described by Eq. (3.3). Fig. 5.19 shows the comparison of the normalised impedance of the network model, the CST model and the fabricated prototype for the simple patch antenna on a Smith Chart. Fig. 5.18(a) also shows the comparison of return loss measured from the fabricated prototype and calculated with the analytical model and numerically predicted model, for a patch antenna with a 'via' bridged to the ground plane through switches which are in the

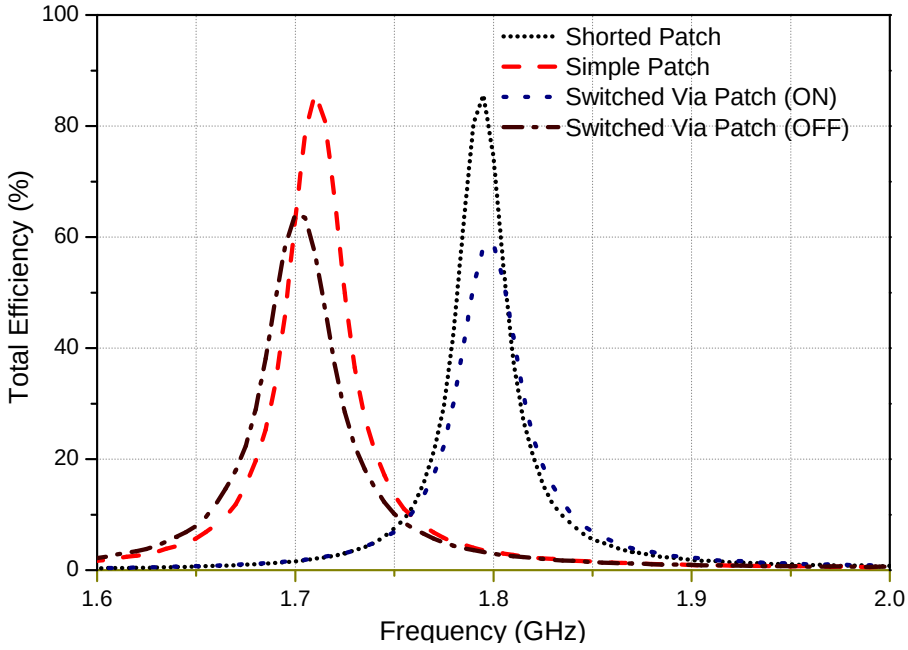

Figure 5.21: Predicted total efficiency of the simple patch, permanently shorted patch and the reconfigurable patch antenna with the ON and OFF states of the PIN diode. The losses in metal, dielectric and the active devices have been included in efficiency calculations.

OFF mode as described by Eq. (5.4). The comparison of the normalised impedance of the patch antenna with a 'via' bridged to the ground plane through switches which are in the OFF mode can be found in Fig. 5.19. In the OFF mode, measured 10dB return loss bandwidth is about 13MHz. The bandwidth is small due to the thin substrate used. Measured resonant frequencies for a simple patch and a patch antenna with a 'via' bridged to the ground plane through switches which are in the OFF mode are 1723 MHz and 1712 MHz, respectively.

For the permanently shorted patch antenna design described by Eq. (4.3), Fig. 5.18(b) compares the return loss measured from the prototype and calculated with the analytical model and numerically predicted values. Fig. 5.20 shows the comparison of the normalised impedance of the network model, the CST model and the fabricated prototype on a Smith Chart. Fig. 5.18(b) also shows the measured return loss and the analytical and numerical solutions for the patch antenna with a 'via' bridged to the ground plane through switches which are in the ON mode as described by Eq. (5.4). The comparison of the normalised impedance of the patch antenna with a 'via'

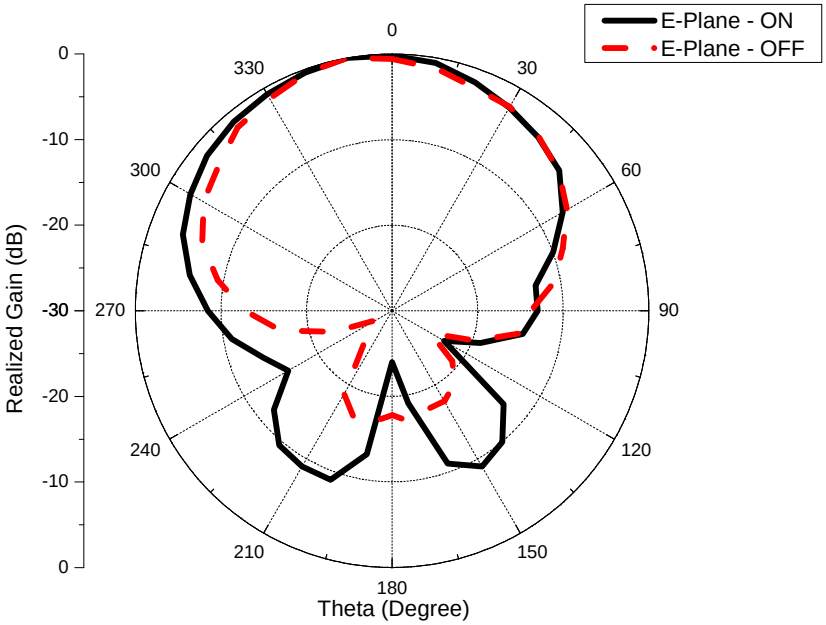

(a)

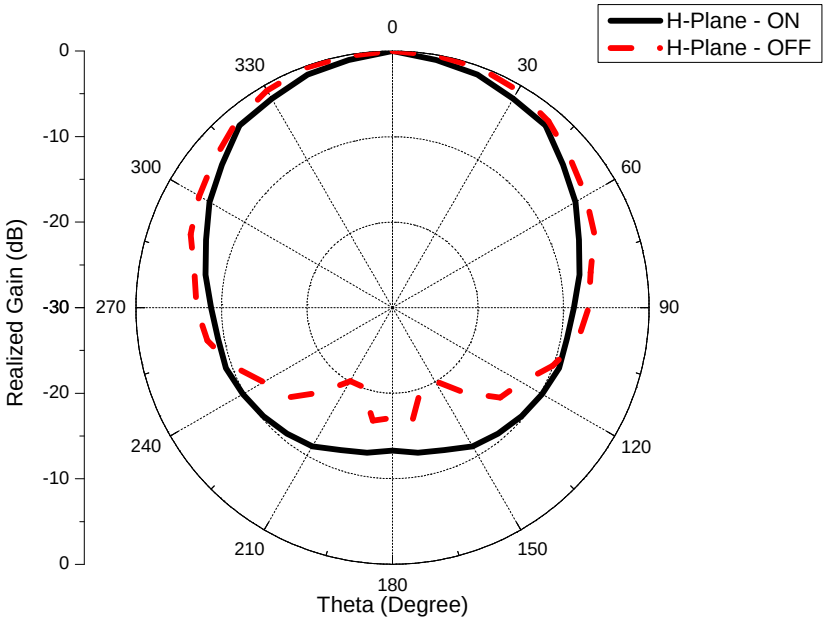

(b)

Figure 5.22: Measured normalized farfield pattern on the E-Plane and H-Plane at the OFF mode (1710 MHz) and ON mode (1795 MHz), respectively.

bridged to the ground plane through switches which are in the ON mode can be found in Fig. 5.20. In the ON mode, measured 10dB return loss bandwidth is about 12MHz. Measured resonant frequencies for a patch antenna with a permanently shorted 'via' and a patch antenna with a 'via' bridged to the ground plane through switches which are in the ON mode are 1797 MHz and 1793 MHz, respectively.

The predicted total antenna efficiency deteriorates in the reconfigurable mode due to apparent losses of the active device. Fig. 5.21 shows the predicted total antenna efficiency for a simple patch antenna, a patch antenna with a permanent shorting 'via' to the ground and a reconfigurable patch antenna in the ON and OFF states, respectively. The use of an active component drops the average total efficiency from about 80% to 60% in both the modes.

Fig. 5.22(a) and Fig. 5.22(b) shows the measured farfield pattern cuts on E-plane and H-plane for both switching states, respectively. For the ON state, the farfield pattern is given for 1710 MHz and for the OFF state, the farfield pattern is given for 1795 MHz. Realised gain in the OFF mode is 5.3 dBi, and in the ON mode, it is 5.7 dBi.

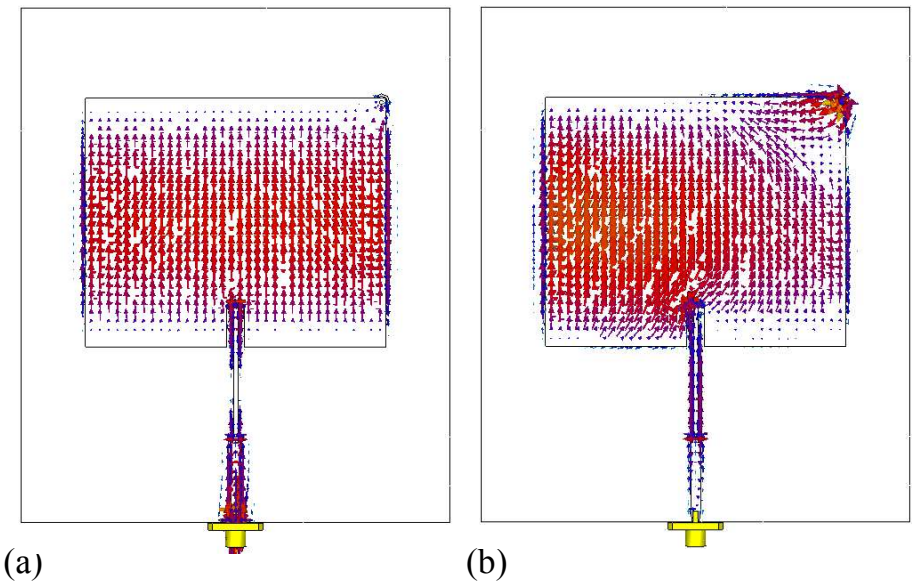

Figure 5.23: Surface current distributions on the patch showing how the switch changes the effective area of the patch. The modes are for (a) OFF state at 1700 MHz with current phase at 0° and (b) ON state at 1800 MHz with current phase at 90°.

Fig. 5.23 indicates the effective patch area due to the switch and its modes. It can be visualised from Fig. 5.23(a) that in the OFF state, current in the corner where the 'via' is placed is almost parallel to the current in the rest of the patch, but it deviates when 'via'-short switch is turned on as shown in Fig. 5.23(b). This makes the antenna resonate at a higher frequency.

5.8 Conclusion

A few extended transmission-line models are presented for inset-fed rectangular microstrip patch antennas loaded with one or more varactor and PIN diodes. More than one type of substrate and layouts were used to validate the models rigorously. The transmission-line models agree with the cos^4 impedance variation for inset-fed microstrip antennas with an addition of a corrective feed length to the inner radiating edge. Verification of the model was concluded with its complex reflection coefficient in good agreements to the measured results. Further extension of the transmission-line models with varactors was found with 69% of forty-two (42) test cases having less than 3% deviation from measured or simulated results. PIN diode results were in good agreement with the extended transmission-line model. Further studies are ongoing to find an explanation for the rest of 31% test cases where the transmission-line models were not as successful. Quick design solutions are possible with the extended transmission-line model to achieve reasonable accuracy without using the time-consuming full wave solvers.

"I have had my results for a long time: but I do not yet know how I am to arrive at them."

Johann Carl Friedrich Gauss

6

Active Antenna Beam Steering: Voltage Controlled Scanning

6.1 Introduction

Traditional phased arrays are implemented with analog or digital phase shifters designed and used externally to the antenna. These antennas are very robust and have a large scan range, but the cost of manufacturing and installation is also quite high. Low-cost beam steering can be useful in consumer electronics where space limitation is also another constraint. A recent work implemented the phase shifting circuitry directly with a travelling wave patch array for beam steering [85]. The easiest way of implementing low-cost beam steering is by using multiple delay lines as shown in [86]. This chapter introduces the phase delay by varactor loading of individual patch

antenna elements. A process of phase response variation of patch elements using an LC resonator is shown in [87]. In this chapter, the difference in phase response is obtained by introducing active and passive phase delays.

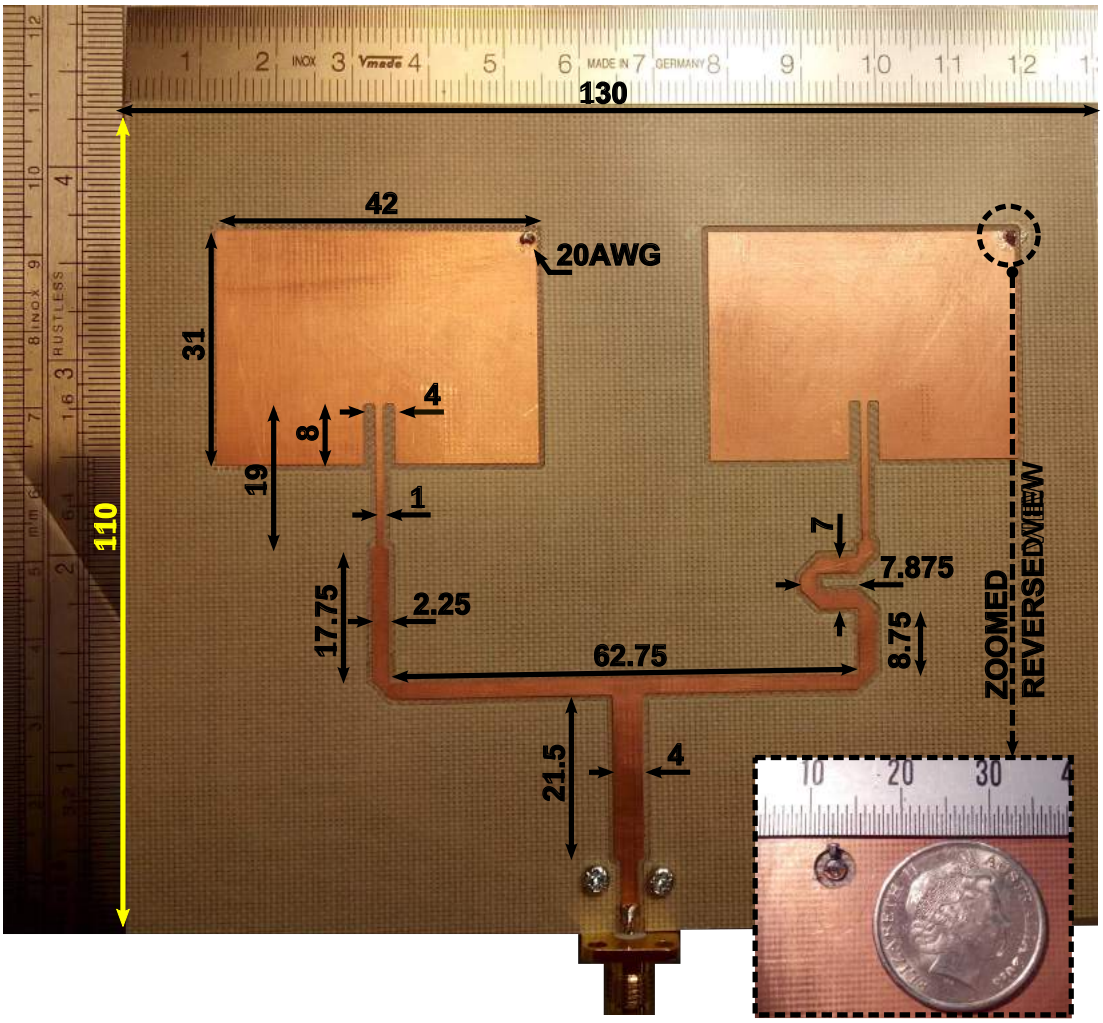

FIGURE 6.1: Fabricated 1×2 patch 'Array Antenna I' showing the top view with all dimensions, and an inset view of the ground plane island and varactor diode zoomed in. All dimensions are in milli-meters.

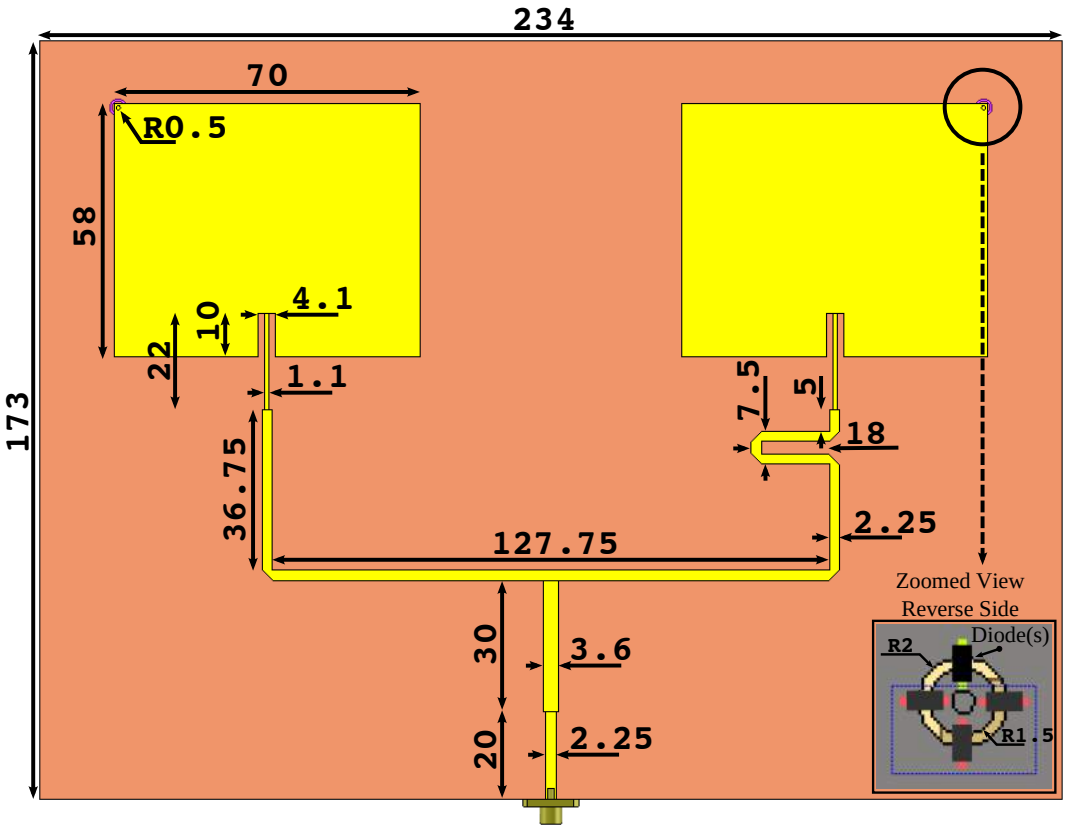

Figure 6.2: Layout of 1×2 patch 'Array Antenna II' showing the top view with all dimensions. All dimensions are in milli-meters.

6.2 Antenna Design and Configuration

Three array antennas are discussed in this chapter. Two of them are 1×2 patch arrays and the third one is a 2×2 patch array. Two different substrates are used for the two separate 1×2 patch array antennas.

6.2.1 Array Antenna I

Fig. 6.1 shows the layout of the one-dimensional (1×2) element phased array antenna. The substrate used is Taconic TRF-43 ($\epsilon_r = 4.3$, $tan\,\delta = 0.0035$) with a thickness of 1.2mm. The manufactured antenna is shown in Fig. 6.1 along with all the relevant dimensions required to reproduce the antenna in a separate instance. An active 'via' is implemented at one of the outer vertices of the patch element opposite to the feed for each of the elements. The 'via' is connected with the patch on one side and to a small

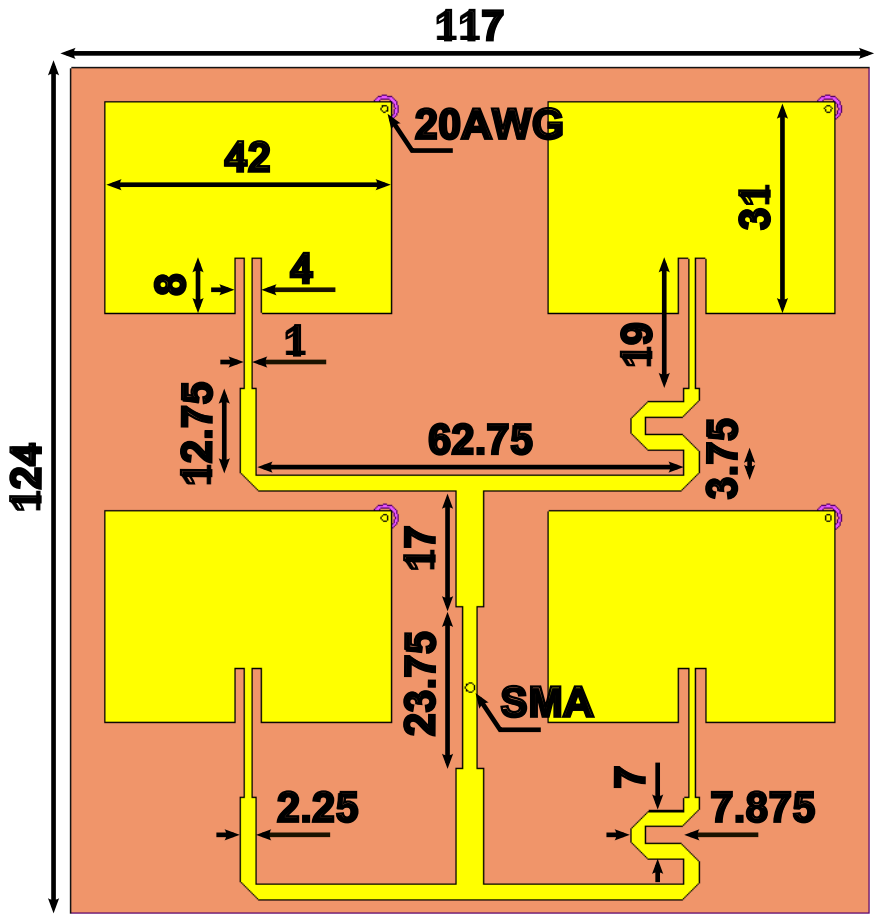

FIGURE 6.3: Layout of 2×2 patch 'Array Antenna III' showing the top view with all dimensions. All dimensions are in milli-meters.

island in the ground plane. The small island is separated from the greater ground plane by an annular gap. For this array, there are two 'via' connecting to different islands in the ground plane. The inset view in Fig. 6.1 shows an island for one patch antenna element. A 20AWG wire has been used as a 'via'. One or more varactor diodes can act as a bridge across the annular ring between the island and the greater ground plane. All the results obtained using 'Array Antenna I' is with one varactor diode soldered across the annular gap for each 'via'. The varactor diodes complete a DC circuit between the feed line and the ground plane, and a DC offset in the input signal is sufficient enough to control the effective capacitance of the varactor. No additional bias lines are required for tuning the circuit, and an external bias-tee is sufficient.

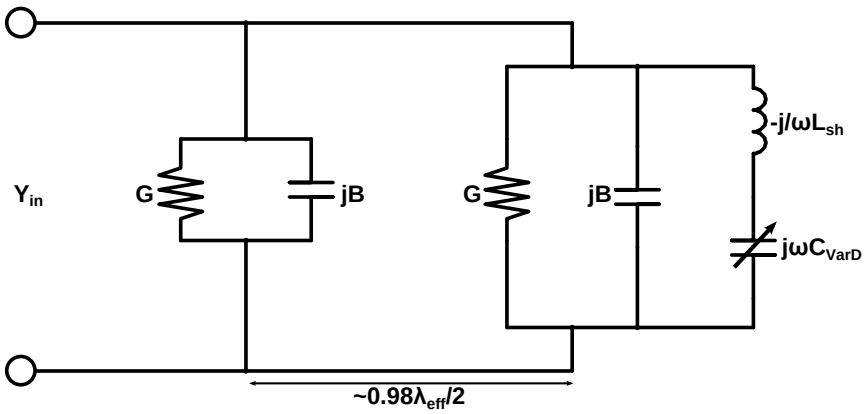

Figure 6.4: Transmission line mode of a half-wavelength patch antenna with a shorting post connected to one or more varactor diodes.

6.2.2 Array Antenna II

Fig. 6.2 shows the layout of the second one-dimensional (1×2) element phased array antenna. The substrate used is Rogers 5880 ($\epsilon_r = 2.2$, $tan\,\delta = 0.0009$) with a thickness of 0.787mm. The layout is similar to 'Array Antenna I' and all relevant dimensions are given in Fig. 6.2 for reproduction and comparison. Similar to 'Array Antenna I', a 20AWG wire has been used as a 'via'. One or more varactor diodes can act as a bridge across the annular ring between the island and the greater ground plane. All the results obtained using 'Array Antenna II' is with one varactor diode soldered across the annular gap for each 'via'.

6.2.3 Array Antenna III

Fig. 6.3 shows the layout of the second one-dimensional (2×2) element phased array antenna. The substrate used is Taconic TRF-43 ($\epsilon_r = 4.3$, $tan\,\delta = 0.0035$) with a thickness of 1.2mm. All relevant dimensions are given in Fig. 6.3 for reproduction and comparison. Similar to 'Array Antenna I' and 'Array Antenna II', a 20AWG wire has been used as a 'via'. One or more varactor diodes can act as a bridge across the annular ring between the island and the greater ground plane. All the results obtained using 'Array Antenna III' is with one varactor diode soldered across the annular gap for each 'via'.

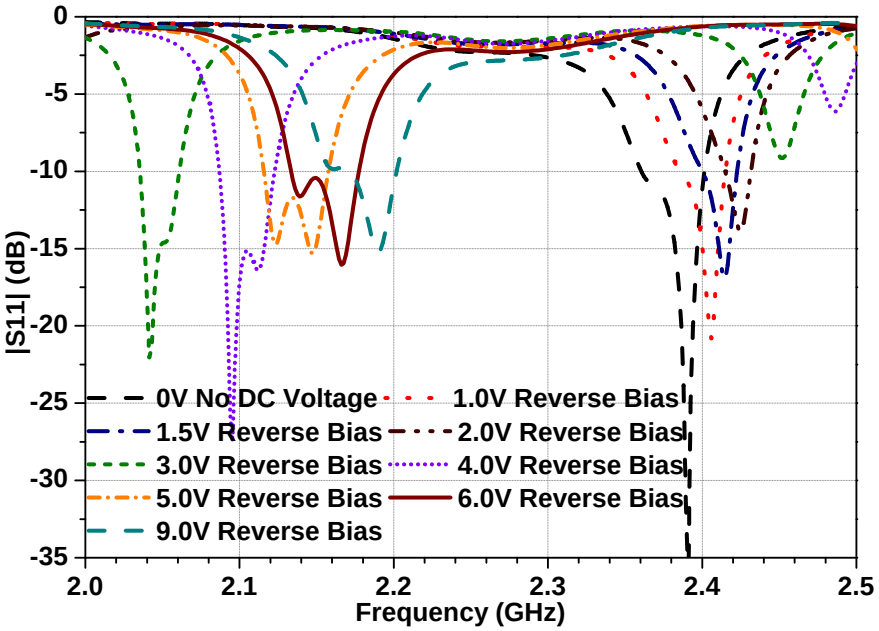

FIGURE 6.5: Simulated return loss for the 1×2 patch 'Array Antenna I' with a single varactor diode per patch, under different bias conditions.

6.3 Transmission-Line Modelling and Reconfigurability

The transmission line model for one patch, with the active 'via' soldered, is given in 6.4. The bias voltage can control the value of C_{VarD}. L_{sh} is the combined 'via' and varactor lead inductance. The values of the radiating slot conductance G and susceptance B can be found in well-known texts [40, 48–51].

This model resonates at a medium frequency mode and a high frequency mode. In the medium frequency mode, the capacitor does not bypass electromagnetic signals and acts as a load to the outer radiating slot creating a phase delay circuit. The value $(\omega L_{sh} - 1/\omega C_{VarD})$ becomes critical in beam steering. The fixed delay decides the net phase delay due to the meandered microstrip feed and the electronic delay made by the varactor.

'Array Antenna I' and 'Array Antenna III' has resonance frequencies in the medium frequency band and the high frequency band. In the high frequency mode, the varactor diode has limited control of the active phase delay as it becomes a bypass capacitor

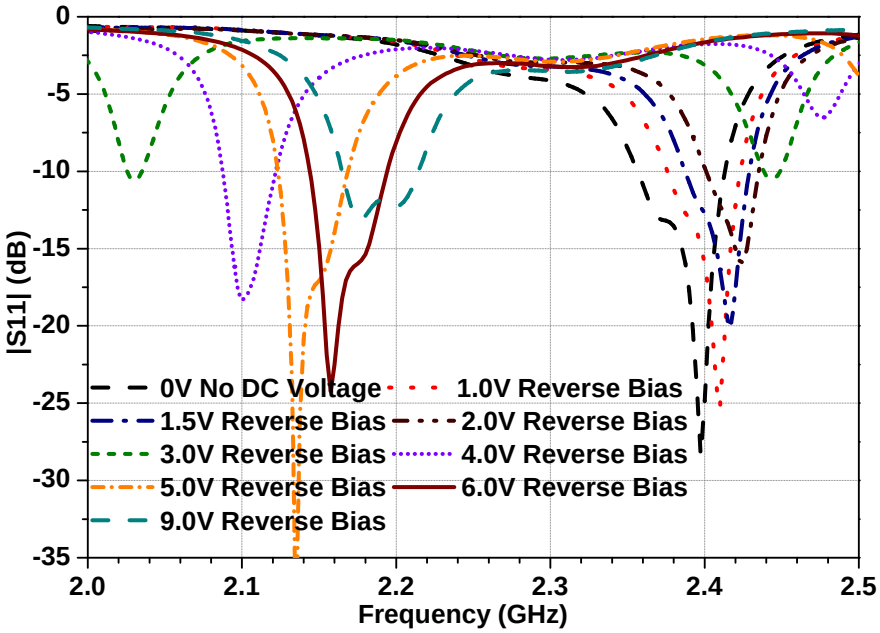

Figure 6.6: Measured return loss for the 1×2 patch 'Array Antenna I' with a single varactor diode per patch, under different bias conditions.

and shorts the patch to the ground plane. The patch antenna acts as a shorted patch and resonates at a higher frequency. The meandered feed mostly decides the effective phase delay in this range.

6.4 Electronic Fixed-Frequency Beam-Steering

The fixed-frequency beam-scanning can be described with the variable phase delay created as an effect of the variable intrinsic capacitance of the varactor diode operating in reverse bias mode in addition to the delay of the meandered line length. The overall insertion phase of each element varies due to the change of individual component admittance.

If Y_P is the patch admittance at the edge, it can be derived to be having the value:

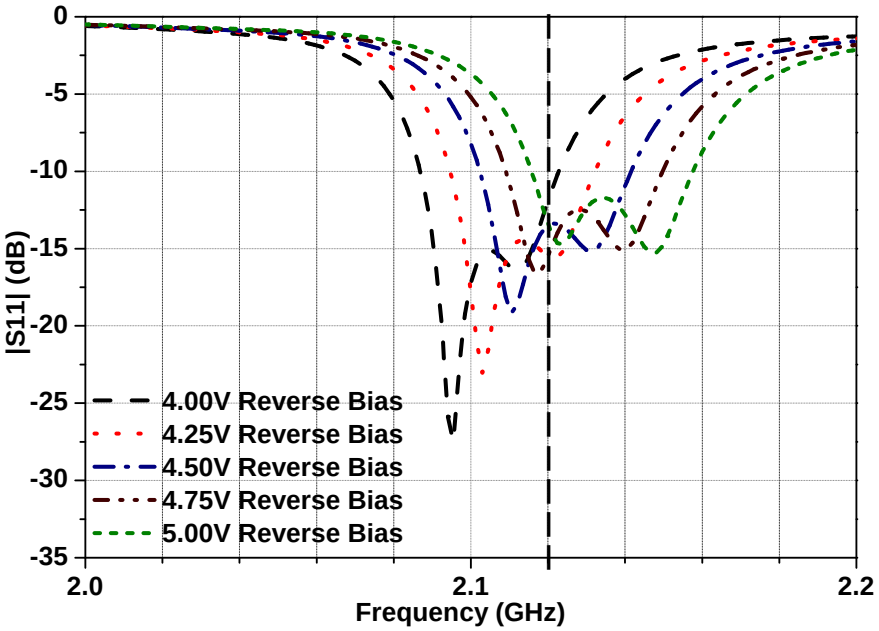

FIGURE 6.7: Band switching of 'Array Antenna I' around the operating frequency, F_{op} = 2120 MHz using one varactor diode per radiating element. F_{op} stays withing the 10dB return loss band for a range of reverse bias voltage between 4V to 5V DC.

$$Y_P = G + jB + Y_p \frac{G + j\left(B - \Psi + Y_p tan\, kL_P\right)}{Y_p - (B - \Psi) tan\, kL_P + jG tan\, kL_P} \tag{6.1a}$$

where

$$\Psi = -\frac{\omega C_{VarD}}{(1 - \omega^2 C_{VarD} L_{sh})} \tag{6.1b}$$

and Y_p is the characteristic admittance of the wide transmission line that makes the patch. G and B are the patch slot admittance and susceptance very well know in the literature [40, 48–51], and L_p is the length of the patch. k is the effective wave number for the material medium. Overall patch impedance with the inset feed [52] and the

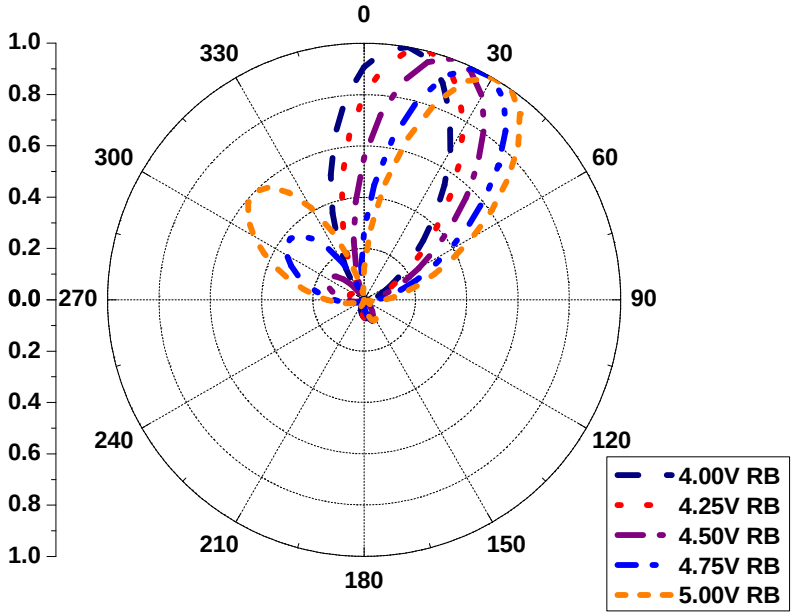

Figure 6.8: Normalized linear farfield pattern (H-Plane) of the 'Array Antenna I' showing frequency controlled beam scanning with main lobe scanning between 7° and 32°, with different bias voltages, for a continuous wave signal F_{op} = 2120 MHz.

quarter wave transformer can be given by the equation:

$$Y_O = Y_T \frac{Y_P sec^4\left(\frac{\pi}{L_P} L_{In}\right) + jY_T tan\, kL_T}{Y_T + jY_P sec^4\left(\frac{\pi}{L_P} L_{In}\right) tan\, kL_T} \tag{6.2}$$

where L_{in} is the length of the inset and L_T length of the quarter wave transformer. Y_T is the characteristic admittance of the transformer.

The overall difference of complex admittance can be given by:

$$Y_\Delta = Y_{50\Omega}\left[\frac{Y_O + jY_{50\Omega} tan\, kL_m}{Y_{50\Omega} + jY_O tan\, kL_m} - \frac{Y_O + jY_{50\Omega} tan\, kL_s}{Y_{50\Omega} + jY_O tan\, kL_s}\right] \tag{6.3}$$

where the effective length of the feed are L_m and L_s for the meandered and straight feed to the patch, respectively. $Y_{50\Omega} = 0.02$ gives the characteristic admittance of the feed lines.

Changing the reverse bias voltage offset across the SMA connector would result in different values of the intrinsic capacitance of the varactor diodes and turn would have a different value of Y_Δ which is responsible for the insertion phase delay of the signal

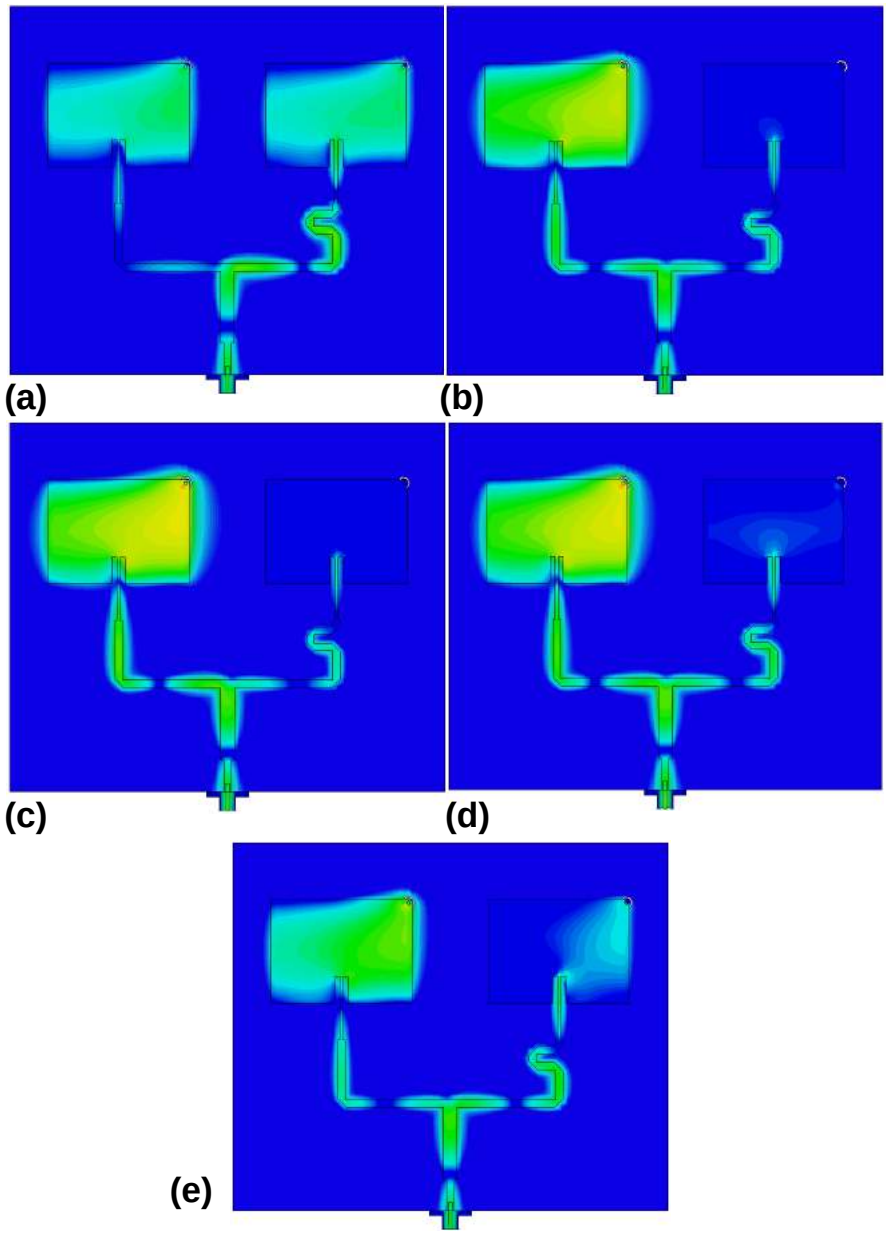

Figure 6.9: Surface current density along the microstrip line and patch under different reverse bias conditions. The input phase at the SMA is zero degree. (a) 5V, (b) 4.75V, (c) 4.5V, (d) 4.25V, and (e) 4V

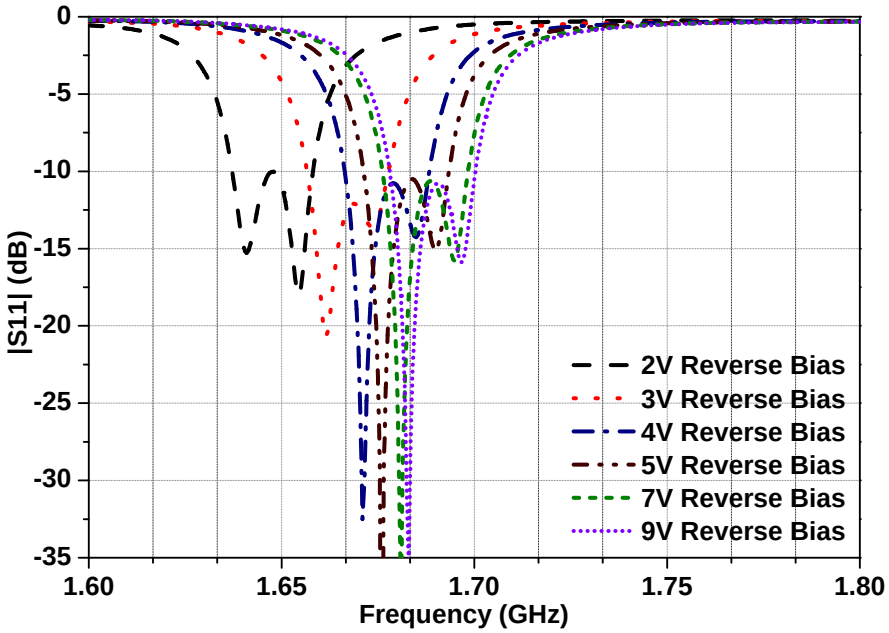

Figure 6.10: Simulated return loss for the 1×2 patch 'Array Antenna II' with a single varactor diode per patch, under different bias conditions.

between two patch elements.

Table 6.1: Phase delay of the signal between the straight fed and the meander fed patch, under various bias conditions, for a CW signal frequency of 2120 MHz

Reverse Bias (V)	Phase Delay (°)
4.00	52
4.25	72
4.50	110
4.75	138
5.00	154

6.5 Antenna Implementation and Results

A prototype was manufactured for 'Array Antenna I' in-house using a combination of CNC routing and chemical etching. Skyworks SMV1232-079LF varactor diode was

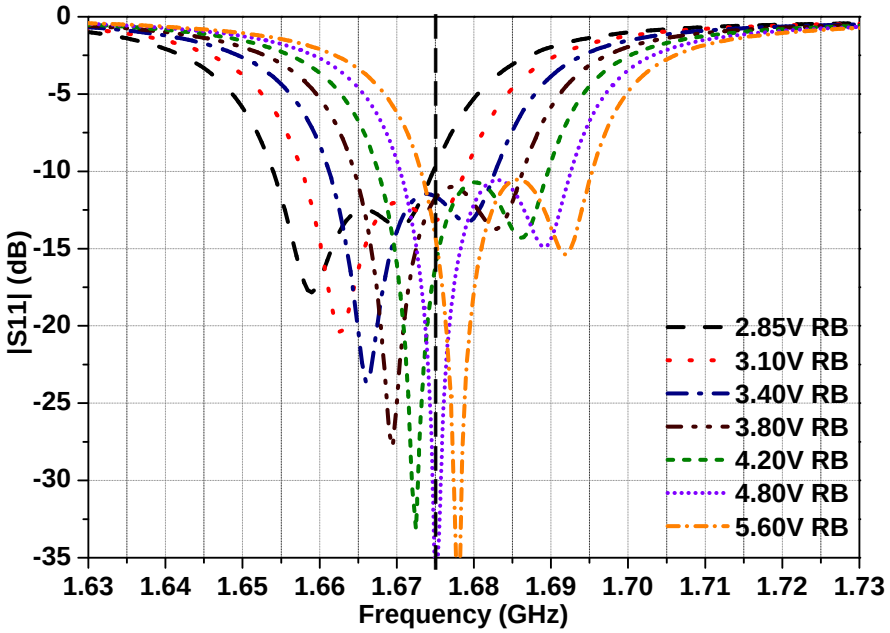

FIGURE 6.11: Band switching of 'Array Antenna II' around the operating frequency, F_{op} = 1675 MHz using one varactor diode per radiating element. F_{op} stays withing the 10dB return loss band for a range of reverse bias voltage between 2.85V to 5.6V DC.

soldered as the tunable variable capacitor for beam steering. A 3D full wave simulation was conducted using CST Studio Suite 2015. Typical values supplied in the datasheet was utilised for the simulation. For 'Array Antenna II' and 'Array Antenna III', only simulation results are provided in this chapter.

6.5.1 Array Antenna I

Fig. 6.5 and Fig. 6.6 shows the simulated and measured return loss for the entire tuning range of the prototype. The bandwidth over the tuning range is from 2027 MHz to 2210 MHz in the medium frequency range and from 2356 MHz to 2450 MHz in the high frequency range, with a single varactor diode per patch. The DC reverse bias voltage required for the tuning is from 0V to 9V.

Beam steering is discussed in this chapter about a continuous wave operating frequency chosen randomly from the medium frequency tunable range of the antenna. The frequency selected is 2120 MHz for 'Array Antenna I'. Table 6.1 shows the numerically obtained phase delay between the straight feed patch and the meander feed

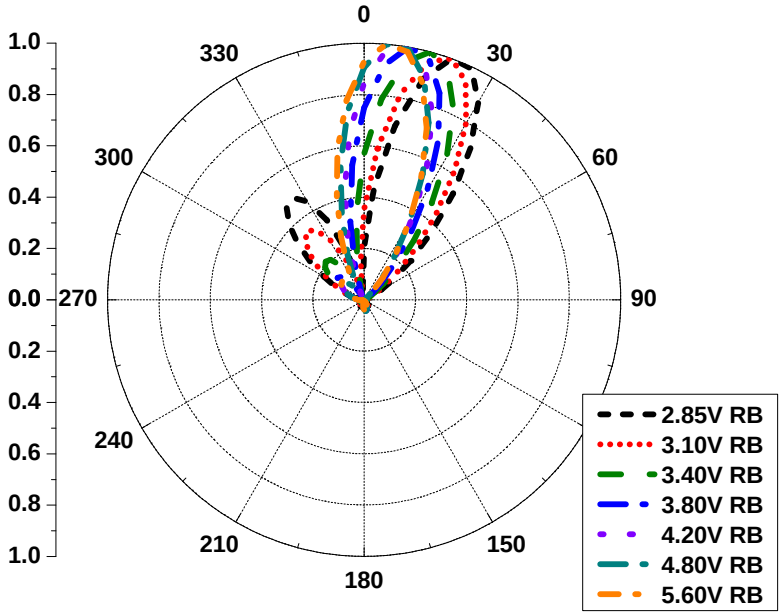

Figure 6.12: Normalized linear farfield pattern (H-Plane) of the 'Array Antenna II' showing frequency controlled beam scanning with main lobe scanning between 5° and 25°, with different bias voltages, for a continuous wave signal F_{op} = 1675 MHz.

patch under various reverse bias voltages. Fig. 6.7 indicates the shift of the return loss plot about varying the reverse bias voltage across the SMA port. The plot shows that the return loss at 2120 MHz is less than 10 dB when the reverse bias is kept between 4V and 5V DC. The farfield pattern makes a scan between 7° and 32° when the reverse bias is tuned between 4V and 5V for a continuous wave input signal at 2120 MHz. Fig. 6.9 shows the surface current at 2120 MHz for different reverse bias voltages with input phase at 0°. The normalised farfield scan pattern is shown in Fig. 6.8.

6.5.2 Array Antenna II

Fig. 6.10 shows the simulated return loss for the entire tuning range of the prototype. The bandwidth over the tuning range is from 1637 MHz to 1678 MHz, with a single varactor diode per patch. The DC reverse bias voltage required for the tuning is from 0V to 9V.

The CW frequency chosen is 1675 MHz for 'Array Antenna II'. Table 6.2 shows the numerically obtained phase delay between the straight feed patch and the meander

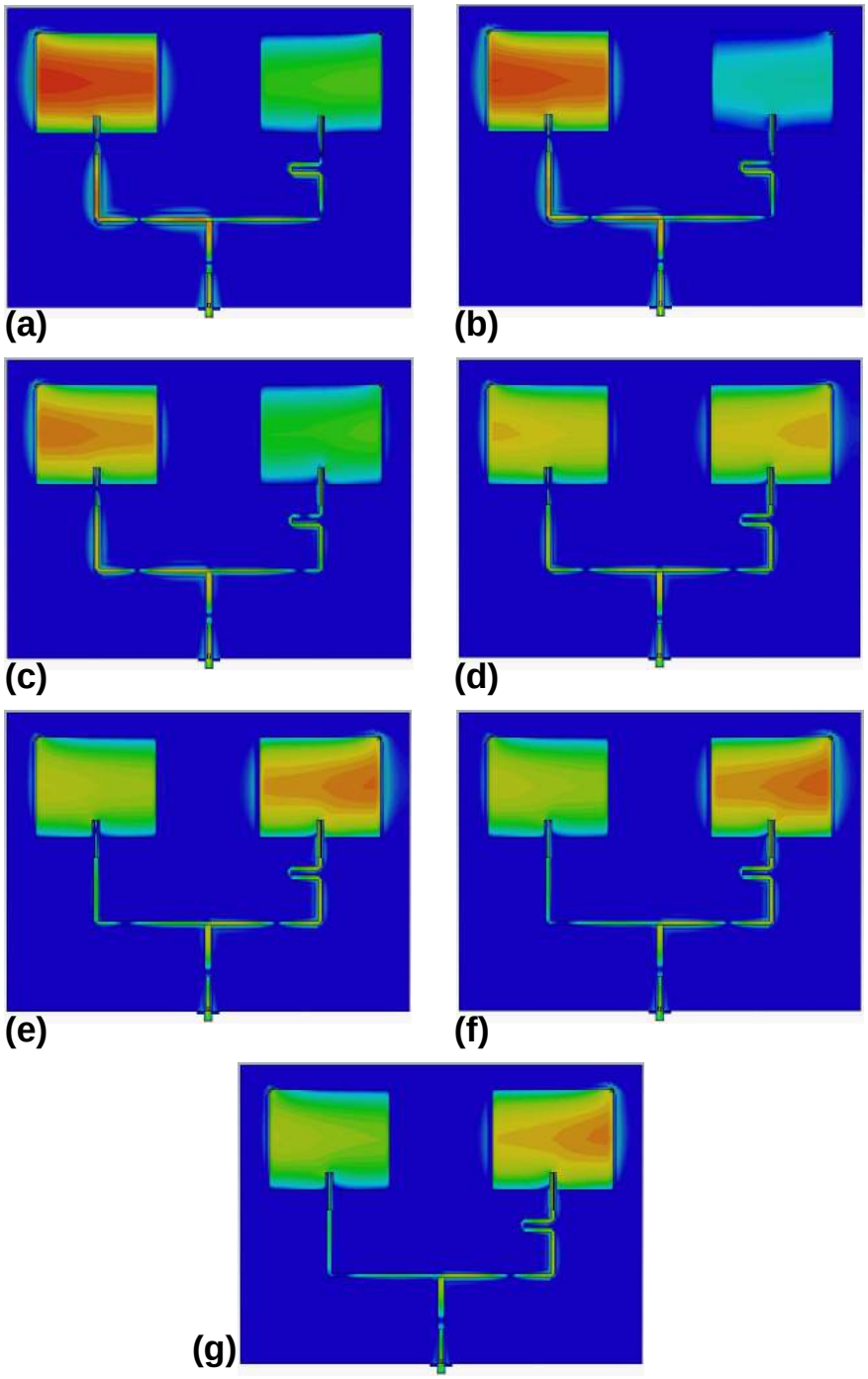

FIGURE 6.13: Surface current density of 'Array Antenna II' along the microstrip line and patch under different reverse bias conditions. The input phase at the SMA is zero degree. (a) 5.6V, (b) 4.8V, (c) 4.2V, (d) 3.8V, (e) 3.4V, (f) 3.1V, and (g) 2.85V.

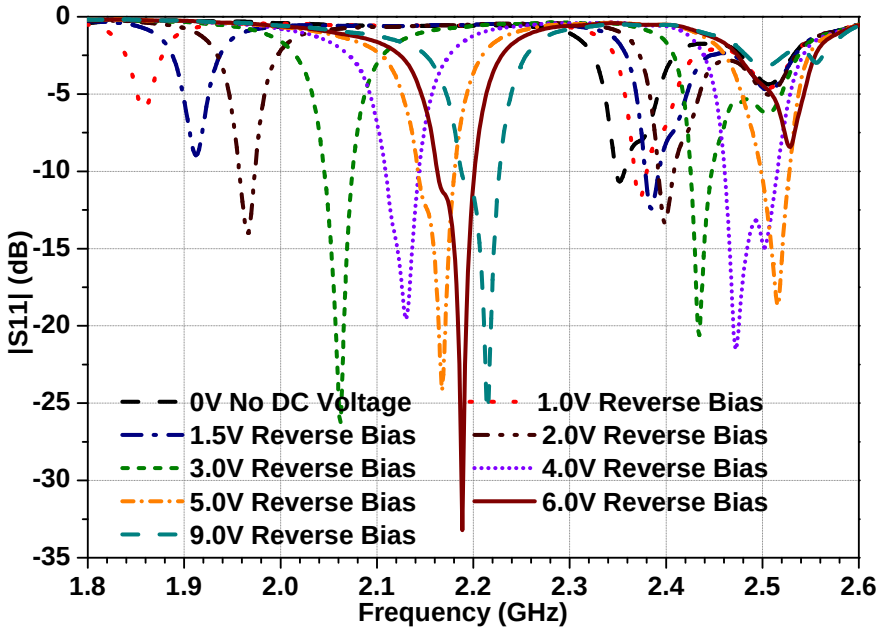

Figure 6.14: Simulated return loss for the 2×2 patch 'Array Antenna III' with a single varactor diode per patch, under different bias conditions.

Table 6.2: Phase delay of the signal between the straight fed and the meander fed patch 'Antenna Array II', under various bias conditions, for a CW signal frequency of 1675 MHz

Reverse Bias (V)	Phase Delay (°)
2.85	140
3.10	120
3.40	91
3.80	67
4.20	52
4.80	42
5.60	36

feed patch under various reverse bias voltages. Fig. 6.11 indicates the shift of the return loss plot about varying the reverse bias voltage across the SMA port. The plot shows that the return loss at 1675 MHz is less than 10 dB when the reverse bias is kept between 2.85V and 5.6V DC. The farfield pattern makes a scan between 5° and 25° when the reverse bias is tuned between 2.85V and 5.6V for a continuous wave input signal at 1675 MHz. Fig. 6.13 shows the surface current at 1675 MHz for different reverse bias voltages with input phase at 0°. The normalised farfield scan pattern is shown in Fig. 6.12.

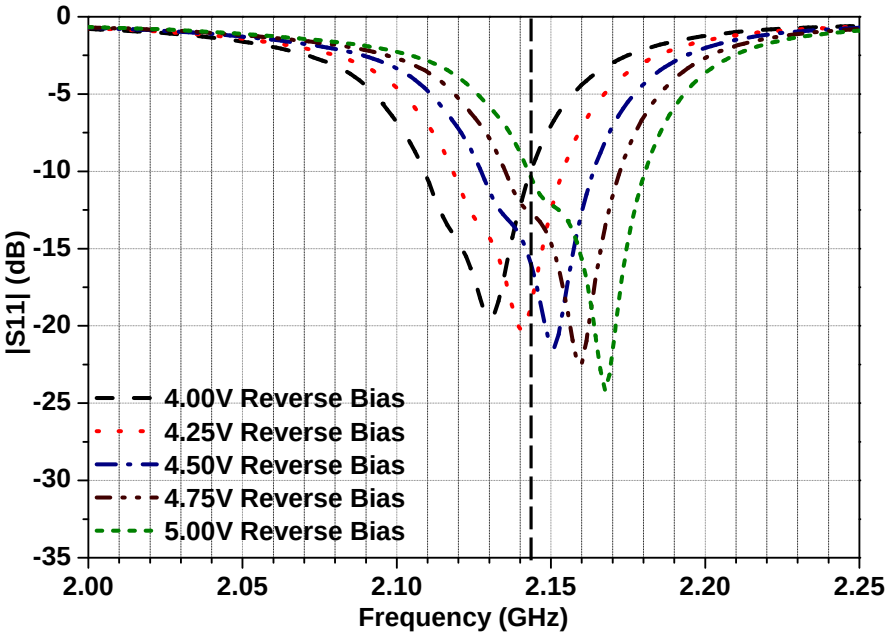

FIGURE 6.15: Band switching of 'Array Antenna III' around the operating frequency, F_{op} = 2143.5 MHz using one varactor diode per radiating element. F_{op} stays withing the 10dB return loss band for a range of reverse bias voltage between 4V to 5V DC.

TABLE 6.3: Phase delay of the signal between the straight fed and the meander fed patch 'Antenna Array III', under various bias conditions, for a CW signal frequency of 2143.5 MHz

Reverse Bias (V)	Phase Delay (°)
4.00	12
4.25	20.5
4.50	39.5
4.75	68.5
5.00	89

6.5.3 Array Antenna III

Fig. 6.14 shows the simulated return loss for the entire tuning range of the prototype. The bandwidth over the tuning range is from 1957 MHz to 2226 MHz in the medium frequency range and from 2349 MHz to 2528 MHz in the high frequency range, with a single varactor diode per patch. The DC reverse bias voltage required for the tuning is from 0V to 9V.

The CW frequency chosen is 2143.5 MHz for 'Array Antenna III'. Table 6.3 shows the numerically obtained phase delay between the straight feed patch and the meander feed patch under various reverse bias voltages. Fig. 6.15 indicates the shift of the

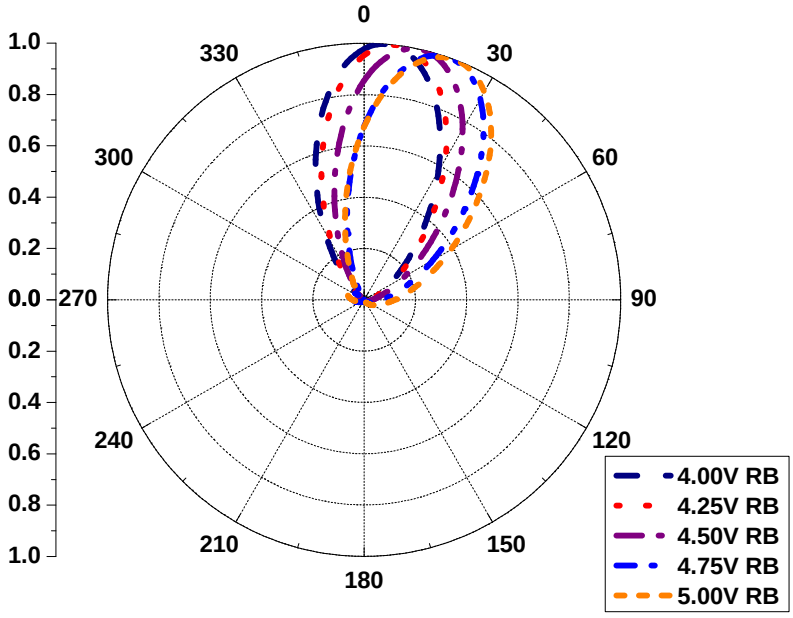

Figure 6.16: Normalized linear farfield pattern (H-Plane) of the 'Array Antenna III' showing frequency controlled beam scanning with main lobe scanning between 4° and 21°, with different bias voltages, for a continuous wave signal F_{op} = 2143.5 MHz.

return loss plot about varying the reverse bias voltage across the SMA port. The plot shows that the return loss at 2120 MHz is less than 10 dB when the reverse bias is kept between 4V and 5V DC. The farfield pattern makes a scan between 4° and 21° when the reverse bias is tuned between 4V and 5V for a continuous wave input signal at 2143.5 MHz. Fig. 6.17 shows the surface current at 2143.5 MHz for different reverse bias voltages with input phase at 0°. The normalised farfield scan pattern is shown in Fig. 6.16.

6.6 Conclusion

Three phased array antennas, where the phase shifter is integrated into the radiator by varactor loading, is proposed. There is no requirement of additional bias paths to control the active components. One external bias-tee is sufficient to scan the primary beam. The main beam can be scanned for any operating frequency within the tunable frequency spectrum. The combination of traditional microstrip delayed approach along with the active delay control beam scanning makes the topology worthy of further

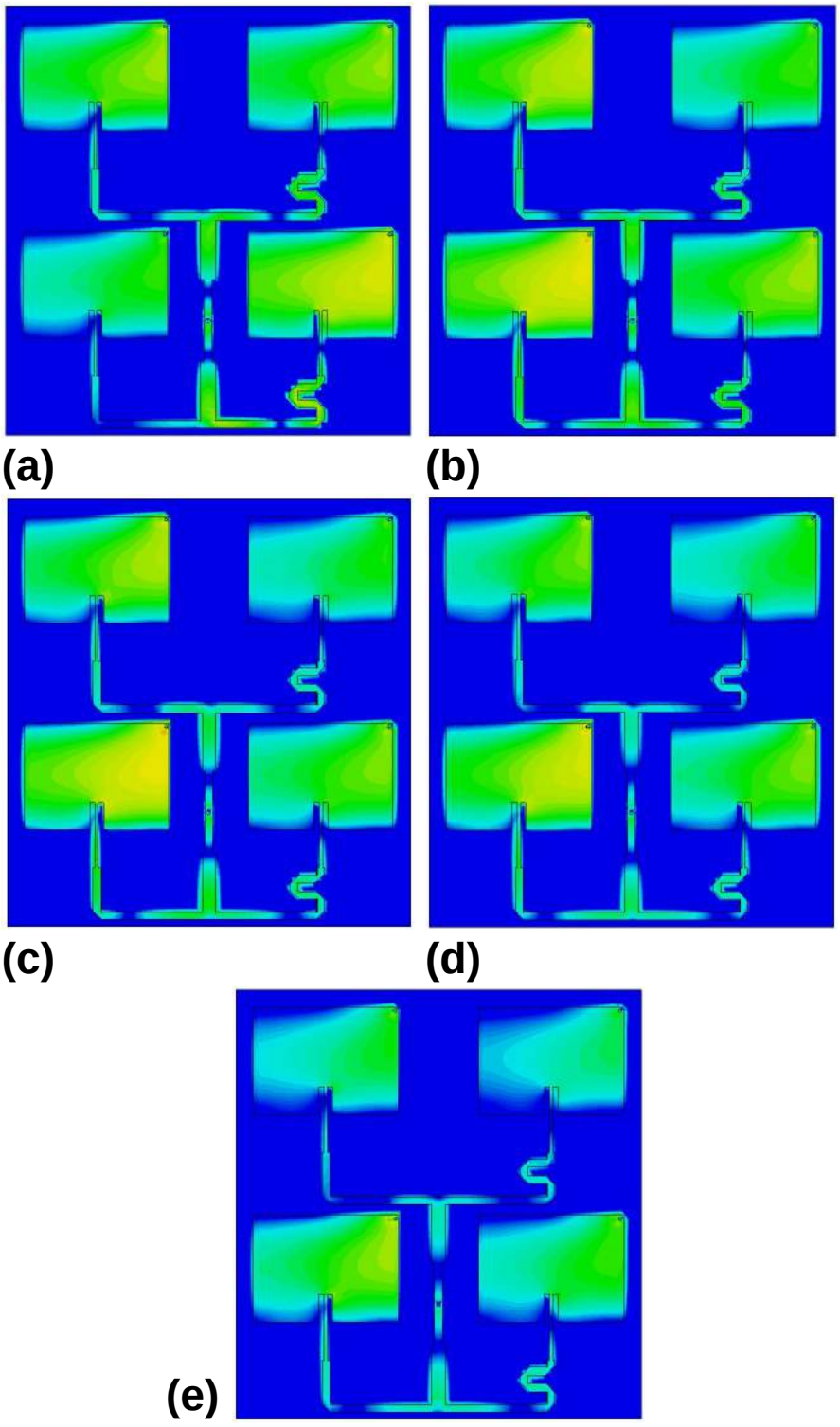

Figure 6.17: Surface current density of 'Array Antenna III' along the microstrip line and patch under different reverse bias conditions. The input phase at the SMA is zero degree. (a) 5V, (b) 4.75V, (c) 4.5V, (d) 4.25V, and (e) 4V

investigation and improvement in the future.

"When I have clarified and exhausted a subject, then I turn away from it, in order to go into darkness again."

Johann Carl Friedrich Gauss

7

New Reconfigurable Meta-Surfaces: Transmission-Line Modelling

7.1 Introduction

Metamaterial engineering started more than a half a century ago [88] as an attractive method for artificial lenses [89], antennas [90, 91], radomes [92, 93], and frequency-selective surfaces [94]. Favourable advantages include cost benefits, size reduction, and performance enhancements. A mixture of metals and easy to procure dielectric materials in a pre-calculated pattern can form a meta-surface. Applications of metamaterials [95–100] are now widespread because of their unique field-manipulation properties not naturally found [101, 102]. The unique properties of metamaterials are a negative

refractive index, negative phase velocity, negative permittivity and negative permeability [95–99]. Initially, these properties were synthesised with a collection of subwavelength metallic rods or split ring resonators [96]. Variations of these designs are now used extensively for high-gain small antennas, perfect lenses, tiny filters and dividers, chokes, absorbers, polarizers, and other wave-manipulation surfaces [95–99, 103–108]. A wide-spread interest lies in the academic and industrial communities about metamaterials and a large number of conferences, special issues [109, 110], journals, and books [95, 96, 99] have been dedicated to it.

Rising interests towards multifunctional systems have brought forward many reconfigurable metamaterial surfaces and structures [110–113]. Tunable components provide a straightforward method to achieve EM reconfigurability of designed metamaterials [111]. Basic concepts can be tested with radio-frequency devices [95, 96] and further extended to microwave applications [99, 111]. Micromechanical devices [114, 115], non-linear materials [116–118], liquid crystals [119–122], microfluidics [117, 123], graphene [124–127], and various semiconductor structures [128, 129] have been used to create metamaterial-inspired structures and have been tested in microwave frequencies [130, 131], terahertz spectrum [126, 132], mid-infrared frequencies [118], near-infrared frequencies [133] and optical bands [122, 134].

The physical tuning device that enables reconfigurability has a greater role in the design process as it directly impacts the performance, cost, manufacturing complexity, and the overall architecture. Early reconfigurable structures were created by adding switches and varactors to the initial design layout [114, 135, 136]. Many reconfigurable metamaterials were initially based on standard building blocks, such as split-ring resonators [135, 136] and complementary split-ring resonators [114]. Characteristics of these standard components were tuned by varactors or voltage controlled resistors [114, 136]. Recently, ad-hoc designs have emerged that take full advantage of the design process of the degrees of freedom of a reconfigurable system [137]. Some of the designs are optimised along their controllable subunit [98, 137–139]. Several different physical principles have been recently considered to achieve reconfigurability

producing many options that include tunable lumped elements [131, 140], micromechanical devices [114, 115], controllable liquid crystals [121, 141], graphene [124, 125] and microfluidic metals [117, 123, 142]. The choice of the suitable tuning technology is adopted depending on the frequency spectrum of the application and the procedure adopted for reconfigurability can be categorised into either microwave, terahertz, infrared or optical [143].

This chapter introduces a special metamaterial inspired surface that becomes a high impedance reflective surface at one instance and otherwise a see-through window at the other. The particular usage of much a surface is demonstrated in the next two chapters. An infinite plane is considered in the $x-y$ plane where the unit cells would be laid out isotropically in multiples. The incidence of electromagnetic waves is assumed to be normal to the $x-y$ plane along the z axis. Fig. 7.1 and Fig. 7.24 defines the unit cells of two structures that are being considered in this chapter. Modelling and analysis have been done separately in the below sections.

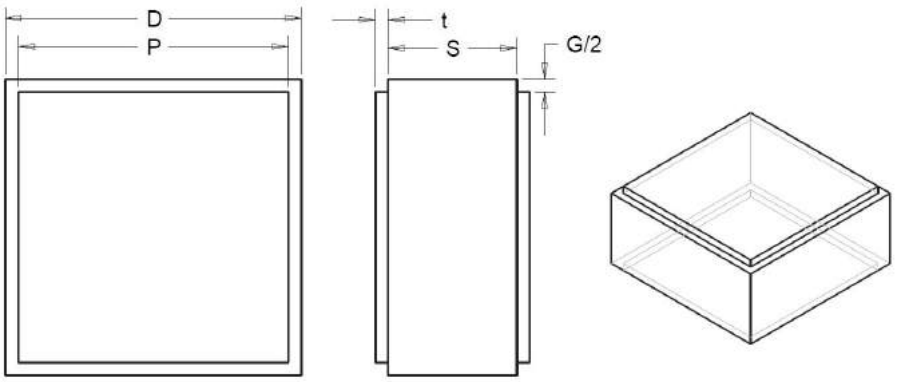

Figure 7.1: Capacitive Unit Cell.

7.2 Capacitive Grid Based Unit Cell

The capacitive grid based unit cell is shown in Fig 7.1. The cell is isotropic in nature and has equal dimensions and periods along both x and y axis. The metal patch has a

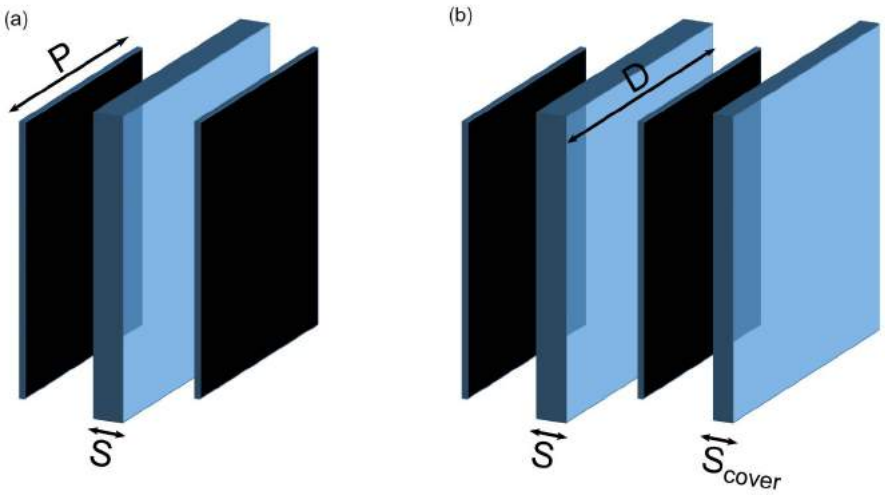

Figure 7.2: Blown up figure of the (a) air or dielectric gap structure unit cell, and (b) parallel grid dielectric gap structure with one grid embedded inside dielectric material where as the other grid is at dielectric-air boundary with S being the dielectric thickness in between the grids and S_{cover} is the height of the dielectric above one grid.

length of P and the period being considered is D. The gap between two metal patch is G, whereas in the unit cell, $G/2$ is considered equally on all four sides. Two sets of metal patches are present in the unit cell along z axis separated by a distance S. This can be considered as the dielectric thickness or an air gap in the absence of it. t is the metal thickness which is usually about $35\mu m$.

Tretyakov [144, 145] derived the *grid impedance* of metal patch arrays by first calculating the respective values for parallel conducting strips of width G and period D and then using Babinet principle to find the respective value of the inverted structure which is an array of isotropic patches. A good explanation can be found in Luukkonen's literature [146, 147].

The *Kontorovich averaged boundary condition* can be stated as [144]:

$$\widehat{E}_x^{tot} = j\frac{\eta_r}{2}\alpha_{ABC}\left[1+\frac{1}{2k_r^2}\right]\left(\widehat{H}_{y-}-\widehat{H}_{y+}\right) \tag{7.1a}$$

$$\widehat{E}_y^{tot} = j\frac{\eta_r}{2}\alpha_{ABC}\left(\widehat{H}_{x-}-\widehat{H}_{x+}\right) \tag{7.1b}$$

where $\widehat{H}_{y+}$ and $\widehat{H}_{y-}$ are the averaged tangential components for two sides of the metal patch along z axis and $\widehat{H}_{y-}-\widehat{H}_{y+}=\widehat{J}_x$ is the average surface current induced along x

axis when TM mode is being considered and similarly $\widehat{H}_{x+}$ and $\widehat{H}_{x-}$ are the averaged tangential components on two sides of the patch in TE mode with $\widehat{H}_{x-} - \widehat{H}_{x+} = \widehat{J}_y$ is the average surface current induced along y axis. Wave impedance $\eta_r = \eta_0/\sqrt{\epsilon_r}$ is the impedance of the medium in which the grid is being considered with ϵ_r being the relative permittivity and $k_r = k_0\sqrt{\epsilon_r}$ is the wave number in a homogeneous medium with relative permittivity ϵ_r. α_{ABC} is the *grid parameter* and for grids where $k_{eff}D \ll 2\pi$ and $\lambda_{eff} = \lambda_0/\sqrt{\epsilon_r}$, it can be approximated as [144–148]:

$$\alpha_{ABC} = \frac{2D}{\lambda_{eff}} log_e \left(csc \frac{\pi G}{2D} \right) \tag{7.2}$$

Babinet principle [144–148] states that the sum of TE mode transmission intensity through a infinitely small periodic metal pattern β and TM mode transmission intensity through a complementary metal pattern β' is equal to 1. I terms of equal circuit reactances this can be written as:

$$Z^{TE}_{grid} Z^{TM}_{grid'} = \frac{\eta_r^2}{4} \tag{7.3a}$$

$$Z^{TM}_{grid} Z^{TE}_{grid'} = \frac{\eta_r^2}{4} \tag{7.3b}$$

The equivalent *grid impedance* for an array of isotropic metal patches can be found using Eq. (7.1) and Eq. (7.3). They can be written as [146, 147]:

$$Z^{TM}_{grid} = -j \frac{\eta_r}{2\alpha_{ABC}} \tag{7.4a}$$

$$Z^{TE}_{grid} = -j \frac{\eta_r}{2\alpha_{ABC} \left(1 - \frac{k_0^2 sin^2\theta}{2k_r^2} \right)} \tag{7.4b}$$

where it is assumed that the wave vector has a x component but no y component with θ being the angle of incidence.

For a single capacitive grid, Luukkonen derived results with a transmission line model which have been extended in this chapter for a simple modelling of parallel grid

structures with air or dielectric gap in between. Only $\theta = 0°$ has been considered, and the grid impedance for both TM and TE modes would be considered as:

$$Z_{grid}^{TM} = Z_{grid}^{TE} = -j\frac{\eta_r}{2\alpha} \tag{7.5}$$

for the rest of the chapter.

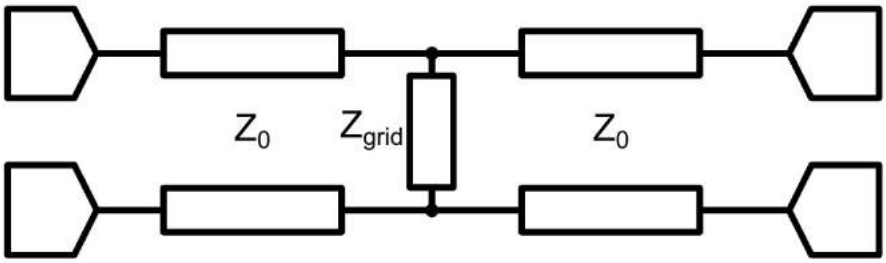

Figure 7.3: Analytical model of capacitive grid based on transmission line diagrams. The input surface impedance is given in Eq. (7.6).

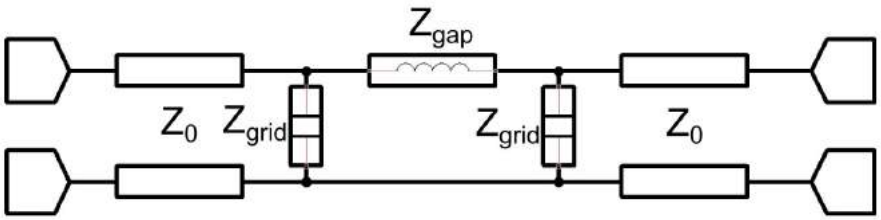

Figure 7.4: Analytical model of parallel grid with air or dielectric gap based surface. The surface impedance is given in Eq. (7.8).

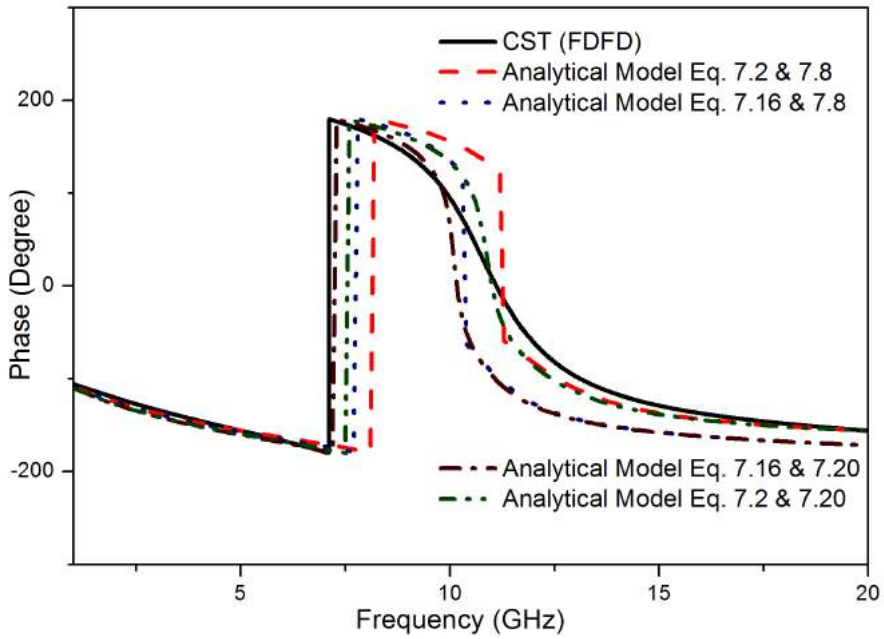

Figure 7.5: Reflection phase for TE polarized normal incident wave on the parallel grid surface with air gap. The parameters are: $D = 11.5$mm, $G = 1$mm, $S = 2.4$mm and $\epsilon_r = 1$ ($\eta_r = \eta_0 = 377\Omega$, $k_r = k_0$).

7.2.1 Air Gap Parallel Grid Structure

The transmission line model for a single grid structure is given in Fig. 7.3 with a blown up view provided in Fig. 7.2(a), where Z_{grid} is loaded as a shunt in free space. The input impedance as seen normal to the grid is the grid impedance parallel to free space impedance [146, 147].

$$Z_{input} = Z_{grid} || Z_0 \tag{7.6}$$

where the free space impedance Z_0 is defined as $\eta_0/cos\theta$ and $\eta_0 cos\theta$ for TE and TM mode respectively with η_0 being 377Ω.

For parallel grid structures in free space, the equivalent transmission line model is shown in Fig. 7.4 where both grids act as capacitive shunts but the air gap in between acts as a series inductive line with inductance:

$$Z_{gap} = jZ_0 sin\, k_0 S \tag{7.7}$$

provided that the gap $S \ll \lambda_0$. Ideally the value of Z_{gap} remains inductive for $S \leq \lambda_0/8$.

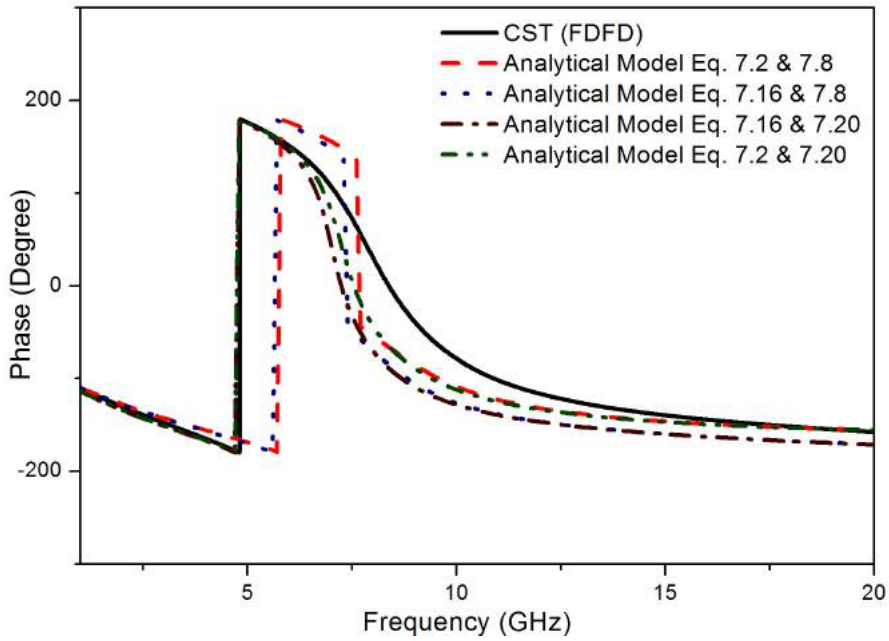

Figure 7.6: Reflection phase for TE polarized normal incident wave on the parallel grid surface with air gap. The parameters are: $D = 11.5$mm, $G = 1$mm, $S = 5$mm and $\epsilon_r = 1$ ($\eta_r = \eta_0 = 377\Omega$, $k_r = k_0$).

The input impedance of the new parallel grid structure in free space can be given as:

$$Z_{inputParGrid} = Z_{grid} || \left[Z_{gap} + (Z_{grid} || Z_0) \right] \tag{7.8}$$

This model works for values of $D \ll \lambda_0$ and $S \sim D$ and has a negligible error for $S \sim D/2$. The model starts to fail for values of $S \ll D$ as higher order Floquet modes have to be considered as reflected components from the second grid which is not recognised in this simple analytical transmission line model. An approximate coupling constant found in the model is provided in the next subsection.

Reflection phase results obtained analytically for TE mode of excitation normally over the surface are compared with numerical results simulated with CST Microwave Studio in the frequency domain and is shown in Fig. 7.5 and Fig. 7.6. The unit cell dimensions used to obtain the results in Fig. 7.5 are, $D = 11.5$mm, $G = 1$mm, $S = 2.4$mm and $\epsilon_r = 1$. The unit cell dimensions used to obtain the results in Fig. 7.6 are the same as the previous one except for $S = 5$mm.

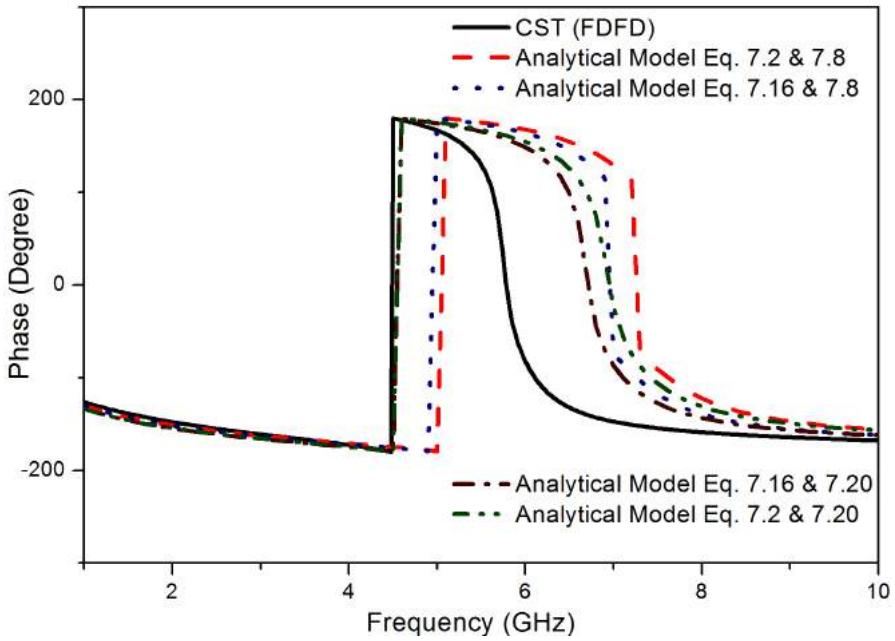

FIGURE 7.7: Reflection phase for TE polarized normal incident wave on the parallel grid surface in air with dielectric material gap. The parameters are: $D = 11.5$mm, $G = 1$mm, $S = 2.4$mm and $\epsilon_r = 4.3$ ($\eta_r = \eta_0/\sqrt{\epsilon_r}$, $k_r = k_0\sqrt{\epsilon_r}$).

7.3 Coupling Between Parallel Grid Structure

The gap between the parallel grids add up to the susceptance of the grid as given in the previous subsection. A coupling factor exists and tends to zero as S becomes comparable to D, but has a significant value when $S \ll D$. A coupling factor can be approximated as:

$$C_{grid} = e^{-2\pi\frac{S}{D}} \tag{7.9}$$

and a parallel shunt add-on to the grid impedance described in the beginning of this section can be given as:

$$Z_{gridCoupling} = -j\frac{\eta_r}{2\alpha C_{grid}} \tag{7.10}$$

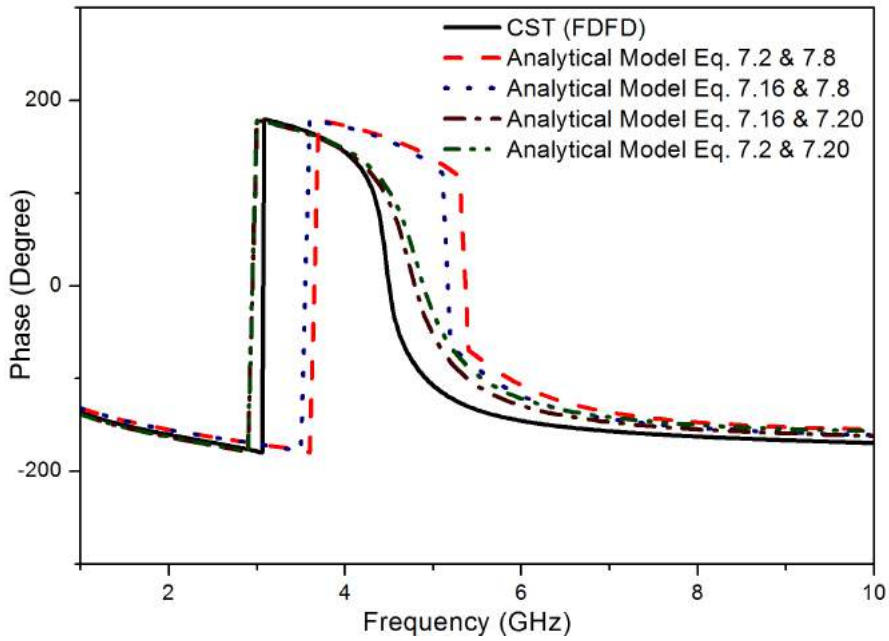

Figure 7.8: Reflection phase for TE polarized normal incident wave on the parallel grid surface in air with dielectric material gap. The parameters are: $D = 11.5$mm, $G = 1$mm, $S = 5$mm and $\epsilon_r = 4.3$ ($\eta_r = \eta_0/\sqrt{\epsilon_r}$, $k_r = k_0\sqrt{\epsilon_r}$).

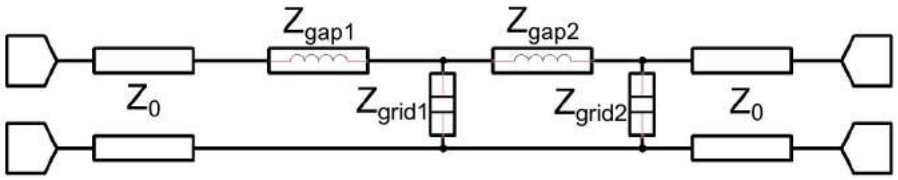

Figure 7.9: Analytical model of parallel grid structure with one grid fully embedded in a dielectric material. The surface impedance is given in Eq. (7.15).

For an infinite layer of closely placed grids, equivalent of each grid impedance can be given as:

$$Z_{Grid} = Z_{grid} || Z_{gridCoupling} \tag{7.11a}$$

$$\Rightarrow Z_{Grid} = -j\frac{\eta_r}{2\alpha\left(C_{grid}+1\right)} \tag{7.11b}$$

7.3.1 Dielectric Gap Parallel Grid Structure

The transmission line model for a parallel grid structure is the same as shown previously in Fig. 7.4 with a blown up view provided in Fig. 7.2(a), except for the fact that the

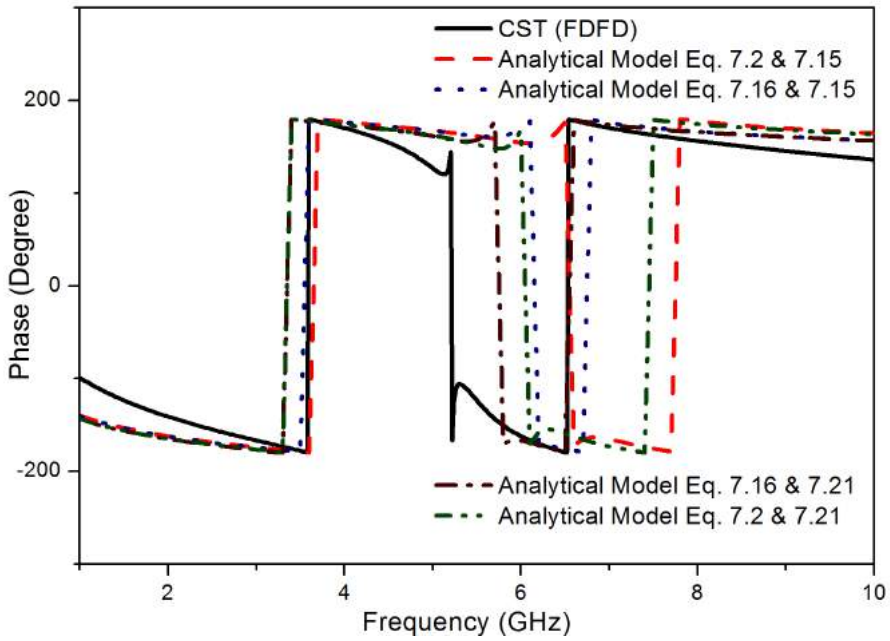

Figure 7.10: Reflection phase for TE polarized normal incident wave on the parallel grid surface with the first grid embedded in dielectric. The parameters are: $D = 11.5$mm, $G = 1$mm, $S = 2.4$mm, $S_{cover} = 1.2$mm and $\epsilon_r = 4.3$ ($\eta_r = \eta_0/\sqrt{\epsilon_r}$, $k_r = k_0\sqrt{\epsilon_r}$).

metal patches are no longer present in a single homogeneous medium. In such cases the Babinet principle used to derive the grid impedance of a single grid fails [144, 145] but an approximate formulation exists [148] and is given as:

$$Z_{grid'} = -j\frac{\eta_0}{2\alpha_{ABC}}\frac{2}{\epsilon_r + 1} \tag{7.12}$$

and Eq. (7.7) tobe modified as:

$$Z_{gap'} = jZ_{0'}sin\, k_r S \tag{7.13}$$

where the wave impedance in the dielectric material is given as $Z_{0'} = Z_0/\sqrt{\epsilon_r}$ and $k_r = k_0\sqrt{\epsilon_r}$. Results obtained analytically are compared again in Fig. 7.7 and Fig. 7.8 for unit cell dimensions previously used to obtain results in Fig. 7.5 and Fig. 7.6 except with a dielectric slab of $\epsilon_r = 4.3$ (FR4).

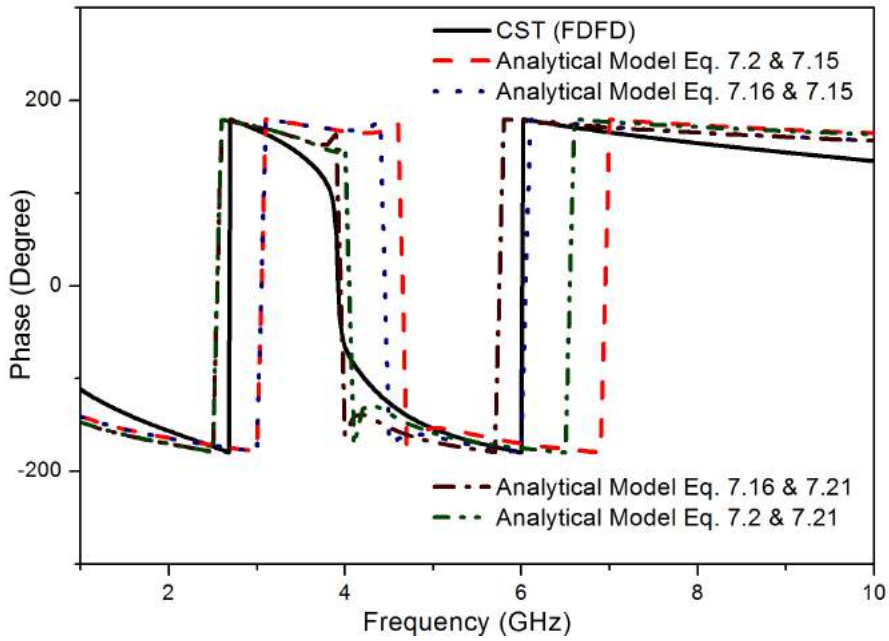

Figure 7.11: Reflection phase for TE polarized normal incident wave on the parallel grid surface with the first grid embedded in dielectric. The parameters are: $D = 11.5$mm, $G = 1$mm, $S = 5$mm, $S_{cover} = 1.2$mm and $\epsilon_r = 4.3$ ($\eta_r = \eta_0/\sqrt{\epsilon_r}$, $k_r = k_0\sqrt{\epsilon_r}$).

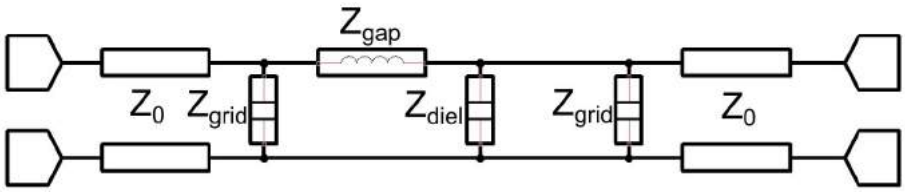

Figure 7.12: Analytical model of parallel grid with air or dielectric gap based surface. The surface impedance is given in Eq. (7.20).

7.3.2 Dielectric Gap Parallel Grid Structure with One Embedded Grid

The transmission line model changes if a thin dielectric plate of the same relative permittivity to that of the substrate is used to cover one side of the parallel grids. Generalizing the design would mean that one of the parallel grids is embedded in a homogeneous dielectric whereas the one one stays at the air-dielectric boundary. Understanding of the surface can be achieved by viewing Fig. 7.2(b) which shows an exploded view. The transmission line model is shown in Fig. 7.9. Unlike the previous two designs of the unit cell, this cell has two different grid impedances for the metal

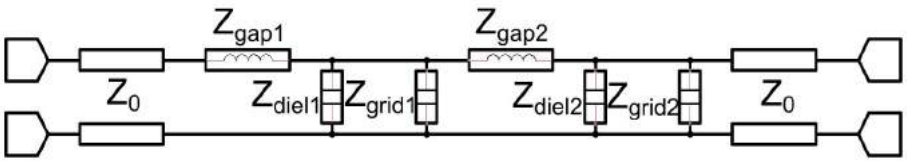

Figure 7.13: Analytical model of parallel grid structure with one grid fully embedded in a dielectric material. The surface impedance is given in Eq. (7.21).

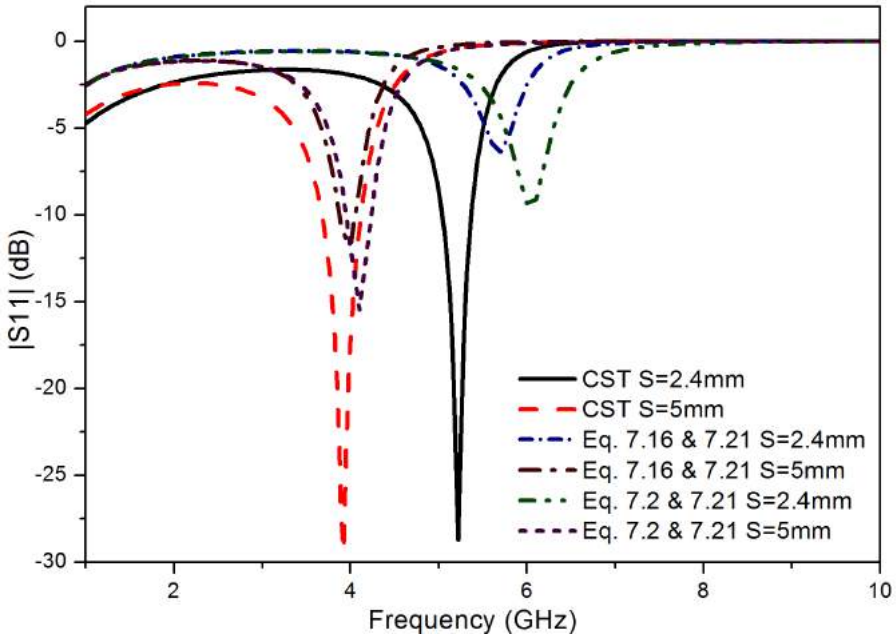

Figure 7.14: Reflection coefficient in dB as incurred by a plane wave incident normally on an infinite surface of the third type i.e. dielectric gap parallel grid structure with one embedded grid.

patches. At normal incidence,the embedded grid impedance is governed by Eq. (7.4b) while the air-dielectric boundary grid is governed by Eq. (7.12) with $\epsilon_r > 1$. Those equations can be rewritten for normal incidence as:

$$Z_{grid1} = -j\frac{\eta_r}{2\alpha_r} \tag{7.14a}$$

$$Z_{grid2} = -j\frac{\eta_0}{2\alpha_0}\frac{2}{\epsilon_r + 1} \tag{7.14b}$$

where

$$\alpha_r = \frac{k_r D}{\pi} log_e \left(csc \frac{\pi G}{2D} \right) \tag{7.14c}$$

$$\alpha_0 = \frac{k_0 D}{\pi} log_e \left(csc \frac{\pi G}{2D} \right) \tag{7.14d}$$

with $\eta_r = \eta_0/\sqrt{\epsilon_r}$, $k_r = k_0\sqrt{\epsilon_r}$ and

$$Z_{gap1} = jZ_{0'} sin\, k_r S_{cover} \tag{7.14e}$$

$$Z_{gap2} = jZ_{0'} sin\, k_r S \tag{7.14f}$$

where S_{cover} is the height above the $grid1$ and S is the thickness of dielectric between $grid1$ and $grid2$. The overall input impedance of the parallel grid structure with one grid embedded in dielectric can be given as:

$$\begin{aligned} Z_{inputParGrid'} &= Z_{gap1} \\ &\quad + Z_{grid1} || \left[Z_{gap2} + (Z_{grid2} || Z_0) \right] \end{aligned} \tag{7.15}$$

Analytical results for reflection phase are provided along with numerical results in Fig. 7.10 and Fig. 7.11 for unit cell dimensions previously used to obtain results in Fig. 7.7 and Fig. 7.8 except with a dielectric cover of height $S_{cover} = 1.2$mm and $\epsilon_r = 4.3$ (FR4). It is quite visible that the analytical results have deteriorated due to approximations which have been detailed in the next subsection.

7.4 Optimization of Analytical Model of Capacitive Unit Cell

In the previous subsection, the transmission line model was devoid of the effects of frequency on the grid structure. It was considered that the period $D << \lambda_{eff}$ which was not the case in high frequency region. The period being $D = 11.5$mm and $\lambda_r = 28.9$mm at 5GHz for the embedded grid in FR4 with $\epsilon_r = 4.3$, the ratio of $D/\lambda_r = 0.398$ has a

great effect on the results obtained analytically. At high frequencies, the effect of this ratio has to be considered by implementing a transitional model [149] from capacitive to inductive state of a single patch grid resonating at $\lambda = G$. This model can be implemented in the grid parameter and rewritten as:

$$\alpha_{ABC'} = \frac{2log_e\left(csc\,\frac{\pi G}{2D}\right)}{\left(\frac{\lambda_{eff}}{D} - \frac{D}{\lambda_{eff}}\right)} \tag{7.16}$$

It can be clearly noted from Eq. (7.16) that when $D \ll \lambda_{eff}$, the value of D/λ_{eff} can be ignored and the equation becomes equivalent to Eq. (7.2). The effect on the unit cells previously considered is recalculated in the below subsections.

7.4.1 Air Gap Parallel Grid Structure

The input impedance for the air gap parallel grid structure is recalculated using Eq. (7.8) except for the calculation of grid parameter, where Eq. (7.16) is used in lieu of Eq. (7.2).

The results for reflection phase with normal incidence has been compared with previously obtained data in Fig. 7.5 and Fig. 7.6 for $S = 2.4$mm and $S = 5$mm respectively. The unit cell dimensions similar to the one used to obtain results given in Fig. 7.5 and Fig. 7.6.

7.4.2 Dielectric Gap Parallel Grid Structure

Recalculated results for optimised analytical model of dielectric gap parallel grid structure computed using Eq. (7.8) and Eq. (7.16) has been compared with previously computed data in Fig. 7.7 and Fig. 7.8 for unit cell dimensions similar to the one used to obtain results given in Fig. 7.7 and Fig. 7.8 respectively.

7.4.3 Dielectric Gap Parallel Grid Structure with One Embedded Grid

Recalculated results using Eq. (7.15) and Eq. (7.16) has been plotted comparing results from previous subsection and has been shown again in Fig. 7.10 and Fig. 7.11. The unit cell dimensions are similar to the one used in previous subsection.

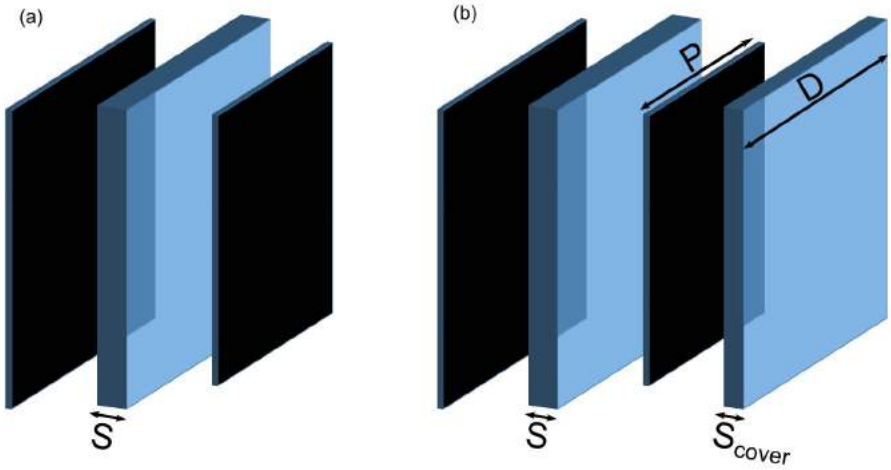

Figure 7.15: Blown up figure of the (a) PEC backed patch loaded unit cell structure with air or dielectric gap in between, and (b) PEC backed dielectric embedded patch loaded unit cell structure with S being the dielectric thickness in between the patch and the ground plane and S_{cover} is the height of the dielectric above the patch.

7.5 Improvement of Analytical Model with Dielectric Shunt Susceptance

So far in the model described in all the previous subsections, the effects of any capacitance due to the dielectric or air gap has been ignored. The next model will include a

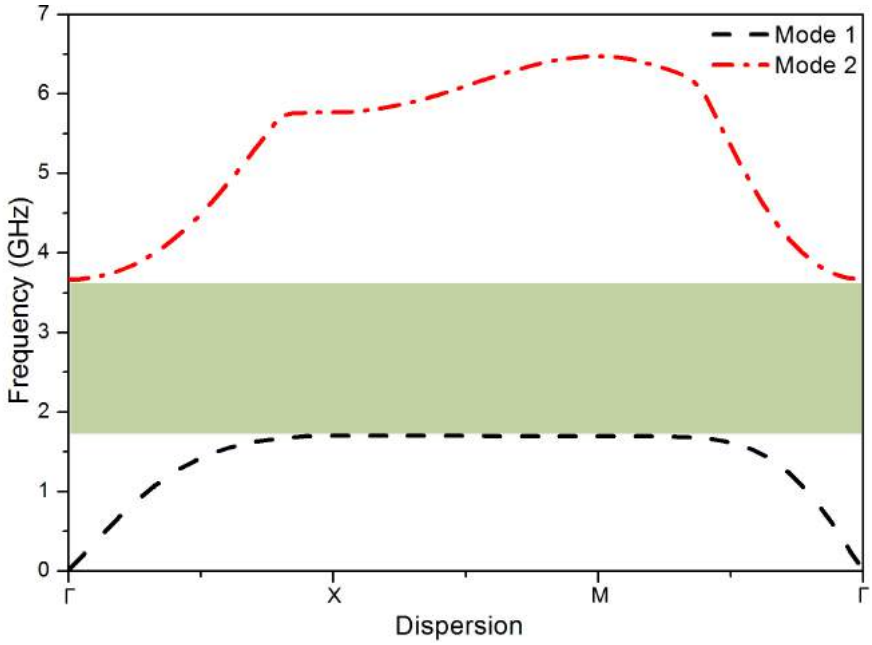

Figure 7.16: Dispersion diagram of mushroom type structure with a PEC ground plane, and the unit cell design assumes similarity with Fig. 7.25 with a 'via' connecting the PEC ground plane to the patch at the centre. The parameters are: $D = 11.5$mm, $G = 1$mm, $S = 2.4$mm, $S_{cover} = 1.2$mm and $\epsilon_r = 4.3$.

lumped capacitance relating the effects of dielectric susceptance. For a thin dielectric slab the impedance boundary condition can be written as

$$\vec{E}_t = -\frac{j}{\omega\epsilon_0 S\left(\epsilon_r - 1\right)}\left(\hat{n} \times \vec{H}_{t+} - \hat{n} \times \vec{H}_{t-}\right) \tag{7.17}$$

where h_{diel} is the thickness of the thin dielectric cover over one of the parallel grids. The upper dielectric cover makes the grid embedded in the dielectric substance and is now embedded in a homogeneous medium. The surface impedance of the thin dielectric sheet can be written as

$$Z_{diel} = -\frac{j}{\omega\epsilon_0 S\left(\epsilon_r - 1\right)} \tag{7.18}$$

in case of air gap, Eq. (7.18) becomes invalid and a good approximation can be given as

$$Z_{diel} = -\frac{jZ_0}{sin\, k_0 S} \tag{7.19}$$

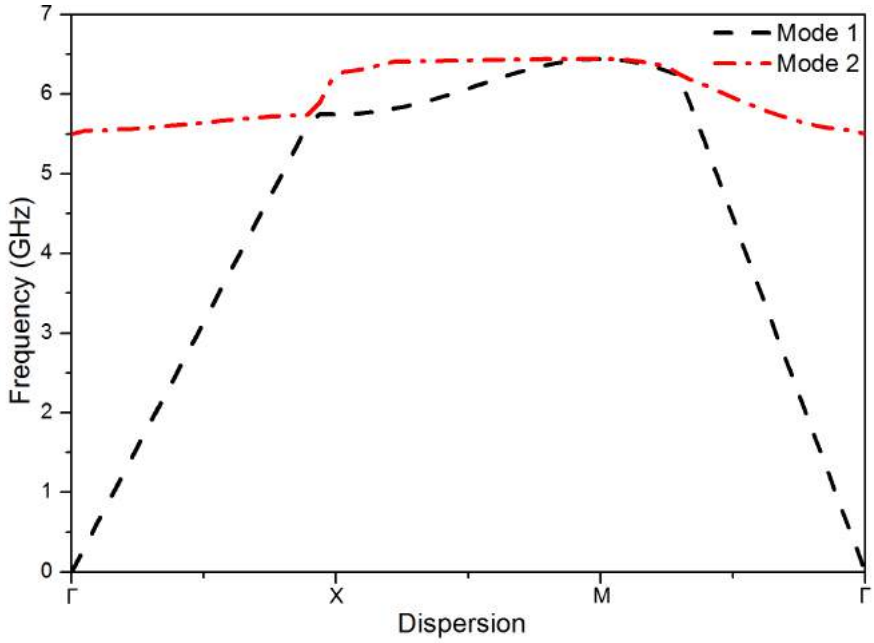

FIGURE 7.17: Dispersion diagram of patch loaded structure, and the unit cell design assumes similarity with Fig. 7.25. The parameters are: $D = 11.5$mm, $G = 1$mm, $S = 2.4$mm, $S_{cover} = 1.2$mm and $\epsilon_r = 4.3$.

where $\epsilon_0 = 8.854187817... \times 10^{-12}$ is the absolute permittivity of free space and Z_0 is the wave impedance in free space. The modified equivalent circuit model for air and dielectric gap parallel grid structure is shown in Fig. 7.12 and that of one embedded in dielectric parallel grid structure is shown in Fig. 7.13. Implementation of the improvement technique in Eq. (7.8) gives way to a new input impedance and can be given as

$$Z_{inputParGrid} = Z_{grid} || \left[Z_{gap} + (Z_{diel} || Z_{grid} || Z_0) \right] \tag{7.20}$$

and subsequently Eq. (7.15) can be transformed into

$$\begin{aligned} Z_{inputParGrid'} = Z_{gap1} + [Z_{diel1} || Z_{grid1} || \\ \{ Z_{gap2} + (Z_{diel2} || Z_{grid2} || Z_0) \}] \end{aligned} \tag{7.21}$$

where the first values are relevant to the initial embedded grid and its dielectric cover with thickness S_{cover}, and the second values are for the second parallel grid at the

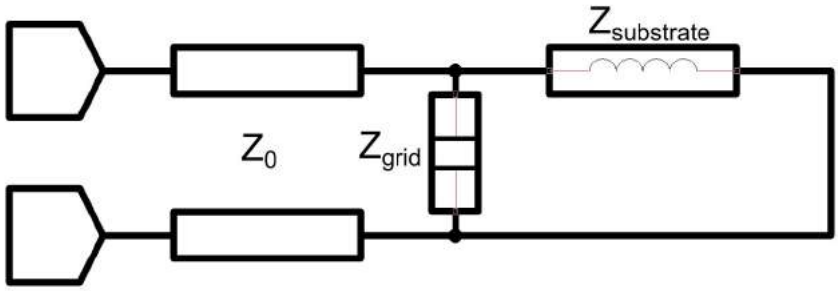

Figure 7.18: Analytical model of PEC backed patch loaded surface based on transmission line diagrams. The input surface impedance is given in Eq. (7.22).

dielectric-air boundary at a dielectric thickness of S apart from the first grid.

The return loss pattern as incurred by a plane wave incident normally on an infinite surface of the third type described in the Sec. 7.4.3 (dielectric gap parallel grid structure with one embedded grid) is shown in Fig. 7.14 for $S = 2.4$mm and $S = 5$mm. The surface acts as a filter and becomes transparent in nature during its shift in susceptance. The surface cannot be used for guiding surface waves in the band where it acts as a filter for normal incidence. Results for the reflection phase calculated with Eq. (7.20) and Eq. (7.21) along with the original and optimized grid parameter Eq. (7.2) and Eq. (7.16) respectively. The plots can be viewed again in Fig. 7.5 to Fig. 7.11 for the three different topologies described in the previous subsection. The plot verifies the fact that using Eq. (7.16) and Eq. (7.21) results in comparable data numerically computed with full wave computational methods.

7.6 Reflective High Impedance Surface Unit Cell

Sievenpiper [150, 151] showed that mushroom-like structures with 'vias' connected to the ground have a two-fold effect on electromagnetic waves. It acts as a band gap structure for surface electromagnetic waves for a group of frequencies. Additionally, it also results in a 0° reflection phase for waves incident normally on it. Yang [152]

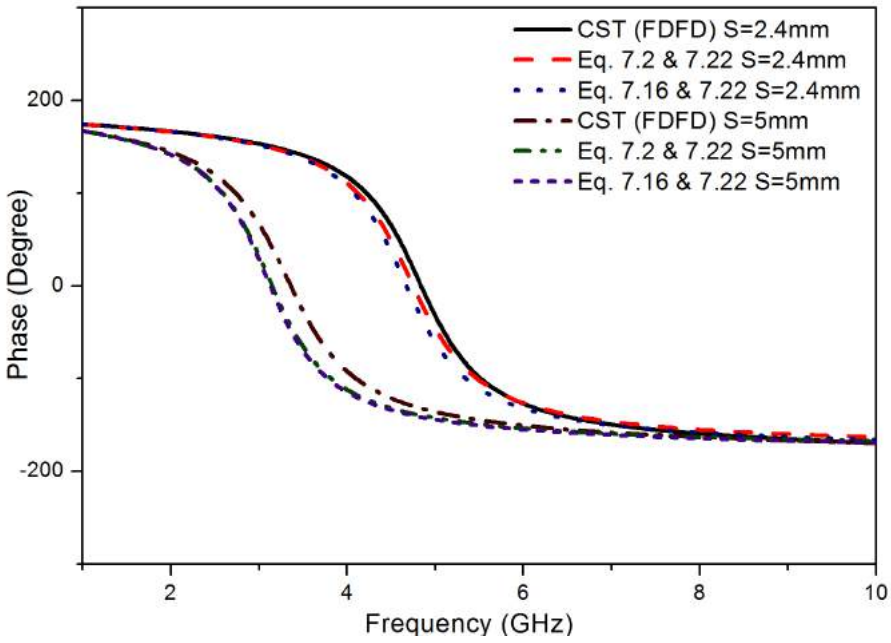

Figure 7.19: Reflection phase for TE polarized normal incident wave on the PEC backed patch loaded dielectric surface with the first grid present in air-dielectric boundary. The parameters are: $D = 11.5\text{mm}$, $G = 1\text{mm}$, $S = (2.4, 5)\text{mm}$ and $\epsilon_r = 4.3$ ($\eta_r = \eta_0/\sqrt{\epsilon_r}$, $k_r = k_0\sqrt{\epsilon_r}$).

made a comparison between a mushroom based surface and a patch loaded surface which is without the 'vias'. It was found that the reflection phase remains similar for both surfaces of comparable dimensions but the band gap vanishes. This phenomenon brought in the surface wave antenna which is low profile yet radiating like a monopole. Fig. 7.16 and Fig. 7.17 shows the disappearance of the band gap for the patch loaded design as the via between the PEC ground plane and the patch is removed.

Investigations were with 'via'-less patch loaded ground planes with dimensions comparably lower than the free space wavelength of the desired frequency of operation. It was found that even though there exists a solution for Maxwell's Equations for the Eigen Modes of the structure, a relatively high surface impedance exists at normal incidence of the electromagnetic wave on the surfaces and is still useful as a reflector for antenna purposes.

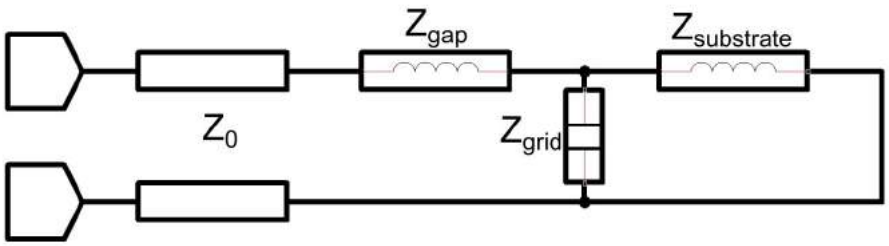

Figure 7.20: Analytical model of PEC backed dielectric embedded patch loaded based on transmission line diagrams. The input surface impedance is given in Eq. (7.24).

7.6.1 PEC Backed Patch Loaded Dielectric Structure

The most common type of 'via'-less high impedance structure that has been discussed in different literature is the PEC backed patch loaded dielectric structure first compared by Yang [152]. Fig. 7.15(a) shows a blown up model of the structure and the transmission line equivalent model is shown in Fig. 7.18. Tretyakov [144, 145] analysed the transmission line model and showed that the equivalent surface impedance can be given as:

$$Z_{inputPatchLoaded} = Z_{grid}||Z_{substrate} \tag{7.22}$$

where the Z_{grid} is the grid impedance given Eq. (7.12) and $Z_{substrate}$ is the impedance of the dielectric substrate backed with a PEC ground plane that has been considered as a shunted inductor connected to ground and can be given as:

$$Z_{substrate} = jZ_{0'}tan\, k_r S \tag{7.23}$$

with $Z_{0'} = Z_0/\sqrt{\epsilon_r}$ and $k_r = k_0\sqrt{\epsilon_r}$ being the effective wave impedance and wave number in the medium respectively. Results obtained using Eq. (7.22) along with Eq. (7.2) and Eq. (7.16) has been given in Fig. 7.19 for dimensions $D = 11.5$mm, $G = 1$mm, $S = (2.4, 5)$mm and $\epsilon_r = 4.3$.

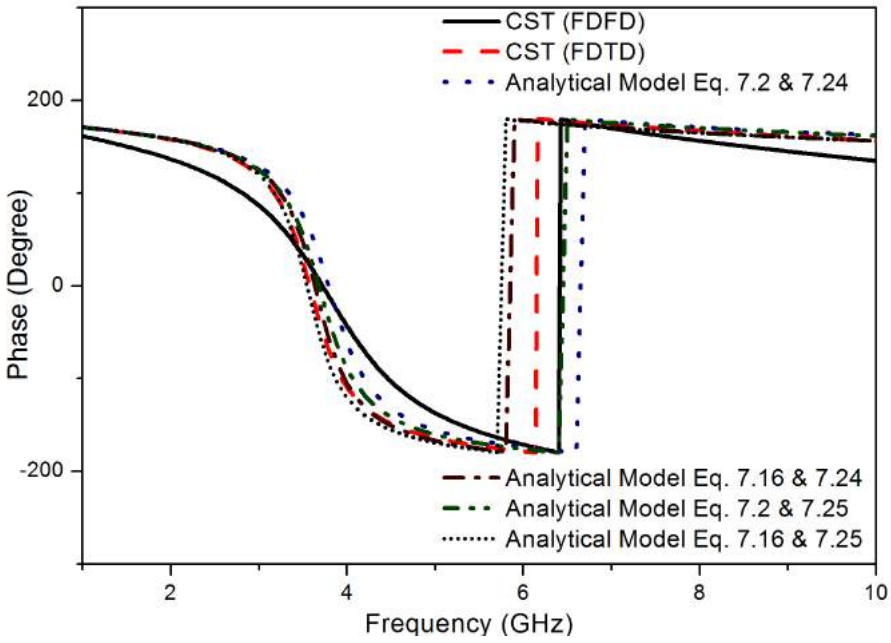

Figure 7.21: Reflection phase for TE polarized normal incident wave on the PEC backed patch loaded dielectric surface with the grid embedded in the dielectric material. The parameters are: $D = 11.5$mm, $G = 1$mm, $S = 2.4$mm, $S_{cover} = 1.2$mm and $\epsilon_r = 4.3$ ($\eta_r = \eta_0/\sqrt{\epsilon_r}$, $k_r = k_0\sqrt{\epsilon_r}$).

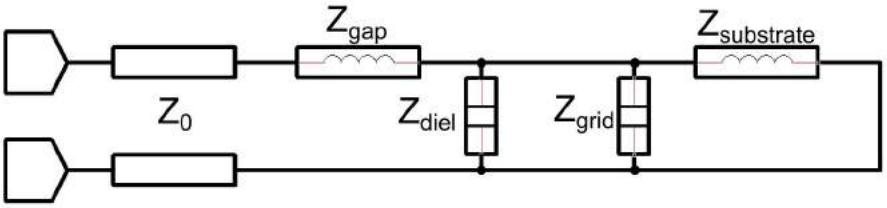

Figure 7.22: Modified analytical model of PEC backed dielectric embedded patch loaded based on transmission line diagrams. The input surface impedance is given in Eq. (7.25).

7.6.2 PEC Backed Patch Loaded Dielectric Structure with Patch Embedded in Dielectric

The transmission line changes its characteristics when the patch is embedded in a dielectric medium or in other words, a thin dielectric plate is used to cover the patch. The modified transmission line model is given in Fig. 7.20 and Fig. 7.15(b) showcases an exploded view of the unit cell. The inductive reactance Z_{gap} can be given again by

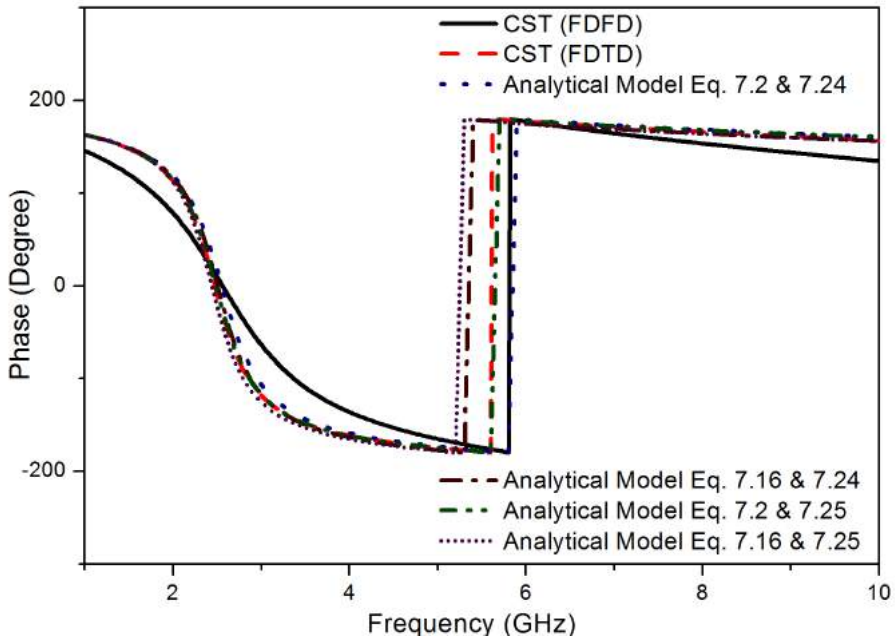

Figure 7.23: Reflection phase for TE polarized normal incident wave on the PEC backed patch loaded dielectric surface with the grid embedded in the dielectric material. The parameters are: $D = 11.5$mm, $G = 1$mm, $S = 5$mm, $S_{cover} = 1.2$mm and $\epsilon_r = 4.3$ ($\eta_r = \eta_0/\sqrt{\epsilon_r}$, $k_r = k_0\sqrt{\epsilon_r}$).

Eq. (7.14e) and the overall input impedance can be written as:

$$Z_{inputPatchLoaded'} = Z_{gap} + (Z_{grid}||Z_{substrate}) \tag{7.24}$$

where Z_{grid} and $Z_{substrate}$ is defined in Eq. (7.12) and Eq. (7.23) respectively. The reflection phase obtained using Eq. (7.12) along with Eq. (7.2) and Eq. (7.16) has been shown in Fig. 7.21 and Fig. 7.23 for $S = 2.4$mm and $S = 5$mm respectively with $S_{cover} = 1.2$mm, $D = 11.5$mm, $G = 1$mm and $\epsilon_r = 4.3$.

Section 7.4 described the improvement of analytical model with the inclusion of dielectric shunt susceptance. The dielectric susceptance can be added to the previous analytical model given in Fig. 7.20 and a modified analytical model can be generated as is given in Fig. 7.22. Z_{diel} remains the same and is defined by Eq. (7.18) and the improved input impedance of the covered patch loaded surface can be given as:

$$Z_{inputPatchLoaded''} = Z_{gap} + (Z_{diel}||Z_{grid}||Z_{substrate}) \tag{7.25}$$

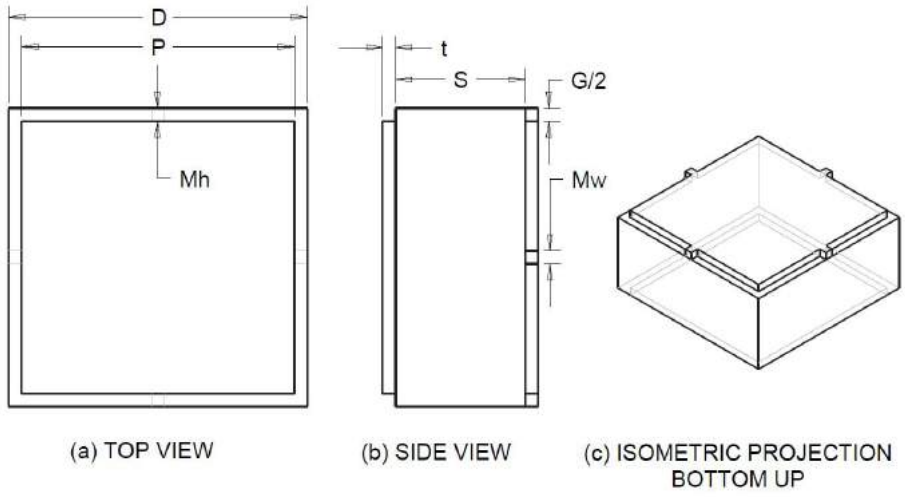

Figure 7.24: High Impedance Unit Cell.

with Z_{grid} and $Z_{substrate}$ already defined before. Results obtained with Eq. (7.25) along with Eq. (7.2) and Eq. (7.16) has been shown in Fig. 7.21 and Fig. 7.23 for $S = 2.4$mm and $S = 5$mm respectively with other dimensions same as the previous sample.

7.7 Reconfigurable Unit Cell

The reconfigurable surface that has been used in a later chapter to design a beam-steerable antenna is a combination of the two distinct structures described in the previous subsections, namely the parallel grid structure and the PEC backed loaded patch structure. The Combination is achieved by using two parallel grids separated by a dielectric medium, and one of the grid is shorted using a load which is reconfigurable. With a thin metal inductive load, the unit cell design looks like Fig. 7.24 and the blown up view is given in Fig. 7.25. Practical implementation of this structure can be done using a solid state switch having a lumped impedance of Z_{switch}, connected between each patch in the grid. For an isotropic grid, each patch would be connected to 4 lumped component, all having an equal value of Z_{switch}. The analytical model can be intuitively created with the lumped impedance Z_{switch} placed parallel to the value of Z_{grid}. The susceptance of the switch is capacitive when off, and inductive when on but the topology of the transmission line model remains the same. When the susceptance

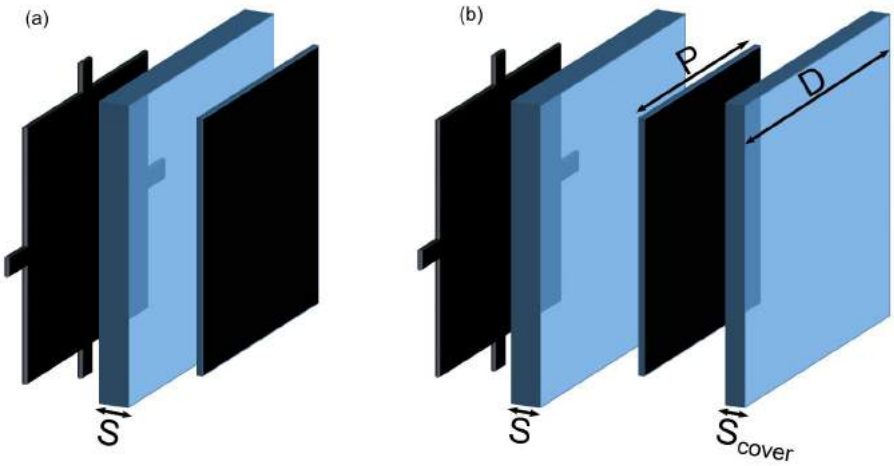

Figure 7.25: Blown up figure of the (a) air or dielectric gap structure unit cell with one connected and the other disconnected grid, and (b) parallel grid dielectric gap structure with one connected grid at air-dielectric boundary and one disconnected grid embedded inside dielectric material with S being the dielectric thickness in between the grids and S_{cover} is the height of the dielectric above the disconnected grid.

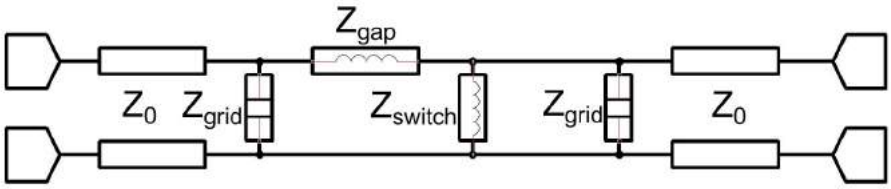

Figure 7.26: Analytical model of dielectric gap parallel grid structure with one grid connected to lumped switch, based on transmission line diagrams. The input surface impedance is given in Eq. (7.26).

of the switch is capacitive, the structure behaves as a capacitive surface waveguide, and when the susceptance of the switch is inductive, it creates an LC tank with the grid. At low frequencies, it shorts the grid and makes the structure behave similarly to the PEC backed patch loaded high impedance structure.

7.7.1 Dielectric Gap Parallel Grid Structure with One Grid Connected to Lumped Switch

The transmission line model is given in Fig. 7.26 and the equivalent surface impedance can be calculated using the same grid parameters and grid impedances discussed in

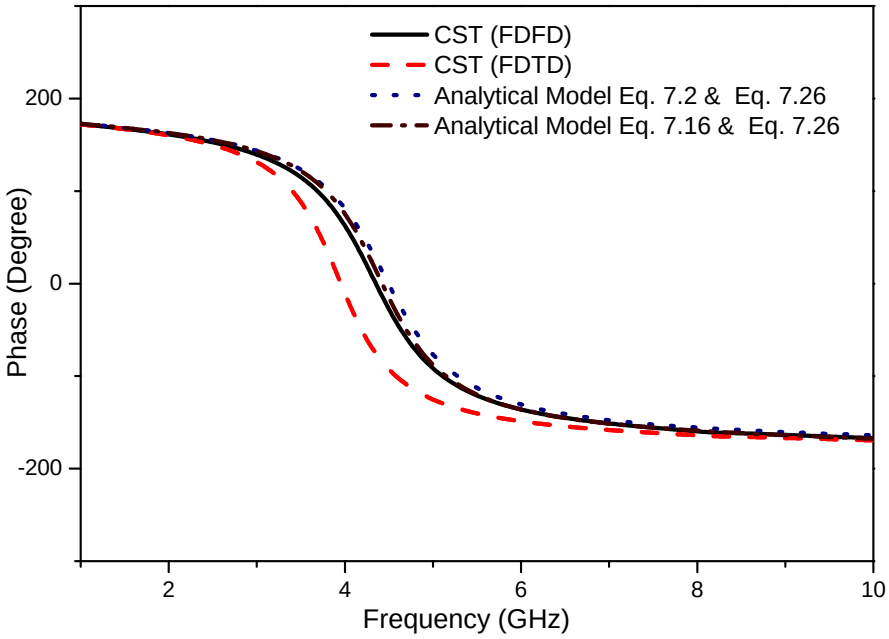

Figure 7.27: Reflection phase for TE polarized normal incident wave on the switched (rear) grid loaded dielectric surface with the first grid present in air-dielectric boundary. The parameters are: $D = 11.5$mm, $G = 1$mm, $S = 2.4$mm and $\epsilon_r = 4.3$ ($\eta_r = \eta_0/\sqrt{\epsilon_r}$, $k_r = k_0\sqrt{\epsilon_r}$).

the previous subsections and can be given as:

$$Z_{reconf.} = Z_{grid} || \left[Z_{gap} + (Z_{switch} || Z_{grid} || Z_0) \right] \tag{7.26}$$

where Z_{grid} and Z_{gap} is given in Eq. (7.4) and Eq. (7.13) respectively.

Results obtained from Eq. (7.26) does not change with the inclusion of dielectric surface impedance as the inductive reactance overrides the grid capacitance and acts as a PEC. The dielectric surface impedance in parallel to a short makes no difference to the problem and hence have been ignored. Fig. 7.27 and Fig. 7.28 shows comparative results obtained numerically and analytically with unit cell dimensions, $D = 11.5$mm, $G = 1$mm, $S = 2.4$ and $S = (2.4, 5)$mm and $\epsilon_r = 4.3$. For analytical calculation, the low frequency inductance of a connecting strip at air-dielectric boundary is calculated using the formula given in Terman's Radio Engineers Handbook [153] for straight rectangular bar. The dimensions of the metal connector used for both numerical and analytical calculations are $l = 1$mm and $w = 0.5$mm at air-dielectric boundary which

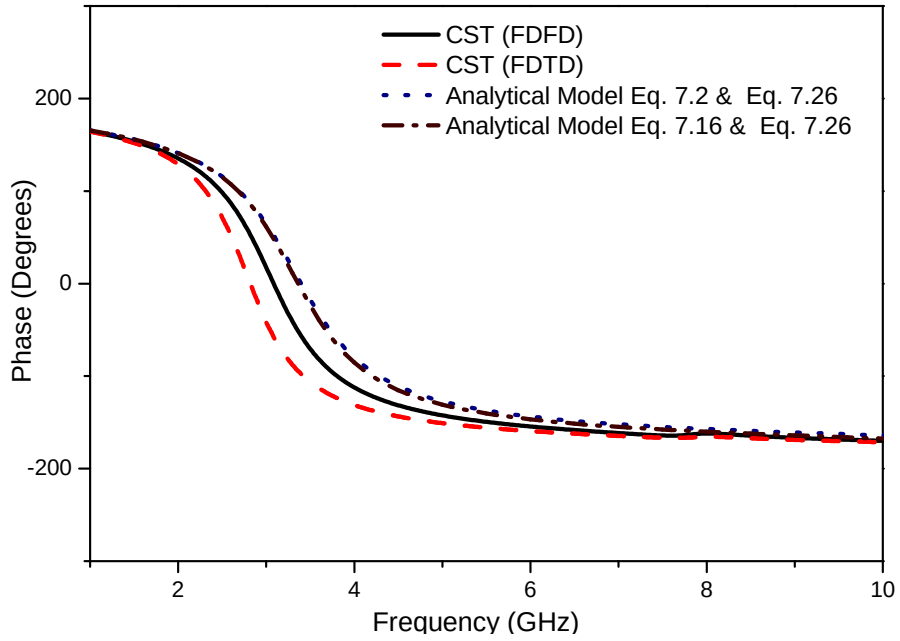

Figure 7.28: Reflection phase for TE polarized normal incident wave on the switched (rear) grid loaded dielectric surface with the first grid present in air-dielectric boundary. The parameters are: $D = 11.5$mm, $G = 1$mm, $S = 5$mm and $\epsilon_r = 4.3$ ($\eta_r = \eta_0/\sqrt{\epsilon_r}$, $k_r = k_0\sqrt{\epsilon_r}$).

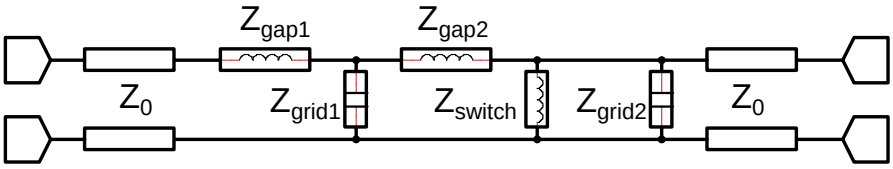

Figure 7.29: Analytical model of dielectric gap parallel grid structure with the front grind fully embedded in a dielectric material and the rear grid connected to lumped switch, based on transmission line diagrams. The input surface impedance is given in Eq. (7.28).

makes $l_{eff} = 1.62$mm and $w_{eff} = 0.81$mm. For completeness, the formula for low frequency inductance of a flat rectangular bar is given again as [154]:

$$L_0 = 2l\left[ln\frac{2l}{w+t} + 0.5 + 0.2235\frac{w+t}{l}\right] \tag{7.27}$$

where t is the copper thickness of 35μm. The calculated low frequency inductance used to obtain analytical results is 0.635225nH.

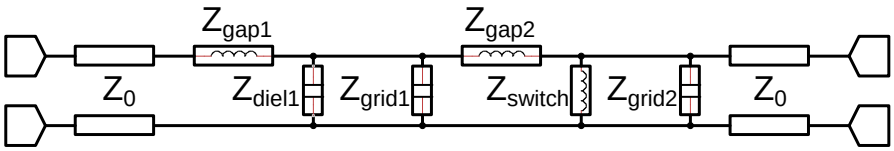

Figure 7.30: Modified analytical model of dielectric gap parallel grid structure with the front grind fully embedded in a dielectric material and the rear grid connected to lumped switch, based on transmission line diagrams. The input surface impedance is given in Eq. (7.29).

7.7.2 Dielectric Gap Parallel Grid Structure with One Grid Embedded in Dielectric Medium and the Other Grid Connected to Lumped Switch

The basic transmission line model is given in Fig. 7.29. The equivalent surface impedance can be calculated using the same grid parameters and grid impedances discussed in the previous subsections and can be given as:

$$Z_{reconf.'} = Z_{gap1} + Z_{grid1} || \left[Z_{gap2} + (Z_{switch} || Z_{grid2} || Z_0) \right] \tag{7.28}$$

where Z_{grid} and Z_{gap} is given in Eq. (7.4) and Eq. (7.13) respectively. The modified transmission line model is given in Fig. 7.30 and the equivalent surface impedance can be calculated as:

$$Z_{reconf.''} = Z_{gap1} + \left[Z_{diel1} || Z_{grid1} || \left\{ Z_{gap2} + (Z_{switch} || Z_{grid2} || Z_0) \right\} \right] \tag{7.29}$$

where Z_{grid1}, Z_{grid2}, Z_{gap1} and Z_{gap2} is given in Eq. (7.4) and Eq. (7.13) respectively.

Results obtained from Eq. (7.28) and Eq. (7.29) does not change with the inclusion of dielectric surface impedance as the inductive reactance overrides the grid capacitance and acts as a PEC. However the modifications of Eq. (7.28) do contribute to the first grid. Fig. 7.31 and Fig. 7.32 shows comparative results obtained numerically and analytically with unit cell dimensions, $D = 11.5$mm, $G = 1$mm, $S = 2.4$ and $S = (2.4, 5)$mm and $\epsilon_r = 4.3$.

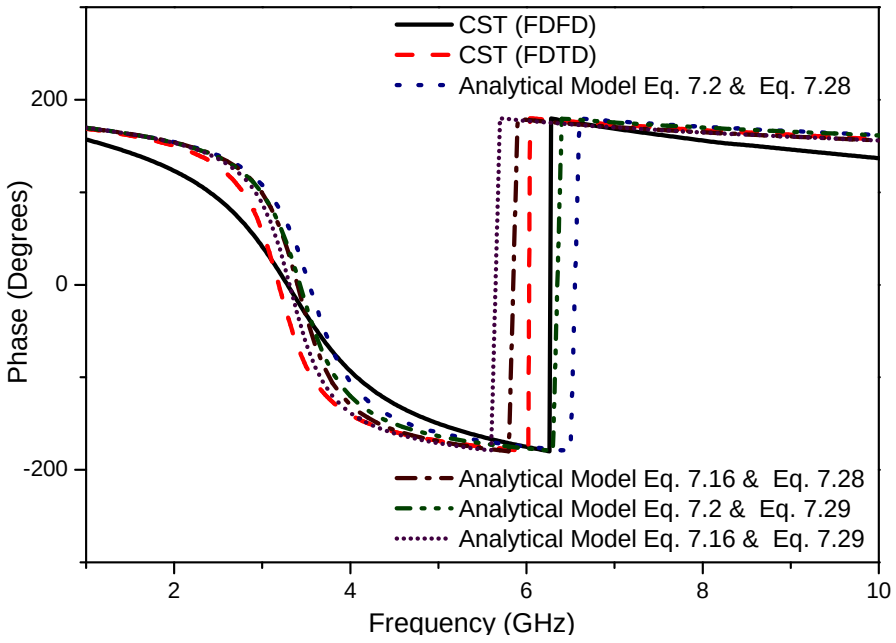

Figure 7.31: Reflection phase for TE polarized normal incident wave on the switched (rear) grid loaded dielectric surface with the first grid completely embedded in the dielectric medium. The parameters are: $D = 11.5$mm, $G = 1$mm, $S = 2.4$mm and $\epsilon_r = 4.3$ ($\eta_r = \eta_0/\sqrt{\epsilon_r}$, $k_r = k_0\sqrt{\epsilon_r}$).

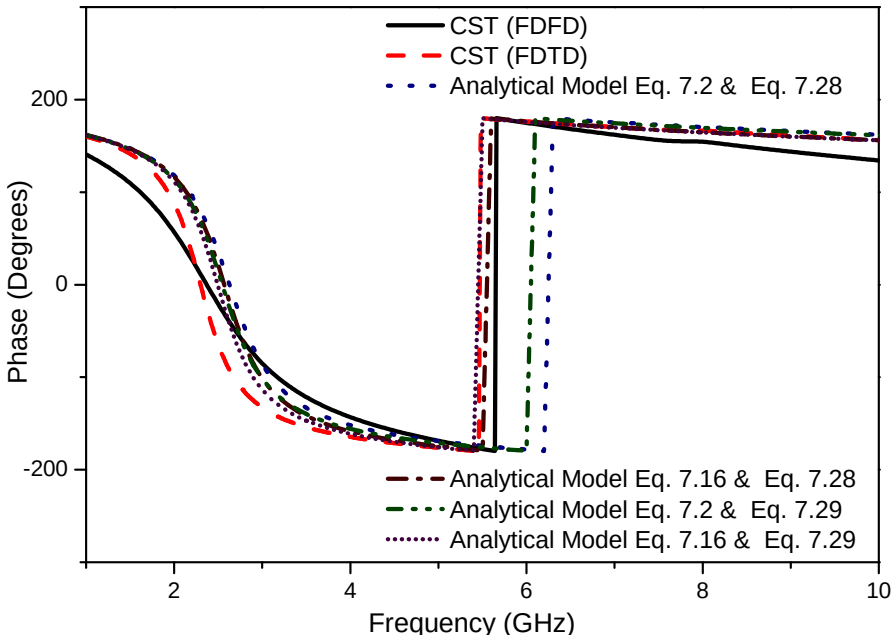

Figure 7.32: Reflection phase for TE polarized normal incident wave on the switched (rear) grid loaded dielectric surface with the first grid completely embedded in the dielectric medium. The parameters are: $D = 11.5$mm, $G = 1$mm, $S = 5$mm and $\epsilon_r = 4.3$ ($\eta_r = \eta_0/\sqrt{\epsilon_r}$, $k_r = k_0\sqrt{\epsilon_r}$).

7.8 Conclusion

Reconfigurable surfaces that appear opaque or transparent, for electromagnetic waves, depending on the mode are proposed in this chapter. Step-by-step and rigorous analysis are done for multiple unit-cells. Unit-cells from an infinite plane of a parallel grid structure with and without a dielectric cover is analysed. A high-impedance surface with a grid (with and without dielectric cover) backed by PEC is also analysed. And a hybrid of these two designs where one grid has switches connected to each other is intended and analysed. The transmission-line model results for all the unit-cells (including the reconfigurable unit-cell) are in fair to good agreements with the CST Microwave Studio simulation results. In the next two chapters, practical applications of this unit-cell have been discussed on waveguide and antenna designs.

"When the globe is covered with a net of railroads and telegraph wires, this net will render services comparable to those of the nervous system in the human body, partly as a means of transport, partly as a means for the propagation of ideas and sensations with the speed of lightning."

Wilhelm Eduard Weber

8

Periodic 3D Array of Square Plates: EM Energy Transport

8.1 Introduction

Few interesting works in nano-optics took the challenge to transport light energy through guiding structures that are considerably smaller in size than the wavelength of light. Recently guiding effects of subwavelength linear chains of silver nanoparticles were characterised by transmission loss as a function of dimensions and spacing [155]. Periodic cylinder arrays as a transmission line were investigated for microwave frequencies half a century ago [156] and similar work in plasmonics were done about a decade ago [157]. Periodic parallel pairs of nanoplates as plasmonic waveguides were found to have better wave guiding properties than a continuous parallel plate waveguide

[158, 159].

In this chapter, an analogous microwave work is demonstrated for a three-dimensional array of periodic parallel square plates as a waveguide. The previous chapter contains the transmission line model analysis for the unit cell.

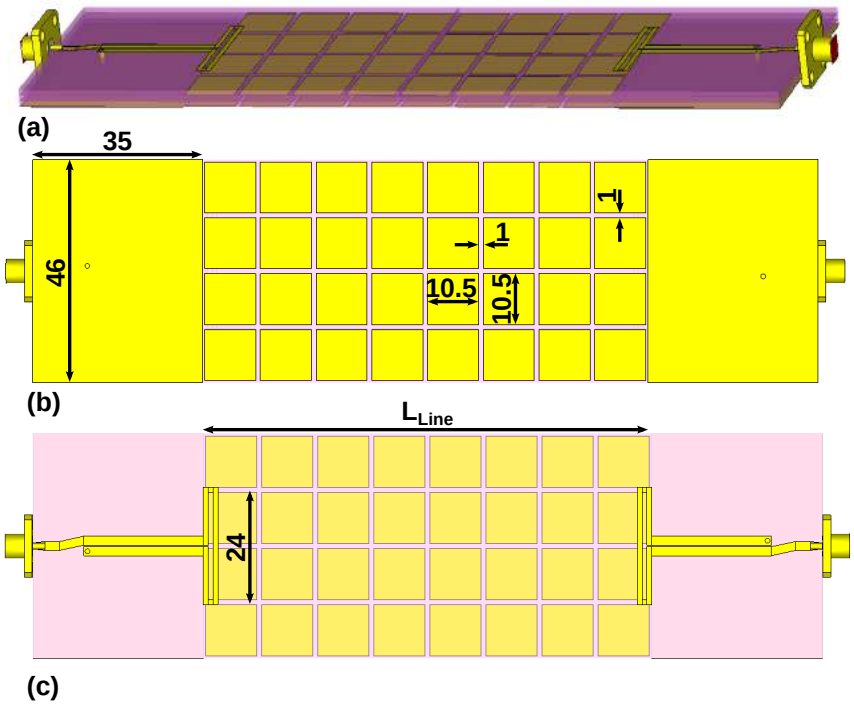

FIGURE 8.1: The layout of the three dimensional periodic parallel square plates. (a) The perspective view of the design made up of 3 TRF43 1.2 mm substrates, (b) the bottom view with relevant dimensions, and (c) the top view with the relevant dimensions.

8.2 Waveguide Geometry

The structure and relevant dimensions of the transmission line including the transmitting and receiving folded dipole are shown in Fig. 8.1. Three different lengths were considered for the proposed structure. The values of L_{Line} used in the FDTD simulation were 92 mm, 184 mm and 276 mm, respectively.

The periodic parallel square plates were realised by microstrip structures on copper clad Taconic TRF43 ($\epsilon = 4.3$, $\tan\delta = 0.0035$) 1.2 mm substrates. The waveguide

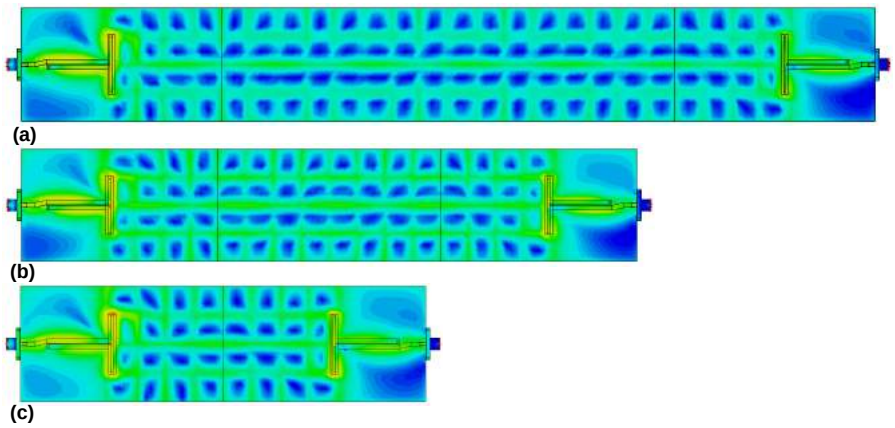

Figure 8.2: Absolute E-Field amplitude at 2.75 GHz along the periodic parallel plate waveguide showing energy transport for different values of L_{Line}. (a) L_{Line} = 276 mm, (b) L_{Line} = 184 mm, and (c) L_{Line} = 92 mm.

itself is made of two 1.2 mm panels with one side of each panel having no copper, and the other side has the periodic square plates, placed back to back together. Thus the waveguide has a height of 2.4 mm. The width of the waveguide is 46 mm. One period of the square plate is 11.5 mm × 11.5 mm with the dimension of the copper plate being 10.5 mm × 10.5 mm. The rest is the spacing between the plates. In terms of square plates, the waveguide is 4 plates × 8 plates (L_{Line} = 92 mm) × 2 plates, 4 plates × 16 plates (L_{Line} = 184 mm) × 2 plates, and 4 plates × 24 plates (L_{Line} = 276 mm) × 2 plates. The transmit and receive the probe, or the folded dipole is placed separately on top of the waveguide, unlike a rectangular waveguide where the probe is placed inside it. This design would result in radiation losses in the microwave spectrum, but the radiation losses occur only at the probe discontinuities and not along the waveguide as leaky waves [157].

8.3 Guiding Effects of Periodic Loaded Transmission Line

A preliminary analysis of a three-dimensional model can always be done using the transmission line analogy. If the dielectric substrate for printed antennas is considered

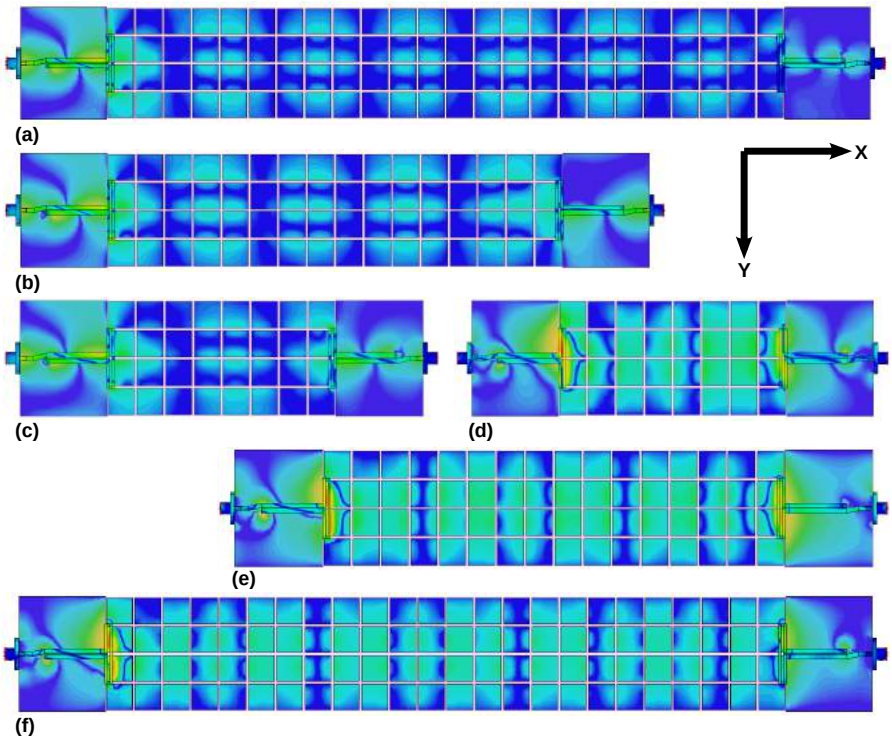

FIGURE 8.3: Surface Current at 2.75 GHz along the periodic parallel plate waveguide showing energy transport for different values of L_{Line} in the X and Y direction. (a) L_{Line} = 276 mm ; X direction, (b) L_{Line} = 184 mm ; X direction, and (c) L_{Line} = 92 mm ; X direction. (d) L_{Line} = 92 mm ; Y direction, (e) L_{Line} = 184 mm ; Y direction, and (f) L_{Line} = 276 mm ; Y direction.

as a transmission line for the radiated fields for any antenna printed on it, then it has a characteristic impedance Z_0 and phase constant $\beta_0 = 2\pi/\lambda_0$. Any further addition of printed structures along the direction of radiation may be considered as reactive components that have been shunted along the transmission line. If such elements are periodically placed then, the layout becomes a periodically loaded transmission line.

Two port voltage and current equations for each unit cell can be represented by

$$\begin{bmatrix} V_{n-1} \\ I_{n-1} \end{bmatrix} = \begin{bmatrix} A & B \\ C & D \end{bmatrix} \begin{bmatrix} V_n \\ I_n \end{bmatrix} \tag{8.1}$$

Floquet-Bloch's theorem states that the condition for sustaining a wave like phenomenon is

$$\begin{bmatrix} V_{n-1} \\ I_{n-1} \end{bmatrix} = e^{-jkp} \begin{bmatrix} V_n \\ I_n \end{bmatrix} \tag{8.2}$$

where p is the periodicity. Comparing Eq. (8.1) and (8.2)

$$\begin{bmatrix} A & B \\ C & D \end{bmatrix} \begin{bmatrix} V_n \\ I_n \end{bmatrix} = e^{-jkp} \begin{bmatrix} V_n \\ I_n \end{bmatrix} \tag{8.3}$$

The eigenvalue equation for the ABCD matrix provides the solution for the phasor e^{-jkp} and is given by

$$e^{-jkp} = \frac{1}{2}(A+D) \pm \left\{ \left[\frac{1}{2}(A+D) \right]^2 - 1 \right\}^{\frac{1}{2}} \tag{8.4}$$

The solution for the eigenvalue equation gives the dispersion relation and propagating Bloch waves sustain when the propagation constant k is real or $|\frac{1}{2}(A+D)| < 1$. When k is imaginary, presence of a forbidden band supersedes with $|\frac{1}{2}(A+D)| \geq 1$.

The parameters for the ABCD matrix given in Eq. (8.1) can be defined for a shunted lossless susceptance jX as

$$\begin{aligned} A &= \left(cos\frac{2\pi p}{\lambda_0} - \frac{Z_0}{2X} sin\frac{2\pi p}{\lambda_0} \right) \\ B &= j\left(sin\frac{2\pi p}{\lambda_0} + \frac{Z_0}{2X} cos\frac{2\pi p}{\lambda_0} - \frac{Z_0}{2X} \right) \\ C &= j\left(sin\frac{2\pi p}{\lambda_0} + \frac{Z_0}{2X} cos\frac{2\pi p}{\lambda_0} + \frac{Z_0}{2X} \right) \\ D &= \left(cos\frac{2\pi p}{\lambda_0} - \frac{Z_0}{2X} sin\frac{2\pi p}{\lambda_0} \right) \end{aligned} \tag{8.5}$$

From Eq. (8.4) and (8.5) the propagation constant can be derived as

$$cos\frac{2\pi p}{\lambda_g} = cos\frac{2\pi p}{\lambda_0} - \frac{Z_0}{2X} sin\frac{2\pi p}{\lambda_0} \tag{8.6}$$

where $k = 2\pi p/\lambda_g$ and λ_g is the guided wavelength.

Assuming no radiation from the shunt reactances, Eq. (8.4) and (8.6) states that the transmission line will guide unattenuated waves when the following condition is met [156, 160]

$$\left| cos\frac{2\pi}{\lambda_0}p + \frac{Z_0}{2X}sin\frac{2\pi}{\lambda_0}p \right| < 1 \tag{8.7}$$

Eq. (8.6) showcases that the guided wavelength is a function of the period p. For layouts where $p/\lambda \ll 1$ Eq. (8.6) can be approximated as

$$\begin{aligned} \left(\frac{2\pi p}{\lambda_g}\right)^2 &= \left(\frac{2\pi p}{\lambda_0}\right)^2 + \frac{Z_0}{2X}\frac{2\pi p}{\lambda_0} \\ \Rightarrow \frac{\lambda_g}{\lambda_0} &= \left[1 + \left(\frac{Z_0}{2\pi X}\right)\frac{\lambda_0}{p}\right]^{-\frac{1}{2}} \\ \Rightarrow \frac{\lambda_g}{\lambda_0} &= \left[1 - \left(\frac{Z_0}{4\pi X}\right)\frac{\lambda_0}{p}\right] \\ \Rightarrow \lambda_g &< \lambda_0 \end{aligned} \tag{8.8}$$

Eq. (8.8) showcases the design criterion for a periodic surface waveguide structure. Irrespective of the material used to create the period, it should be capacitive in nature on the transmitted wave to be guided. In the case of printed layouts, the length of the metal should be greater than $\lambda_{eff}/4$ but less than $\lambda_{eff}/2$ to have a capacitive effect for the travelling surface wave where λ_{eff} is the effective wavelength for the dielectric-air boundary.

8.4 Results

The proposed structure was simulated using CST Microwave Studio 2015 to obtain results for S-parameters, E-field and surface current densities. Fig. 8.2 shows the absolute E-field magnitude along the structure for all the three different lengths of waveguides. Fig. 8.3 shows the surface current density along the X and Y direction of the proposed structure. It can be noted from the figure that there is no significant

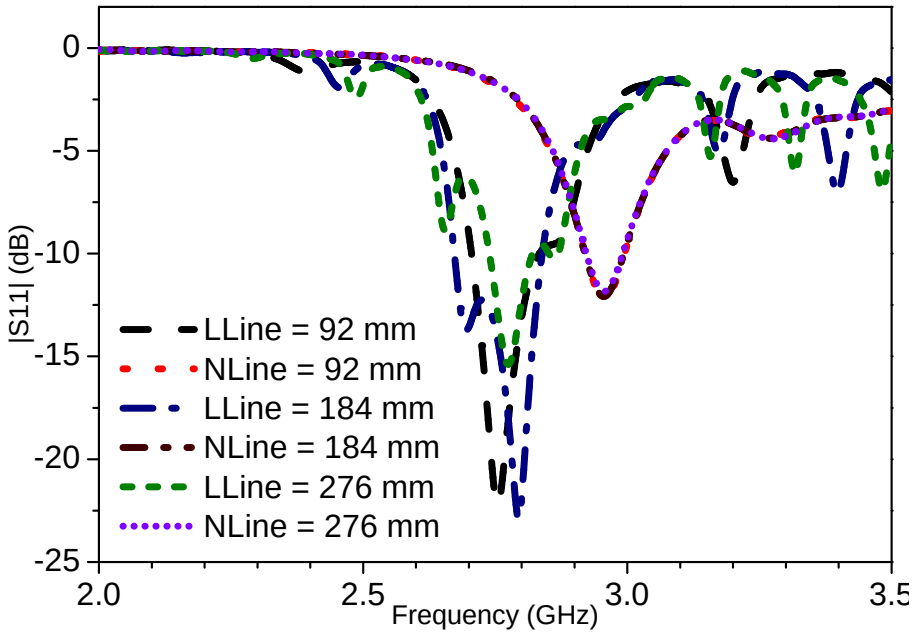

(a) Return Loss

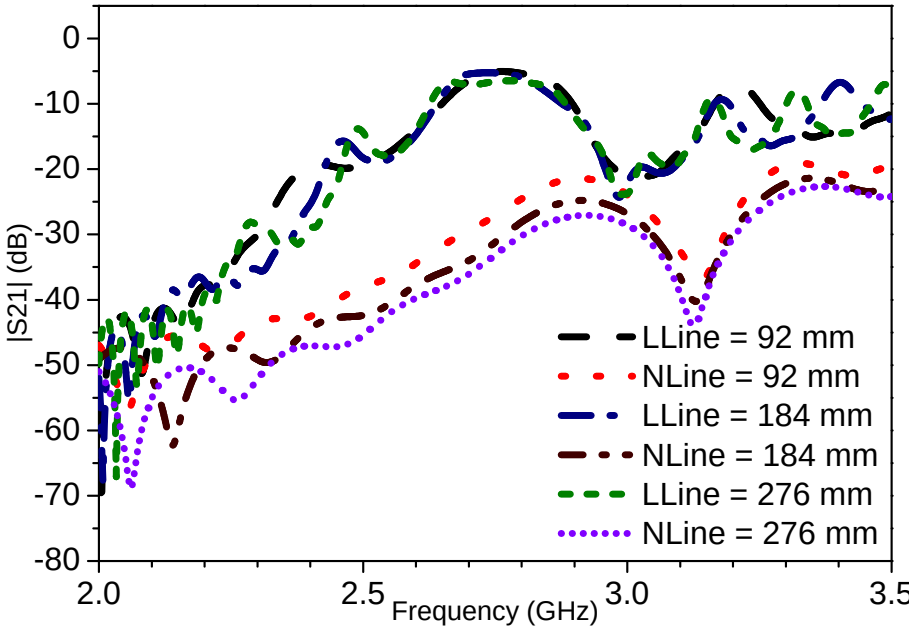

(b) Insertion Loss

Figure 8.4: Predicted return loss and insertions loss with and without the parallel plate waveguide for different values of L_{Line} and N_{Line}. L_{Line} represents length of the waveguide and N_{Line} represents an equivalent length of the substrate without the waveguide.

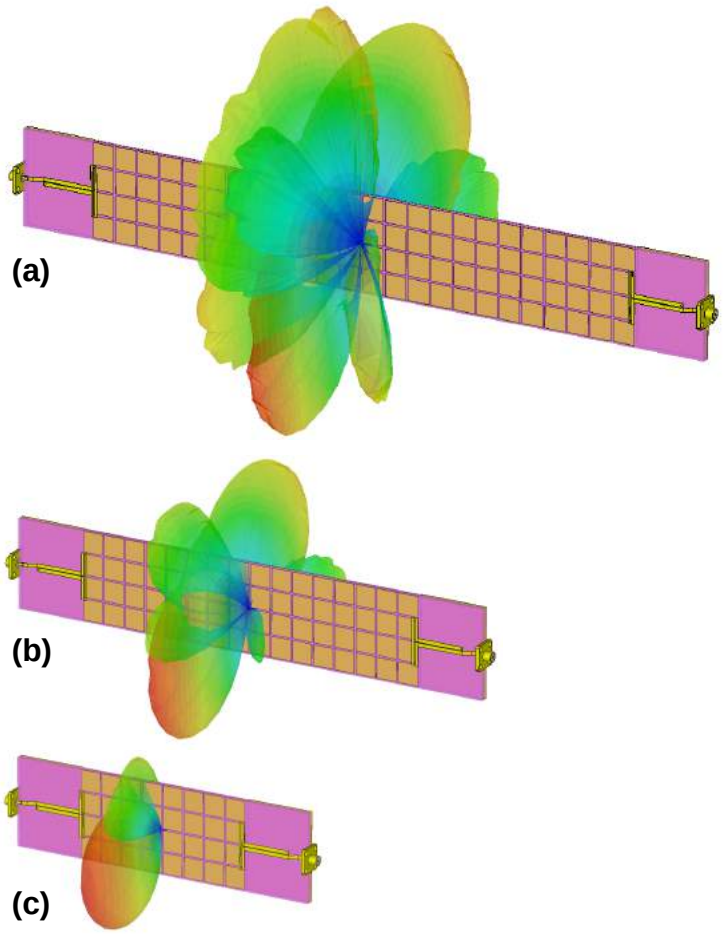

FIGURE 8.5: The farfield pattern of the redundant radiation for (a) L_{Line} = 92 mm, (b) L_{Line} = 184 mm, and (c) L_{Line} = 276 mm.

drop in the surface current density as the wave progresses from one port to another. Both Fig. 8.2 and Fig. 8.3 are obtained from simulated results at 2.75 GHz. This was done as the folded dipole of the feed has an excellent resonance at that frequency.

Fig. 8.4(a) shows the return loss characteristics with and without the proposed waveguide for all the three different lengths. With the waveguide structure, the feeding dipole has an excellent resonance at 2.75 GHz. Without the proposed waveguide structure but the substrate existing, the feeding dipole has a good resonance at 2.95 GHz. The insertion loss (Fig. 8.4(b)) between the ports, with the proposed waveguide, including substrate and radiation loss are -5.1 dB, -5.3 dB and -6.5 dB, respectively, for L_{Line} = 92 mm, 184 mm and 276 mm at 2.75 GHz. The insertion loss between the

Table 8.1: Power losses and output power for the proposed waveguide for various line lengths.

Category	L_{Line}=92 mm	L_{Line}=184 mm	L_{Line}=276 mm
Input Power	100%	100%	100%
Mismatch Loss	0%	4%	6%
Dielectric Loss	10%	10.42%	12.77%
Metal Loss	4%	4.17%	4.26%
Radiation Loss	56%	54.17%	59.57%
Output Power	30%	31.25%	23.4%

ports, without the waveguide except the substrate, are -21.9 dB, -25.1 dB and -27.3 dB, respectively, for the different values of L_{Line}, at 2.95 GHz.

For this experimental structure, the power losses and the output power at the end of the waveguide is tabulated in Table 8.1 for various line lengths. It can be noted from Table 8.1 that the radiation loss is about the same for the different waveguide lengths which are mostly due to the feed which is placed on top of the waveguide and not enclosed by it. In the optical frequencies, it is expected that the radiation loss will be negligible [157].

The redundant far-field radiation patterns for the waveguide structure is shown in Fig. 8.5. For shorter lengths, the number of grating lobes is less. The number of side lobes increases with the increasing waveguide length due to more surface wave propagation. From simulations, the realized gain for the redundant radiations are 3.73 dBi, 2.95 dBi, and 2.48 dBi, respectively, for L_{Line} = 92 mm, 184 mm and 276 mm at 2.75 GHz.

8.5 Conclusion

A unique periodic parallel plate transmission line is proposed in this chapter. The three-dimensional waveguide structure can be used in the microwave frequencies for surface wave propagation and electromagnetic energy transport where the waveguide dimensions much less than the operational wavelength is necessary.

"I do not think you can name many great inventions that have been made by married men."

Nikola Tesla

9

Fixed-Frequency Broadside-Endfire Scanning: A New Antenna

9.1 Introduction

Fixed-frequency beam-steerable antennas are a formidable choice in low power communication equipment like Bluetooth BLE and portable Wi-Fi systems. They are a better choice over commonly available omnidirectional or broadside antennas for accommodating multiple positions and alleviating noise in signals and improving overall signal quality. In array formation, broadside-endfire beam steerable antennas have the

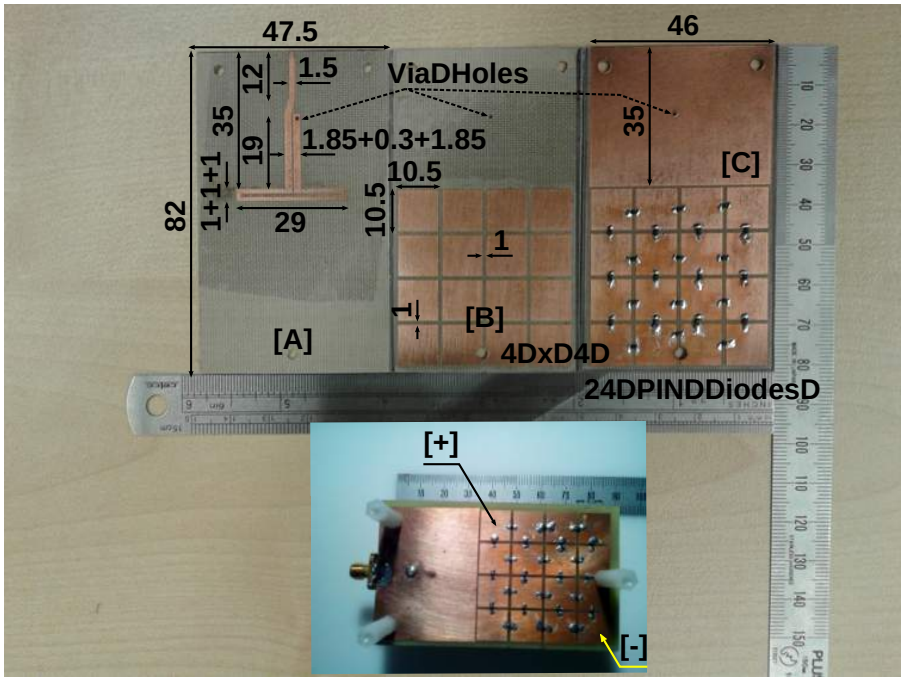

FIGURE 9.1: The manufactured broadside-endfire beam steerable antenna before assembly with all the required dimensions for reproduction. All the PIN diodes are soldered in the third printed board. Inset: Assembled antenna with the via soldered.

benefit of overriding the $cos\,\theta$ gain roll-over limitation past the well known 60° limit.

In the recent past, a few interesting beam-steerable (fixed-frequency) antennas are discussed in the literature. A Yagi-Uda based antenna was proposed in [161] where the length of the reflector and the director are reconfigured (interchanged) using PIN diodes to get endfire radiations in opposite directions. Keeping both the switches on or off resulted in an omnidirectional pattern. A similar work but with a HIS surface below the Yagi-Uda is discussed in [162]. The results from [162] showed two wide beam endfire radiations which can be reconfigured in the same way as [161]. Another similar work but with fixed directors and reconfigurable reflectors are proposed in [163]. The main feed in [163] is a circular patch without a ground-plane. The antenna suggested in [163] has both broadside and backside radiation when both the reflectors are engaged, much similar to [161]. The latest addition to the Yagi-Uda based reconfigurable antennas is explored in [164]. In this antenna, the reflectors and directors are replaced with H-shaped structures. The H-shaped structures in [164] are connected with PIN diodes which when switched on, make up a reflector. They act as directors when disconnected.

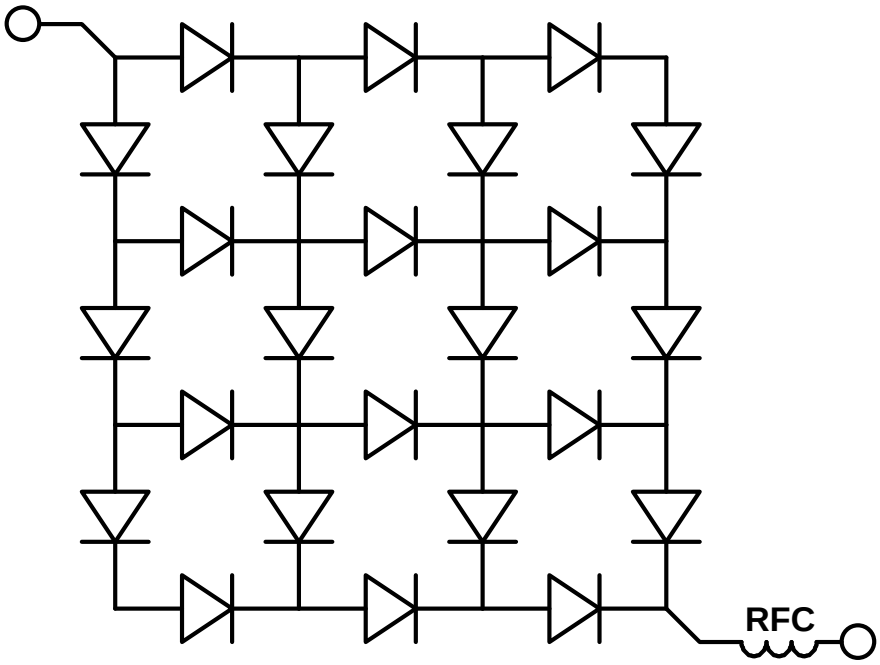

Figure 9.2: Diode connection formation used during soldiering of the twenty four PIN diodes (Infineon BAR64-02V-SC79).

Again, like [161, 163] this antenna radiated more in an omnidirectional pattern when both reflectors are disengaged.

This chapter proposes a new Yagi-Uda inspired antenna with a reconfigurable ground-plane. Multiple PIN diodes are utilised to form a long chain of switches which can either engage a kind of a surface waveguide (discussed in the previous chapter) or engage a high impedance surface (HIS) reflector ground plane (the unit cell was discussed in Chapter 7) and vice-versa. The surface waveguide is similar to the periodic cylinder based waveguide [156] or microstrip equivalent [157] but is made up of periodic square patches similar to a microstrip Yagi antenna [165]. Additionally, it has a parallel dual analogous to the formation discussed in [158]. This parallel dual makes up the ground-plane when the switches are engaged. The ground-plane along with the other group of periodic square patches make up a HIS similar to the one proposed in [152] and results in a broadside radiation. Endfire radiation takes place when the ground-plane is disengaged, and the surface waveguide is engaged.

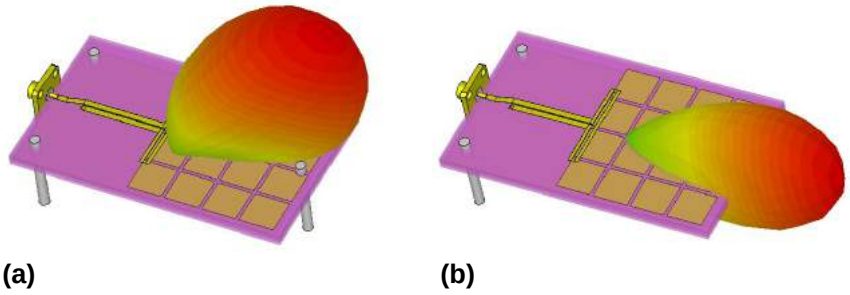

FIGURE 9.3: Simulated radiation pattern obtained from CST Microwave Studio 2015. (a) All PIN diodes are ON - Broadside radiation, and (b) All PIN diodes are OFF - Endfire radiation.

9.2 Design and Implementation

The proposed antenna is designed to be manufactured with three discrete printed substrates assembled using nylon hex screws. The fabricated boards along with all the relevant dimensions are given in Fig. 9.1. The substrate used for the design is Taconic TRF-43 ($\epsilon = 4.3$, $\delta = 0.0035$, thickness=$1.2mm$). The design can also be reproduced on a generic FR4 or Rogers TMM4 with very fundamental design changes. The topmost printed board ([A]) consists of the radiating folded dipole along with a microstrip to edge coupled differential pair strip line (sometimes also known as coplanar stripline) balun. One of the differential lines is directly connected to the microstrip feed, and the other one is shorted to the ground plane of the third printed board using a via. The second board ([B]) consists of the 4×4 array of square microstrip patches. The second board is designed to be the upper section of the parallel plate surface waveguide in endfire mode. In broadside mode, it forms the periodic square patches of the HIS as discussed in [152]. The third printed board ([C]) forms the lower section of the parallel plate surface waveguide in endfire mode and the ground-plane in broadside mode. Twenty-four PIN diodes (Infineon BAR64-02V-SC79) are soldered on the third board using the formation shown in Fig. 9.2. The parallel paths cut down the Ohmic losses of the overall section when the PIN diodes are switched on. There are always six diodes in series, in any path taken between the two external terminals. The minimum voltage required to turn on the network is six times the junction voltage of PIN diodes.

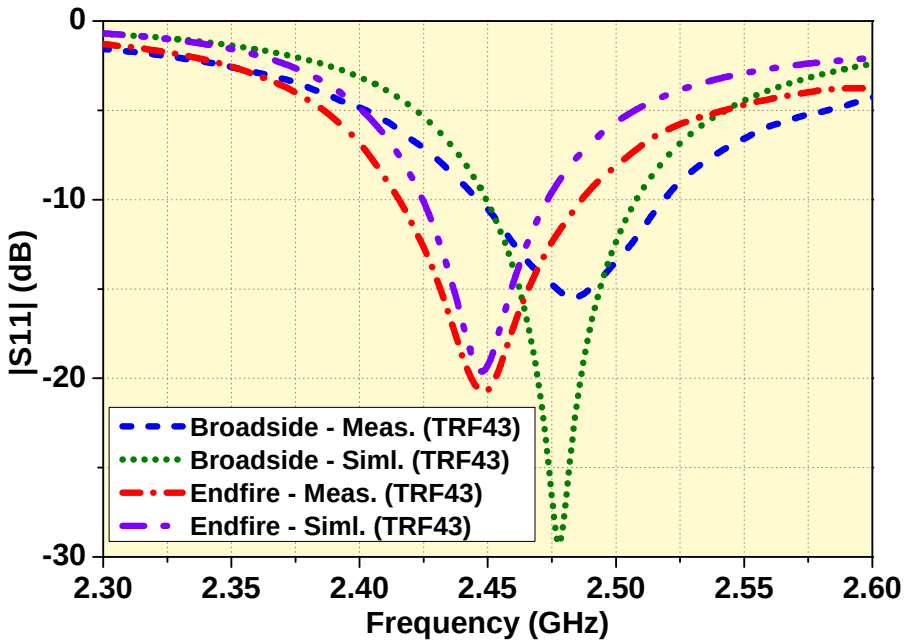

Figure 9.4: Predicted and measured return loss of the proposed beam steerable antenna.

All the three boards are printed on a single side of the substrate using a 3040 portable CNC router with a IsoPro numerical control software. Remaining copper claddings are etched out using a hydrochloric acid - hydrogen peroxide solution.

Assembly of the three boards is done with three M3 nylon hex screws, with the first board containing the folded dipole facing towards the boresight. The second board is placed right below the first one also facing the boresight. The third board is placed facing the opposite way so that the soldered face is opposite to the boresight. In this assembly formation, the substrate height between any two parallel square patches is (1.2 mm + 1.2 mm) 2.4 mm at any place. The folded dipole is 1.2 mm over the top square patched and 3.6 mm over the bottom square patch. A 3.6 mm long 18 SWG wire is placed inside the via hole and soldered on the top and bottom plane. A 4 hole panel type tab terminated SMA connector is soldered to the microstrip line to finish the assembly. Care has to be taken during assembly of the three printed boards to make sure that their alignment and placement is correct and confirming to the design. The square patches of the board [B] should be exactly on top of the reversed board [C] during assembly else the operation of the antenna may be affected.

The feed antenna is completely disjoint to the switching lines and hence does not

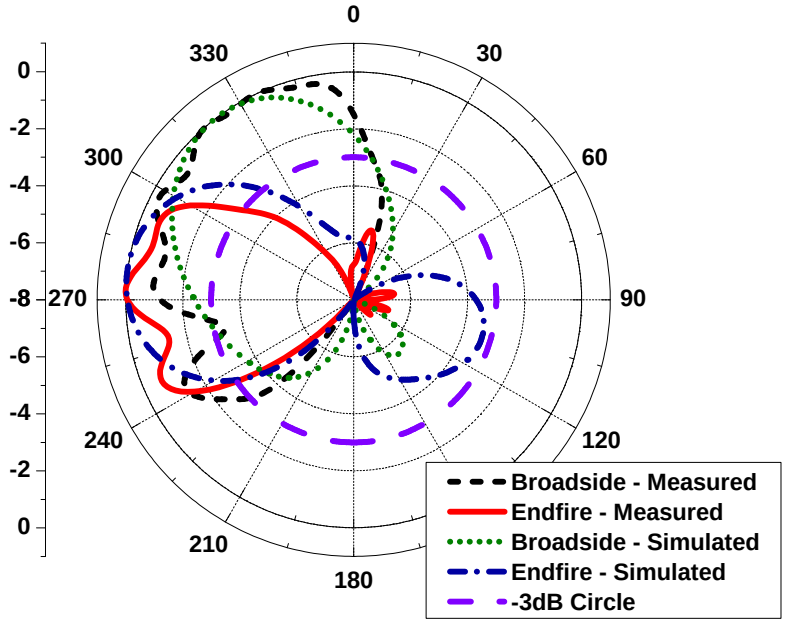

FIGURE 9.5: Normalized farfield patten (H-Plane) of the proposed antenna at 2.45 GHz.

require any Bias-T. The switching network needs only two wires connected to the two diagonal square patches following the diode network (shown in Fig. 9.1 inset), which were probe fitted during measurements with an external RFC coil hand wound out of 18 SWG enamelled copper wire. A 9V battery with a 500Ω resistor connected in series was used as a power source during measurements. A 5V power supply with a 100Ω resistor may also be used if combined with standard hardware solutions.

It is interesting to note here that the surface waveguide is operational even though the waveguide feed is placed on top of it and not in between the parallel plates. It should also be noted that during broadside radiation mode, the effective dielectric constant is enhanced due to the capacitive effects between the square patches [151], but the value shifts during the endfire radiation mode and the balun play an important role to match the folded dipole impedance for both the modes. The balun has been optimised to create a balance between the lengths of the microstrip quarter wave transformer and the coplanar strips along with the length of the ground plane to find a suitable impedance matching between both modes.

9.3 Simulation and Measurements

The design was developed and simulated using CST Microwave Studio 2015. Characterization of the PIN diode was done separately, and obtained values were put into the CST design as a lumped LRC component. A perspective view of the simulated 3D results is shown in Fig. 9.3. Fig. 9.3(a) shows the broadside radiation when the PIN diodes are switched on, and the HIS reflects the radiation of the folded dipole. The endfire radiation is shown in Fig. 9.3(b) with all the diodes switched off.

When the battery is connected, around 10 mA of DC flows through the circuit. The overall voltage drop across the diode network is 4 V. The current can be controlled by changing the resistance connected to the battery but has limited effect on the operation of the antenna as long the switches are on. If the overall voltage drop across the diode network falls below 4 V, the PIN diode network will cease to operate and will fall back in the off mode.

The predicted and measured return loss is shown in Fig. 9.4. The results from simulation and measurement are in good agreement with each other. The combined 2:1 VSWR bandwidth is 110 MHz (between 2.41 GHz and 2.52 GHz) and the overlapping 2:1 VSWR bandwidth is 50 MHz (between 2.44 GHz and 2.49 GHz). The normalised radiation pattern at H-Plane is shown Fig. 9.5. From measurements, the broadside beam has a peak directivity at $-26°$ from the normal with a half power beam width of 107° (from $-99°$ to $+8°$). The peak directivity of the endfire beam is at $-88°$ from the normal with a half power beam width of 74° (from $-125°$ to $-51°$). The combined coverage with both the modes is 133°, with an overlapping sector of 48°. The simulated farfield results are in good agreement with measurements. The measured endfire gain at 2.45 GHz is 5.8 dBi. The total efficiency at 2.45 GHz is 77%. The measured broadside gain at 2.47 GHz is 5.4 dBi with an overall efficiency of 74%.

9.4 Conclusion

A new broadside endfire beam steerable antenna is proposed with a combined coverage of 133° on H-Plane. The proposed antenna is easy to manufacture with three separate printed boards assembled and can be scaled up or down for operation in any other frequency band. Results obtained from measurements are promising, and further research is ongoing about the performance of steering in an array formation, which can help in reduction of the $cos\,\theta$ gain roll-over limitation past 60° for present industrial phased array antennas.

"The man of true genius never lives before his time, he never undertakes impossibilities, and always embarks on his enterprise at the suitable place and period. Though he may catch a glimpse of the coming light as it gilds the mountain top long before it reaches the eyes of his contemporaries, and he may hazard a prediction as to the future, he acts with the present."

Joseph Henry

10

Conclusions and Future Work

10.1 Summary of the Study

This thesis developed the theoretical analysis of a few reconfigurable designs and implemented them into two different fixed frequency beam-steerable antennas. Rectangular microstrip antennas with inset-feed were analysed first, and a corrective transmission-line model proposed in Chapter 3 gave accurate results when compared with measurements. Results from the corrected transmission-line model are 99% accurate. Effect of a thin shorting post, placed arbitrarily at any position of the outer radiating edge of a rectangular microstrip patch antenna has an effect on its resonance frequency. Chapter 4 described the equivalent circuit model and the transmission-line equations for the antenna with any arbitrary shorting post. Results from the transmission-line model are again 99% accurate for all the different test-cases. Forty-two test cases were

applied in Chapter 5 to examine five different reconfigurable antennas. The accuracy is 97% for twenty-six out of forty-two test cases. For the remaining sixteen test cases, the accuracy was less than 97% but not by far in many instances. A few active array antennas were designed using the elements from Chapter 5. Chapter 6 described the design layout and results for three different active array antennas that achieved fixed frequency voltage controlled beam-steering. A maximum of 25° beam shift was possible from the prototypes.

Reconfigurable pseudo meta-surfaces can be modelled using transmission-line theory. Chapter 7 deduced the transmission-line model, and rigorously analysed the model with different substrate heights and covers. The optimised results were in fair agreement with the simulation results. The reconfigurable meta-surface designed in Chapter 7 either reflects or transmits electromagnetic energy. The transmission mode design unit-cell was used to create a surface waveguide. Chapter 8 described a periodically loaded surface waveguide of different lengths and using two microstrip folded dipole antennas used as a transmitter and a receiver. Spurious radiations occurred when the surface waveguide was simulated in free space (without shields), but the transmission efficiency was much better (at least 17 dB better with the dipoles kept at 92 mm apart) by fifty times when compared to the energy transfer without periodic loadings. Finally, in Chapter 9, a new broadside-endfire beam-steering antenna design gave incredible results after measurement. The reconfigurable meta-surface became a reflector for the folded dipole to radiate broadside. In the other mode, it acted as a surface waveguide for the dipole like a Yagi-Uda antenna. Two ways of the new reconfigurable antenna can cover a total beamwidth of 133° in the H-plane.

10.2 Future Scope of Work

Future scope of work exists for all the contributions documented in this thesis. Further improvements in the transmission-line model described in Chapter 3, and Chapter 4 is possible. More investigating into the transmission-line model discussed in Chapter 5 is necessary. It is still unknown why the present transmission-line model succeeds for

only 62% of the forty-two test cases. Derivation of the transmission-line equations for the array antenna developed in Chapter 6 is not complete. Extension of the analytical equation for transmission and reflection coefficients is a future work. Creation of a behavioural modelling software for the antennas discussed in Chapter 3 to Chapter 6 (both including) and its commercialization is also in the future scope.

Further optimisation and generalisation of the transmission-line model of the reconfigurable meta-surface discussed in Chapter 7, are possible. Other forms of input and output port for the surface waveguide, discussed in Chapter 8, is a future work. The $cos\,\theta$ gain roll-over limitation past 60° for present day phased array antennas motivated the development of the fixed frequency beam-steerable antenna discussed in Chapter 9. The future scope of work is an implementation of the newly developed antenna in an array formation and check its performance.

A

MATLAB Codes

The transmission-line model results generated for this thesis were coded into MATLAB. Out of them, few important ones are given here. Two programs from Chapter 3, two programs from Chapter 4, three programs from Chapter 5 and three programs from Chapter 7 are printed here.

MATLAB R2014a (8.3.0.532) was used to run the following codes, but given their simplicity, they are supposed to run in older versions of MATLAB as well. The programs may also run in FreeMAT, SciLab or Octave open source software with little or no modifications.

A.1 Chapter 3

A.1.1 Base Design I

The MATLAB code for 'Base Design I' transmission-line model is given below.

```
%************************************
%******Chapter 3**********************
%******File 1*************************
%*******(c) Budhaditya Majumdar*********
%******2016**************************
%******Base Desgin I******************

%Frequency Sweep 1.5 GHz to 2.0 GHz
f = 1.5e9:0.001e9:2.0e9;
c = 3e8; %speed of light
lambda0 = c ./ f; %wavelength
k0 = (2 * pi) ./ lambda0; %wavenumber
W = 0.070; %width of patch
er = 2.2; %dielectric constant of substrate
h =0.000787; %height of substrate

%effective permittivity (patch element)
eff = (er + 1)/2 + (er - 1)/(2*sqrt(1 + 12*h/W));

W1 = W*sqrt(eff); %free space width of patch
h1 = h;
X = (k0*W1);
W2 = W1;
X1 = (k0*W2);
I1 = -2 + cos(X) + X.*sinint(X) + sinc(X);
I2 = -2 + cos(X1) + X1.*sinint(X1) + sinc(X1);
G1 = I1 ./ (120*pi*pi);
G2 = I2 ./ (120*pi*pi);
B1 = (W1 ./ (120*lambda0)) .* (1 - 0.636.*log(k0*h1));
```

```
30 B2 = (W2 ./ (120*lambda0)) .* (1 - 0.636.*log(k0*h1));
31
32 Lins = 0.011*sqrt(eff); %effective inset length
33 Z0 = 2.75; %line impedance of patch
34 l = 0.0585*sqrt(eff);%effective length of patch
35
36 Y1 = (G1+j.*B1);
37 Z1 = 1./Y1;
38
39 Y2 = (G2+j.*B2);
40 Z2 = 1./Y2;
41
42 num = Z2+j*Z0.*tan(k0.*l);
43 den = Z0+j*Z2.*tan(k0.*l);
44 Zin = Z0*num./den;
45
46 Zin2 = Zin + Z1;
47 alpha = -0;
48
49 %cos^4 impedance reduction
50 Zin2a = Zin2 * (cos ((pi * Lins) / l) - (pi * alpha)/2)^4;
51 Z01 = 82.29; %transformer line impedance
52 W01 = 0.001; %transformer line width
53
54 %effective permittivity (transformer)
55 eff01 = (er + 1)/2 + (er - 1)/(2*sqrt(1 + 12*h/W01));
56 l1 = 0.04388*sqrt(eff01); %effective transformer length including inset
57 num1 = Zin2a+j*Z01.*tan(k0.*l1);
58 den1 = Z01+j*Zin2a.*tan(k0.*l1);
59 Zin3 = Z01*num1./den1;
60
61 Z02 = 51.45; %feed line impedance
62 W02 = 0.00225; %feed line width
63
64 %effective permittivity (feed line)
65 eff02 = (er + 1)/2 + (er - 1)/(2*sqrt(1 + 12*h/W02));
```

```
66 l2 = 0.025*sqrt(eff02); %effective feed length including SMA
67 num2 = Zin3+j*Z02.*tan(k0.*l2);
68 den2 = Z02+j*Zin3.*tan(k0.*l2);
69 Zin4 = Z02*num2./den2;
70
71 Z03 = 50;
72 gamma= z2gamma(Zin4,Z03);
73 rloss = 20*log10(abs(gamma));
74
75 subplot(3,1,1)
76 plot(f,abs(Zin4))
77 subplot(3,1,2)
78 plot(f, angle(Zin4)*180/pi)
79 subplot(3,1,3)
80 plot(f, rloss)
81
82 figure
83 smithchart(gamma)
84
85 dataA = [f; rloss; angle(gamma)*180/pi];
86 dataB = [f; real(gamma); imag(gamma)];
87
88 dlmwrite('RLOSS.txt', dataA, '\t');
89 dlmwrite('RLOSS_R_I.txt', dataB, '\t');
90
91 %*****end of code**********************
```

A.1.2 Base Design II

The MATLAB code for 'Base Design II' transmission-line model is given below.

```
%************************************
%******Chapter 3**********************
%******File 2*************************
%******(c) Budhaditya Majumdar*********
%******2016***************************
%******Base Desgin II*****************

%Frequency Sweep 2.2 GHz to 2.7 GHz
f = 2.2e9:0.001e9:2.7e9;
c = 3e8; %speed of light
lambda0 = c ./ f; %wavelength
k0 = (2 * pi) ./ lambda0; %wavenumber
W = 0.042; %width of patch
er = 4.3; %dielectric constant of substrate
h =0.0012; %height of substrate

%effective permittivity (patch element)
eff = (er + 1)/2 + (er - 1)/(2*sqrt(1 + 12*h/W));

W1 = W*sqrt(eff); %free space width of patch
h1 = h;
X = (k0*W1);
W2 = W1;
X1 = (k0*W2);
I1 = -2 + cos(X) + X.*sinint(X) + sinc(X);
I2 = -2 + cos(X1) + X1.*sinint(X1) + sinc(X1);
G1 = I1 ./ (120*pi*pi);
G2 = I2 ./ (120*pi*pi);
B1 = (W1 ./ (120*lambda0)) .* (1 - 0.636.*log(k0*h1));
B2 = (W2 ./ (120*lambda0)) .* (1 - 0.636.*log(k0*h1));

Lins = 0.007*sqrt(eff); %effective inset length
```

```
33 Z0 = 4.77; %line impedance of patch
34 l = 0.0315*sqrt(eff);%effective length of patch
35
36 Y1 = (G1+j.*B1);
37 Z1 = 1./Y1;
38
39 Y2 = (G2+j.*B2);
40 Z2 = 1./Y2;
41
42 num = Z2+j*Z0.*tan(k0.*l);
43 den = Z0+j*Z2.*tan(k0.*l);
44 Zin = Z0*num./den;
45
46 Zin2 = Zin + Z1;
47 alpha = -0;
48
49 %cos^4 impedance reduction
50 Zin2a = Zin2 * (cos ((pi * Lins) / l) - (pi * alpha)/2)^4;
51 Z01 = 76.55; %transformer line impedance
52 W01 = 0.001; %transformer line width
53
54 %effective permittivity (transformer)
55 eff01 = (er + 1)/2 + (er - 1)/(2*sqrt(1 + 12*h/W01));
56 l1 = 0.0255*sqrt(eff01); %effective transformer length including inset
57 num1 = Zin2a+j*Z01.*tan(k0.*l1);
58 den1 = Z01+j*Zin2a.*tan(k0.*l1);
59 Zin3 = Z01*num1./den1;
60
61 Z02 = 50.99; %feed line impedance
62 W02 = 0.0022; %feed line width
63
64 %effective permittivity (feed line)
65 eff02 = (er + 1)/2 + (er - 1)/(2*sqrt(1 + 12*h/W02));
66 l2 = 0.0225*sqrt(eff02); %effective feed length including SMA
67 num2 = Zin3+j*Z02.*tan(k0.*l2);
68 den2 = Z02+j*Zin3.*tan(k0.*l2);
```

```
69 Zin4 = Z02*num2./den2;
70
71 Z03 = 50;
72 gamma= z2gamma(Zin4,Z03);
73 rloss = 20*log10(abs(gamma));
74
75 subplot(3,1,1)
76 plot(f,abs(Zin4))
77 subplot(3,1,2)
78 plot(f, angle(Zin4)*180/pi)
79 subplot(3,1,3)
80 plot(f, rloss)
81
82 figure
83 smithchart(gamma)
84
85 dataA = [f; rloss; angle(gamma)*180/pi];
86 dataB = [f; real(gamma); imag(gamma)];
87
88 dlmwrite('RLOSS.txt', dataA, '\t');
89 dlmwrite('RLOSS_R_I.txt', dataB, '\t');
90
91 %*****end of code**********************
```

A.2 Chapter 4

A.2.1 Base Design I with a Shorting Post

The MATLAB code for Base Antenna I transmission-line model with a shorting post at the outer vertex of the rectangular microstrip patch is given below.

```
%************************************
%******Chapter 4***********************
%******File 1**************************
%******(c) Budhaditya Majumdar*********
%******2016****************************
%*****Base Desgin I with shorting post*

%Frequency Sweep 1.5 GHz to 2.0 GHz
f = 1.5e9:0.001e9:2.0e9;
c = 3e8; %speed of light
lambda0 = c ./ f; %wavelength
k0 = (2 * pi) ./ lambda0; %wavenumber
W = 0.070; %width of patch
er = 2.2; %dielectric constant of substrate
h =0.000787; %height of substrate

%effective permittivity (patch element)
eff = (er + 1)/2 + (er - 1)/(2*sqrt(1 + 12*h/W));

W1 = W*sqrt(eff); %free space width of patch
h1 = h;
X = (k0*W1);
W2 = W1;
X1 = (k0*W2);
I1 = -2 + cos(X) + X.*sinint(X) + sinc(X);
I2 = -2 + cos(X1) + X1.*sinint(X1) + sinc(X1);
G1 = I1 ./ (120*pi*pi);
G2 = I2 ./ (120*pi*pi);
```

```
29 B1 = (W1 ./ (120*lambda0)) .* (1 - 0.636.*log(k0*h1));
30 B2 = (W2 ./ (120*lambda0)) .* (1 - 0.636.*log(k0*h1));
31
32 Lins = 0.011*sqrt(eff); %effective inset length
33 Z0 = 2.75; %line impedance of patch
34 l = 0.0585*sqrt(eff);%effective length of patch
35
36 Y1 = (G1+j.*B1);
37 Z1 = 1./Y1;
38 L1 = 1.6e-9; %post inductance
39 Psi = 71; %can be any value from 2 to 71 and upto infinity
40 Psi2 = Psi/(Psi-1);
41 YA = j.*(B2/Psi) - (Psi*j)./(2*pi.*f*L1);
42 YB = j.*(B2/Psi2);
43 YC = - (Psi2*j)./(2*pi.*f*L1);
44 YAB = (YA .* YB)/(YA + YB);
45 YABC = YAB + YC;
46 Y2 = G2 + YABC;
47 Z2 = 1./Y2;
48
49 num = Z2+j*Z0.*tan(k0.*l);
50 den = Z0+j*Z2.*tan(k0.*l);
51 Zin = Z0*num./den;
52
53 Zin2 = Zin + Z1;
54 alpha = -0;
55
56 %cos^4 impedance reduction
57 Zin2a = Zin2 * (cos ((pi * Lins) / l) - (pi * alpha)/2)^4;
58 Z01 = 82.29; %transformer line impedance
59 W01 = 0.001; %transformer line width
60
61 %effective permittivity (transformer)
62 eff01 = (er + 1)/2 + (er - 1)/(2*sqrt(1 + 12*h/W01));
63 l1 = 0.04388*sqrt(eff01); %effective transformer length including inset
64 num1 = Zin2a+j*Z01.*tan(k0.*l1);
```

```
65 den1 = Z01+j*Zin2a.*tan(k0.*l1);
66 Zin3 = Z01*num1./den1;
67
68 Z02 = 51.45; %feed line impedance
69 W02 = 0.00225; %feed line width
70
71 %effective permittivity (feed line)
72 eff02 = (er + 1)/2 + (er - 1)/(2*sqrt(1 + 12*h/W02));
73 l2 = 0.025*sqrt(eff02); %effective feed length including SMA
74 num2 = Zin3+j*Z02.*tan(k0.*l2);
75 den2 = Z02+j*Zin3.*tan(k0.*l2);
76 Zin4 = Z02*num2./den2;
77
78 Z03 = 50;
79 gamma= z2gamma(Zin4,Z03);
80 rloss = 20*log10(abs(gamma));
81
82 subplot(3,1,1)
83 plot(f,abs(Zin4))
84 subplot(3,1,2)
85 plot(f, angle(Zin4)*180/pi)
86 subplot(3,1,3)
87 plot(f, rloss)
88
89 figure
90 smithchart(gamma)
91
92 dataA = [f; rloss; angle(gamma)*180/pi];
93 dataB = [f; real(gamma); imag(gamma)];
94
95 dlmwrite('RLOSS.txt', dataA, '\t');
96 dlmwrite('RLOSS_R_I.txt', dataB, '\t');
97
98 %*****end of code*********************
```

A.2.2 Base Design II with a Shorting Post

The MATLAB code for Base Antenna II transmission-line model with a shorting post at the middle of the outer radiating edge of the rectangular microstrip patch is given below.

```
%************************************
%******Chapter 4**********************
%******File 2*************************
%******(c) Budhaditya Majumdar*********
%******2016***************************
%****Base Desgin II with shorting post*

%Frequency Sweep 2.2 GHz to 2.7 GHz
f = 2.2e9:0.001e9:2.7e9;
c = 3e8; %speed of light
lambda0 = c ./ f; %wavelength
k0 = (2 * pi) ./ lambda0; %wavenumber
W = 0.042; %width of patch
er = 4.3; %dielectric constant of substrate
h =0.0012; %height of substrate

%effective permittivity (patch element)
eff = (er + 1)/2 + (er - 1)/(2*sqrt(1 + 12*h/W));

W1 = W*sqrt(eff); %free space width of patch
h1 = h;
X = (k0*W1);
W2 = W1;
X1 = (k0*W2);
I1 = -2 + cos(X) + X.*sinint(X) + sinc(X);
I2 = -2 + cos(X1) + X1.*sinint(X1) + sinc(X1);
G1 = I1 ./ (120*pi*pi);
G2 = I2 ./ (120*pi*pi);
B1 = (W1 ./ (120*lambda0)) .* (1 - 0.636.*log(k0*h1));
```

```
30 B2 = (W2 ./ (120*lambda0)) .* (1 - 0.636.*log(k0*h1));
31
32 Lins = 0.007*sqrt(eff); %effective inset length
33 Z0 = 4.77; %line impedance of patch
34 l = 0.0315*sqrt(eff);%effective length of patch
35
36 Y1 = (G1+j.*B1);
37 Z1 = 1./Y1;
38
39 L1 = 2.0e-9; %post inductance
40 Psi = 2; %can be any value from 2 to 31 and upto infinity
41 Psi2 = Psi/(Psi-1);
42 YA = j.*(B2/Psi) - (Psi*j)./(2*pi.*f*L1);
43 YB = j.*(B2/Psi2);
44 YC = - (Psi2*j)./(2*pi.*f*L1);
45 YAB = (YA .* YB)/(YA + YB);
46 YABC = YAB + YC;
47 Y2 = G2 + YABC;
48 Z2 = 1./Y2;
49
50 num = Z2+j*Z0.*tan(k0.*l);
51 den = Z0+j*Z2.*tan(k0.*l);
52 Zin = Z0*num./den;
53
54 Zin2 = Zin + Z1;
55 alpha = -0;
56
57 %cos^4 impedance reduction
58 Zin2a = Zin2 * (cos ((pi * Lins) / l) - (pi * alpha)/2)^4;
59 Z01 = 76.55; %transformer line impedance
60 W01 = 0.001; %transformer line width
61
62 %effective permittivity (transformer)
63 eff01 = (er + 1)/2 + (er - 1)/(2*sqrt(1 + 12*h/W01));
64 l1 = 0.0255*sqrt(eff01); %effective transformer length including inset
65 num1 = Zin2a+j*Z01.*tan(k0.*l1);
```

```
66 den1 = Z01+j*Zin2a.*tan(k0.*l1);
67 Zin3 = Z01*num1./den1;
68
69 Z02 = 50.99; %feed line impedance
70 W02 = 0.0022; %feed line width
71
72 %effective permittivity (feed line)
73 eff02 = (er + 1)/2 + (er - 1)/(2*sqrt(1 + 12*h/W02));
74 l2 = 0.0225*sqrt(eff02); %effective feed length including SMA
75 num2 = Zin3+j*Z02.*tan(k0.*l2);
76 den2 = Z02+j*Zin3.*tan(k0.*l2);
77 Zin4 = Z02*num2./den2;
78
79 Z03 = 50;
80 gamma= z2gamma(Zin4,Z03);
81 rloss = 20*log10(abs(gamma));
82
83 subplot(3,1,1)
84 plot(f,abs(Zin4))
85 subplot(3,1,2)
86 plot(f, angle(Zin4)*180/pi)
87 subplot(3,1,3)
88 plot(f, rloss)
89
90 figure
91 smithchart(gamma)
92
93 dataA = [f; rloss; angle(gamma)*180/pi];
94 dataB = [f; real(gamma); imag(gamma)];
95
96 dlmwrite('RLOSS.txt', dataA, '\t');
97 dlmwrite('RLOSS_R_I.txt', dataB, '\t');
98
99 %*****end of code*********************
```

A.3 Chapter 5

A.3.1 Antenna I with One Varactor Diode

The MATLAB code for Antenna I transmission-line model with one varactor diode (at a 2V reverse bias) connected between the outer vertex of the rectangular microstrip patch, and the ground plane is given below.

```
%************************************
%******Chapter 5*********************
%******File 1************************
%******(c) Budhaditya Majumdar*********
%******2016**************************
%*****Antenna I with 1 varactor********

%Frequency Sweep 1.5 GHz to 2.0 GHz
f = 1.5e9:0.001e9:2.0e9;
c = 3e8; %speed of light
lambda0 = c ./ f; %wavelength
k0 = (2 * pi) ./ lambda0; %wavenumber
W = 0.070; %width of patch
er = 2.2; %dielectric constant of substrate
h =0.000787; %height of substrate

%effective permittivity (patch element)
eff = (er + 1)/2 + (er - 1)/(2*sqrt(1 + 12*h/W));

W1 = W*sqrt(eff); %free space width of patch
h1 = h;
X = (k0*W1);
W2 = W1;
X1 = (k0*W2);
I1 = -2 + cos(X) + X.*sinint(X) + sinc(X);
I2 = -2 + cos(X1) + X1.*sinint(X1) + sinc(X1);
G1 = I1 ./ (120*pi*pi);
```

```
28 G2 = I2 ./ (120*pi*pi);
29 B1 = (W1 ./ (120*lambda0)) .* (1 - 0.636.*log(k0*h1));
30 B2 = (W2 ./ (120*lambda0)) .* (1 - 0.636.*log(k0*h1));
31
32 Lins = 0.011*sqrt(eff); %effective inset length
33 Z0 = 2.75; %line impedance of patch
34 l = 0.0585*sqrt(eff);%effective length of patch
35
36 Y1 = (G1+j.*B1);
37 Z1 = 1./Y1;
38
39 L1 = 1.6e-9; %post inductance
40 L2 = 0.7e-9; %diode lead
41 C1 = 1.29e-12; %variable capacitance 2V reverse bias
42 C2 = 0.68e-12; %static capacitance
43
44 %modified outer radiating slot admittance
45 GR = (j*2*pi.*f*C1*0.667/(0.667+j*2*pi.*f*C1))+j*2*pi.*f*C2;
46 Y2 = G2 + j.*B2 + GR./(1+j*2*pi.*f*(L1+L2).*GR);
47 Z2 = 1./Y2;
48
49 num = Z2+j*Z0.*tan(k0.*l);
50 den = Z0+j*Z2.*tan(k0.*l);
51 Zin = Z0*num./den;
52
53 Zin2 = Zin + Z1;
54 alpha = -0;
55
56 %cos^4 impedance reduction
57 Zin2a = Zin2 * (cos ((pi * Lins) / l) - (pi * alpha)/2)^4;
58 Z01 = 82.29; %transformer line impedance
59 W01 = 0.001; %transformer line width
60
61 %effective permittivity (transformer)
62 eff01 = (er + 1)/2 + (er - 1)/(2*sqrt(1 + 12*h/W01));
63 l1 = 0.04388*sqrt(eff01); %effective transformer length including inset
```

```
num1 = Zin2a+j*Z01.*tan(k0.*l1);
den1 = Z01+j*Zin2a.*tan(k0.*l1);
Zin3 = Z01*num1./den1;

Z02 = 51.45; %feed line impedance
W02 = 0.00225; %feed line width

%effective permittivity (feed line)
eff02 = (er + 1)/2 + (er - 1)/(2*sqrt(1 + 12*h/W02));
l2 = 0.025*sqrt(eff02); %effective feed length including SMA
num2 = Zin3+j*Z02.*tan(k0.*l2);
den2 = Z02+j*Zin3.*tan(k0.*l2);
Zin4 = Z02*num2./den2;

Z03 = 50;
gamma= z2gamma(Zin4,Z03);
rloss = 20*log10(abs(gamma));

subplot(3,1,1)
plot(f,abs(Zin4))
subplot(3,1,2)
plot(f, angle(Zin4)*180/pi)
subplot(3,1,3)
plot(f, rloss)

figure
smithchart(gamma)

dataA = [f; rloss; angle(gamma)*180/pi];
dataB = [f; real(gamma); imag(gamma)];

dlmwrite('RLOSS.txt', dataA, '\t');
dlmwrite('RLOSS_R_I.txt', dataB, '\t');

%*****end of code*********************
```

A.3.2 Antenna II with One Varactor Diode

The MATLAB code for Antenna I transmission-line model with one varactor diode (at a 8V reverse bias) connected between the outer vertex of the rectangular microstrip patch, and the ground plane is given below.

```
%************************************
%******Chapter 5**********************
%******File 2*************************
%******(c) Budhaditya Majumdar*********
%******2016***************************
%****Antenna II with 1 varactor********

%Frequency Sweep 2.0 GHz to 2.5 GHz
f = 2.0e9:0.001e9:2.5e9;
c = 3e8; %speed of light
lambda0 = c ./ f; %wavelength
k0 = (2 * pi) ./ lambda0; %wavenumber
W = 0.042; %width of patch
er = 4.3; %dielectric constant of substrate
h =0.0012; %height of substrate

%effective permittivity (patch element)
eff = (er + 1)/2 + (er - 1)/(2*sqrt(1 + 12*h/W));

W1 = W*sqrt(eff); %free space width of patch
h1 = h;
X = (k0*W1);
W2 = W1;
X1 = (k0*W2);
I1 = -2 + cos(X) + X.*sinint(X) + sinc(X);
I2 = -2 + cos(X1) + X1.*sinint(X1) + sinc(X1);
G1 = I1 ./ (120*pi*pi);
G2 = I2 ./ (120*pi*pi);
B1 = (W1 ./ (120*lambda0)) .* (1 - 0.636.*log(k0*h1));
```

```
30 B2 = (W2 ./ (120*lambda0)) .* (1 - 0.636.*log(k0*h1));
31
32 Lins = 0.007*sqrt(eff); %effective inset length
33 Z0 = 4.77; %line impedance of patch
34 l = 0.0315*sqrt(eff);%effective length of patch
35
36 Y1 = (G1+j.*B1);
37 Z1 = 1./Y1;
38
39 L1 = 2.0e-9; %post inductance
40 L2 = 0.75e-9; %diode lead
41 C1 = 0.13e-12; %variable capacitance 8V reverse bias
42 C2 = 0.68e-12; %static capacitance
43
44 %modified outer radiating slot admittance
45 GR = (j*2*pi.*f*C1*0.667/(0.667+j*2*pi.*f*C1))+j*2*pi.*f*C2;
46 Y2 = G2 + j.*B2 + GR./(1+j*2*pi.*f*(L1+L2).*GR);
47 Z2 = 1./Y2;
48
49 num = Z2+j*Z0.*tan(k0.*l);
50 den = Z0+j*Z2.*tan(k0.*l);
51 Zin = Z0*num./den;
52
53 Zin2 = Zin + Z1;
54 alpha = -0;
55
56 %cos^4 impedance reduction
57 Zin2a = Zin2 * (cos ((pi * Lins) / l) - (pi * alpha)/2)^4;
58 Z01 = 76.55; %transformer line impedance
59 W01 = 0.001; %transformer line width
60
61 %effective permittivity (transformer)
62 eff01 = (er + 1)/2 + (er - 1)/(2*sqrt(1 + 12*h/W01));
63 l1 = 0.0255*sqrt(eff01); %effective transformer length including inset
64 num1 = Zin2a+j*Z01.*tan(k0.*l1);
65 den1 = Z01+j*Zin2a.*tan(k0.*l1);
```

```
66 Zin3 = Z01*num1./den1;
67
68 Z02 = 50.99; %feed line impedance
69 W02 = 0.0022; %feed line width
70
71 %effective permittivity (feed line)
72 eff02 = (er + 1)/2 + (er - 1)/(2*sqrt(1 + 12*h/W02));
73 l2 = 0.0225*sqrt(eff02); %effective feed length including SMA
74 num2 = Zin3+j*Z02.*tan(k0.*l2);
75 den2 = Z02+j*Zin3.*tan(k0.*l2);
76 Zin4 = Z02*num2./den2;
77
78 Z03 = 50;
79 gamma= z2gamma(Zin4,Z03);
80 rloss = 20*log10(abs(gamma));
81
82 subplot(3,1,1)
83 plot(f,abs(Zin4))
84 subplot(3,1,2)
85 plot(f, angle(Zin4)*180/pi)
86 subplot(3,1,3)
87 plot(f, rloss)
88
89 figure
90 smithchart(gamma)
91
92 dataA = [f; rloss; angle(gamma)*180/pi];
93 dataB = [f; real(gamma); imag(gamma)];
94
95 dlmwrite('RLOSS.txt', dataA, '\t');
96 dlmwrite('RLOSS_R_I.txt', dataB, '\t');
97
98 %*****end of code*********************
```

A.3.3 PIN Loaded Antenna

The MATLAB code for Antenna I transmission-line model with 4 PIN diodes (ON mode) connected between the outer vertex of the rectangular microstrip patch, and the ground plane is given below.

```
%************************************
%******Chapter 5**********************
%******File 3*************************
%*******(c) Budhaditya Majumdar*********
%******2016**************************
%*****Antenna I with 4 PIN diodes******

%Frequency Sweep 1.5 GHz to 2.0 GHz
f = 1.5e9:0.001e9:2.0e9;
c = 3e8; %speed of light
lambda0 = c ./ f; %wavelength
k0 = (2 * pi) ./ lambda0; %wavenumber
W = 0.070; %width of patch
er = 2.2; %dielectric constant of substrate
h =0.000787; %height of substrate

%effective permittivity (patch element)
eff = (er + 1)/2 + (er - 1)/(2*sqrt(1 + 12*h/W));

W1 = W*sqrt(eff); %free space width of patch
h1 = h;
X = (k0*W1);
W2 = W1;
X1 = (k0*W2);
I1 = -2 + cos(X) + X.*sinint(X) + sinc(X);
I2 = -2 + cos(X1) + X1.*sinint(X1) + sinc(X1);
G1 = I1 ./ (120*pi*pi);
G2 = I2 ./ (120*pi*pi);
B1 = (W1 ./ (120*lambda0)) .* (1 - 0.636.*log(k0*h1));
```

```
30 B2 = (W2 ./ (120*lambda0)) .* (1 - 0.636.*log(k0*h1));
31
32 Lins = 0.011*sqrt(eff); %effective inset length
33 Z0 = 2.75; %line impedance of patch
34 l = 0.0585*sqrt(eff);%effective length of patch
35
36 Y1 = (G1+j.*B1);
37 Z1 = 1./Y1;
38
39 L1 = 1.6e-9; %post inductance
40 L2 = 0.175e-9; %4 diode leads
41 C1 = 0.68e-12; %PIN diode capacitance (4 diodes)
42
43 %modified outer radiating slot admittance
44 GR = 1.6 + j*2*pi.*f*C1; %ON mode
45 %GR = 0.0013 + j*2*pi.*f*C1; %OFF mode
46 Y2 = G2 + j.*B2 + GR./(1+j*2*pi.*f*(L1+L2).*GR);
47 Z2 = 1./Y2;
48
49 num = Z2+j*Z0.*tan(k0.*l);
50 den = Z0+j*Z2.*tan(k0.*l);
51 Zin = Z0*num./den;
52
53 Zin2 = Zin + Z1;
54 alpha = -0;
55
56 %cos^4 impedance reduction
57 Zin2a = Zin2 * (cos ((pi * Lins) / l) - (pi * alpha)/2)^4;
58 Z01 = 82.29; %transformer line impedance
59 W01 = 0.001; %transformer line width
60
61 %effective permittivity (transformer)
62 eff01 = (er + 1)/2 + (er - 1)/(2*sqrt(1 + 12*h/W01));
63 l1 = 0.04388*sqrt(eff01); %effective transformer length including inset
64 num1 = Zin2a+j*Z01.*tan(k0.*l1);
65 den1 = Z01+j*Zin2a.*tan(k0.*l1);
```

```
66 Zin3 = Z01*num1./den1;
67
68 Z02 = 51.45; %feed line impedance
69 W02 = 0.00225; %feed line width
70
71 %effective permittivity (feed line)
72 eff02 = (er + 1)/2 + (er - 1)/(2*sqrt(1 + 12*h/W02));
73 l2 = 0.025*sqrt(eff02); %effective feed length including SMA
74 num2 = Zin3+j*Z02.*tan(k0.*l2);
75 den2 = Z02+j*Zin3.*tan(k0.*l2);
76 Zin4 = Z02*num2./den2;
77
78 Z03 = 50;
79 gamma= z2gamma(Zin4,Z03);
80 rloss = 20*log10(abs(gamma));
81
82 subplot(3,1,1)
83 plot(f,abs(Zin4))
84 subplot(3,1,2)
85 plot(f, angle(Zin4)*180/pi)
86 subplot(3,1,3)
87 plot(f, rloss)
88
89 figure
90 smithchart(gamma)
91
92 dataA = [f; rloss; angle(gamma)*180/pi];
93 dataB = [f; real(gamma); imag(gamma)];
94
95 dlmwrite('RLOSS.txt', dataA, '\t');
96 dlmwrite('RLOSS_R_I.txt', dataB, '\t');
97
98 %*****end of code*********************
```

A.4 Chapter 7

Numerous MATLAB codes were used in Chapter 7, but only three major codes used to generate the phase plot of the reconfigurable unit-cell are given below for comparison. All other codes are variants of these.

A.4.1 Parallel Grid Surface with First Grin in Dielectric

The MATLAB code for the parallel grid surface with the first grid embedded in dielectric material (Fig. 7.11).

```
%************************************
%******Chapter 7***********************
%******File 1**************************
%******(c) Budhaditya Majumdar*********
%******2016****************************
%***Parallel Grid (1 in diel). h=5mm***
%********Fig. 7.11**********************

%Frequency Sweep 1 GHz to 10 GHz
f= 1e9:0.1e9:10e9;
w= 2*pi*f; %Omega - Angular velocity
u0=4*pi*10^-7; %permeability of free space
e0 =  8.854187817*10^-12; %permittivity of free space
h= 5e-3; %distance between grid and PEC (also 2.4 is used)
h2 = 1.2e-3; %cover height
z0 =(377 + j*0); %impedance of free space
c= 3e8; %speed of light
lambda0 = c./f; %free space wavelength
er= 4.3; %dielectric constant
eff = (er + 1)/2; %approx. effective dielectric constant
k0 = (2*pi)./lambda0; %free space wave number
keff= k0*(sqrt(eff)); %effective eave number
k= k0*(sqrt(er)); %effective wave number
zr = z0 / sqrt(er); %free space impedance inside dielectric
```

```
25 lambdar = lambda0./sqrt(er); %wavelength inside dielectric
26
27 d = 11.5e-3; %unit cell width
28 wd = 1e-3; %gap width
29
30 %Zdiel as given in equation
31 zdiel1 = 1./(j*w*e0*h2*(er-1));
32 zdiel2 = 1./(j*w*e0*h*(er-1));
33
34 %Equation 7.2
35 %a1 = ((k*d)/pi)*log((2*d)/(pi*wd));
36 %a2 = ((k0*d)/pi)*log((2*d)/(pi*wd));
37
38 %Equation 7.16
39 a1 = (2*log(csc((pi*wd)/(2*d)))./(lambdar./d - d./lambdar);
40 a2 = (2*log(csc((pi*wd)/(2*d)))./(lambda0./d - d./lambda0);
41
42 %Zgrid
43 zgrid1 = -(j*zr)./(2*a1);
44 zgrid2 = -(j*z0*2)./(2*a2*(er+1));
45
46 %Zgap
47 zTL = j*zr.*sin(k*h);
48 zTL2 = j*zr.*sin(k*h2);
49
50 % Zgrid2 || Z0
51 zf1 = (z0.*zgrid2)./(z0+zgrid2);
52
53 % Zdiel2 || Zgrid2 || Z0
54 zf1a = (zdiel2.*zf1)./(zdiel2+zf1);
55
56 %Zgap2 + Zdiel2 || Zgrid2 || Z0
57 zf2 = zTL + zf1a;
58
59 %Zgrid1 || [Zgap2 + Zdiel2 || Zgrid2 || Z0]
60 zfinal = (zgrid1.*zf2)./(zgrid1+zf2);
```

```
61
62 % Zdiel1 || Zgrid1 || [Zgap2 + Zdiel2 || Zgrid2 || Z0]
63 zfinal1 = (zdiel1.*zfinal)./(zdiel1+zfinal)
64
65 % Zgap1 + Zdiel1 || Zgrid1 || [Zgap2 + Zdiel2 || Zgrid2 || Z0] Eq. 7.21
66 zfinal2 = zTL2 + zfinal1;
67
68 gamma= z2gamma(zfinal2,z0);
69 gang= (180/pi)*angle(gamma);
70
71 rloss = 20*log10(abs(gamma))
72
73 plot(f,gang)
74 A = [f;gang]
75
76 figure
77 smithchart(gamma)
78
79
80 dlmwrite('Phase.txt', A, '\t');
81
82 %*******end of code********************
```

A.4.2 PEC Backed Dielectric Embedded Grid

The MATLAB code for the PEC backed patch loaded dielectric surface with grid embedded in the dielectric material (Fig. 7.23).

```
%************************************
%******Chapter 7**********************
%******File 2*************************
%******(c) Budhaditya Majumdar*********
%******2016***************************
%*****PEC Backed Grid in Diel. h=5mm***
%********Fig. 7.23**********************

%Frequency Sweep 1 GHz to 10 GHz
f= 1e9:0.1e9:10e9;
w= 2*pi*f; %Omega - Angular velocity
u0=4*pi*10^-7; %permeability of free space
e0 =  8.854187817*10^-12; %permittivity of free space
h= 5e-3; %distance between grid and PEC (also 2.4 is used)
h2 = 1.2e-3; %cover height
z0 =(377 + j*0); %impedance of free space
c= 3e8; %speed of light
lambda0 = c./f; %free space wavelength
er= 4.3; %dielectric constant
eff = (er + 1)/2; %approx. effective dielectric constant
k0 = (2*pi)./lambda0; %free space wave number
keff= k0*(sqrt(eff)); %effective eave number
k= k0*(sqrt(er)); %effective wave number
zr = z0 / sqrt(er); %free space impedance inside dielectric
lambdar = lambda0./sqrt(er); %wavelength inside dielectric

%Zdiel as given in equation
zdiel1 = 1./(j*w*e0*h2*(er-1));

d = 11.5e-3; %unit cell width
```

```
wd = 1e-3; %gap width

%Equation 7.2
%a1 = ((k*d)/pi)*log((2*d)/(pi*wd));

%Equation 7.16
a1 = (2*log(csc((pi*wd)/(2*d))))./(lambdar./d - d./lambdar);

%Zgrid
zgrid1 = -(j*zr)./(2*a1);

%Zsubstrate
zTL = j*zr.*tan(k*h);

%Zgap
zTL2 = j*zr*sin(k*h2);

% Zgrid || Zsubstrate
zf1 = (zTL.*zgrid1)./(zTL+zgrid1);

% Zdiel || Zgrid || Zsubstrate
zf2 = (zdiel1.*zf1)./(zdiel1+zf1);

% Zgap + [Zdiel || Zgrid || Zsubstrate] Eq. 7.25
zfinal = zTL2 + zf2;

gamma= z2gamma(zfinal,z0);
gang= (180/pi)*angle(gamma);

rloss = 20*log10(abs(gamma))

plot(f,gang)
A = [f;gang]

figure
smithchart(gamma)
```

```
67
68 dlmwrite('Phase.txt', A, '\t');
69
70 %********end of code*********************
```

A.4.3 Reconfigurable Unit-Cell

The MATLAB code for the switchable rear-grid backed patch loaded dielectric surface with the front grid embedded in the dielectric material (Fig. 7.32).

```
%************************************
%******Chapter 7*********************
%******File 3************************
%******(c) Budhaditya Majumdar*********
%******2016*****************************
%*****Reconfigurable Unit Cell h=5mm***
%********Fig. 7.32*********************

%Frequency Sweep 1 GHz to 10 GHz
f= 1e9:0.1e9:10e9;
w= 2*pi*f; %Omega - Angular velocity
u0=4*pi*10^-7; %permeability of free space
e0 =  8.854187817*10^-12; %permittivity of free space
h= 5e-3; %distance between grids (also 2.4 is used)
h2 = 1.2e-3; %cover height
z0 =(377 + j*0); %impedance of free space
c= 3e8; %speed of light
lambda0 = c./f; %free space wavelength
er= 4.3; %dielectric constant
eff = (er + 1)/2; %approx. effective dielectric constant
k0 = (2*pi)./lambda0; %free space wave number
keff= k0*(sqrt(eff)); %effective eave number
k= k0*(sqrt(er)); %effective wave number
zr = z0 / sqrt(er); %free space impedance inside dielectric
lambdar = lambda0./sqrt(er); %wavelength inside dielectric

%Zdiel as given in equations
zdiel2 = 1./(j*w*e0*h*(er-1));
zdiel1 = 1./(j*w*e0*h2*(er-1));

```

```
31 LH = 0.635225*10^-9; %switch inductance
32 d = 11.5e-3; %unit cell width
33 wd = 1e-3; %gap width
34 zL = (0 + j*2*pi.*f*LH); %switch impedance Zswitch
35
36 %Equation 7.2
37 a2 = ((k0*d)/pi)*log((2*d)/(pi*wd));
38 a1 = ((k*d)/pi)*log((2*d)/(pi*wd));
39
40 %Equation 7.16
41 %a2 = (2*log(csc((pi*wd)/(2*d)))./(lambda0./d - d./lambda0);
42 %a1 = (2*log(csc((pi*wd)/(2*d)))./(lambdar./d - d./lambdar);
43
44 %Zgrid
45 zgrid2 = -(j*z0*2)./(2*a2*(er+1));
46 zgrid1 = -(j*zr)./(2*a1);
47
48 %Zgap
49 zTL = j*zr.*sin(k*h);
50 zTL2 = j*zr*sin(k*h2);
51
52 %Zgrid2 || Zwitch
53 zgrid2a = (zgrid2.*zL)./(zgrid2+zL);
54
55 %Z0 || Zgrid2 || Zswitch
56 zf1 = (z0.*zgrid2a)./(z0+zgrid2a);
57
58 % Zgap2 + Z0 || Zgrid2 || Zswitch
59 zf2 = zTL + zf1;
60
61 % Optimization - Zdiel1 || Zgrid1 Eq. 7.29
62 %zgrid1a = (zdiel1.*zgrid1)./(zdiel1+zgrid1);
63
64 % Zgrid1 || [Zgap2 + Z0 || Zgrid2 || Zswitch]
65 zf3 = (zgrid1.*zf2)./(zgrid1+zf2);
66
```

```
% Optimization – Zdiel1 || Zgrid1 || [Zgap2 + Z0 || Zgrid2 || ...
    Zswitch] Eq. 7.29
%zf3 = (zgrid1a.*zf2)./(zgrid1a+zf2);

% Zgap1 + Zgrid1 || [Zgap2 + Z0 || Zgrid2 || Zswitch] Eq. 7.28
zf4 = zTL2 + zf3;

%Overall Impedance
zfinal = zf4;

gamma= z2gamma(zfinal,z0);
gang= (180/pi)*angle(gamma);

rloss = 20*log10(abs(gamma));

plot(f,gang)
A = [f;gang]

figure
smithchart(gamma)

dlmwrite('Phase.txt', A, '\t');

%*******end of code********************
```

References

[1] C. Peixeiro. *Microstrip patch antennas: An historical perspective of the development.* In *Microwave & Optoelectronics Conference (IMOC), 2011 SBMO/IEEE MTT-S International*, pp. 684–688. 3

[2] E. Antonino-Daviu, M. Cabedo-Fabres, M. Ferrando-Bataller, and A. Vila-Jimenez. *Active uwb antenna with tunable band-notched behaviour.* Electronics Letters **43**(18), 959 (2007). 8

[3] N. Behdad and K. Sarabandi. *A varactor-tuned dual-band slot antenna.* IEEE Transactions on Antennas and Propagation **54**(2), 401 (2006).

[4] W. S. Jeong, S. Y. Lee, W. G. Lim, H. Lim, and J. W. Yu. *Tunable band-notched ultra wideband (uwb) planar monopole antennas using varactor.* In *Microwave Conference, 2008. EuMC 2008. 38th European*, pp. 266–268.

[5] H. Jiang, M. Patterson, C. Zhang, and G. Subramanyam. *Frequency tunable microstrip patch antenna using ferroelectric thin film varactor.* In *Proceedings of the IEEE 2009 National Aerospace & Electronics Conference (NAECON)*, pp. 248–250.

[6] S. S. Oh, Y. B. Jung, Y. R. Ju, and H. D. Park. *Frequency-tunable open-ring microstrip antenna using varactor.* In *Electromagnetics in Advanced Applications (ICEAA), 2010 International Conference on*, pp. 624–626.

[7] C. R. White and G. M. Rebeiz. *Single- and dual-polarized tunable slot-ring antennas.* IEEE Transactions on Antennas and Propagation **57**(1), 19 (2009). 8

[8] R. H. Chen and J. S. Row. *Single-fed microstrip patch antenna with switchable polarization.* IEEE Transactions on Antennas and Propagation **56**(4), 922 (2008). 8

[9] S. H. Chen, J. S. Row, and K. L. Wong. *Reconfigurable square-ring patch antenna with pattern diversity.* IEEE Transactions on Antennas and Propagation **55**(2), 472 (2007).

[10] M. K. Fries, M. Grani, and R. Vahldieck. *A reconfigurable slot antenna with switchable polarization.* IEEE Microwave and Wireless Components Letters **13**(11), 490 (2003).

[11] N. Jin, Y. Fan, and Y. Rahmat-Samii. *A novel patch antenna with switchable slot (pass): dual-frequency operation with reversed circular polarizations.* IEEE Transactions on Antennas and Propagation **54**(3), 1031 (2006).

[12] B. Kim, B. Pan, S. Nikolaou, Y. S. Kim, J. Papapolymerou, and M. M. Tentzeris. *A novel single-feed circular microstrip antenna with reconfigurable polarization capability.* IEEE Transactions on Antennas and Propagation **56**(3), 630 (2008).

[13] D. Peroulis, K. Sarabandi, and L. P. B. Katehi. *Design of reconfigurable slot antennas.* IEEE Transactions on Antennas and Propagation **53**(2), 645 (2005).

[14] J. Perruisseau-Carrier, P. Pardo-Carrera, and P. Miskovsky. *Modeling, design and characterization of a very wideband slot antenna with reconfigurable band rejection.* IEEE Transactions on Antennas and Propagation **58**(7), 2218 (2010).

[15] P. Y. Qin, A. R. Weily, Y. J. Guo, T. S. Bird, and C. H. Liang. *Frequency reconfigurable quasi-yagi folded dipole antenna.* IEEE Transactions on Antennas and Propagation **58**(8), 2742 (2010).

[16] J. Sarrazin, Y. Mahe, S. Avrillon, and S. Toutain. *Pattern reconfigurable cubic antenna*. IEEE Transactions on Antennas and Propagation **57**(2), 310 (2009).

[17] S. Shelley, J. Costantine, C. G. Christodoulou, D. E. Anagnostou, and J. C. Lyke. *Fpga-controlled switch-reconfigured antenna*. IEEE Antennas and Wireless Propagation Letters **9**, 355 (2010).

[18] N. Symeon, R. Bairavasubramanian, C. Lugo, I. Carrasquillo, D. C. Thompson, G. E. Ponchak, J. Papapolymerou, and M. M. Tentzeris. *Pattern and frequency reconfigurable annular slot antenna using pin diodes*. IEEE Transactions on Antennas and Propagation **54**(2), 439 (2006).

[19] S. J. Wu and T. G. Ma. *A wideband slotted bow-tie antenna with reconfigurable cpw-to-slotline transition for pattern diversity*. IEEE Transactions on Antennas and Propagation **56**(2), 327 (2008). 8

[20] B. A. Cetiner, G. R. Crusats, L. Jofre, and N. Biyikli. *Rf mems integrated frequency reconfigurable annular slot antenna*. IEEE Transactions on Antennas and Propagation **58**(3), 626 (2010). 8

[21] J. Chang won, L. Ming-jer, G. P. Li, and F. D. Flaviis. *Reconfigurable scan-beam single-arm spiral antenna integrated with rf-mems switches*. IEEE Transactions on Antennas and Propagation **54**(2), 455 (2006).

[22] E. Erdil, K. Topalli, M. Unlu, O. A. Civi, and T. Akin. *Frequency tunable microstrip patch antenna using rf mems technology*. IEEE Transactions on Antennas and Propagation **55**(4), 1193 (2007).

[23] A. Grau, J. Romeu, M. J. Lee, S. Blanch, L. Jofre, and F. D. Flaviis. *A dual-linearly-polarized mems-reconfigurable antenna for narrowband mimo communication systems*. IEEE Transactions on Antennas and Propagation **58**(1), 4 (2010).

[24] G. H. Huff and J. T. Bernhard. *Integration of packaged rf mems switches with*

radiation pattern reconfigurable square spiral microstrip antennas. IEEE Transactions on Antennas and Propagation **54**(2), 464 (2006).

[25] S. Nikolaou, N. D. Kingsley, G. E. Ponchak, J. Papapolymerou, and M. M. Tentzeris. *Uwb elliptical monopoles with a reconfigurable band notch using mems switches actuated without bias lines.* IEEE Transactions on Antennas and Propagation **57**(8), 2242 (2009). 8

[26] M. R. Chaharmir, J. Shaker, M. Cuhaci, and A. R. Sebak. *Novel photonically-controlled reflectarray antenna.* IEEE Transactions on Antennas and Propagation **54**(4), 1134 (2006). 8

[27] C. J. Panagamuwa, A. Chauraya, and J. C. Vardaxoglou. *Frequency and beam reconfigurable antenna using photoconducting switches.* IEEE Transactions on Antennas and Propagation **54**(2), 449 (2006). 9

[28] L. N. Pringle, P. H. Harms, S. P. Blalock, G. N. Kiesel, E. J. Kuster, P. G. Friederich, R. J. Prado, J. M. Morris, and G. S. Smith. *A reconfigurable aperture antenna based on switched links between electrically small metallic patches.* IEEE Transactions on Antennas and Propagation **52**(6), 1434 (2004).

[29] Y. Tawk, A. R. Albrecht, S. Hemmady, G. Balakrishnan, and C. G. Christodoulou. *Optically pumped frequency reconfigurable antenna design.* IEEE Antennas and Wireless Propagation Letters **9**, 280 (2010). 9

[30] Y. Tawk, J. Costantine, S. E. Barbin, and C. G. Christodoulou. *Integrating laser diodes in a reconfigurable antenna system.* In *Microwave & Optoelectronics Conference (IMOC), 2011 SBMO/IEEE MTT-S International*, pp. 794–796. 8

[31] J. C. Langer, J. Zou, C. Liu, and J. T. Bernhard. *Micromachined reconfigurable out-of-plane microstrip patch antenna using plastic deformation magnetic actuation.* IEEE Microwave and Wireless Components Letters **13**(3), 120 (2003). 8

[32] S. J. Mazlouman, M. Soleimani, A. Mahanfar, C. Menon, and R. G. Vaughan. *Pattern reconfigurable square ring patch antenna actuated by hemispherical dielectric elastomer*. Electronics Letters **47**(3), 164 (2011). 10

[33] Y. Tawk and C. G. Christodoulou. *A cellular automata reconfigurable microstrip antenna design*. In *2009 IEEE Antennas and Propagation Society International Symposium*, pp. 1–4.

[34] Y. Tawk, J. Costantine, and C. G. Christodoulou. *A frequency reconfigurable rotatable microstrip antenna design*. In *2010 IEEE Antennas and Propagation Society International Symposium*, pp. 1–4. 8

[35] L. Dixit and P. K. S. Pourush. *Radiation characteristics of switchable ferrite microstrip array antenna*. IEE Proceedings - Microwaves, Antennas and Propagation **147**(2), 151 (2000). 9

[36] W. Hu, M. Y. Ismail, R. Cahill, J. A. Encinar, V. F. Fusco, H. S. Gamble, D. Linton, R. Dickie, N. Grant, and S. P. Rea. *Liquid-crystal-based reflectarray antenna with electronically switchable monopulse patterns*. Electronics Letters **43**(14), 1 (2007). 10

[37] L. Liu and R. J. Langley. *Liquid crystal tunable microstrip patch antenna*. Electronics Letters **44**(20), 1179 (2008). 10

[38] D. Pozar and V. Sanchez. *Magnetic tuning of a microstrip antenna on a ferrite substrate*. Electronics Letters **24**(12), 729 (1988). 9, 10

[39] S. Yang, C. Zhang, H. K. Pan, A. E. Fathy, and V. K. Nair. *Frequency-reconfigurable antennas for multiradio wireless platforms*. IEEE Microwave Magazine **10**(1), 66 (2009). 9

[40] C. A. Balanis. *Antenna Theory: Analysis and Design* (Wiley-Interscience, 2005). 13, 15, 16, 17, 25, 42, 82, 84

[41] J. T. Bernhard. *Reconfigurable antennas*. Synthesis Lectures on Antennas **2**(1), 1 (2007). 9

[42] C. Kittel. *Introduction to solid state physics* (Wiley, 1976). 9

[43] M. C. Tang, T. Shi, and R. W. Ziolkowski. *Flexible efficient quasi-yagi printed uniplanar antenna*. IEEE Transactions on Antennas and Propagation **63**(12), 5343 (2015). 10

[44] D. Sievenpiper, J. Schaffner, R. Loo, G. Tangonan, S. Ontiveros, and R. Harold. *A tunable impedance surface performing as a reconfigurable beam steering reflector*. IEEE Transactions on Antennas and Propagation **50**(3), 384 (2002). 11

[45] D. F. Sievenpiper, J. H. Schaffner, H. J. Song, R. Y. Loo, and G. Tangonan. *Two-dimensional beam steering using an electrically tunable impedance surface*. IEEE Transactions on Antennas and Propagation **51**(10), 2713 (2003). 12

[46] D. Sievenpiper, J. Schaffner, J. J. Lee, and S. Livingston. *A steerable leaky-wave antenna using a tunable impedance ground plane*. IEEE Antennas and Wireless Propagation Letters **1**(1), 179 (2002). 12

[47] C. G. Christodoulou, Y. Tawk, S. A. Lane, and S. R. Erwin. *Reconfigurable antennas for wireless and space applications*. Proceedings of the IEEE **100**(7), 2250 (2012). 12

[48] R. Munson. *Conformal microstrip antennas and microstrip phased arrays*. Antennas and Propagation, IEEE Transactions on **22**(1), 74 (1974). 13, 25, 42, 82, 84

[49] A. G. Derneryd. *Linearly polarized microstrip antennas*. Antennas and Propagation, IEEE Transactions on **24**(6), 846 (1976). 17

[50] A. G. Derneryd. *A theoretical investigation of the rectangular microstrip antenna element*. Antennas and Propagation, IEEE Transactions on **26**(4), 532 (1978). 13, 17

[51] K. R. Carver and J. Mink. *Microstrip antenna technology.* Antennas and Propagation, IEEE Transactions on **29**(1), 2 (1981). 13, 15, 17, 25, 42, 82, 84

[52] R. Ghatak and M. Pal. *Revisiting relations for modeling the input resistance of a rectangular microstrip antenna [antenna designer's notebook].* Antennas and Propagation Magazine, IEEE **57**(4), 116 (2015). 13, 14, 17, 18, 84

[53] L. I. Basilio, M. A. Khayat, J. T. Williams, and S. A. Long. *The dependence of the input impedance on feed position of probe and microstrip line-fed patch antennas.* Antennas and Propagation, IEEE Transactions on **49**(1), 45 (2001). 13, 18

[54] H. Ying, D. R. Jackson, J. T. Williams, S. A. Long, and V. R. Komanduri. *Characterization of the input impedance of the inset-fed rectangular microstrip antenna.* Antennas and Propagation, IEEE Transactions on **56**(10), 3314 (2008). 14, 17

[55] C. Garvin, R. Munson, L. Ostwald, and K. Schroeder. *Missile base mounted microstrip antennas.* Antennas and Propagation, IEEE Transactions on **25**(5), 604 (1977). 23

[56] H. K. Kan and R. B. Waterhouse. *Size reduction technique for shorted patches.* Electronics Letters **35**(12), 948 (1999). 23

[57] S. Reed, L. Desclos, C. Terret, and S. Toutain. *Patch antenna size reduction by means of inductive slots.* Microwave and Optical Technology Letters **29**(2), 79 (2001).

[58] L. Desclos, Y. Mahe, S. Reed, G. Poilasne, and S. Toutain. *Patch antenna size reduction by combining inductive loading and short-points technique.* Microwave and Optical Technology Letters **30**(6), 385 (2001). 23

[59] D. Schaubert, F. Farrar, A. Sindoris, and S. Hayes. *Microstrip antennas with frequency agility and polarization diversity.* Antennas and Propagation, IEEE Transactions on **29**(1), 118 (1981). 23, 41, 42

[60] D. L. Sengupta. *Resonant frequency of a tunable rectangular patch antenna.* Electronics Letters **20**(15), 614 (1984). 23

[61] G. L. Lan and D. L. Sengupta. *Tunable circular patch antennas.* Electronics Letters **21**(22), 1022 (1985). 24

[62] R. Garg. *Microstrip Antenna Design Handbook* (Artech House, 2001). 24

[63] T. Chakravarty and A. De. *Design of tunable modes and dual-band circular patch antenna using shorting posts.* IEE Proceedings - Microwaves, Antennas and Propagation **146**(3), 224 (1999). 24

[64] T. Chakravarty and A. De. *Resonant frequency of a shorted circular patch with the use of a modified impedance expression for a metallic post.* Microwave and Optical Technology Letters **33**(4), 252 (2002). 24

[65] D. Ghosh, S. K. Ghosh, S. Chattopadhyay, S. Nandi, D. Chakraborty, R. Anand, R. Raj, and A. Ghosh. *Physical and quantitative analysis of compact rectangular microstrip antenna with shorted non-radiating edges for reduced cross-polarized radiation using modifi ed cavity model.* IEEE Antennas and Propagation Magazine **56**(4), 61 (2014). 24

[66] Y. J. Wang and C. K. Lee. *Compact and broadband microstrip patch antenna for the 3g imt-2000 handsets applying styrofoam and shorting-posts.* Progress In Electromagnetics Research **47**, 75 (2004). 24

[67] B. Majumdar and K. P. Esselle. *A dual-mode reconfigurable patch antenna and an extended transmission line model.* Microwave and Optical Technology Letters **58**(1), 57 (2016). 24, 46

[68] B. Majumdar and K. P. Esselle. *Modelling the effect of a thin shorting post in an arbitrary position along the outer radiating edge of a rectangular patch antenna.* In *2015 International Symposium on Antennas and Propagation (ISAP)*, pp. 1–3. 24, 47

[69] W.-F. Chen, D. Yu, and S.-X. Gong. *An omnidirectional triple-band circular patch antenna based on open elliptical-ring slots and the shorting vias.* Progress In Electromagnetics Research **150**, 197 (2015). 24

[70] M. Biswas and A. Mandal. *Experimental and theoretical investigation to predict the effect of superstrate on the impedance, bandwidth, and gain characteristics for a rectangular patch antenna.* Journal of Electromagnetic Waves and Applications **29**(16), 2093 (2015). 24

[71] W. Richards, L. Yuen, and D. Harrison. *An improved theory for microstrip antennas and applications.* Antennas and Propagation, IEEE Transactions on **29**(1), 38 (1981). 41

[72] P. M. Haskins, P. S. Hall, and J. S. Dahele. *Polarisation-agile active patch antenna.* Electronics Letters **30**(2), 98 (1994). 41

[73] P. M. Haskins and J. S. Dahele. *Varactor-diode loaded passive polarisation-agile patch antenna.* Electronics Letters **30**(13), 1074 (1994). 42

[74] P. M. Haskins and J. S. Dahele. *Four-element varactor diode loaded polarisation-agile microstrip antenna array.* Electronics Letters **33**(14), 1186 (1997). 41, 42

[75] P. M. Haskins, P. S. Hall, and J. S. Dahele. *Active patch antenna element with diode tuning.* Electronics Letters **27**(20), 1846 (1991). 41

[76] R. B. Waterhouse. *Modelling of schottky-barrier diode loaded microstrip array elements.* Electronics Letters **28**(19), 1799 (1992). 41

[77] R. B. Waterhouse and N. V. Shuley. *Dual frequency microstrip rectangular patches.* Electronics Letters **28**(7), 606 (1992). 42

[78] R. B. Waterhouse and N. V. Shuley. *Scan performance of infinite arrays of microstrip patch elements loaded with varactor diodes.* Antennas and Propagation, IEEE Transactions on **41**(9), 1273 (1993). 41, 42

[79] R. B. Waterhouse and N. V. Shuley. *Full characterisation of varactor-loaded, probe-fed, rectangular, microstrip patch antennas.* Microwaves, Antennas and Propagation, IEE Proceedings **141**(5), 367 (1994). 41, 42

[80] T. Chakravarty, S. K. Sanyal, and A. De. *Resonant modes of circular microstrip radiator loaded with varactor diode.* Radio Science **42**(4), RS4024 (2007). 41

[81] R. B. Waterhouse. *The use of shorting posts to improve the scanning range of probe-fed microstrip patch phased arrays.* Antennas and Propagation, IEEE Transactions on **44**(3), 302 (1996). 42

[82] W.-B. Wei, Q.-Z. Liu, Y.-Z. Yin, and H.-J. Zhou. *Reconfigurable microstrip patch antenna with switchable polarization.* Progress In Electromagnetics Research **75**, 63 (2007). 42

[83] W. Kin-Lu and L. Yi-Fang. *Small broadband rectangular microstrip antenna with chip-resistor loading.* Electronics Letters **33**(19), 1593 (1997). 42

[84] S. V. Hum, J. Z. Chu, R. H. Johnston, and M. Okoniewski. *Efficiency of a resistively loaded microstrip patch antenna.* Antennas and Wireless Propagation Letters, IEEE **2**(1), 22 (2003). 42

[85] E. Ojefors, C. Shi, K. From, I. Skarin, P. Hallbjorner, and A. Rydberg. *Electrically steerable single-layer microstrip traveling wave antenna with varactor diode based phase shifters.* Antennas and Propagation, IEEE Transactions on **55**(9), 2451 (2007). 77

[86] M. H. Nemati, R. Kazemi, and I. Tekin. *Pattern reconfigurable patch array for 2.4 ghz wlan systems.* Microwave and Optical Technology Letters **56**(10), 2377 (2014). 77

[87] P. Padilla, J. M. Fernandez-Gonzalez, A. Munoz-Acevedo, J. L. Padilla, and M. Sierra-Castaner. *Electronically tunable phase response for phased array patches.* Electronics Letters **46**(18), 1248 (2010). 78

[88] J. Brown and W. Jackson. *The properties of artificial dielectrics at centimetre wavelengths.* Proceedings of the IEE - Part B: Radio and Electronic Engineering **102**(1), 11 (1955). 97

[89] W. Rotman and R. Turner. *Wide-angle microwave lens for line source applications.* IEEE Transactions on Antennas and Propagation **11**(6), 623 (1963). 97

[90] K. C. Gupta. *Narrow-beam antennas using an artificial dielectric medium with permittivity less than unity.* Electronics Letters **7**(1), 16 (1971). 97

[91] I. Bahl and K. Gupta. *A leaky-wave antenna using an artificial dielectric medium.* IEEE Transactions on Antennas and Propagation **22**(1), 119 (1974). 97

[92] D. M. Bowie and K. S. Kelleher. *Rapid measurement of dielectric constant and loss tangent.* IRE Transactions on Microwave Theory and Techniques **4**(3), 137 (1956). 97

[93] K. Gupta. *Waveguide-sandwich electromagnetic window.* Electronics Letters **3**(12), 540 (1967). 97

[94] T. Chich-Hsing and R. Mittra. *A spectral-iteration approach for analyzing scattering from frequency selective surfaces.* IEEE Transactions on Antennas and Propagation **30**(2), 303 (1982). 97

[95] C. Caloz and T. Itoh. *Electromagnetic Metamaterials: Transmission Line Theory and Microwave Applications* (Wiley, 2005). 97, 98

[96] N. Engheta and R. Ziolkowski. *Metamaterials: Physics and Engineering Explorations* (Wiley, 2006). 98

[97] D. H. Kwon and D. H. Werner. *Transformation electromagnetics: An overview of the theory and applications.* IEEE Antennas and Propagation Magazine **52**(1), 24 (2010).

[98] S. Maci, G. Minatti, M. Casaletti, and M. Bosiljevac. *Metasurfing: Addressing waves on impenetrable metasurfaces.* IEEE Antennas and Wireless Propagation Letters **10**, 1499 (2011). 98

[99] D. Werner and D. Kwon. *Transformation Electromagnetics and Metamaterials: Fundamental Principles and Applications* (Springer London, 2013). 98

[100] E. Martini, G. M. Sardi, and S. Maci. *Homogenization processes and retrieval of equivalent constitutive parameters for multisurface-metamaterials.* IEEE Transactions on Antennas and Propagation **62**(4), 2081 (2014). 97

[101] J. B. Pendry, A. J. Holden, D. J. Robbins, and W. J. Stewart. *Magnetism from conductors and enhanced nonlinear phenomena.* IEEE Transactions on Microwave Theory and Techniques **47**(11), 2075 (1999). 97

[102] R. A. Shelby, D. R. Smith, and S. Schultz. *Experimental verification of a negative index of refraction.* Science **292**(5514), 77 (2001). 97

[103] M. Bosiljevac, M. Casaletti, F. Caminita, Z. Sipus, and S. Maci. *Non-uniform metasurface luneburg lens antenna design.* IEEE Transactions on Antennas and Propagation **60**(9), 4065 (2012). 98

[104] G. Minatti, F. Caminita, M. Casaletti, and S. Maci. *Spiral leaky-wave antennas based on modulated surface impedance.* IEEE Transactions on Antennas and Propagation **59**(12), 4436 (2011).

[105] G. Minatti, S. Maci, P. D. Vita, A. Freni, and M. Sabbadini. *A circularly-polarized isoflux antenna based on anisotropic metasurface.* IEEE Transactions on Antennas and Propagation **60**(11), 4998 (2012).

[106] W. Tang, C. Argyropoulos, E. Kallos, W. Song, and Y. Hao. *Discrete coordinate transformation for designing all-dielectric flat antennas.* IEEE Transactions on Antennas and Propagation **58**(12), 3795 (2010).

[107] A. Demetriadou and Y. Hao. *A grounded slim luneburg lens antenna based on transformation electromagnetics*. IEEE Antennas and Wireless Propagation Letters **10**, 1590 (2011).

[108] C. Mateo-Segura, A. Dyke, H. Dyke, S. Haq, and Y. Hao. *Flat luneburg lens via transformation optics for directive antenna applications*. IEEE Transactions on Antennas and Propagation **62**(4), 1945 (2014). 98

[109] F. Bilotti and L. Sevgi. *Metamaterials: Rf and microwave applications*. International Journal of RF and Microwave Computer-Aided Engineering **22**(4), 421 (2012). 98

[110] G. Oliveri, D. Werner, F. Bilotti, and C. Craeye. *Reconfigurable electromagnetics through metamaterials*. International Journal of Antennas and Propagation **2014**, 2 (2014). 98

[111] J. P. Turpin, J. A. Bossard, K. L. Morgan, D. H. Werner, and P. L. Werner. *Reconfigurable and tunable metamaterials: A review of the theory and applications*. International Journal of Antennas and Propagation **2014**, 18 (2014). 98

[112] D. Gonz, x00E, O. lez, E. Martini, B. Loiseaux, C. Tripon-Canseliet, J. Chazelas, and S. Maci. *Reconfigurable transmission lines based on self-complementary metasurfaces*. In *The 8th European Conference on Antennas and Propagation (EuCAP 2014)*, pp. 271–275.

[113] S. C. Pavone, E. Martini, M. Albani, S. Maci, C. Renard, and J. Chazelas. *A novel approach to low profile scanning antenna design using reconfigurable metasurfaces*. In *2014 International Radar Conference*, pp. 1–4. 98

[114] I. Gil, F. Martin, X. Rottenberg, and W. D. Raedt. *Tunable stop-band filter at q-band based on rf-mems metamaterials*. Electronics Letters **43**(21), 1153 (2007). 98, 99

[115] T. Hand and S. Cummer. *Characterization of tunable metamaterial elements*

using mems switches. IEEE Antennas and Wireless Propagation Letters **6**, 401 (2007). 98, 99

[116] M. D. Goldflam, T. Driscoll, B. Chapler, O. Khatib, N. Marie Jokerst, S. Palit, D. R. Smith, B.-J. Kim, G. Seo, H.-T. Kim, M. D. Ventra, and D. N. Basov. *Reconfigurable gradient index using vo2 memory metamaterials.* Applied Physics Letters **99**(4), 044103 (2011). 98

[117] C. L. Holloway, E. F. Kuester, J. A. Gordon, J. O. Hara, J. Booth, and D. R. Smith. *An overview of the theory and applications of metasurfaces: The two-dimensional equivalents of metamaterials.* IEEE Antennas and Propagation Magazine **54**(2), 10 (2012). 98, 99

[118] J. Lee, S. Jung, P.-Y. Chen, F. Lu, F. Demmerle, G. Boehm, M.-C. Amann, A. Al, and M. A. Belkin. *Ultrafast electrically tunable polaritonic metasurfaces.* Advanced Optical Materials **2**(11), 1057 (2014). 98

[119] Q. Zhao, L. Kang, B. Du, B. Li, J. Zhou, H. Tang, X. Liang, and B. Zhang. *Electrically tunable negative permeability metamaterials based on nematic liquid crystals.* Applied Physics Letters **90**(1), 011112 (2007). 98

[120] J. A. Bossard, X. Liang, L. Li, S. Yun, D. H. Werner, B. Weiner, T. S. Mayer, P. F. Cristman, A. Diaz, and I. C. Khoo. *Tunable frequency selective surfaces and negative-zero-positive index metamaterials based on liquid crystals.* IEEE Transactions on Antennas and Propagation **56**(5), 1308 (2008).

[121] D. H. Werner, D.-H. Kwon, I.-C. Khoo, A. V. Kildishev, and V. M. Shalaev. *Liquid crystal clad near-infrared metamaterials with tunable negative-zero-positive refractive indices.* Optics Express **15**(6), 3342 (2007). 99

[122] A. Minovich, D. N. Neshev, D. A. Powell, I. V. Shadrivov, and Y. S. Kivshar. *Tunable fishnet metamaterials infiltrated by liquid crystals.* Applied Physics Letters **96**(19), 193103 (2010). 98

[123] T. S. Kasirga, Y. N. Ertas, and M. Bayindir. *Microfluidics for reconfigurable electromagnetic metamaterials.* Applied Physics Letters **95**(21), 214102 (2009). 98, 99

[124] B. Sensale-Rodr, x00Ed, guez, R. Yan, L. Liu, D. Jena, and H. G. Xing. *Graphene for reconfigurable terahertz optoelectronics.* Proceedings of the IEEE **101**(7), 1705 (2013). 98, 99

[125] B. Vasi, M. M. Jakovljevi, G. Isi, and R. Gaji. *Tunable metamaterials based on split ring resonators and doped graphene.* Applied Physics Letters **103**(1), 011102 (2013). 99

[126] C. Pai-Yen, S. Jason, R. P. Yashwanth, M. B. Hossein, B. Y. Alexander, and A. Andrea. *Nanostructured graphene metasurface for tunable terahertz cloaking.* New Journal of Physics **15**(12), 123029 (2013). 98

[127] E. Forati, G. W. Hanson, A. B. Yakovlev, and A. Al. *Planar hyperlens based on a modulated graphene monolayer.* Physical Review B **89**(8), 081410 (2014). PRB. 98

[128] M. Kafesaki, N. H. Shen, S. Tzortzakis, and C. M. Soukoulis. *Optically switchable and tunable terahertz metamaterials through photoconductivity.* Journal of Optics **14**(11), 114008 (2012). 98

[129] K. Fan, X. Zhao, J. Zhang, K. Geng, G. R. Keiser, H. R. Seren, G. D. Metcalfe, M. Wraback, X. Zhang, and R. D. Averitt. *Optically tunable terahertz metamaterials on highly flexible substrates.* IEEE Transactions on Terahertz Science and Technology **3**(6), 702 (2013). 98

[130] F. Martin, J. L. Carreras, J. Bonache, F. Falcone, T. Lopetegi, M. A. G. Laso, and M. Sorolla. *Frequency tuning in electromagnetic bandgap nonlinear transmission lines.* Electronics Letters **39**(5), 440 (2003). 98

[131] I. Gil, J. Garcia-Garcia, J. Bonache, F. Martin, M. Sorolla, and R. Marques.

Varactor-loaded split ring resonators for tunable notch filters at microwave frequencies. Electronics Letters **40**(21), 1347 (2004). 98, 99

[132] P.-Y. Chen, H. Huang, D. Akinwande, and A. Al. *Graphene-based plasmonic platform for reconfigurable terahertz nanodevices.* ACS Photonics **1**(8), 647 (2014). 98

[133] D.-H. Kwon, X. Wang, Z. Bayraktar, B. Weiner, and D. H. Werner. *Near-infrared metamaterial films with reconfigurable transmissive/reflective properties.* Optics Letters **33**(6), 545 (2008). 98

[134] I. C. Khoo, A. Diaz, J. Liou, M. V. Stinger, J. Huang, and Y. Ma. *Liquid crystals tunable optical metamaterials.* IEEE Journal of Selected Topics in Quantum Electronics **16**(2), 410 (2010). 98

[135] I. Gil, J. Bonache, J. Garcia-Garcia, and F. Martin. *Tunable metamaterial transmission lines based on varactor-loaded split-ring resonators.* IEEE Transactions on Microwave Theory and Techniques **54**(6), 2665 (2006). 98

[136] K. Aydin and E. Ozbay. *Capacitor-loaded split ring resonators as tunable metamaterial components.* Journal of Applied Physics **101**(2), 024911 (2007). 98

[137] I. Martinez, A. H. Panaretos, D. H. Werner, G. Oliveri, and A. Massa. *Ultra-thin reconfigurable electromagnetic metasurface absorbers.* In *Antennas and Propagation (EuCAP), 2013 7th European Conference on*, pp. 1843–1847. 98

[138] P. Rocca, M. Benedetti, M. Donelli, D. Franceschini, and A. Massa. *Evolutionary optimization as applied to inverse scattering problems.* Inverse Problems **25**(12), 123003 (2009).

[139] P. Rocca, G. Oliveri, and A. Massa. *Differential evolution as applied to electromagnetics.* IEEE Antennas and Propagation Magazine **53**(1), 38 (2011). 98

[140] L. Sungjoon, C. Caloz, and T. Itoh. *Metamaterial-based electronically controlled transmission-line structure as a novel leaky-wave antenna with tunable radiation*

angle and beamwidth. IEEE Transactions on Microwave Theory and Techniques **53**(1), 161 (2005). 99

[141] X. Wang, D.-H. Kwon, D. H. Werner, I.-C. Khoo, A. V. Kildishev, and V. M. Shalaev. *Tunable optical negative-index metamaterials employing anisotropic liquid crystals.* Applied Physics Letters **91**(14), 143122 (2007). 99

[142] J. Wang, S. Liu, S. Guruswamy, and A. Nahata. *Reconfigurable liquid metal based terahertz metamaterials via selective erasure and refilling to the unit cell level.* Applied Physics Letters **103**(22), 221116 (2013). 99

[143] G. Oliveri, D. H. Werner, and A. Massa. *Reconfigurable electromagnetics through metamaterials - a review.* Proceedings of the IEEE **103**(7), 1034 (2015). 99

[144] S. A. Tretyakov and C. R. Simovski. *Dynamic model of artificial reactive impedance surfaces.* Journal of Electromagnetic Waves and Applications **17**(1), 131 (2003). 100, 101, 107, 117

[145] S. A. Tretyakov, A. J. Viitanen, S. I. Maslovski, and I. E. Saarela. *Impedance boundary conditions for regular dense arrays of dipole scatterers.* IEEE Transactions on Antennas and Propagation **51**(8), 2073 (2003). 100, 107, 117

[146] O. Luukkonen, C. Simovski, G. Granet, G. Goussetis, D. Lioubtchenko, A. V. Raisanen, and S. A. Tretyakov. *Simple and accurate analytical model of planar grids and high-impedance surfaces comprising metal strips or patches.* IEEE Transactions on Antennas and Propagation **56**(6), 1624 (2008). 100, 101, 103

[147] O. Luukkonen, C. R. Simovski, A. V. Raisanen, and S. A. Tretyakov. *An efficient and simple analytical model for analysis of propagation properties in impedance waveguides.* IEEE Transactions on Microwave Theory and Techniques **56**(7), 1624 (2008). 100, 101, 103

[148] R. C. Compton, L. B. Whitbourn, and R. C. McPhedran. *Strip gratings at a dielectric interface and application of babinet?s principle.* Applied Optics **23**(18), 3236 (1984). 101, 107

[149] L. B. Whitbourn and R. C. Compton. *Equivalent-circuit formulas for metal grid reflectors at a dielectric boundary.* Applied Optics **24**(2), 217 (1985). 111

[150] D. Sievenpiper. *High-Impedance Electromagnetic Surfaces.* Phd (1999). 115

[151] D. Sievenpiper, Z. Lijun, R. F. J. Broas, N. G. Alexopolous, and E. Yablonovitch. *High-impedance electromagnetic surfaces with a forbidden frequency band.* IEEE Transactions on Microwave Theory and Techniques **47**(11), 2059 (1999). 115, 142

[152] F. Yang, A. Aminian, and Y. Rahmat-Samii. *A novel surface-wave antenna design using a thin periodically loaded ground plane.* Microwave and Optical Technology Letters **47**(3), 240 (2005). 115, 117, 139, 140

[153] F. Terman. *Radio engineer's handbook* (McGraw-Hill Book Company, inc., 1943). 122

[154] E. Rosa and F. Grover. *Formulas and tables for the calculation of mutual and self-inductance* (U.S. Dept. of Commerce and Labor, Bureau of Standards, 1912). 123

[155] M. Quinten, A. Leitner, J. R. Krenn, and F. R. Aussenegg. *Electromagnetic energy transport via linear chains of silver nanoparticles.* Optics Letters **23**(17), 1331 (1998). 127

[156] J. Shefer. *Periodic cylinder arrays as transmission lines.* IEEE Transactions on Microwave Theory and Techniques **11**(1), 55 (1963). 127, 132, 139

[157] S. A. Maier, M. L. Brongersma, and H. A. Atwater. *Electromagnetic energy transport along arrays of closely spaced metal rods as an analogue to plasmonic devices.* Applied Physics Letters **78**(1), 16 (2001). 127, 129, 135, 139

[158] W. M. Saj, T. J. Antosiewicz, J. Pniewski, and T. Szoplik. *Energy transport in plasmon waveguides on chains of metal nanoplates.* Opto-Electronics Review **14**(3), 243 (2006). 128, 139

[159] W. M. Saj, T. J. Antosiewicz, J. Pniewski, and T. Szoplik. *Plasmon waveguides on silver nanoelements.* vol. 6195, pp. 61950Y–61950Y–11. 10.1117/12.662932. 128

[160] J. O. Spector. *An investigation of periodic rod structures for yagi aerials.* Proceedings of the IEE - Part B: Radio and Electronic Engineering **105**(19), 38 (1958). 132

[161] S. K. Sharma, F. Fideles, and A. Kalikond. *Planar yagi-uda antenna with reconfigurable radiation patterns.* Microwave and Optical Technology Letters **55**(12), 2946 (2013). 138, 139

[162] L. Mei, X. Shao-Qiu, W. Zhao, and W. Bing-Zhong. *Compact surface-wave assisted beam-steerable antenna based on his.* Antennas and Propagation, IEEE Transactions on **62**(7), 3511 (2014). 138

[163] D. Xiao and W. Bing-Zhong. *A novel wideband antenna with reconfigurable broadside and endfire patterns.* Antennas and Wireless Propagation Letters, IEEE **12**, 995 (2013). 138, 139

[164] R. Jian, Y. Xi, Y. Jiayuan, and Y. Yingzeng. *A novel antenna with reconfigurable patterns using h-shaped structures.* IEEE Antennas and Wireless Propagation Letters **14**, 915 (2015). 138

[165] J. Huang and A. C. Densmore. *Microstrip yagi array antenna for mobile satellite vehicle application.* Antennas and Propagation, IEEE Transactions on **39**(7), 1024 (1991). 139